

An X-ray Census of the Youngest Galactic Star Clusters



Patrick Kavanagh, B.Sc.
School of Physical Sciences
Dublin City University

A thesis submitted for the degree of
Doctor of Philosophy

March 2011

Supervisors
Dr. Laura Norci
Prof. Evert Meurs

For my mother ...

Acknowledgements

This thesis would not have been possible without the help of many people during my time as a PhD student, with regard to both the work and general support.

Work

First and foremost. I would like to thank my supervisors Dr. Laura Norci and Prof. Evert Meurs, who took me on as a student and whose help and guidance was excellent and very much appreciated throughout the years. I would also like to thank the rest of the DCU School of Physical Sciences academic staff who were always helpful, particularly Dr. Tony Cafolla who sorted out registration and financial problems for me more than once! In addition, the support staff of DCU were always great during my time there, especially Lisa Peyton and Sheila Boughton, not to mention Ray Murphy who I annoyed most often!

As well as the staff I would like to thank the other students who made my time in DCU enjoyable, particularly my office mates over the years: Conor, Justina, Mairead, Ruth, Daragh and Matty. In addition I would like to thank Susanna, Paul and Colin for their help with all things astronomy in the early days, and Emma for her help with IRAF towards the end. Finally I would like to thank the lunch crew of Wayne, John and Barry, with whom I had many a nonsensical discussion.

Support

Behind all of the work I had people who were always supportive and helpful during my PhD time. First of all, there is of course Paddy,

Wayney and Johnny, with whom I have come through my entire university life. It was great to have such friends throughout, even the dog! Then there is my family who, through thick and thin, kept my feet firmly planted on the ground. Thanks to my Dad, Jimmy, Claire, Paul, Dayde, Sandra and even Stevo, and my fantastic nieces Rachel, Leah, Amy and Kayla, who always reminded me of what life is really all about. Also thanks to my aunts, uncles and cousins, particularly Jackie, Sheila and Claire, and also to Mary and Teresa for their support. Someone who was vital towards the end was my thesis angel, without whom I'm not sure what I would have done or how I would have finished! She is forever in my gratitude.

Lastly, and most importantly, I would like to thank my mother. None of this would have been possible without that timely kick up the backside she gave me all those years ago, as well as the unending support she has given me throughout my life. This thesis is dedicated to her.

Abstract

Stellar clusters are vitally important laboratories for astrophysical research. These clusters, some of which have populations numbering in the hundreds of thousands, comprise a coeval stellar population of similar chemical composition at the same distance, the analysis of which can confront stellar evolution theory as well as offering insights into the distribution of stellar masses in the Galaxy, the so called Initial Mass Function. Additionally, these clusters are the engines by which material in the Universe is recycled through the evolution and destruction of massive stars which redistribute material throughout a region via a cluster wind. This is a process best observed at X-ray wavelengths due to the temperature of the winds, however the actual strength of a cluster wind can be masked by apparent diffuse emission from unresolved sources in the region. In this Ph.D. project I have investigated this issue by characterising the X-ray emission from the youngest Galactic star clusters and quantifying the strength of the relative contributions to the observed diffuse emission. These observational results were found to be in agreement with theoretical models in the literature. Additionally, this analysis provided a wealth of information on the various cluster sub-populations as well as the clusters as a whole. Trends in the properties of the sub-populations with cluster age were investigated verifying previous observational results from the literature as well as demonstrating new trends, such as the frequency of magnetic wind sources in the youngest clusters. Supplementary to these analyses, the universality of the Initial Mass Function was probed in these clusters using the distribution of X-ray luminosities in a population known as the X-ray Luminosity Function. This was achieved by comparing the derived cluster X-ray Luminosity Functions to a well known and surveyed stellar population. It was found that the shape of the X-ray Luminosity Function of the clusters were generally consistent with that of the calibration cluster implying a similar underlying Initial Mass Function.

Contents

1	Introduction	1
1.1	Young Stellar Clusters in X-rays	1
1.2	The Initial Mass Function and the X-ray Luminosity Function	2
1.3	Rationale and Plan of the Thesis	5
1.4	X-ray Emission from Across the Mass Spectrum	6
1.4.1	Massive Stars - Radiatively Driven Instability Shocks (RDIS)	6
1.4.2	Massive Stars - Magnetically Confined Wind Shocks (MCWS)	7
1.4.3	Massive Stars - Wolf Rayets	8
1.4.4	Colliding Wind Binaries	9
1.4.5	Low Mass Pre-Main Sequence Stars	10
1.4.6	Post-Supernova	11
1.4.6.1	Young Supernovae and Supernova Remnants	12
1.4.6.2	Collapsed Objects	13
1.4.7	Diffuse Sources	13
1.4.7.1	Cluster Wind	14
1.4.7.2	Unresolved PMS Stars	16
1.5	X-ray Astronomy	17
1.6	Chandra	17
1.6.1	HRMA	18
1.6.2	ACIS	19
1.7	Programme Clusters Selection	20
1.7.1	Cluster Selection	20
1.7.2	Cluster Location	24
1.7.3	Cluster Completeness	26

2	Data Reduction and Analysis	27
2.1	Data Reduction and Analysis Procedures	27
2.1.1	Observational Data Processing	27
2.1.2	Point Source Analysis	29
2.1.2.1	Source Detection	29
2.1.2.2	Source Extraction, Photometry, Spectroscopy and Temporal Analysis	30
2.1.2.3	2MASS Catalogue Matching	31
2.1.2.4	Galactic Contamination	32
2.1.2.5	Extragalactic Contamination	33
2.1.3	Diffuse Emission Analysis	35
2.2	Spectral Fitting and <i>XSPEC</i>	37
3	Programme Cluster Results	39
3.1	IC 1805	40
3.1.1	Analysis	41
3.1.1.1	Known High Mass Stars	44
3.1.1.2	Candidate OB Stars	46
3.1.1.3	Pre-Main Sequence Stars	48
3.1.1.4	Diffuse Emission	52
3.1.1.5	XLF	53
3.1.1.6	Summary	56
3.2	Bica 1 and Bica 2	57
3.2.1	Summary	58
3.3	IC 1590	64
3.3.1	Summary	65
3.4	NGC 1893	68
3.4.1	Summary	70
3.5	NGC 2362	73
3.5.1	Summary	74
3.6	NGC 3603	78
3.6.1	Summary	79
3.7	NGC 6611	84
3.7.1	Summary	85
3.8	NGC 6618	89
3.8.1	Summary	90

3.9	Trumpler 14	94
3.9.1	Summary	95
3.10	Trumpler 16	99
3.10.1	Summary	100
3.11	Westerlund 1	104
3.11.1	Summary	106
3.12	Westerlund 2	110
3.12.1	Summary	113
4	Diffuse Thermal X-ray Emission in the Core of Westerlund 1	117
4.1	Introduction	117
4.2	Observations and Analysis	118
4.2.1	Point Sources	118
4.2.2	Diffuse Analysis	119
4.3	Discussion	125
4.3.1	Origin of 6.7 keV Emission Line	125
4.3.1.1	Point Source Contamination	125
4.3.1.2	Reflection	126
4.3.1.3	Instrumental Background	127
4.3.1.4	Cosmic Background	128
4.3.2	Sources of Hard Emission	128
4.3.2.1	Cluster Wind	129
4.3.2.2	Supernova Remnants	131
4.3.2.3	Unresolved Pre-Main Sequence Stars	132
4.4	Conclusions	133
5	Results	136
5.1	General Results of the Sub-Populations	136
5.1.1	Massive Stars	136
5.1.1.1	Radiatively Driven Instability Shock Emitters	138
5.1.1.2	Magnetically Confined Wind Shock Emitters	139
5.1.2	Colliding Wind Binaries	142
5.1.3	PMS Stars	144
5.2	Evolution of X-ray Emission in the Clusters	147
5.3	Probing the IMF using the XLF	151
6	Conclusions and Future Prospects	154

A	Data Reduction and Analysis Commands	157
A.1	<i>Chandra</i> Data Reduction	157
A.1.1	Diffuse Emission	161
A.2	<i>ACIS Extract</i> Setup and Usage	164
A.2.1	Setup	166
A.2.2	Usage	167
B	Programme Cluster Figures and Tables	174
B.1	Bica 1 and Bica 2	175
B.2	IC 1590	185
B.3	NGC 1893	190
B.4	NGC 2362	197
B.5	NGC 3603	202
B.6	NGC 6611	207
B.7	NGC 6618	214
B.8	Trumpler 14	220
B.9	Trumpler 16	226
B.10	Westerlund 1	232
B.11	Westerlund 2	239
	References	254

List of Figures

1.1	Salpeter and Kroupa Initial Mass Functions	3
1.2	X-ray luminosity against bolometric luminosity for a flux limited sample of OB stars observed during the <i>ROSAT</i> All-Sky Survey	7
1.3	Schematic of Magnetically Confined Wind Shock model to explain X-ray emission from magnetic early type stars	8
1.4	Stages of Young Stellar Object evolution	11
1.5	Schematic showing the winds from uniformly distributed stars in a cluster interacting to produce a cluster wind	14
1.6	2-8 keV XLF of the M 17 PMS population with scaled Orion Nebular Cluster XLF for comparison	16
1.7	A rendered image of <i>Chandra</i> and its instruments	18
1.8	The four nested HRMA mirror pairs and associated structures	19
1.9	A Schematic Drawing of the ACIS chip arrays	20
1.10	Plot of the variation of fractional encircled energy with radius calculated for an on-axis point source at selected energies	21
1.11	Plot of the variation of encircled energy radius for circles enclosing 50% and 90% of the power at 1.49 keV and 6.40 keV with source off-axis angle calculated for each of the ACIS-I chips	21
1.12	Plots of the HRMA/ACIS effective area against photon energy and vignetting against photon energy at selected angles	22
1.13	All-sky Aitoff projection showing the position of the programme clusters in relation to the Galactic disk	25
3.1	DSS Image of IC 1805.	41
3.2	<i>Chandra</i> 17'×17' ACIS-I 0.5-8 keV image of IC 1805 with detected sources marked in blue.	42
3.3	Adaptively smoothed <i>Chandra</i> soft (0.5-2 keV, shown in red) and hard (2-8 keV, shown in blue) image of IC 1805.	44

LIST OF FIGURES

3.4	IC 1805 2MASS J vs J-H colour magnitude diagram.	47
3.5	Global properties of the bright IC 1805 PMS population.	49
3.6	Lightcurve of the unusually bright PMS star CXO J023309.98+612459.5	50
3.7	Plots of the 2-8 keV L_X against the median detected photon energy (E_{median}) for the IC 1805 PMS population marked according to E_{median} (left) and variability (right).	51
3.8	Masked and adaptively smoothed 0.5-8 keV image of IC 1805 diffuse emission	52
3.9	IC 1805 all FOV diffuse emission spectrum (left) and cluster core diffuse emission spectrum (right)	53
3.10	IC 1805 bright PMS star spectroscopic/photometric 2-8 keV X-ray luminosity comparison	54
3.11	IC 1805 total cluster 2-8 keV XLF.	55
3.12	IC 1805 2-8 keV XLF (solid line) and the COUP 2-8 keV XLF (dashed line) with high mass stars removed.	56
3.13	Image of Bica 1 and Bica 2 in the Cyg OB2 Association from the Palomar Sky Survey	58
3.14	<i>Chandra</i> ACIS-I 0.5-8 keV image of Bica 1 and Bica 2 with detected sources marked in blue (left) and adaptively smoothed <i>Chandra</i> soft (0.5-2 keV, shown in red) and hard (2-8 keV, shown in blue) image.	59
3.15	Left: Bica 1 total cluster 2-8 keV XLF. Right: Bica 1 PMS star 2-8 keV XLF (solid line) and the COUP 2-8 keV XLF (dashed line).	62
3.16	Left: Bica 2 total cluster 2-8 keV XLF. Right: Bica 2 PMS star 2-8 keV XLF (solid line) and the COUP 2-8 keV XLF (dashed line).	64
3.17	DSS Image of IC 1590.	66
3.18	<i>Chandra</i> ACIS-I 0.5-8 keV image of IC 1590 with detected sources marked in blue (left) and adaptively smoothed <i>Chandra</i> soft (0.5-2 keV, shown in red) and hard (2-8 keV, shown in blue) image.	67
3.19	Left: IC 1590 total cluster 2-8 keV XLF. Right: IC 1590 PMS star 2-8 keV XLF (solid line) and the COUP 2-8 keV XLF (dashed line).	69
3.20	<i>HST</i> Image of NGC 1893.	70
3.21	<i>Chandra</i> ACIS-I 0.5-8 keV image of NGC 1893 with detected sources marked in blue (left) and adaptively smoothed <i>Chandra</i> soft (0.5-2 keV, shown in red) and hard (2-8 keV, shown in blue) image.	71

LIST OF FIGURES

3.22	Left: NGC 1893 total cluster 2-8 keV XLF. Right: NGC 1893 PMS star 2-8 keV XLF (solid line) and the COUP 2-8 keV XLF (dashed line).	73
3.23	DSS Image of NGC 2362.	75
3.24	<i>Chandra</i> ACIS-I 0.5-8 keV image of NGC 2362 with detected sources marked in blue (left) and adaptively smoothed <i>Chandra</i> soft (0.5-2 keV, shown in red) and hard (2-8 keV, shown in blue) image.	76
3.25	Masked and adaptively smoothed 0.5-8 keV image of NGC 2362 diffuse emission	78
3.26	Left: NGC 2362 total cluster 2-8 keV XLF. Right: NGC 2362 PMS star 2-8 keV XLF (solid line) and the COUP 2-8 keV XLF (dashed line).	79
3.27	<i>HST</i> Image of NGC 3603.	80
3.28	<i>Chandra</i> ACIS-I 0.5-8 keV image of NGC 3603 with detected sources marked in blue (left) and adaptively smoothed <i>Chandra</i> soft (0.5-2 keV, shown in red) and hard (2-8 keV, shown in blue) image.	81
3.29	Left: NGC 3603 total cluster 2-8 keV XLF. Right: NGC 3603 unidentified source 2-8 keV XLF (solid line) and the COUP 2-8 keV XLF (dashed line).	84
3.30	<i>HST</i> Image of M 16 with NGC 6611 located in the centre of the nebula.	85
3.31	<i>Chandra</i> 17'×17' ACIS-I 0.5-8 keV image of NGC 6611 with detected sources marked in blue (left) and adaptively smoothed <i>Chandra</i> soft (0.5-2 keV, shown in red) and hard (2-8 keV, shown in blue) image.	86
3.32	Left: NGC 6611 total cluster 2-8 keV XLF. Right: NGC 6611 PMS star 2-8 keV XLF (solid line) and the COUP 2-8 keV XLF (dashed line).	88
3.33	2MASS Image of NGC 6618.	90
3.34	<i>Chandra</i> ACIS-I 0.5-8 keV image of NGC 6618 with detected sources marked in blue (left) and adaptively smoothed <i>Chandra</i> soft (0.5-2 keV, shown in red) and hard (2-8 keV, shown in blue) image. The M17 N and KWO cluster regions are identified in the north and southwest of the left image respectively.	91
3.35	Left: NGC 6618 total cluster 2-8 keV XLF. Right: NGC 6618 PMS star 2-8 keV XLF (solid line) and the COUP 2-8 keV XLF (dashed line).	94
3.36	2MASS Image of Trumpler 14.	95

LIST OF FIGURES

3.37	<i>Chandra</i> ACIS-I 0.5-8 keV image of Trumpler 14 with detected sources marked in blue (left) and adaptively smoothed <i>Chandra</i> soft (0.5-2 keV, shown in red) and hard (2-8 keV, shown in blue).	96
3.38	Left: Trumpler 14 total cluster 2-8 keV XLF. Right: Trumpler 14 PMS star 2-8 keV XLF (solid line) and the COUP 2-8 keV XLF (dashed line).	99
3.39	<i>HST</i> Image of Trumpler 16.	100
3.40	<i>Chandra</i> ACIS-I 0.5-8 keV image of Trumpler 16 with detected sources marked in blue (left) and adaptively smoothed <i>Chandra</i> soft (0.5-2 keV, shown in red) and hard (2-8 keV, shown in blue).	101
3.41	Left: Trumpler 16 total cluster 2-8 keV XLF. The black arrows indicate a lower limit as to the L_X of η Carinae. Right: Trumpler 16 PMS star 2-8 keV XLF (solid line) and the COUP 2-8 keV XLF (dashed line).	105
3.42	2MASS Image of Westerlund 1.	106
3.43	<i>Chandra</i> ACIS-S 0.5-8 keV image of Westerlund 1 with detected sources marked in blue (left) and adaptively smoothed <i>Chandra</i> soft (0.5-2 keV, shown in red) and hard (2-8 keV, shown in blue) image.	107
3.44	Left: Westerlund 1 total cluster 2-8 keV XLF. Right: Westerlund 1 unidentified source 2-8 keV XLF (solid line) and the COUP 2-8 keV XLF (dashed line).	111
3.45	<i>Spitzer</i> Image of Westerlund 2.	112
3.46	<i>Chandra</i> ACIS-I 0.5-8 keV image of Westerlund 2 with detected sources marked in blue (left) and adaptively smoothed <i>Chandra</i> soft (0.5-2 keV, shown in red) and hard (2-8 keV, shown in blue) image.	113
3.47	Left: Westerlund 2 total cluster 2-8 keV XLF. Right: Westerlund 2 unidentified source 2-8 keV XLF (solid line) and the COUP 2-8 keV XLF (dashed line).	116
4.1	Combined MOS/PN false colour image of Westerlund 1 with red, green and blue corresponding to the 0.3-2 keV, 2-4.5 keV and 4.5-10 keV energy bands, respectively	119
4.2	Smoothed, non-background subtracted, combined MOS1/MOS2 image with the CCDs most affected by the reflection omitted	121
4.3	Combined MOS inner 2' spectrum binned with S/N=3 and fit with an absorbed two temperature thermal plasma model	123

LIST OF FIGURES

4.4	Combined MOS spectrum of sources within a 2' region centered on the cluster core.	126
4.5	Combined MOS background subtracted reflection spectrum, extracted from those regions most contaminated by the out of FOV source. . .	127
4.6	Combined MOS cosmic background spectrum, extracted from those regions least contaminated by the reflection.	128
4.7	Distribution of massive stars in the Westerlund 1 cluster core in relation to the diffuse emission	134
5.1	0.5-8 keV L_X/L_{bol} diagram (top) and 2-8 keV L_X/L_{bol} diagram (bottom) for all high mass sources	137
5.2	Plots of derived kT values for the various spectral types and luminosity classes, where spectral type 3 corresponds to O3, 4 to O4, 10 to B0, etc., emitting via RDIS.	140
5.3	Plots of derived L_X values for the various spectral types and luminosity classes, where spectral type 3 corresponds to O3, 4 to O4, 10 to B0, etc., emitting via RDIS	141
5.4	Plots of spectrally derived N_H against E_{median} for all of the PMS stars in the programme clusters with > 50 counts.	145
5.5	Left: Plots of median 2-8 keV L_X for all of the PMS stars (red) and quiescent PMS stars (blue) against the age of the programme clusters. Right: Plots of median E_{median} for all of the PMS stars (red) and quiescent PMS stars (blue) against the age of the programme clusters.	146
5.6	Left: Plots of median 2-8 keV L_X of the brightest PMS stars against age of the programme clusters. Right: Plots of median kT values against age of the programme clusters. The NGC 3603, Wd1 and Wd2 data points are omitted here due to several of their sources likely being OB stars.	147
5.7	Plot of the cluster X_r values against age	149
5.8	Plot of the cluster X_r values against X_{cl}	151
5.9	The PMS X-ray luminosity function (XLF) for all the programme clusters is shown in comparison with the COUP XLF.	153
B.1	Bica 1 2MASS J vs J-H colour magnitude diagram.	175
B.2	Global properties of the Bica 1 bright PMS population	177

LIST OF FIGURES

B.3	Plots of the 2-8 keV L_X against the median detected photon energy (E_{median}) for the Bica 1 PMS population separated according to E_{median} (left) and variability (right).	178
B.4	Bica 1 total cluster diffuse emission spectrum (left) and cluster core diffuse emission spectrum (right)	179
B.5	Bica 2 2MASS J vs J-H colour magnitude diagram.	180
B.6	Global properties of the Bica 2 bright PMS population	182
B.7	Plots of the 2-8 keV L_X against the median detected photon energy (E_{median}) for the Bica 2 PMS population separated according to E_{median} (left) and variability (right).	183
B.8	Bica 2 total cluster diffuse emission spectrum (left) and cluster core diffuse emission spectrum (right)	184
B.9	IC 1590 2MASS J vs J-H colour magnitude diagram.	185
B.10	Global properties of the IC 1590 bright PMS population	187
B.11	Plots of the 2-8 keV L_X against the median detected photon energy (E_{median}) for the IC 1590 PMS population separated according to E_{median} (left) and variability (right).	188
B.12	IC 1590 total cluster diffuse emission spectrum	189
B.13	NGC 1893 2MASS J vs J-H colour magnitude diagram.	190
B.14	Global properties of the BNGC 1893 bright PMS population	194
B.15	Plots of the 2-8 keV L_X against the median detected photon energy (E_{median}) for the NGC 1893 PMS population separated according to E_{median} (left) and variability (right).	195
B.16	NGC 1893 total cluster diffuse emission spectrum (left) and cluster core diffuse emission spectrum (right)	196
B.17	NGC 2362 2MASS J vs J-H colour magnitude diagram.	197
B.18	Global properties of the NGC 2362 bright PMS population	199
B.19	Plots of the 2-8 keV L_X against the median detected photon energy (E_{median}) for the NGC 2362 PMS population separated according to E_{median} (left) and variability (right).	200
B.20	NGC 2362 total cluster diffuse emission spectrum (left) and cluster core diffuse emission spectrum (right)	201
B.21	NGC 3603 2MASS J vs J-H colour magnitude diagram.	202
B.22	Global properties of the NGC 3603 bright ‘unidentified’ source population	204

LIST OF FIGURES

B.23 Plots of the 2-8 keV L_X against the median detected photon energy (E_{median}) for the NGC 3603 ‘unidentified’ source population separated according to E_{median} (left) and variability (right).	205
B.24 NGC 3603 total cluster diffuse emission spectrum (left) and cluster core diffuse emission spectrum (right)	206
B.25 NGC 6611 2MASS J vs J-H colour magnitude diagram.	207
B.26 Global properties of the NGC 6611 bright PMS population	211
B.27 Plots of the 2-8 keV L_X against the median detected photon energy (E_{median}) for the NGC 6611 PMS population separated according to E_{median} (left) and variability (right).	212
B.28 NGC 6611 all FOV diffuse emission spectrum (left) and cluster core diffuse emission spectrum (right)	213
B.29 NGC 6618 2MASS J vs J-H colour magnitude diagram.	214
B.30 Global properties of the NGC 6618 bright PMS population	217
B.31 Plots of the 2-8 keV L_X against the median detected photon energy (E_{median}) for the NGC 6618 PMS population separated according to E_{median} (left) and variability (right).	218
B.32 NGC 6618 all FOV diffuse emission spectrum (left) and cluster core diffuse emission spectrum (right)	219
B.33 Trumpler 14 2MASS J vs J-H colour magnitude diagram.	220
B.34 Global properties of the Trumpler 14 bright PMS population	223
B.35 Plots of the 2-8 keV L_X against the median detected photon energy (E_{median}) for the Trumpler 14 PMS population separated according to E_{median} (left) and variability (right).	224
B.36 Trumpler 14 total cluster diffuse emission spectrum (left) and cluster core diffuse emission spectrum (right)	225
B.37 Trumpler 16 2MASS J vs J-H colour magnitude diagram.	226
B.38 Global properties of the Trumpler 16 bright PMS population	229
B.39 Plots of the 2-8 keV L_X against the median detected photon energy (E_{median}) for the Trumpler 16 PMS population separated according to E_{median} (left) and variability (right).	230
B.40 Trumpler 16 total cluster diffuse emission spectrum (left) and cluster core diffuse emission spectrum (right)	231
B.41 Westerlund 1 2MASS J vs J-H colour magnitude diagram.	232
B.42 Global properties of the Westerlund 1 bright ‘unidentified’ source population	236

LIST OF FIGURES

B.43 Plots of the 2-8 keV L_X against the median detected photon energy (E_{median}) for the Westerlund 1 ‘unidentified’ source population separated according to E_{median} (left) and variability (right).	237
B.44 Westerlund 1 total cluster diffuse emission spectrum (left) and cluster core diffuse emission spectrum (right)	238
B.45 Westerlund 2 2MASS J vs J-H colour magnitude diagram.	239
B.46 Global properties of the Westerlund 2 bright ‘unidentified’ source population	241
B.47 Plots of the 2-8 keV L_X against the median detected photon energy (E_{median}) for the Westerlund 2 ‘unidentified’ source population separated according to E_{median} (left) and variability (right).	242
B.48 Westerlund 2 total cluster diffuse emission spectrum (left) and cluster core diffuse emission spectrum (right)	243

List of Tables

1.1	Dias et al. Catalogue of Open Clusters with Known Ages $\lesssim 5$ Myr . . .	23
1.2	Dias et al. Catalogue of Open Clusters with Known Ages $\lesssim 5$ Myr and <i>Chandra</i> Observations	24
2.1	<i>Chandra</i> Datasets Retrieved for Analysis	28
3.1	IC 1805 <i>Chandra</i> Catalogue: Basic Source Properties	43
3.2	IC 1805 Known High Mass Star X-ray Spectral Parameters	45
3.3	IC 1805 Candidate OB Star X-ray Spectral Parameters	45
3.4	IC 1805 Diffuse Emission X-ray Spectral Parameters	53
4.1	Westerlund 1 <i>XMM-Newton</i> Point Sources.	120
4.2	Diffuse Spectral Fits.	124
5.1	RDIS X-ray Emitting Properties of the Various Spectral Types	139
5.2	Detected Colliding Wind Binaries	144
5.3	Properties of the Diffuse X-ray Emission of the Programme Clusters .	148
A.1	<i>ACIS Extract</i> Dependent Softwares and Versions	165
A.2	<i>ACIS Extract</i> Standard Directory Structure and Initial Files	168
B.1	Bica 1 Known High Mass Star X-ray Spectral Parameters	176
B.2	Bica 1 Candidate OB Star X-ray Spectral Parameters	176
B.3	Bica1 Diffuse Emission X-ray Spectral Parameters	179
B.4	Bica 2 Known High Mass Star X-ray Spectral Parameters	181
B.5	Bica 2 Candidate OB Star X-ray Spectral Parameters	181
B.6	Bica 2 Diffuse Emission X-ray Spectral Parameters	184
B.7	IC 1590 Known High Mass Star X-ray Spectral Parameters	186
B.8	IC 1590 Candidate OB Star X-ray Spectral Parameters	186
B.9	IC 1590 Diffuse Emission X-ray Spectral Parameters	189

LIST OF TABLES

B.10 NGC 1893 Known High Mass Star X-ray Spectral Parameters	191
B.11 NGC 1893 Candidate OB Star X-ray Spectral Parameters	192
B.12 NGC 1893 Candidate OB Star X-ray Spectral Parameters (Cont.) . . .	193
B.13 NGC 1893 Diffuse Emission X-ray Spectral Parameters	196
B.14 NGC 2362 Known High Mass Star X-ray Spectral Parameters	198
B.15 NGC 2362 Candidate OB Star X-ray Spectral Parameters	198
B.16 NGC 2362 Diffuse Emission X-ray Spectral Parameters	201
B.17 NGC 3603 Known High Mass Star X-ray Spectral Parameters	203
B.18 NGC 3603 Candidate OB Star X-ray Spectral Parameters	203
B.19 NGC 3603 Diffuse Emission X-ray Spectral Parameters	206
B.20 NGC 6611 Known High Mass Star X-ray Spectral Parameters	208
B.21 NGC 6611 Candidate OB Star X-ray Spectral Parameters	209
B.22 NGC 6611 Candidate OB Star X-ray Spectral Parameters (Cont.) . . .	210
B.23 NGC 6611 Diffuse Emission X-ray Spectral Parameters	213
B.24 NGC 6618 Known High Mass Star X-ray Spectral Parameters	215
B.25 NGC 6618 Candidate OB Star X-ray Spectral Parameters	216
B.26 NGC 6618 Diffuse Emission X-ray Spectral Parameters	219
B.27 Trumpler 14 Known High Mass Star X-ray Spectral Parameters	221
B.28 Trumpler 14 Candidate OB Star X-ray Spectral Parameters	222
B.29 Trumpler 14 Diffuse Emission X-ray Spectral Parameters	225
B.30 Trumpler 16 Known High Mass Star X-ray Spectral Parameters	227
B.31 Trumpler 16 Candidate OB Star X-ray Spectral Parameters	228
B.32 Trumpler 16 Diffuse Emission X-ray Spectral Parameters	231
B.33 Westerlund 1 Known High Mass Star X-ray Spectral Parameters	233
B.34 Westerlund 1 Known High Mass Star X-ray Spectral Parameters (Cont.)	234
B.35 Westerlund 1 Candidate OB Star X-ray Spectral Parameters	235
B.36 Westerlund 1 Diffuse Emission X-ray Spectral Parameters	238
B.37 Westerlund 2 Known High Mass Star X-ray Spectral Parameters	240
B.38 Westerlund 2 Candidate OB Star X-ray Spectral Parameters	240
B.39 Westerlund 2 Diffuse Emission X-ray Spectral Parameters	243

Chapter 1

Introduction

1.1 Young Stellar Clusters in X-rays

Stellar clusters are vitally important laboratories for astrophysical research. These clusters, some of which have populations numbering in the hundreds of thousands, contain stars with a wide range of masses, all of which formed from the same parent molecular cloud at about the same time. As such, these clusters comprise a coeval stellar population of similar chemical composition at the same distance, the analysis of which can confront stellar evolution theory as well as offering insights into the distribution of stellar masses in the Galaxy, the so called Initial Mass Function (IMF), which is crucial for the understanding of the evolution of stellar systems. Massive young star clusters will, depending on their initial mass, harbour a massive star population. Such clusters could be argued to be of additional importance as, not only do they allow investigation of the IMF to higher masses, but also can have dramatic effects on their surroundings due to massive stellar winds and later Supernovae (SNe) ejecta driving a cluster outflow, known as a cluster wind. This process enriches the local InterStellar Medium (ISM), as well as potentially triggering further star formation in the region. The pinnacles of young stellar clusters are the extragalactic Super Star Clusters (SSCs). SSCs¹ are young (1-10 Myr), massive ($10^5 - 10^7 M_{\odot}$) objects with extremely dense cores ($\lesssim 10^5 M_{\odot} \text{ pc}^{-3}$). Such objects can not only drive star formation in the region but can drive, or potentially kill, star formation in entire galaxies when several of SSCs contribute to a galactic scale superwind. Due to its temperature, this cluster wind is best observed in the X-ray regime. Advances in X-ray imaging and spectroscopy over the last decade

¹There exists some ambiguity in the literature as to the classification of SSCs. One of the many sets of classification criteria is adopted here, as in [Whitmore \(2000\)](#)

1.2 The Initial Mass Function and the X-ray Luminosity Function

have allowed observations of cluster winds from Galactic young stellar clusters, as well as extragalactic SSCs. The problem with many of these observations is that, particularly for distant clusters, the observed diffuse X-ray emission cannot be unambiguously attributed to a cluster wind. In such stellar clusters, huge numbers of unresolved X-ray emitting sources can also contribute to diffuse emission. Often in analyses of stellar clusters the contribution of these sources is not quantitatively determined or, in some cases, is completely ignored and thus the contribution of a cluster wind can be overestimated. [Oskinova \(2005\)](#) model the X-ray emission from a massive stellar cluster considering both the stellar population and the cluster wind. This author finds that for massive clusters younger than 2 Myr, the cluster wind contributes little to the diffuse emission. Only after this time when evolved stars with powerful stellar winds appear, does the cluster wind begin to dominate the diffuse X-ray emission, a configuration which is maintained by the addition of SNe ejecta later in the cluster's life. Model predictions were compared to several Large Magellanic Cloud (LMC) clusters as well as three massive Galactic clusters and agreement was found with observation. This result demonstrates the overwhelming importance of including an unresolved stellar population in such analyses. Quantitating its contribution however relies on certain assumptions, in particular with regard to the IMF.

1.2 The Initial Mass Function and the X-ray Luminosity Function

The initial mass of a star is perhaps the most important of its physical parameters. This value essentially determines the remainder of its life, governing its movement around the Hertzsprung-Russell diagram. As such, knowledge of the distribution of initial masses in a cluster population is hugely important in predicting the evolution of that population. This distribution is known as the IMF. The IMF is a somewhat mysterious construct as stellar evolution theory is unable to predict its form. Rather, the IMF is an empirically derived quantity. What makes it mysterious is that the IMF is seen to be universal, meaning it describes some unknown underlying process that governs the conversion of interstellar matter to stars ([Lada and Lada, 2003](#)). Mathematically the IMF is the number of stars formed per unit logarithmic mass

1.2 The Initial Mass Function and the X-ray Luminosity Function

interval. The slope of the IMF is then:

$$\Gamma = d\log F(\log M_*)/d\log M_* \quad (1.1)$$

Several studies of the IMF for Galactic stars and open clusters exist in the literature (see [Meyer et al., 2000](#), for a review). In general, estimates of the slope of the IMF for stars with $M > 1M_\odot$ are consistent with $\Gamma \sim -1.3$ (in the IMF formulation above), similar to the original IMF estimate of [Salpeter \(1955\)](#) for field stars. For stars with $M < 1M_\odot$ the function breaks from the Salpeter slope and flattens ([Kroupa et al., 1993](#)). For the lowest mass stars however, there is considerable debate as to the shape of the IMF. For illustrative purposes, the Salpeter and Kroupa IMFs are shown in Figure 1.1.

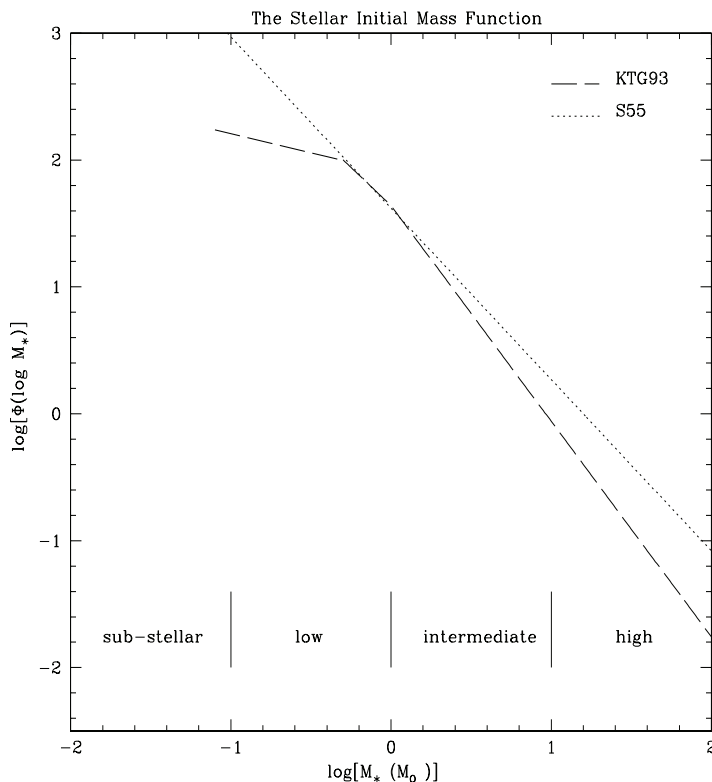


Figure 1.1: Salpeter (S55) and Kroupa (KTG93) Initial Mass Functions derived from field stars in the Solar neighbourhood. (Figure 1 of [Meyer et al., 2000](#))

The implication of these results with regard to X-ray observations is that if there are various X-ray emitting sub-populations in a cluster and assuming for a moment

1.2 The Initial Mass Function and the X-ray Luminosity Function

that all X-ray sources in a cluster have derived X-ray luminosities (L_X), these L_X values must also conform to some distribution. This is known as the X-ray Luminosity Function (XLF) which, like the IMF, should be universally observed. As X-ray observations of clusters suffer less from observational issues like source contamination and obscuration effects, the XLF provides a probe of the universality of the IMF given the relative ease of deriving the XLF and the ability to observe deeply embedded stellar populations. In practice not all of the X-ray emitting sources in a cluster will be detected with non-detection resulting from limiting flux sensitivities, etc. In addition, age effects must also be considered as sources, such pre-main sequence stars, have decaying X-ray luminosities. However, it should be the case that the high luminosity end of the XLF for clusters of a given age have the same shape. Thus, if we have one cluster of a well known age, with 100% completeness and know the decay rates of the X-ray emitting populations, we can infer the total populations of other observed clusters based on a comparison of the high luminosity end of their respective XLFs. This postulate holds only for single stellar systems in the clusters however. The number of binary systems emitting X-rays, such as colliding wind binaries, depend on further parameters such as the binary fraction and binary separations, etc, which are different for each cluster and each system.

In their X-ray/NIR study of the Cepheus B star forming region, [Getman et al. \(2006\)](#) investigate the link between the IMF and XLF of the stellar population and find that these quantities are tightly connected. They additionally use the well known Orion Nebular Cluster (ONC) data, taken during the *Chandra* Orion Ultradeep Project (COUP) to scale the ONC XLF to the Cepheus B XLF and derive the numbers and contributions of the undetected stellar population. Various authors use this method (see [Broos et al., 2007](#); [Wang et al., 2007](#), for example) to derive the properties of the stellar population which all assume, and subsequently find, a common shape to the high luminosity end of the XLFs, thus inferring a common shape to the IMF of these clusters, that of the standard IMF for masses $> 0.5M_{\odot}$ found for the ONC [Hillenbrand \(1997\)](#). Thus, this technique not only provides a quantitative estimate of the X-ray emission from the unresolved stellar population of these clusters, but also serves to test the universality of the IMF.

1.3 Rationale and Plan of the Thesis

Considering the preceding discussions, the scientific goal for this Ph.D. project is three fold:

1. First and foremost, to facilitate points 2 and 3, I will carry out an X-ray census of the youngest Galactic star clusters. To this end I will, using archival *Chandra* data, identify the X-ray emitting point source population in each of the clusters and use these data to quantify the unresolved stellar population contribution to observed diffuse emission as well as determining the contribution due to a cluster wind. Though some of these clusters have already been subject to detailed X-ray treatments, the data reductions and analyses are repeated to ensure homogeneity in the results.
2. I will investigate the predictions of the ‘ideal’ massive cluster model of [Oskina \(2005\)](#) and how they pertain to Galactic clusters of all sizes with ages up to 5 Myr, when the overall diffuse cluster emission is expected to slowly decline.
3. Finally, supplementary to these analyses, I will qualitatively probe the universality of the IMF in these clusters using the XLF.

The remainder of this introduction describes the various X-ray emitting sources expected in these clusters including classification criteria and quantitative methods. I will then give a brief history of X-ray astronomy and the *Chandra* telescope before discussing the programme cluster selection.

Chapter 2 - Data Reduction and Analysis

Of prime importance in the analysis of the *Chandra* data is consistent reduction and analysis methods. These are described in Chapter 2.

Chapter 3 - Programme Cluster Results

Chapter 3 highlights the results for each of the programme clusters. A detailed account of the analysis of one cluster is given before summarizing those of the remaining clusters.

1.4 X-ray Emission from Across the Mass Spectrum

Chapter 4 - Diffuse Thermal X-ray Emission in the Core of Westerlund 1

Data reduction and analysis in this project were carried out with specific goals in mind, namely the characterisation of the X-ray emitting populations of the programme clusters. However, on occasion, additional research avenues presented themselves and, where time allowed, these were investigated to the full with a view to publication. In this chapter, one of those results is presented, namely the identification of hard thermal X-ray emission in the core of Westerlund 1 using *XMM-Newton* observational data.

Chapter 5 - Global Properties of the Programme Clusters and their Sub-Populations

In this results chapter I will first describe the various cluster sub-populations and their global properties before discussing the results of the nature of the diffuse emission in each of the clusters and how they fit with the model predictions of [Oskinova \(2005\)](#). Finally, I will detail the variation in the cluster XLFs and how they fit with a universal IMF.

1.4 X-ray Emission from Across the Mass Spectrum

Given the distribution of stellar masses in young clusters, a variety of X-ray sources emitting via various mechanisms will be present in these clusters. I will now describe the various X-ray emitting subpopulations we can expect in the clusters and highlight the observationally derived properties of the sources which will be used to classify detected sources during the cluster analyses.

1.4.1 Massive Stars - Radiatively Driven Instability Shocks (RDIS)

Strong X-ray emission from single hot stars was one of the first scientific results from observations with the *Einstein* Observatory. [Lucy and White \(1980\)](#) and [Lucy \(1982\)](#) attributed the observed emission from these stars to shock heated gas resulting from radiatively driven instabilities in their powerful stellar winds, a model which has changed little to this day. Early surveys of massive stars and star forming regions with *Einstein* identified the so called ‘canonical’ relation $L_X/L_{bol} \sim 10^{-7}$ (see [Seward and Chlebowski, 1982](#), for example). A systematic study of the X-ray

1.4 X-ray Emission from Across the Mass Spectrum

emission from hot stars detected in the *ROSAT* All-Sky Survey by [Berghoefer et al. \(1997\)](#) confirmed this relation showing it to hold down to stars of B3 spectral type, see Figure 1.2. Stars of later spectral type do not have sufficient radiation fields to radiatively accelerate a wind out of their gravitational fields and thus cannot emit X-rays via this mechanism.

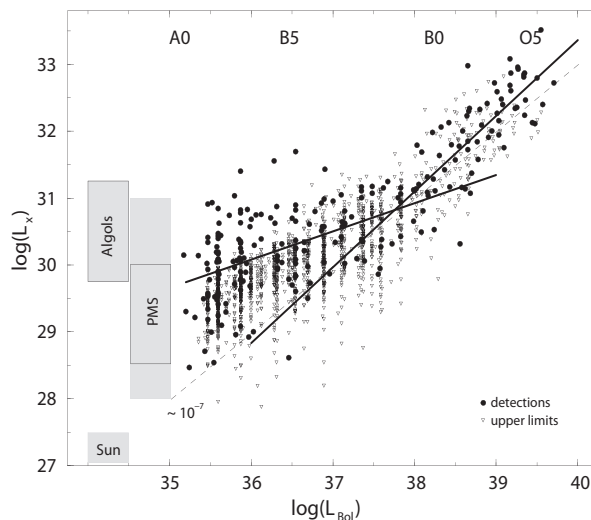


Figure 1.2: X-ray luminosity against bolometric luminosity for a flux limited sample of OB stars observed during the *ROSAT* All-Sky Survey. Typical ranges for later type stars are indicated by the bars on the left. (Figure 4 of [Berghoefer et al., 1997](#))

Since $\sim 10^{-7}$ of the bolometric luminosity of these massive OB stars is emitted via X-rays, absorption corrected L_X values in the $\sim 10^{31} - 10^{33}$ erg s $^{-1}$ luminosity range are expected for RDIS emitters. In addition, [Berghoefer et al. \(1997\)](#) find that all of the detected massive stars are soft X-ray emitters with value of $kT \sim 0.5$ keV. Thus, classification criteria for massive stars emitting via RDIS mechanism of $kT \lesssim 1$ keV and $0.5-8$ keV $L_X \sim 10^{31} - 10^{33}$ erg s $^{-1}$ are set.

1.4.2 Massive Stars - Magnetically Confined Wind Shocks (MCWS)

Toward the end of the *ROSAT* era, the RDIS emission from single hot stars was well known and characterized. However, some massive stars evaded this classification and presented with peculiar hard and/or periodic X-ray emission which could not be explained using the RDIS model (see [Babel and Montmerle, 1997b](#); [Gagne](#)

1.4 X-ray Emission from Across the Mass Spectrum

et al., 1997, for example). To explain this emission, Babel and Montmerle (1997b) devised a model which supposes the presence of a magnetic field that channels the stellar wind down to the equatorial plane where the winds from the two hemispheres collide producing a hot shocked plasma with temperatures exceeding 10^7 K (see Figure 1.3), sufficient for the production of moderately hard X-ray emission with luminosities comparable to those achieved in the RDIS model. This model was successfully applied to many sources including the O7V star θ^1 Ori C (Babel and Montmerle, 1997a), an O star with a known magnetic field. However, in these OB stars the ability of the magnetic fields to channel the winds to the magnetic equator is expected to fall quickly as the stellar mass loss rates increase (Schulz et al., 2003). Consequently, it is likely that only later O or early B stars will emit via this mechanism. Thus, classification criteria for massive stars emitting via the MCWS mechanism have been chosen as $kT \gtrsim 1$ keV and $0.5\text{-}8$ keV $L_X \sim 10^{31} - 10^{32}$ erg s $^{-1}$.

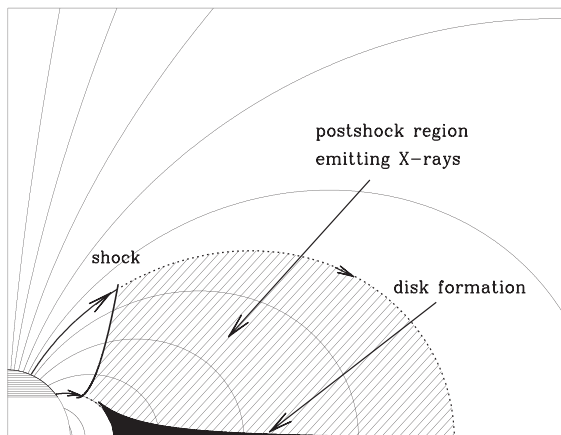


Figure 1.3: Schematic of Magnetically Confined Wind Shock model to explain X-ray emission from magnetic early type stars. (Figure 7 of Babel and Montmerle, 1997b)

1.4.3 Massive Stars - Wolf Rayets

Wolf-Rayet (WR) stars are evolved massive O-type stars in advanced nuclear burning stages. These sources are characterized by their extremely powerful metal rich winds that enrich the ISM. WRs are subdivided based on the dominant features in their spectra, i.e.- nitrogen rich (WN), carbon rich (WC) and oxygen rich (WO).

1.4 X-ray Emission from Across the Mass Spectrum

WRs have long been known to be X-ray emitters with the first detections coming from the *Einstein* observatory. WN stars are strong X-ray emitters yet the emission processes are not well understood. [Skinner et al. \(2010\)](#) perform an analysis of several apparently single WN systems and find that the spectra are well fit with a heavily absorbed (due to local absorption by the winds) two temperature model with one cool ($kT < 1$ keV) and one hot ($kT > 2$ keV) component, with derived L_X values in the 10^{31-33} erg s⁻¹ range. The soft component is consistent with RDIS in the stellar winds, as in OB stars. However, the hard component is not consistent with this picture. As such, these authors discuss alternative sources for the hot plasma including MCWS emission. Though they determine MCWS to be a good candidate, they highlight the fact that no magnetic field has ever been detected from a WR star. WC stars on the other hand are found to be X-ray faint (or perhaps X-ray quiet) by several authors (see [Oskinova et al., 2003](#); [Skinner et al., 2010](#), for example) with no conclusive detections to date. This is most likely due to much larger wind opacity than the WN stars, an idea tested by [Skinner et al. \(2010\)](#) who determine that moderately hard (~ 3 keV) X-ray emission would need to occur far out in the stellar wind (on the order of thousands of Solar radii) to escape the dense wind. X-ray emission has been detected from WO stars which have even denser winds. [Oskinova et al. \(2009\)](#) detect hard (~ 10 keV) faint ($L_X \sim 10^{30}$ erg s⁻¹) X-ray emission from the WO star W142. Thus X-rays from this source are sufficiently hard to penetrate the circumstellar material, though, as in the analysis of [Skinner et al. \(2010\)](#), it is unclear as to the emission mechanism producing these hard X-rays.

1.4.4 Colliding Wind Binaries

Many of the high mass stars in young open clusters are contained in binary systems. Observationally derived binary fractions for high mass stars in clusters range from about 10-80% ([Mermilliod and García, 2001](#)). In addition, the mass ratio in massive binaries approaches unity meaning these binary systems consist of two high mass stars. When such stars are in close proximity, their powerful winds collide forming a hot shocked plasma which radiates at X-ray energies. This process was initially proposed by [Prilutskii and Usov \(1976\)](#) and [Cherepashchuk \(1976\)](#) and was later cited to be the mechanism responsible for WRs in binary systems being more X-ray luminous than in single systems ([Pollock, 1987](#)). Now, these so called Colliding

1.4 X-ray Emission from Across the Mass Spectrum

Wind Binaries (CWBs) are relatively common with several very well known examples including the enigmatic η Carinae and the ‘canonical’ CWB WR 140. These source typically exhibit two temperature spectra with a soft thermal component (< 1 keV) describing the shock stellar wind of one or both the stars (RDIS) and a hot component (> 2 keV) to describe the shock heated material due to the colliding wind zone. In addition, these sources can be extremely bright, with η Carinae having an L_X well in excess of 10^{35} erg s $^{-1}$ (see [Leutenegger et al., 2003](#); [Seward et al., 2001](#), for example). On the lower scale, these sources have L_X values $\gtrsim 10^{32}$ erg s $^{-1}$.

1.4.5 Low Mass Pre-Main Sequence Stars

Low mass stars ($M \lesssim 2M_\odot$) while still in their Pre-Main Sequence (PMS) evolutionary phase are collectively called Young Stellar Objects (YSOs). The very youngest YSOs (Class 0, $\sim 10^4$ yr) are completely embedded in their parental molecular cloud core, undetectable at optical or even Near InfraRed (NIR) wavelengths. As the star evolves it accretes material from the surrounding cloud, reducing the amount of absorbing material until the star is visible at NIR wavelengths (Class I, $\sim 10^5$ yr). Once the star emerges from the gaseous envelope it enters its T Tauri phase. Initially, the surrounding material settles into an accretion disk forming a classical T Tauri system (Class II, $\sim 10^{6-7}$ yr). Finally, when the disk has been either accreted or dispersed, the star enters the weak lined T Tauri phase (Class III) and though it may resemble a main sequence star, is still in a contraction phase.

Class I to Class III YSOs are known to be moderately bright X-ray emitters ([Favata and Micela, 2003](#); [Feigelson and Montmerle, 1999](#)) with signs of strong non-periodic flaring. Class I YSOs will, due to the surrounding material, be more absorbed at X-ray wavelengths than Class II or III YSOs unless the viewing angle of the Class II YSO is such that it is hidden behind its accretion disk (see [Figure 1.4](#)). The X-ray emission from YSOs is largely due to the presence of a magnetic field ([Feigelson and Montmerle, 1999](#)). In Class I and Class II YSOs, the observed quiescent X-ray emission (or part thereof in the case of Class II YSOs) is thought to be due to the stars accreting material from the surrounding cloud or disk along the magnetic field lines onto confined regions of the stellar surface, so called hot-spot accretion zones. At these points, the infalling material is shocked and heated to X-ray emitting temperatures. Emission from Class III YSOs is fundamentally different given these objects are not accreting. The X-ray emission from these objects

1.4 X-ray Emission from Across the Mass Spectrum

is thought to be a scaled-up Solar corona like activity, due to the same emission mechanisms but 3-4 orders of magnitude brighter than the Sun. This emission process likely contributes to emission from Class II YSOs also. In addition to quiescent emission, YSOs are observed to undergo flaring events. [Montmerle et al. \(2000\)](#) propose that interactions in the star-disk magnetosphere are responsible of the flaring events in accreting objects. This model suggests that magnetic field lines anchored to both the star and the disk become twisted due to the differential rotation. Magnetic energy builds up and is released and converted to thermal energy in powerful magnetic reconnection events which heat the confined plasma giving rise to a burst of X-ray emission.

PROPERTIES	<i>Infalling Protostar</i>	<i>Evolved Protostar</i>	<i>Classical T Tauri Star</i>	<i>Weak-lined T Tauri Star</i>
SKETCH				
AGE (YEARS)	10^4	10^5	$10^6 - 10^7$	$10^6 - 10^7$
mm/INFRARED CLASS	Class 0	Class I	Class II	Class III
DISK	Yes	Thick	Thick	Thin or Non-existent
X-RAY	?	Yes	Strong	Strong

Figure 1.4: Stages of Young Stellar Object evolution. (From Figure 1 of [Feigelson and Montmerle, 1999](#))

In the clusters to be analyzed in this thesis, any cluster source that is not a high mass source is likely a low mass PMS object. As such, any source without a high mass stellar counterpart is labelled as a PMS source. These PMS sources are expected to have 0.5-8 keV L_X values from 10^{29-32} erg s⁻¹ though strongly flaring sources may be brighter. Additionally, their plasma temperatures are expected to cover a broad range (\approx 0.1-1.5 keV) for quiescent sources, increasing during flaring events.

1.4.6 Post-Supernova

The clusters to be studied in this project have ages < 5 Myr. Because of their young age and because only the most massive clusters will host stars producing SNe after

1.4 X-ray Emission from Across the Mass Spectrum

~ 3 Myr, it is unlikely that post-SN objects will be detected often given that only a small number of the clusters to be studied are of sufficient age to host a SN (see Section 1.7) and that only the most massive of these would have contained the most massive stars which undergo a SN event after ~ 3 Myr. Nevertheless, potential X-ray sources resulting from these events are briefly discussed in case that any of these are contained in the clusters.

1.4.6.1 Young Supernovae and Supernova Remnants

Once an evolved star undergoes a SN event the short time scale X-ray luminosity and emission mechanisms vary considerably. The first, most spectacular stage is the shock breakout burst. SNe produce no electromagnetic radiation until the explosion shock reaches the stellar surface. At this point the shock breaks through the surface producing a brilliant burst of X-ray or extreme ultraviolet photons. If a total of 10^{51} erg of energy is released in the supernova explosion, some $\sim 10^{45-47}$ erg are expected to be released in X-rays during shock break-out (Calzavara and Matzner, 2004). After the break-out burst, the X-ray luminosity reduces considerably. The dominant emission mechanism after the break-out is the ejecta/CircumStellar Medium (CSM) interaction. The X-ray luminosities from this phase can range from $\sim 10^{36-41}$ erg s^{-1} depending on the wind properties of the SN progenitor and the time after SN event. Inverse Compton cooling of relativistic electrons produced in the explosion can also contribute to the X-ray emission from some young SNe. Upscattering of optical or UV photons to X-ray energies can, depending on the Lorentz factor and the effective temperature of the photospheric emission, produce a detectable X-ray flux for the first few days after the outburst. A further contribution to the X-ray emission comes from the radioactive decay of the ejecta. γ -rays due to the radioactive decay of isotopes of Fe, Ni and Co are produced. After a few hundred years the ejecta reach the boundary between the CSM and the Interstellar Medium (ISM). The same interaction occurs as with the CSM but the reduction in ejecta velocity and density over time causes the X-ray luminosity to be somewhat reduced. This is known as a SuperNova Remnant (SNR). SNRs can also interact with the stellar winds of nearby massive stars in the clusters (Velázquez et al., 2003). Although SNRs are very bright objects in the X-ray regime ($\sim 10^{34-36}$ erg s^{-1} or brighter depending on their environment) they are somewhat short lived lasting only a few tens of thousands of years (Immler and Lewin, 2003).

1.4.6.2 Collapsed Objects

Isolated

An OB star supernova event will, depending on its initial mass, produce either a neutron star or black hole. As one might expect, isolated black holes are not X-ray emitters, however neutron stars in their normal, pulsar and magnetar variety are. Emission can either be a product of synchrotron emission of charged particles due to the immense magnetic fields or due to the surface temperature of the stars themselves, particularly from the polar caps where the star is bombarded with relativistic particles returning from the magnetosphere to the surface (see [Kaspi et al., 2004](#), for a review). In reality, X-ray emission from single collapsed objects results from a combination of the aforementioned processes. Observationally, these X-ray emitting objects would present as bright objects ($L_X > 10^{32}$ erg s⁻¹) without a stellar counterpart and have featureless X-ray spectra, described by either a cool blackbody ($kT \sim 1$ keV) and/or a power law model.

Binary

In high mass binary systems, which likely comprise a CWB system, the primary star will eventually undergo a supernova event. Providing the system is not disrupted by a SN kick, this will leave one high mass star with a compact companion (either neutron star or black hole) known as a High Mass X-ray Binary (HMXB). In such a system X-rays will be produced via the relativistic accretion of material onto the compact object. This mechanism can, depending on the binary configuration, produce large X-ray luminosities $\sim 10^{38}$ erg s⁻¹ ([Liu et al., 2006](#)). In the wider configurations, the luminosity is reduced ($\sim 10^{35-36}$ erg s⁻¹ [Liu et al., 2006](#)) as the transfer of material to the compact object is via the stellar wind of the high mass star, which is known as wind-fed accretion.

1.4.7 Diffuse Sources

It is likely that there will be diffuse emission observed in many of the clusters to be studied in this project. This emission may be truly diffuse resulting from a cluster wind for example, or maybe due to unresolved point sources in the cluster. However, it can be difficult to determine the true nature of diffuse emission and models of possible sources must be used to assess the strength of each individual contributor.

1.4 X-ray Emission from Across the Mass Spectrum

The possible sources of diffuse cluster emission are described below including the methods by which their contributions are determined.

1.4.7.1 Cluster Wind

Many of the young clusters studied in this project harbour a massive star population. These massive stars are the source of large amounts of energy and mass being injected into the cluster volume via stellar winds. The winds collide and thermalize, filling the cluster core volume with a hot, shocked plasma. After some time, the outflow from these thermalized winds becomes stationary and a steady state cluster wind ensues (Cantó et al., 2000, and references therein). The temperature of this hot, diffuse plasma in the cluster volume is sufficiently high to radiate at X-ray energies and hence, depending on the strength and number of stellar winds, may contribute to the observed diffuse emission in the clusters. Cantó et al. (2000) describe an analytic model for this process with individual stars in a spherically symmetric cluster injecting mass and energy into a cluster wind, see Figure 1.5.

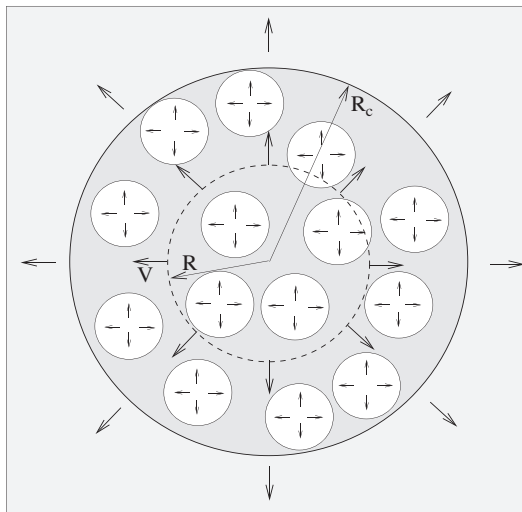


Figure 1.5: Schematic showing the winds from uniformly distributed stars in a cluster with radius R_C interacting to produce a cluster wind. (Figure 1 of Cantó et al., 2000)

Stevens and Hartwell (2003) refined this model, incorporating lower thermalization efficiencies and mass loading, to predict the properties of the cluster wind for some Galactic and Magellanic Cloud clusters and compared them to observations finding some trends in the input model parameters with observed X-ray luminosities.

1.4 X-ray Emission from Across the Mass Spectrum

However, these authors do not consider a possible contribution from an unresolved population in their analysis. To predict the contribution of a cluster wind to any observed diffuse emission in the clusters, the [Cantó et al. \(2000\)](#) model is used here in combination with the mass and energy input equations of [Stevens and Hartwell \(2003\)](#) to derive theoretical cluster wind parameters, namely the central ion number density and the central plasma temperature. These are given as:

$$\left(\frac{n_0}{\text{cm}^{-3}}\right) = 0.1N \left(\frac{\dot{M}}{10^{-5}M_{\odot} \text{ yr}^{-1}}\right) \left(\frac{v_w}{10^3 \text{ km s}^{-1}}\right)^{-1} \left(\frac{R_C}{\text{pc}}\right)^{-2} \quad (1.2)$$

$$\left(\frac{T_0}{\text{K}}\right) = 1.55 \times 10^7 \left(\frac{v_w}{10^3 \text{ km s}^{-1}}\right)^2 \quad (1.3)$$

where N is the number of stars contributing to the thermalized cluster wind, \dot{M} is the average mass loss rate per star, v_w is a weighted average wind velocity of the stars and R_C is the radius of the region containing the stars. To determine \dot{M} and v_w , the known spectral types of the high mass population were used to determine the O star wind terminal velocities from [Kudritzki and Puls \(2000\)](#) and mass loss rates from [Howarth and Prinja \(1989\)](#). Similarly, WR wind terminal velocities and mass loss rates were adopted from [Crowther \(2007\)](#). To determine an estimate for the X-ray luminosity due to a cluster wind, the method of [Muno et al. \(2006b\)](#) is used. The derived central ion density (n_0) is used in combination with the cluster radius (R_C) to calculate an emission measure using the equation:

$$K_{\text{EM}} = \frac{4}{3}\pi R_C^3 n_0^2 \quad (1.4)$$

This emission measure is then used to calculate a normalization for a thermal plasma model in *XSPEC* (see Section 2.2), which, in combination with the derived central plasma temperature (kT_0), is used to extract X-ray fluxes and derive X-ray luminosities. One must be aware however that the model used for these cluster analyses does not incorporate the thermalization efficiency and mass loading of the cluster wind described by [Stevens and Hartwell \(2003\)](#). In practice, the adopted model assumes no mass loading and a thermalization efficiency of 1 (i.e. - no radiative losses in the conversion of the stellar wind energies to the cluster wind). This may be simplistic and it is noted here that a change in either parameter would serve to increase the predicted overall X-ray luminosity and reduce the kT_0 value.

1.4.7.2 Unresolved PMS Stars

Although the PMS sources in a cluster will be detected, many more will fall below the detection threshold of the observation. These sources, though point-like in nature, will manifest as diffuse emission in the cluster volume. To assess the contribution of unresolved PMS population, the methods adopted by Broos et al. (2007); Getman et al. (2006); Wang et al. (2007); and others are used. An XLF is constructed for the brighter low mass PMS sources in each of the clusters and compared to that of the ONC using data from the COUP. Assuming that the clusters have similar IMFs which infers similar PMS XLFs, the shape of the high end PMS XLFs for each of the clusters should be similar to that of the ONC. As such, the ONC XLF can be somewhat reliably scaled to that of the cluster, illustrated using the M 17 XLF of Broos et al. (2007) in Figure 1.6. Integration of the ‘missing’ PMS population of the XLF (indicated by the region with diagonal lines in Figure 1.6) thus provides an estimate for the contribution from the unresolved sources.

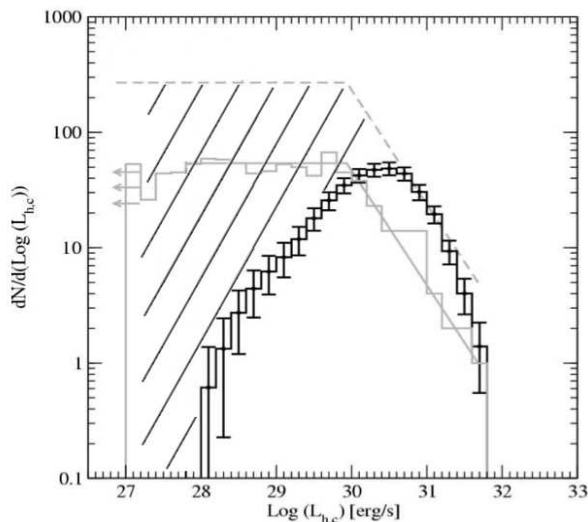


Figure 1.6: 2-8 keV XLF of the M 17 PMS population from Broos et al. (2007) (their Figure 9(a)). The black solid line indicates the M 17 population XLF, the grey solid line indicates the COUP XLF. The grey dashed line indicates the scaled COUP XLF. The diagonal lines mark the ‘missing’ PMS population region which is integrated to determine an estimate of the X-ray luminosity due to an unresolved PMS population.

1.5 X-ray Astronomy

Observing in X-rays is one of the more recent branches of astronomy. X-ray radiation is absorbed by the Earth's atmosphere so detectors must be sent to high altitudes or to space itself. The first cosmic X-ray source was detected by accident in the sixties with a detector mounted on a rocket sent high into the atmosphere. Subsequent experiments were mounted on balloons which could observe at the top of the atmosphere for longer periods but still suffered from atmospheric absorption. Eventually X-ray telescopes were built into satellites and placed into orbit high above the atmosphere where the entire X-ray spectrum could be observed. Past satellites such as *Einstein*, *ASCA*, *BeppoSax* and *ROSAT* gave observers the first insight into cosmic X-ray production. The current generation of imaging X-ray observatories (*XMM-Newton*, *Chandra* and *Suzaku*) are capable of high spatial and spectral resolutions and as such have led to the discovery of new classes of celestial objects and processes. Of these current generation telescopes, *Chandra*, with its very high spatial resolution, is most suited to the requirements of this Ph.D. project. *Chandra* is capable of resolving individual sources in clusters from the diffuse emission. Though the other telescopes such as *XMM-Newton* are incredible instruments in their own right, for the study of stellar clusters they are slightly less suited than *Chandra*. In the following section I will give a description of the *Chandra* satellite and the instrument of choice for this project, the Advanced CCD Imaging Spectrometer.

1.6 Chandra

Chandra is a space observatory that is used to study a variety of X-ray phenomena in the Universe in the 0.1-10 keV energy range. At the front of the X-ray telescope is the High Resolution Mirror Assembly (HRMA), which is capable of focussing X-ray photons to sub-arcsecond spatial resolution. *Chandra*'s Integrated Scientific Instrument Module (ISIM) houses two focal plane instruments (the Advanced CCD Imaging Spectrometer (ACIS) and the High Resolution Camera (HRC)) along with two transmission grating spectrometers (the Low Energy Transmission Grating (LETG) and the High Energy Transmission Grating (HETG)), see Figure 1.7. These instruments can be placed in various configurations and/or run in various modes to suit the needs of the observer be they spatial, spectral or temporal. *Chandra*, along with the *Hubble Space Telescope* and the *Spitzer Space Telescope*, is one of NASA's Great

Observatories still operational. The satellite was launched by the shuttle Columbia (STS-93) on 23rd July, 1999, into a high elliptical orbit allowing uninterrupted observing times of over 48 hours.

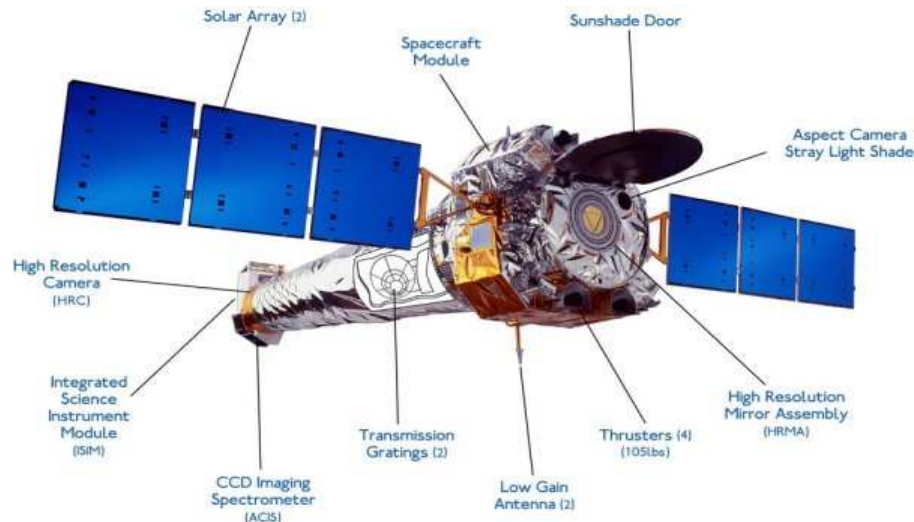


Figure 1.7: A rendered image of *Chandra* and its instruments

Chandra has now been collecting data for some 11 years, the majority of which is publicly available via the Chandra Data Archive (<http://cda.harvard.edu/chaser/mainEntry.do>). Only those data taken 12 months prior to an archive search are unavailable to the public. The Chandra X-ray Center maintains the Chandra Interactive Analysis of Observations (CIAO) data reduction software, and the Chandra CALibration DataBase (CALDB), retrievable at <http://asc.harvard.edu/ciao/>.

With regard to this Ph.D. project, the ACIS instrument is ideal for the study of stellar clusters. Placing the ACIS in the focal plane of the HRMA offers sub-arcsecond resolution (allowing point sources to be resolved from the diffuse background) with moderate spectral capabilities (allowing reasonable spectral analysis of point and extended sources). Hence, I limit the description of *Chandra's* scientific payload to the HRMA and the ACIS instrument.

1.6.1 HRMA

The HRMA consists of four pairs of concentric, grazing-incidence Wolter Type-I mirrors (see Figure 1.8) with a total focal length of 10.07 m. The mirrors were fabricated from Zerodur glass, a material that chemically and thermally is highly

stable (thus suited to the harsh environment of space), which can be polished to a very high accuracy (see [Aschenbach, 1985](#), for a discussion of the X-ray optics and fabrication techniques). The mirror assembly has a ghost-free FOV of 30' diameter and, depending on the focal plane instrument used, has an on-axis Point Spread Function (PSF) FWHM of $< 0.5''$ (this value is limited by the physical size of the instrument CCD pixels and not the HRMA). This PSF FWHM will vary depending on the incident photon energies and off-axis angle of any source focussed by the HRMA (see Figures [1.10](#) and [1.11](#)).

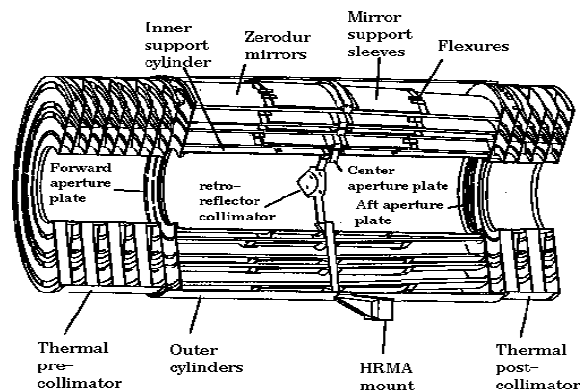


Figure 1.8: The four nested HRMA mirror pairs and associated structures. (From the *Chandra* Proposer' Observatory Guide¹)

1.6.2 ACIS

The ACIS instrument (<http://cxc.harvard.edu/proposer/POG/html/ACIS.html>) onboard Chandra consists of two CCD arrays, the ACIS-I and the ACIS-S, which are capable of imaging the sky with high spatial resolution while simultaneously taking moderate resolution spectra ($\frac{E}{\Delta E} = 20 - 50$) in the 0.3-10 keV energy range. The ACIS-I consists of four CCDs in a square arrangement and lie tangent to the focal surface of the telescope. The ACIS-S consists of 6 CCDs in a linear arrangement and lie tangent to the HETG Rowland circle used during the grating readout mode (see Figure [1.9](#)). The ACIS-I has a $16.9' \times 16.9'$ FOV whereas the ACIS-S has a $8.3' \times 50.6'$ FOV in imaging mode.

The spatial resolution for both ACIS arrays is $\sim 0.49''$ on-axis and increases with increasing incident photon energy and off-axis angle (see Figures [1.10](#) and [1.11](#)). The

1.7 Programme Clusters Selection

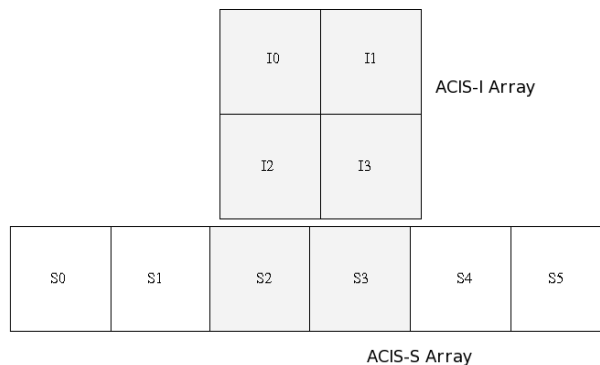


Figure 1.9: A Schematic Drawing of the ACIS chip arrays. The shaded area indicates the active CCDs during ACIS-I observations. (From the *Chandra* Proposers' Observatory Guide)

effective area (the ability of the telescope mirrors to collect radiation at different photon energies folded through the detector response) also varies with incident photon energy and off-axis angle (see Figure 1.12). The primary difference, apart from chip arrangement, between the ACIS-I and ACIS-S arrays is their operating configurations. The ACIS-I CCDs are front illuminated chips (the surface containing the gate structures facing the HRMA) whereas the ACIS-S CCDs are back illuminated (the depletion layer (the sensing region of the pixels) are exposed to the photon beam from the HRMA). The effect of these two configurations is that the ACIS-S has a lower spectral resolution than the ACIS-I array while in imaging mode but is more sensitive to lower energy photons. Because of this, the ACIS-S array is typically used while observing faint extended objects, such as distant or heavily absorbed stellar clusters, over limited exposure times. However, for the majority of stellar cluster observations, the ACIS-I is used.

1.7 Programme Clusters Selection

1.7.1 Cluster Selection

In order to select Galactic clusters appropriate for study in this PhD thesis, a well established and frequently updated catalogue of open clusters is required. For this reason I have selected the Catalogue of Optically Visible Open Clusters and Candidates (Dias et al., 2002, henceforth, the Dias et al. catalogue) which has been updated some 19 times since the initial Version 1.0 of the catalogue was released

1.7 Programme Clusters Selection

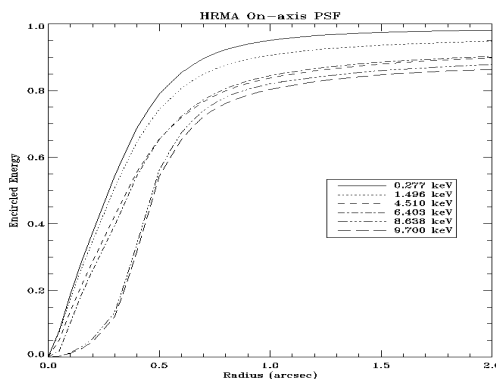


Figure 1.10: Plot of the variation of fractional encircled energy (defined as the two dimensional integral of the PSF) with radius calculated for an on-axis point source at selected energies. (From the *Chandra* Proposers' Observatory Guide)

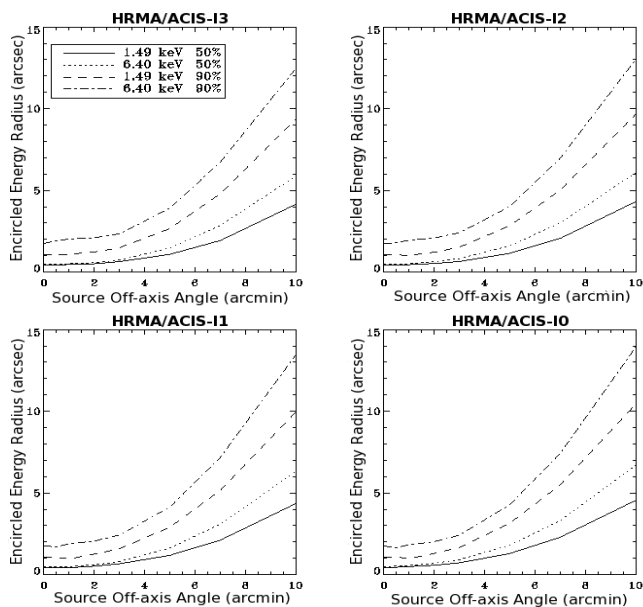


Figure 1.11: Plot of the variation of encircled energy radius for circles enclosing 50% and 90% of the power at 1.49 keV and 6.40 keV with source off-axis angle calculated for each of the ACIS-I chips. (From the *Chandra* Proposers' Observatory Guide)

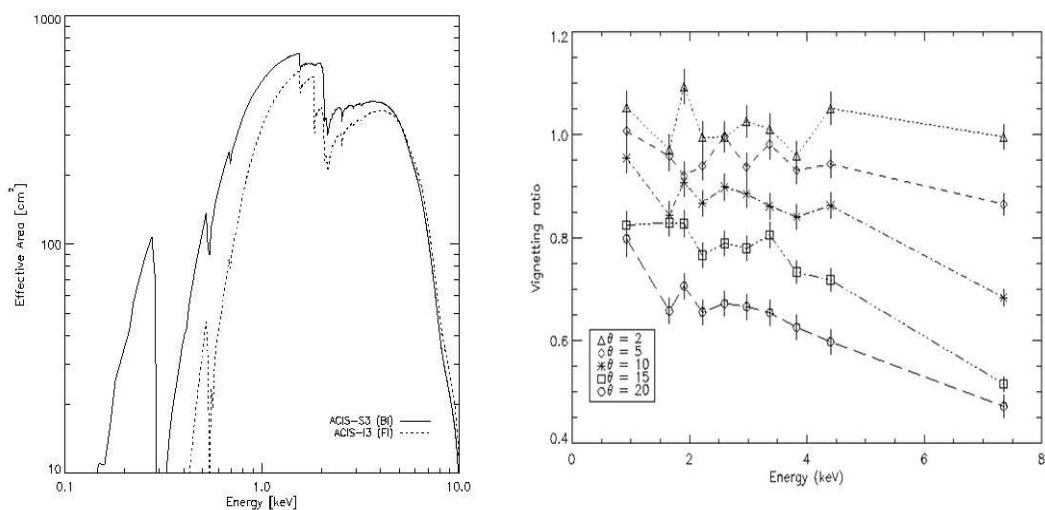


Figure 1.12: Plots of the HRMA/ACIS effective area against photon energy and vignetting (the ratio of off-axis to on-axis effective area) against photon energy at selected angles. Each of these plots clearly indicates the variation of effective area with photon energy and off-axis angle. (From the *Chandra* Proposers' Observatory Guide)

in 2002 (see <http://www.astro.iag.usp.br/~wilton/whatsnew.txt>). Not only do the maintainers of the catalogue continually update cluster properties (such as ages, distances, etc.), they also examine the data from different authors on the same object for inclusion. As this catalogue is maintained so rigorously, it is well recognised by the astronomical community and, prior to the February 2009 release, had been used and cited in more than 100 papers (which does not include references to WEBDA, the web interface of the BDA database of stellar clusters in the Galaxy and Magellanic Clouds, on which this catalogue is based, see <http://www.univie.ac.at/webda/>). The latest version of this catalogue (Version 2.10) which contains 1787 clusters can be obtained via the online catalogue website, available at <http://www.astro.iag.usp.br/~wilton/clusters.txt>. I have chosen this optically visible open cluster catalogue over catalogues from other wavebands (particularly IR) for several reasons. First of all, optically visible clusters tend to be studied in detail across all wavebands making it much more likely that the stellar populations (particularly high mass) have had spectral types derived either spectroscopically or photometrically. In addition, it is also quite probable that X-ray observations of the clusters have been performed with the current generation of X-ray telescopes. This is in contrast to the IR cluster catalogues (eg.- [Bica et al., 2003](#); [Dutra et al., 2003](#); [Froebrich et al., 2007](#)) which collectively add about 700 clusters to the total number

1.7 Programme Clusters Selection

from the optical catalogue, yet the vast majority is poorly studied. Combine this with the limited cluster property data of the IR catalogues (in general, only cluster positions and dimensions are given) and the advantages of using the Dias et al. catalogue are evident.

To identify the clusters appropriate for study in this project (i.e. - clusters of age $\lesssim 5$ Myr), the table was sorted into ascending age leaving 27 suitable clusters, shown in Table 1.1). To make the final selection of clusters for study in this project, those clusters in Table 1.1 that have archived *Chandra* observations need to be identified. To this end the searched the *Chandra* Data Archive was searched for publicly available observational data for each of these clusters. This search yielded a final number of 15 programme clusters with one or more *Chandra* observation. Table 1.2 lists the resulting clusters and their corresponding archived X-ray observations.

Table 1.1: Dias et al. Catalogue of Open Clusters with Known Ages $\lesssim 5$ Myr

Name	RA	DEC	Age (Myr)	Name	RA	DEC	Age (Myr)
NGC 6618	18 20 47	-16 10 18	1.0	Berkeley 7	01 54 12	+62 22 00	4.0
IC 5146	21 53 24	+47 16 00	1.0	Roslund 4	20 04 54	+29 13 00	4.0
NGC 3603	11 15 07	-61 15 36	1.0	Bica 1	20 33 10	+41 13 07	4.0
NGC 6611	18 18 48	-13 48 24	1.3	Bica 2	20 33 15	+41 18 45	4.0
Collinder 232	10 44 39	-59 33 36	2.0	ASCC 75	13 47 10	-62 25 12	4.5
Stock 8	05 28 07	+34 25 24	2.0	ASCC 117	22 04 59	+62 16 12	4.7
Trumpler 14	10 43 56	-59 33 00	2.0	Bochum 2	06 48 54	+00 23 00	4.7
Westerlund 2	10 24 02	-57 46 00	2.0	Bochum 1	06 25 25	+19 46 00	4.9
IC 1805	02 32 42	+61 27 00	3.0	Trumpler 16	10 45 10	-59 43 00	5.0
NGC 1893	05 22 44	+33 24 42	3.0	NGC 2362	07 18 41	-24 57 18	5.0
NGC 6823	19 43 09	+23 18 00	3.2	Westerlund 1	16 47 04	-45 50 36	5.0
IC 1590	00 52 49	+56 37 42	3.5	Collinder 69	05 35 06	+09 56 00	5.0
Feigelson 1	11 59 51	-78 12 27	4.0	NGC 2367	07 20 06	-21 52 54	5.0
Havlen-Moffat	17 18 54	-38 49 00	4.0				

1.7 Programme Clusters Selection

Table 1.2: Dias et al. Catalogue of Open Clusters with Known Ages $\lesssim 5$ Myr and *Chandra* Observations

Name	No. of Obs.	Exp. Time(s) (ks)
NGC 6618	6	4,30,34,35,40,151
NGC 3603	1	50
NGC 6611	1	78
Collinder 232	6	15,15,15,15,20,60
Trumpler 14	1	60
Westerlund 2	3	40,50,50
IC 1805	1	80
NGC 1893	5	43,54,108,117,128
IC 1590	3	13,23,62
Feigelson 1	2	3,3
Bica 1	1	98
Bica 2	1	98
Trumpler 16	7	14,15,15,15,15,20,90
NGC 2362	1	100
Westerlund 1	7	15,15,20,20,20,25,40

1.7.2 Cluster Location

As those clusters listed in Table 1.2 are of young age, one can assume that each is a site of a recent star formation burst. Indeed most of these clusters are likely still forming stars (which would be evident if the clusters contain a PMS population). It is well known that star formation regions in spiral galaxies such as the Milky Way are localised in the spiral arms on or near the galactic plane (i.e. - in the Galactic disk), given that these regions are subject to the tidal forces required to initiate the gravitational collapse of dense regions of molecular clouds. Hence, it is expected that those clusters in Table 1.2 are located in the Galactic disk. To illustrate this the locations of the clusters in Table 1.2 were plotted on an all-sky Aitoff projection in Galactic coordinates along with those clusters younger than 5 Myr without X-ray observations and those clusters older than 5 Myr from the Dias et al catalogue, Figure 1.13.

Figure 1.13 clearly shows that all of the programme clusters lie, as expected,

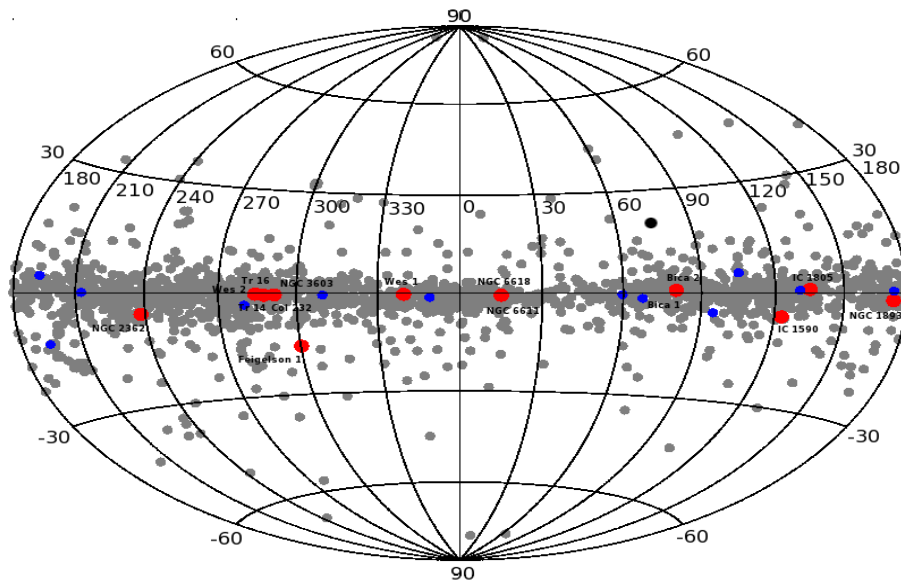


Figure 1.13: All-sky Aitoff projection of the clusters listed in Table 1.2 obtained from Dias et al. Catalogue (red), the clusters listed in Table 1.1 without *Chandra* observations (blue) and the clusters from the Dias et al. Catalogue older than 5 Myr (grey). This plot clearly shows that all of the programme clusters lie in or near the Galactic disk.

in or near the Galactic disk. One very noticeable feature of the distribution of the programme clusters in Figure 1.13 is the grouping of Collinder 232, NGC 3603, Trumpler 14, Trumpler 16 and Westerlund 2. This is in fact unsurprising as these clusters are all situated in the Carina spiral arm. Collinder 232, Trumpler 14 and Trumpler 16 are all contained in the Carina Complex star forming region at a distance of ≈ 2.5 kpc. Westerlund 2, the heart of the RCW 49 HII region, is more distant at 6.4 kpc, while NGC 3603 is located still further at 6.9 kpc (see Table 1.1).

1.7.3 Cluster Completeness

The Dias et al. Catalogue used for the selection of programme clusters in the project contains approximately 1800 clusters, the furthest being at a distance of ~ 14 kpc. However, within this distance the catalogue is incomplete due to effects such as clusters being faint or heavily obscured. To estimate the completeness of the age ordered cluster table (Table 1.1), we must first know how complete the entire sample is. Unfortunately, there are no completeness estimates for the Dias et al. Catalogue. There are, however, much more detailed studies of total numbers of Galactic open clusters in the literature that incorporate the clusters in the Dias et al. Catalogue as well as several others. Two such studies are those of Piskunov et al. (2006) and Bonatto et al. (2006a) which take into account factors such as the disk scale height and scale length, the variation in stellar density due to the spiral arms, etc. Each of these studies estimates $\sim 10^5$ open clusters in the Galaxy. Given that 27 of the 982 clusters with ages in the Dias et al. Catalogue are younger than 5 Myr ($\approx 3\%$) and assuming this cluster age distribution scales to the estimated Galactic population, it is expected that there are $\approx 3 \times 10^3$ clusters with ages $\lesssim 5$ Myr. Hence, it follows that the sample of 27 clusters listed in Table 1.1 is approximately 1% of the estimated total number of Galactic open clusters with ages $\lesssim 5$ Myr.

Chapter 2

Data Reduction and Analysis

2.1 Data Reduction and Analysis Procedures

Given the number of clusters analyzed in this project, consistent reduction and analysis procedures are required to ensure each cluster is analyzed in an identical manner. The following sections outline the reduction procedures employed for *Chandra* data for the analysis of both point sources and diffuse emission.

2.1.1 Observational Data Processing

The *Chandra* datasets for those program clusters where *Chandra* data are available were obtained via the *Chandra* Data Archive (CDA). Only datasets with the highest exposure times and suitable observation modes were retrieved to reduce data processing and analysis times. For example, Trumpler 16 was observed by *Chandra*'s ACIS instrument 7 times: one exposure of 14 ks, 4 of 15 ks, one of 20 ks and one of 90 ks. Only the 90 ks observation was retrieved for analysis as the addition of the shorter exposure datasets greatly increases analysis time without adding significantly to the results. Although this would increase the total counts for each source with some improvement in source statistics, etc., given the number of clusters to be analyzed, a limit to the amount of data analyzed per cluster must be imposed to keep the analysis timescales reasonable. In the case of Westerlund 1, which was also observed with the ACIS instrument 7 times, 5 of these observations were taken in the 'continuous clocking' observation mode which provides very high temporal resolution at the expense of 1 dimension of spatial resolution and are thus not suitable for analysis in this project. Table 2.1 lists the datasets retrieved from the CDA for

2.1 Data Reduction and Analysis Procedures

the programme clusters¹.

Table 2.1: *Chandra* Datasets Retrieved for Analysis

Name	No. of Obs.	Seq No(s).	Obs. ID(s).	Inst.	Exp. Time(s) (ks)
NGC 6618	1	200395	6420	ACIS-I	151
NGC 3603	1	200058	633	ACIS-I	50
NGC 6611	1	200085	978	ACIS-I	78
Trumpler 14	1	200264	4495	ACIS-I	60
Westerlund 2	3	200196,100385,200386	3501,6410,6411	ACIS-I	40,50,50
IC 1805	1	900449	7033	ACIS-I	80
NGC 1893	3	200383,200383,200383	6406,6407,6408	ACIS-I	108,117,128
IC 1590	1	200357	5425	ACIS-I	62
Bica 1	1	200280	4511	ACIS-I	98
Bica 2	1	200280	4511	ACIS-I	98
Trumpler 16	1	200379	6402	ACIS-I	90
NGC 2362	1	200238	4469	ACIS-I	100
Westerlund 1	2	200344,200344	5411,6283	ACIS-S	20,40

Each of the retrieved datasets consists of ‘primary’ and ‘secondary’ data product directories. The primary data product directory contains all of the necessary data files required for most analyses. Included in these files is a Level 2 event file which has been produced by Standard Data Processing, an automated data processing pipeline run at the CXC. The ‘Level’ of a data product refers to the stage of the pipeline reached in processing the data. Level 2 event files are calibrated and filtered event files and are of sufficient quality for data analysis. In principle one could extract these pre-processed Level 2 event files and use them for further analysis. However it was decided not to take this approach, for two reasons. First of all, when the Level 1 observational data files (files with only instrument-dependent corrections applied) are processed in the pipeline, a default set of processing parameters is used which may or may not be conducive to the users requirements. Essentially the user must relinquish some control of the data processing to the pipeline, which could cause problems later in the analysis. Secondly, the Level 2 event file produced by the pipeline has been calibrated using the most recently available calibration

¹This table of retrieved datasets does not include all of the clusters marked for analysis in Table 1.2. Reasons for the omission of two of these clusters, namely Collinder 232 and Feigelson 1, are given at the beginning of Chapter 3

2.1 Data Reduction and Analysis Procedures

files and pipeline software. Hence, the primary products in the datasets listed in Table 2.1 may have had different calibrations applied with different versions of the pipeline software. This is problematic for two reasons. Firstly, when analyzing clusters with more than one dataset, this can lead to file conflicts when trying to merge data files from each of the observations. Such merged data files are required for tasks such as source detection and are thus very important for the rest of the cluster analysis. Secondly, to ensure homogeneity in the analysis of clusters in this project, it is preferable to have the same calibrations and processing applied to each of the data sets. For these reasons it was decided to reprocess the datasets locally using the *CIAO* software. The data files required for this processing (the Level 1 data products) are contained in the primary and secondary data directories of the retrieved datasets.

Data processing was performed using *CIAO 4.0* with version 3.4.2 of the *CALDB*. The Level 2 event files were produced following the ACIS Data Preparation thread on the *CIAO* website¹. Actual software commands used are deferred to Appendix A.1. These Level 2 event files were filtered to the 0.5-8 keV energy range (the energy range at which *Chandra* is most sensitive). The processed and energy filtered Level 2 event files are then ready for further analysis.

2.1.2 Point Source Analysis

2.1.2.1 Source Detection

The first step in any point source analysis is to identify the sources in the FOV. This was achieved using *CIAO's wavdetect* wavelet source detection algorithm (Freeman et al., 2002). *wavdetect* works by detecting probable source pixels in a dataset by repeatedly correlating it with “Mexican Hat” wavelet functions of different scale sizes. *wavdetect* then uses the results of these correlations to generate a source list including estimates of source dimensions and properties. *wavdetect* is a computationally heavy task and in general is only run for sub-regions of the FOV. However, *wavdetect* can be applied to the entire ACIS array by implementing the `Large_detect.pl` Perl script of T. Maeda² which runs *wavdetect* on a series of regions within the

¹See http://cxc.harvard.edu/ciao/guides/acis_data.html. It is noted here that *CIAO* is currently at version 4.2 and the webpage given is the analysis guide for the current version of the software. The processing steps have not changed apart from the introduction of the ACIS TGAIn calibrations in version 4.1.

²Available at <http://www.astro.psu.edu/xray/acis/recipes/wavdetect.html>

2.1 Data Reduction and Analysis Procedures

FOV, the results of which are consolidated in a master source list. The *wavdetect* Perl script was run for each of the clusters with wavelet radii (scales) of 1,2,4,8 and 16 pixels, and with a significance threshold of 1×10^{-6} which corresponds to about 1 spurious source in the ACIS FOV. Additionally, the final source lists were visually inspected using the *SAOImage DS9* data visualization software¹ to identify and remove any further spurious sources (due to detector artifacts, etc.) and to supplement the source list with obvious point sources that *wavdetect* has missed. In those clusters with more than one dataset, it was first necessary to merge the separate Level 2 event files into one combined event list before running *wavdetect*. This was achieved using the *CIAO* tasks *reproject_events* (http://cxc.harvard.edu/ciao/ahelp/reproject_events.html) and *dmmerge* (<http://cxc.harvard.edu/ciao/ahelp/dmmerge.html>). After choosing one ‘base’ observation from those observations to be merged, *reproject_events* was used to change the sky coordinate tangent point of the other observation(s) to match that of the base observation. This allows the recalculated event files to be merged with the base observation using the *dmmerge* task to create a master Level 2 event file.

2.1.2.2 Source Extraction, Photometry, Spectroscopy and Temporal Analysis

The primary goal of point source extraction is to produce point source spectra with associated backgrounds and ancillary files for every detected source in the FOV by extracting events from source and background regions. These files can in turn be used to perform photometric, spectroscopic and temporal analyses for each of the sources. Given that the FOV of a particular observation may contain a few tens to several thousand point sources, this at first seems a very daunting and time consuming task. *ACIS Extract (AE)* is a software package that contains the tools required to perform both point source extraction and the photometric, spectroscopic and temporal analysis for each of the sources in a semi-automated fashion, greatly reducing analysis timescales. The *AE* package is written in the *IDL* language and incorporates many other analysis software including *CIAO*, *SAOImage DS9*, *MARX* (the *Chandra* ray-trace simulation software), *FTOOLS* (the fits file manipulation tools), *XSPEC* (the X-ray spectral fitting package), the *IDL Astronomy User’s Library* (a set of *IDL* procedures for astronomical data analysis) and *TARA* (a set of *IDL* procedures for the analysis of ACIS data), see Table A.1 for software versions,

¹Available at <http://hea-www.harvard.edu/RD/ds9/>

2.1 Data Reduction and Analysis Procedures

etc. The setup and usage of *AE* is quite involved and thus, the descriptions and commands used are deferred to Appendix A.2. When the *AE* point source analyses are completed, the combined results for each of the sources in the FOV are collated into one master file that contains point source and background properties, source photometry, results of spectral fits, source statistics, etc., which is used for further individual source and cluster analysis.

2.1.2.3 2MASS Catalogue Matching

Once the X-ray sources in the FOV have been identified and data products for each have been produced, we wish to determine whether or not each of the sources has a stellar counterpart. As such, an all-sky catalogue of sources is required to match our detected X-ray sources. For the purposes of this project, optically identified sources are of limited use due to some of the programme clusters suffering from heavy foreground extinction. Thus it was decided to use the 2 Micron All-Sky Survey (2MASS) which is an all-sky IR catalogue and is not as affected by foreground absorption as much as other wavebands. However, there are some limitations to using the 2MASS. First of all, identifying stellar counterparts to X-ray sources beyond 1 kpc is not easy due to cluster members being faint and/or poorly resolved. For clusters within this distance, the 2MASS catalogue is sufficient to identify almost all *Chandra* stellar sources (see Feigelson and Lawson, 2004; Getman et al., 2006). Secondly, some of the programme clusters are embedded in molecular clouds or are located in HII regions thus limiting the detection of fainter stars. For these reasons, it is impossible to assess the completeness of the determining of stellar counterparts of the X-ray sources in these clusters but it is very likely, with very few exceptions (e.g. - IR luminous AGNs and foreground sources), that all of the stellar counterparts identified are cluster members. In addition, the 2MASS photometry of the identified stellar counterparts may be used to supplement the X-ray data in determining cluster properties and to identify candidate OB stars.

The 2MASS All-Sky Point Source Catalogue (PSC) was accessed via the NASA/IPAC Infrared Science Archive Gator catalogue interface¹. The 2MASS PSC was searched around each of the programme clusters and the output, which usually contained several thousand sources, was saved accordingly. This output file was used in conjunction with the results of the X-ray source detection above and the ‘match_xy.pro’

¹Available at <http://irsa.ipac.caltech.edu/applications/Gator/>

2.1 Data Reduction and Analysis Procedures

catalogue matching tool in the *TARA* package¹ to match sources from each catalogue. Rather than using a fixed matching radius as is commonly done, the *TARA* catalogue matching algorithm employs the positional uncertainties for individual sources and a match significance threshold. This is particularly useful given the *Chandra* PSF would require a varying match radius should that technique be used. This catalogue matching tool, when completed, provides the matched *Chandra* and 2MASS source properties as well as match statistics.

2.1.2.4 Galactic Contamination

Not all of the X-ray sources detected in the FOV will be associated with the cluster. As such, estimates of possible contaminants are required. Given the large distances to some of the programme clusters, it is very likely that there are thousands of X-ray emitting stars in the line of sight. It is the distance and luminosity of these foreground stars that will determine whether or not they are detected in the *Chandra* observations. To estimate the contamination due to these sources, techniques similar to those described in the COUP membership study and the *Chandra* study of the Cep B star forming region were used (Getman et al., 2006, 2005). Simulations were run based on the stellar population synthesis model of Galactic disk stars by the Besançon group (Robin et al., 2003), using their web-based model interface², centered on the coordinates of the programme clusters for a solid angle of 0.08 deg² (which roughly corresponds to the ACIS-I FOV) out to the cluster distances. The simulated foreground stellar populations often numbered in the thousands, as was expected, and the simulation output includes spectral types, distances, reddening, etc., for all of the stars in the cluster line of sight. Of the simulated sources, the likely contaminants are main sequence stars of spectral type F,G,K and M and late type giant stars. OB stars were almost never produced in the simulations, whereas A type stars are very weak or none X-ray emitters and were thus ignored.

In order to assign X-ray luminosities to these simulated sources, the XLFs determined from *ROSAT* observations for main sequence K-M stars (Schmitt et al., 1995), F-G stars (Schmitt, 1997) and late type giants (Huensch et al., 1996) from a volume limited sample in the solar neighbourhood were adopted. Monte Carlo simulations were then run by placing these simulated stars across the ACIS background.

¹See http://www.astro.psu.edu/xray/docs/TARA/TARA_users_guide/node11.html

²Available at <http://model.obs-besancon.fr/>

2.1 Data Reduction and Analysis Procedures

Synthetic source spectra were then generated using the *XSPEC* ‘fakeit’¹ command assuming an absorbed thermal plasma model with the absorbing hydrogen column (N_{H}) derived from the A_V value² for each simulated source and kT derived using the relation $kT \approx (4\pi d^2 F_X \times 5.5 \times 10^{-26})^{0.2} / 11.34$ keV (Gudel et al., 1998) where the $4\pi d^2 F_X$ term is the X-ray luminosity assigned from the XLFs in the *ROSAT* PSPC 0.1-2.4 keV energy range. Background spectra from the nearest real sources were then assigned to each of the simulated sources. Source significance for each of the simulated sources was then calculated using these local backgrounds and compared to a detection threshold of significance to determine whether or not the source would be detected by *Chandra*.

The number of detectable foreground stars determined using this method was typically low for each cluster (at most a few tens of stars). Such foreground sources may sometimes be distinguished from cluster sources by having relatively bright stellar counterparts or, if they are sufficiently bright in the X-ray band, having spectra that have low absorption. Where such sources could be identified, they were removed from the analysis. Even then there will easily be some contamination from foreground stars however, without further information, it is not possible to remove them. As such, any remaining foreground contamination is ignored in the cluster analyses which, given the low numbers of detectable foreground stars following from the Monte Carlo simulations, is statistically safe. It was decided not to run similar simulations for background Galactic source contamination as, due to the large distances to the clusters, such already faint sources would be subject to the even larger absorption with ISM, intra-cluster medium and possibly a HII region or molecular cloud all contributing. Because of this there would be few, if any, background Galactic sources detected.

2.1.2.5 Extragalactic Contamination

In addition to Galactic contamination, Active Galactic Nuclei (AGN) can be significant extragalactic contributors to the X-ray sources detected in a given *Chandra* observation. The expected contamination due to background AGNs can be estimated using a similar technique to that used in the foreground contamination analysis, which again is similar to that described in the COUP membership study and

¹See <http://heasarc.nasa.gov/xanadu/xspec/xspec11/manual/node33.html#SECTION00632500000000000000>

² $N_{\text{H}} / A_V = 1.6 \times 10^{21} \text{ cm}^{-2} \text{ mag}^{-1}$ (Vuong et al., 2003)

2.1 Data Reduction and Analysis Procedures

the *Chandra* study of the Cep B star forming region (Getman et al., 2006, 2005). Monte Carlo simulations were constructed by placing fake AGNs randomly across the ACIS background with the AGNs numbers and fluxes following the log N -log S distribution of Moretti et al. (2003). Synthetic source spectra were again generated using the *XSPEC* ‘fakeit’ command. Each source was modeled using an absorbed power law with the photon index (Γ) ranging between 1.5-2.5, which is the accepted range for the hard emission from AGN (Ishibashi and Courvoisier, 2010, , and references therein), and the N_{H} value set to the sum of the absorption to the programme cluster, taken as the median N_{H} of the spectral fits of the OB stars, and the H_I column density through the entire Galactic disk in the direction of the programme cluster (Dickey and Lockman, 1990)¹. As with the foreground contamination simulations, background spectra from the nearest real sources were then assigned and source significances for each of the simulated sources were calculated and compared to a detection threshold to determine whether or not the source would be detected by *Chandra*.

Potential extragalactic sources can be distinguished from cluster members via their source properties. Typically, background AGN would exhibit hard X-ray spectra ($E_{\text{median}} > 2.0$ keV) and not have a 2MASS counterpart. Thus, any hard sources in the FOV without a 2MASS counterpart were tentatively labelled as extragalactic. However, at the distance of some of the programme clusters, it is also likely that some of the PMS population will not have a stellar counterpart in addition to having similarly hard spectra. To separate these actual cluster members from background AGNs, a source lightcurve analysis was employed. In general, detected PMS stars in the clusters will, at some point during the exposure, undergo a flaring period. AGN in contrast show relatively consistent X-ray lightcurves. To keep those variable hard sources without 2MASS counterparts (i.e. - PMS stars) for the cluster analysis, the results of the temporal analysis of AE was used. During the temporal analysis of each source, a uniform count rate model is compared to the distribution of source counts in time and a 1-sample Kolmogorov-Smirnov statistic (P_{KS}) is computed. The value of P_{KS} indicates the likelihood that a source is variable with values of P_{KS} near 0 suggesting variability. As such, a variability limit of $P_{\text{KS}} < 0.1$ was set and sources with $P_{\text{KS}} > 0.1$ are flagged as potential extragalactic sources and removed

¹Calculated using the HEASARC N_{H} tool, available at <http://heasarc.gsfc.nasa.gov/cgi-bin/Tools/w3nh/w3nh.pl>.

from further consideration.

2.1.3 Diffuse Emission Analysis

X-ray diffuse emission analysis is somewhat more involved than point source analysis. Diffuse emission is not confined to a small region as is the case with a point source but rather can cover much, or sometimes all of the detector. This presents some problems for the analysis, particularly with background selection. In some cases, the program clusters take up the entire ACIS FOV. Because of this there are no background ‘sky’ regions one can define and thus, any extracted diffuse spectrum has not been corrected for background. A further problem with diffuse emission analysis is that the extraction regions cover so much of the detectors that instrumental fluorescence becomes a significant contaminant in the spectra which manifests as strong emission lines characteristic of the detector materials. While these appear at well defined energies, coupled with the lack of an available background for subtraction they are a blight on the extracted spectra. Another problem with a diffuse emission treatment is the selection of an extraction region itself. This is not such a problem for the analyses of the programme clusters however as spectra will simply be extracted where possible from the total cluster regions and the cluster cores. Taking all these considerations into account, we must assess the potential methods of diffuse emission analysis.

In general, there are three approaches. The first is the selection of a background region from within the FOV and correct this for the position dependent effects due to the variation in the instrumental effects which are particularly pronounced for large diffuse emission regions. While this may be possible for some of the programme clusters it is not adequate for the others due to a lack of a background ‘sky’ region in the FOV. Given we wish to apply the same analysis techniques to each of the clusters, it was decided not to use this method for any of the suitable programme clusters. Similarly, one can define a background extraction region from within the FOV but rather than correct for variation in the instrumental response, one can define a background model in a spectral fitting program, such as *XSPEC*, which explicitly models each of the contributions to the background and simultaneously fit this model to the source and background with an additional model fit the intrinsic source emission. This again is not suited to our need as it again requires a

2.1 Data Reduction and Analysis Procedures

background ‘sky’ region. The final method, which was adopted for the forthcoming analyses, is the use of ‘blank sky’ background files. These are a set of observations of the blank sky (i.e. - free from sources) distributed with the *Chandra CALDB*¹. In this method, appropriate ‘blank sky’ files are determined and corrected to match the observational data aspect. This method has the advantages that it removes the need for a background ‘sky’ region in the observational FOV and that it eliminates the effect of the variation in instrumental performance across the FOV providing backgrounds are extracted from the same instrument regions as the diffuse sources in the observational data. However, it has the disadvantage that it assumes that the background in the ‘blank sky’ observations matches that of the observation. In addition it assumes the instrumental background does not vary in the time between the source and background observations. However, this latter caveat has been shown to be somewhat unimportant with an analysis of the stowed datasets from 2002-2004 showing only a minor variation in the instrumental background². This leaves only the assumption of the ‘blank sky’ background being consistent with that of the observation. This is reduced to some degree by the matching of the observational data to appropriate ‘blank sky’ backgrounds in the analysis procedure, however there is still no guarantee that the observation and ‘blank sky’ backgrounds are consistent. What can be said is that above 2 keV, the instrumental background dominates the ‘blank sky’ backgrounds and so should match the observation background well. As the majority of the programme clusters suffers from quite large foreground absorption, their respective diffuse emission analyses are limited to the hard band. For these clusters at least, the ‘blank sky’ backgrounds should provide an ideal background spectrum.

To extract the diffuse emission spectra for each of the clusters, extraction regions were defined and saved in *CIAO* format using *DS9*. Spectra, backgrounds and response files were created using the *CIAO* task `specextract`. Prior to this, the ‘blank sky’ backgrounds were prepared according following the guidelines on the *Chandra* website³. Following the `specextract` runs the data are ready to be spectrally fit in *XSPEC*. (Actual software commands and steps to extract these spectra are given in Appendix A.1.1)

¹See <http://cxc.harvard.edu/ciao/threads/acisbackground/index.py.html>

²See <http://cxc.harvard.edu/contrib/maxim/stowed/>

³See <http://cxc.harvard.edu/ciao/threads/acisbackground/index.py.html>

2.2 Spectral Fitting and *XSPEC*

One of the main goals of the data reduction and analysis procedures described thus far has been the creation of spectra and detector responses for sources, be they point-like or diffuse. However, these are not the true source spectra but rather photon counts in specific instrument channels (a count spectrum) related to the source spectrum via the instrumental response files. Ideally one would use these response files to derive the original source spectrum, however, in practice this is not possible as such a derivation leads to non-unique answers as well as being highly sensitive to variations in the instrumental channel photon counts. The commonly adopted alternative is to define a model spectrum with various parameters, fold it through the response files to produce a predicted count spectrum and compare it to the observed count spectrum. The model parameters can then be varied until a ‘best-fit’ to the data is found. Several softwares packages exist that perform just such a task but the one used in this Ph.D. thesis is the *XSPEC* software (which has been already been mentioned in the text). *XSPEC* takes as input the observed source and background spectra, response files and a user defined spectral model and proceeds to derive a best-fit model spectrum. *XSPEC* starts with a set of model parameters which are used to predict a count spectrum. This is compared to the observed count spectrum and a fit-statistic is calculated. The model parameters are then systematically varied until the best fit-statistic is found, at which point *XSPEC* outputs the best fit model and its associated parameters. The most commonly adopted ‘goodness of fit’ criteria is the χ^2 statistic with a $(\chi^2/\nu) = 1$ (where ν is the number of degrees of freedom in the fit) indicating a good fit to the observed count spectrum. It must be noted that very often more than one spectral model will give a good fit to the data. It is up to the user to decide which is the more physically representative model.

Spectral fitting of the vast majority of the point sources in this Ph.D. project was performed using the fitting scripts of the *AE* software. These fitting scripts derive spectral parameters by fitting the spectra in *XSPEC* using either absorbed one or two temperature thermal plasma models. Essentially these models consist of two components, the `tbabs` or Tuebingen-Boulder ISM absorption model (Wilms et al., 2000)¹ and the `apec` or Astrophysical Plasma Emission Code (APEC) (Smith et al.,

¹See <http://heasarc.gsfc.nasa.gov/docs/xanadu/xspec/manual/XSmodelTbabs.html> for a description of the model implementation in *XSPEC*.

2.2 Spectral Fitting and *XSPEC*

2001)¹. The APEC model(s) represents the intrinsic X-ray emitting plasma(s) of the source while the `tbabs` model simulates the effect the line-of-sight ISM has on the source X-rays. The combination of these models allows the derivation of equivalent absorbing hydrogen column density (N_{H}), X-ray plasma temperatures (kT) and elemental abundances if desired. For most of the sources in the programme clusters, these models are sufficient, however, some sources require more detailed models, namely the WRs and sources suffering from photon pileup.

WRs have more complex spectra that can be fit by the models in the *AE* fitting scripts due to them having more chemically complex atmospheres than less evolved stars. To fit these sources, the models of Skinner et al. (2010) were adopted which are absorbed one or two temperature APEC models with generic WR abundances apart from those elements with prominent emission lines whose abundances were allowed to vary.

Photon pileup is a serious issue when observing very bright sources². This problem is not due to the source but rather due to the limitations of the detector. Photon detections in the ACIS CCD are not instantaneously logged. Rather, the entire array is read once every integration time (~ 3.2 s in full-frame mode). This has the consequence that, if a source is sufficiently bright that more than one photon arrives at the same region of the detector in one integration time, the many photons are logged as one single event, usually with the combined energy of the many photons. This leads to a loss of information from lower energy photons and an apparent excess of high energy events resulting in an unreliable count spectrum. There are several ways to treat photon pileup, one of which is to simulate its causes when defining an *XSPEC* model to fit the observed data, which is adopted in these analyses. This is achieved through the inclusion of the `pileup` model³ to account for pileup, the contribution of which is subsequently removed leaving a more representative source spectrum.

¹See <http://heasarc.gsfc.nasa.gov/docs/xanadu/xspec/manual/XSmodelApec.html> for a description of the model implementation in *XSPEC*.

²See http://cxc.harvard.edu/ciao/ahelp/acis_pileup.html for a description of ACIS pileup.

³See <http://heasarc.gsfc.nasa.gov/docs/xanadu/xspec/manual/XSmodelPileup.html> for a description of the model implementation in *XSPEC*.

Chapter 3

Programme Cluster Results

In the forthcoming sections I will first give a brief introduction to each of the clusters including their known properties and any previous X-ray analyses. Following this I will present the results of my analysis of the clusters. Due to the large amount of data and results for each of the clusters, a detailed description of the analysis and results is only given for one sample cluster, namely IC 1805. The results for the remaining clusters are summarized in their respective sections without repeating the descriptions of the analysis methods given in the sample cluster section and, to reduce clutter, selected figures and tables will be deferred to Appendix B. However, over the course of the analyses it was found that some of the clusters with X-ray data available (see Table 1.2) were not suitable for analysis, namely Feigelson 1 and Collinder 232. The observations of Feigelson 1 were simply not deep enough for any meaningful analysis. The combined 6 ks *Chandra* observations of the cluster was only sufficient to detect < 10 of the brightest cluster sources, For these reasons, it was decided not to proceed with the analysis of Feigelson 1. Collinder 232 suffers from a different issue. This cluster is located in the Carina star forming region very close in projection to both Trumpler 14 and Trumpler 16 though it is much less massive. The cluster is contained in the Trumpler 14 *Chandra* observation, however, the centre of the clusters lies at the very edge of the ACIS FOV. As such, only a handful of the cluster's sources are observed. In addition, a study of the stellar population of the Carina region by [Tapia et al. \(2003\)](#) showed Collinder 232 not to be a true cluster but rather a random collection of a handful of bright stars with no underlying faint population so it's classification as an open cluster is tenuous at best. For these reasons it was decided to forego the X-ray analysis of Collinder 232.

A note on naming conventions:

During the remainder of the thesis, in tables and figures, values of X-ray flux and luminosity will be quoted in the standard *Chandra* soft, hard and total energy bands corresponding to the 0.5-2 keV, 2-8 keV and 0.5-8 keV energy ranges respectively. Thus, where appropriate, quantities are denoted by the subscripts s , h and t to indicate the range for which they have been determined. Additionally, quantities that have been corrected for line of sight absorption will also be denoted by the subscript c . For example, the X-ray luminosity (L_X) of a source in the 2-8 keV energy range that has been corrected for absorption will be written as ' $L_{X,h,c}$ ', etc.

3.1 IC 1805

IC 1805, better known as the Heart Nebula, is located in the Cas OB6 association. At the centre of the nebula is a rich open cluster whose massive stars are responsible for exciting the surrounding molecular cloud. The cluster has been known for quite some time and there have been many analyses published in the literature. [Massey et al. \(1995\)](#) performed a detailed spectroscopic and photometric analysis of the cluster, identifying 45 stars with spectral types earlier than B3. These authors obtained spectra for the 38 brightest stars in the cluster and derived values of $A_V \approx 2.7$ and $d \approx 2.3$ kpc for the reddening and distance, respectively. In addition, they determine a slope for the cluster IMF of $-1.3(\pm 0.2)$, consistent with a Salpeter IMF, and an age for those stars with $M > 25 M_\odot$ of 1-3 Myr (noting that less massive stars are of younger age). For the following analysis, an age of 1 Myr is adopted. In a later study, [Shi and Hu \(1999\)](#) obtained spectra for 140 stars in the cluster, revising the number of stars earlier than B3 to about 60. In addition, the cluster is thought to have once contained the well known HMXB LS I +61 303, which is a candidate microquasar. [Mirabel et al. \(2004\)](#) show that this HMXB system was likely ejected from the cluster by the 'kick' imparted by the supernova explosion of the primary star.

Chandra performed a deep observation of IC 1805 (~ 80 ks). However, as yet, there has been no X-ray analysis of the cluster published in the literature. Given the rich population of OB stars found by both [Massey et al. \(1995\)](#) and [Shi and Hu \(1999\)](#) it is reasonable to expect that the cluster harbours a rich X-ray emitting population and potentially intracluster diffuse emission. Interestingly, multiplicity studies of several suspected binary systems in the cluster by [Rauw and De Becker](#)

(2004) and De Becker et al. (2006a) confirmed the presence of two high mass binary systems (one being a potential triple system), leading to the possibility of CWBs in the cluster.



Figure 3.1: DSS Image of IC 1805.

3.1.1 Analysis

The 79 ks IC 1805 *Chandra* dataset was aimed at the centre of the cluster. However, given the cluster’s angular size, this was inadequate to observe the entire cluster ($R_{Cl} = 13'$) but was enough to resolve the cluster core ($R_{Co} = 6'$). Overall, the ACIS-I FOV includes just over half of the total cluster area. The data were reduced with *CIAO* and *AE* as outlined in Section 2.1. Background flaring periods were removed leaving $\sim 77ks$ of useable data. The *wavdetect* algorithm detected 348 sources in the FOV and due to the size of the cluster in relation to the FOV, all were tentatively labelled as cluster sources. The 0.5-8 keV ACIS-I image is shown in Figure 3.2.

Cross-correlation with the 2MASS Bright source catalogue yields counterparts for 205 of the 348 detected sources. Foreground and extragalactic contamination simulations yielded 4-10 potential foreground sources and 45-52 potential extragalactic sources in the FOV. The number of potential foreground contaminants in

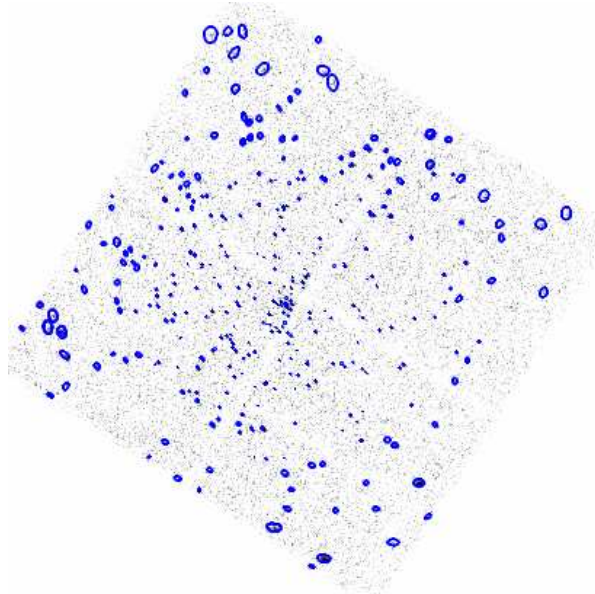


Figure 3.2: *Chandra* 17'×17' ACIS-I 0.5-8 keV image of IC 1805 with detected sources marked in blue.

the FOV is quite small in relation to the number of sources detected in the cluster and, because there is no way to discern these from cluster sources, these are not considered in the rest of the analysis. As of the background sources, individual source data and source statistics were analysed as outlined in 2.1 to identify 50 candidate extragalactic sources in the FOV, in line with the simulation predictions, and were removed from consideration. This left 298 cluster sources whose basic source properties are given in Table 3.1¹, which was produced using the *AE* task *hmsfr_tables*.

A preliminary assessment of potential diffuse emission in the cluster was performed by adaptively smoothing the entire image in the hard (2-8 keV) and soft (0.5-2 keV) bands using the CIAO task *csmooth* (Ebeling et al., 2006). The combined hard/soft adaptively smoothed image is shown in Figure 3.3 with the minimum value of the color scale adjusted to reduce the background contribution².

There is little evidence for cluster wide diffuse emission in Figure 3.3, however

¹This is only a sample of the basic source properties table of IC 1805, shown here to give an example of the data that were available for analysis. Similar tables were created for each of the programme clusters however, due to their very large size, their inclusion in this thesis is not feasible.

²As in <http://hea-www.harvard.edu/RD/ds9/user/rgb/index.html>

Table 3.1: IC 1805 *Chandra* Catalogue: Basic Source Properties

Source		Position				Extraction				Characteristics						
Seq. No.	CXOU J	α (J2000.0)	δ (J2000.0)	Error	θ	$C_{t,net}$	$\sigma_{t,net}$	B_t	$C_{h,net}$	PSF Frac.	Signif.	$\log P_B$	Anom.	Var.	Eff. Exp.	E_{median}
(1)	(2)	(deg)	(deg)	(arcsec)	(arcmin)	(counts)	(counts)	(counts)	(counts)	(11)	(12)	(13)	(14)	(15)	(ks)	(keV)
		(3)	(4)	(5)	(6)	(7)	(8)	(9)	(10)						(16)	(17)
1	023113.75+613045.7	37.807307	61.512718	0.9	10.9	33.9	8.4	24.1	14.6	0.90	3.8	<-5	g...	-	40.3	1.6
2	023121.13+612746.8	37.838071	61.463014	0.8	9.5	21.8	6.9	16.2	5.9	0.89	2.9	-4.7	a	60.2	1.7
3	023121.82+613021.4	37.840947	61.505946	0.7	9.8	39.7	8.8	25.3	24.5	0.90	4.2	<-5	g...	-	56.5	2.6
4	023134.43+612951.1	37.893480	61.497531	0.8	8.3	12.5	5.7	12.5	0.2	0.91	2.0	-2.6	a	63.6	1.3
5	023134.89+613022.0	37.895407	61.506121	0.6	8.4	26.9	7.0	13.1	6.0	0.91	3.6	<-5	a	59.3	1.5
6	023137.49+612814.2	37.906248	61.470618	0.5	7.5	30.9	6.6	6.1	5.7	0.90	4.3	<-5	g...	-	56.0	1.5
7	023139.73+613125.0	37.915582	61.523621	0.5	8.3	34.6	7.5	12.4	14.9	0.90	4.3	<-5	g...	-	60.9	1.9
8	023141.38+612557.4	37.922436	61.432613	0.9	7.2	5.9	4.0	6.1	0.0	0.90	1.3	-1.6	a	64.6	1.1
9	023145.58+612854.7	37.939935	61.481864	0.4	6.7	32.4	6.6	4.6	17.4	0.89	4.5	<-5	g...	-	61.2	2.3
10	023147.02+613204.6	37.945933	61.534637	0.3	7.9	102.4	11.4	13.6	34.6	0.90	8.6	<-5	a	64.1	1.8
11	023147.85+612732.7	37.949410	61.459108	0.5	6.3	17.5	5.2	4.5	5.8	0.90	3.0	<-5	a	70.1	1.6
12	023148.51+612532.6	37.952140	61.425742	0.9	6.4	5.0	3.6	4.0	0.0	0.89	1.2	-1.6	c	68.9	0.8
13	023150.40+612756.7	37.960015	61.465756	0.8	6.0	4.3	3.2	2.7	0.0	0.90	1.1	-1.6	g...	-	64.7	1.0
14	023150.95+613332.1	37.962311	61.558931	0.7	8.6	27.0	6.6	9.0	8.3	0.91	3.8	<-5	g...	-	44.0	1.7
15	023152.21+612725.3	37.967551	61.457040	0.8	5.7	4.2	3.2	2.8	0.0	0.90	1.1	-1.5	c	71.5	0.8
16	023152.54+612827.7	37.968945	61.474368	0.4	5.8	20.7	5.4	3.3	6.8	0.90	3.5	<-5	g...	-	65.3	1.5
17	023155.17+613123.8	37.979888	61.523283	0.3	6.7	53.8	8.3	6.2	20.6	0.90	6.1	<-5	a	69.5	1.8
18	023155.30+612652.9	37.980421	61.448045	0.8	5.4	3.3	3.0	2.7	0.0	0.91	0.9	-1.2	a	72.3	0.5
19	023155.57+613215.0	37.981555	61.537518	0.5	7.3	24.4	6.2	7.6	6.3	0.90	3.6	<-5	b	63.5	1.6
20	023156.85+613235.8	37.986881	61.543284	0.3	7.4	66.3	9.6	13.7	23.9	0.90	6.6	<-5	c	63.1	1.6
21	023200.19+613040.2	38.000814	61.511189	0.8	5.8	4.5	3.4	3.5	0.0	0.90	1.1	-1.5	b	72.0	0.8
22	023201.93+612649.1	38.008081	61.446980	0.3	4.6	20.8	5.2	1.2	0.0	0.90	3.6	<-5	a	74.2	0.9
23	023202.72+612334.6	38.011347	61.392962	0.8	5.8	4.9	3.4	3.1	3.0	0.90	1.2	-1.8	a	60.4	5.6
24	023202.76+612951.8	38.011507	61.497743	0.4	5.1	14.7	4.7	2.3	9.4	0.90	2.8	<-5	g...	-	68.0	2.4
25	023206.41+612458.1	38.026745	61.416166	0.4	4.7	10.5	4.0	1.5	4.9	0.89	2.3	<-5	g...	-	68.6	1.4
26	023207.16+613242.6	38.029834	61.545177	0.3	6.7	60.9	8.8	7.1	19.4	0.90	6.5	<-5	g...	-	55.3	1.6
27	023207.73+612321.2	38.032241	61.389248	0.7	5.5	4.5	3.2	2.5	0.4	0.90	1.2	-1.8	b	65.0	0.8
28	023208.08+612203.5	38.033685	61.367640	0.1	6.5	216.4	15.4	4.6	25.0	0.89	13.6	<-5	c	68.6	1.2
29	023209.06+612630.3	38.037769	61.441761	0.2	3.8	18.3	4.9	0.7	0.5	0.90	3.4	<-5	g...	-	52.9	1.3
30	023209.24+613245.6	38.038529	61.546002	0.5	6.6	23.2	5.6	2.8	13.3	0.90	3.8	<-5	g...	-	26.1	2.6
---	---	---	---	---	---	---	---	---	---	---	---	---	---	---	---	---

(1): X-ray catalog sequence number, sorted by RA. (2): IAU designation. (3) and (4): Right ascension and declination for epoch (J2000.0). (5): Estimated standard deviation of the random component of the position error, $\sqrt{\sigma_x^2 + \sigma_y^2}$. The single-axis position errors, σ_x and σ_y , are estimated from the single-axis standard deviations of the PSF inside the extraction region and the number of counts extracted. (6): Off-axis angle. (7) and (8): Net counts extracted in the total energy band (0.5–8 keV); average of the upper and lower 1σ errors on (7). (9): Background counts expected in the source extraction region (total band). (10): Net counts extracted in the hard energy band (2–8 keV). Col. (11): Fraction of the PSF (at 1.497 keV) enclosed within the extraction region. A reduced PSF fraction (significantly below 90%) may indicate that the source is in a crowded region. (12): Photometric significance computed as net counts divided by the upper error on net counts. (13): Logarithmic probability that extracted counts (total band) are solely from background. Some sources have P_B values above the 1% threshold that defines the catalog because local background estimates can rise during the final extraction iteration after sources are removed from the catalog. (14): Source anomalies: (g) fractional time that source was on a detector (FRACEXPO from *mkarf*) is <0.9 . (e) source on field edge; (p) source piled up; (s) source on readout streak. (15): Variability characterization based on K-S statistic (total band): (a) no evidence for variability ($0.05 < P_{KS}$); (b) possibly variable ($0.005 < P_{KS} < 0.05$); (c) definitely variable ($P_{KS} < 0.005$). No value is reported for sources with fewer than four counts or for sources in chip gaps or on field edges. (16): Effective exposure time: approximate time the source would have to be observed on-axis (no telescope vignetting) on a nominal region of the detector (no dithering over insensitive regions of the detector) to obtain the reported number of counts. (17): Background-corrected median photon energy (total band).

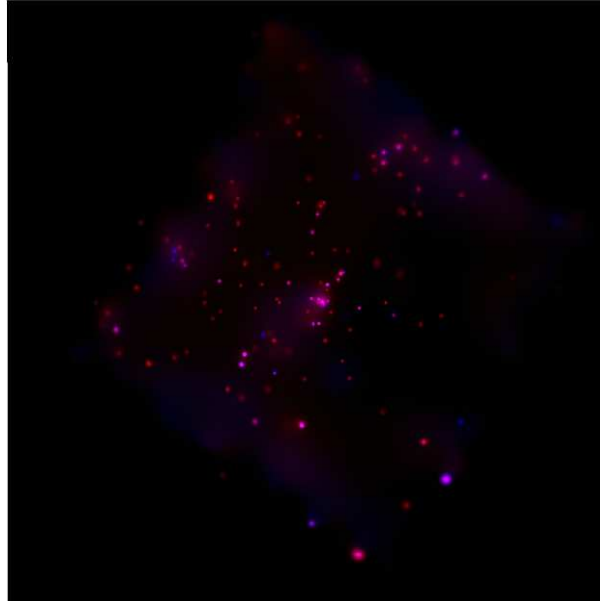


Figure 3.3: Adaptively smoothed *Chandra* soft (0.5-2 keV, shown in red) and hard (2-8 keV, shown in blue) image of IC 1805.

there appears to be relatively faint diffuse emission in the cluster centre, possibly due to the combined effect of winds from the massive stars in this region. It is important to note however that there still may be cluster wide diffuse emission. As the entire FOV is taken up by the cluster, the background contribution to the emission may be overestimated and may contain some cluster related emission. In any case, a diffuse emission analysis is warranted.

3.1.1.1 Known High Mass Stars

High mass sources in the detected X-ray population were identified using the high mass source lists of [Massey et al. \(1995\)](#) and the SIMBAD database. All of the known O stars in the FOV were detected, whereas only 5 of the known B stars were detected. The spectra of each of the high mass sources with enough counts were fit in *XSPEC* with absorbed thermal plasma models during the *AE* reduction and analyses procedures. The results of the spectral fits are given in Table [3.2](#).

The fit results for sources with > 50 counts (Table [3.2](#)) seem to indicate three different emission mechanisms at work in the high mass, OB star regime. First of all, the brightest source, HD 15558, exhibits a moderately hard thermal spectrum

Table 3.2: IC 1805 Known High Mass Star X-ray Spectral Parameters

<i>Chandra</i> Source (CXO J)	Name	Sp. Type	<i>Net Cts.</i>	N_{H} (10^{22} cm^2)	kT (keV)	kT_2 (keV)	χ^2/ν	$\log F_{X_{h,c}}$ ($\text{erg cm}^{-2} \text{ s}^{-1}$)	$\log F_{X_{t,c}}$ ($\text{erg cm}^{-2} \text{ s}^{-1}$)	$\log L_{X_{h,c}}$ (erg s^{-1})	$\log L_{X_{t,c}}$ (erg s^{-1})
023210.80+613307.9	BD+60498	B0.2V	37	-	-	-	-	-	-	-	-
023236.31+612825.7	BD+60501	O7V((f))	259	$0.48^{0.72}_{0.31}$	$0.62^{0.76}_{0.51}$	-	0.91/12	-14.58	-13.20	30.22	31.60
023240.80+612800.2	-	B1V	170	$0.55^{1.00}_{0.24}$	$3.13^{7.43}_{1.84}$	-	1.64/8	-13.46	-13.15	31.34	31.65
023242.58+612721.7	HD 15558	O4III(f)	2904	$0.36^{0.44}_{0.28}$	$0.74^{0.80}_{0.79}$	$2.05^{2.40}_{1.84}$	0.79/95	-12.98	-12.29	31.82	32.51
023243.58+612632.0	Hoag 125	B2.5V	127	$0.50^{0.88}_{0.20}$	$2.56^{5.02}_{1.56}$	-	0.89/5	-13.70	-13.34	31.46	31.10
023243.96+612720.6	-	B0.5V	60	$0.97^{2.37}_{0.39}$	$1.08^{1.74}_{0.35}$	-	0.76/5	-14.63	-13.83	30.18	30.97
023249.47+612242.2	HD 15570	O4If	1521	$1.18^{1.28}_{1.07}$	$0.65^{0.71}_{0.60}$	-	1.24/66	-13.45	-12.13	31.35	32.67
023257.86+612726.7	Hoag 14	B2.5V	32	-	-	-	-	-	-	-	-
023304.80+612821.4	Hoag 11	B2.5V	7	-	-	-	-	-	-	-	-
023320.62+613118.8	HD 15629	O5V((f))	432	$0.32^{0.50}_{0.11}$	$0.48^{0.63}_{0.39}$	-	1.39/19	-14.57	-12.85	30.23	31.95

High mass sources identified using the high mass source lists of [Massey et al. \(1995\)](#) and the SIMBAD database. Only those sources with > 50 counts were fit in *XSPEC*.

Table 3.3: IC 1805 Candidate OB Star X-ray Spectral Parameters

<i>Chandra</i> Source (CXO J)	Name	Sp. Type	<i>Net Cts.</i>	N_{H} (10^{22} cm^2)	kT (keV)	kT_2 (keV)	χ^2/ν	$\log F_{X_{h,c}}$ ($\text{erg cm}^{-2} \text{ s}^{-1}$)	$\log F_{X_{t,c}}$ ($\text{erg cm}^{-2} \text{ s}^{-1}$)	$\log L_{X_{h,c}}$ (erg s^{-1})	$\log L_{X_{t,c}}$ (erg s^{-1})
023314.69+612402.7	Hoag 118	-	63	0.84_{-}	1.49_{-}	-	1.07/3	-14.53	-13.65	31.16	30.27
023201.93+612649.1	Hoag 123	-	21	-	-	-	-	-	-	-	-
023230.63+612121.8	-	-	20	-	-	-	-	-	-	-	-

Source names determined using the SIMBAD database. Only those sources with > 50 counts were fit in *XSPEC*.

with $kT > 1$ keV. This is higher than would be expected for emission via shocks in the stellar wind. Given this high plasma temperature and its brightness, it is very likely that HD 15558 is a CWB. Indeed, HD 15558 was determined to be a massive binary system consisting of O5.5III(f)+O7V stars by De Becker et al. (2006a). The remaining O-type stars BD+60501, HD 15570 and HD 15629 exhibit cooler X-ray spectra all of which have plasma temperatures < 1 keV attributable to emission via the RDIS mechanism. The remaining stars bright enough for a spectral analysis are all early B-type stars. Each of these sources can be described by thermal plasmas with $kT > 1$ keV. However, unlike HD 15558, their absorption corrected X-ray luminosities are relatively low. Thus, it is very likely that a MCWS emission mechanism is responsible for the X-ray emission from these sources. This is not a surprising result as in a cluster of the age of IC 1805 it is possible that the early B stars still retain a fraction of magnetic field of their parental molecular cloud core.

3.1.1.2 Candidate OB Stars

The correlated 2MASS data were filtered to leave only sources with high quality photometry, i.e. - with good S/N ratio and free from contamination flags. The resulting data were used to produce a J vs $J - H$ colour-magnitude diagram. A 1 Myr main sequence isochrone¹ and a 1 Myr pre-main sequence (Siess et al., 2000) isochrone were also plotted on this colour magnitude diagram to give an indication of the the current evolutionary stage of the cluster (Figure 3.4). In addition, an $8 M_{\odot}$ reddening vector was calculated and plotted along with the reddening vector of the peak of the PMS isochrone. This plot highlights five candidate OB stars, however, the candidate sources' coordinates were subsequently searched in the SIMBAD database and 2 were found not to be cluster members but members of the surrounding Cas OB6 association and were thus removed from the analysis.

As with the known high mass stars, the spectrum for each of the candidate OB stars with a high enough photon count was fit in *XSPEC*. The results of the spectral fits are given in Table 3.3 along with some parameters of the less bright sources. The one candidate OB star with enough counts for spectral fitting has similar derived spectral parameters to the known early B-type stars in Table 3.2 and thus its X-ray emission is likely the result of the MCWS mechanism. Due to a lack of counts it is unclear as to the nature of the emission from the remaining candidate OB stars.

¹Obtained using the CMD 2.2 interface. The latest version (CMD 2.3) is available at <http://stev.oapd.inaf.it/cgi-bin/cmd>

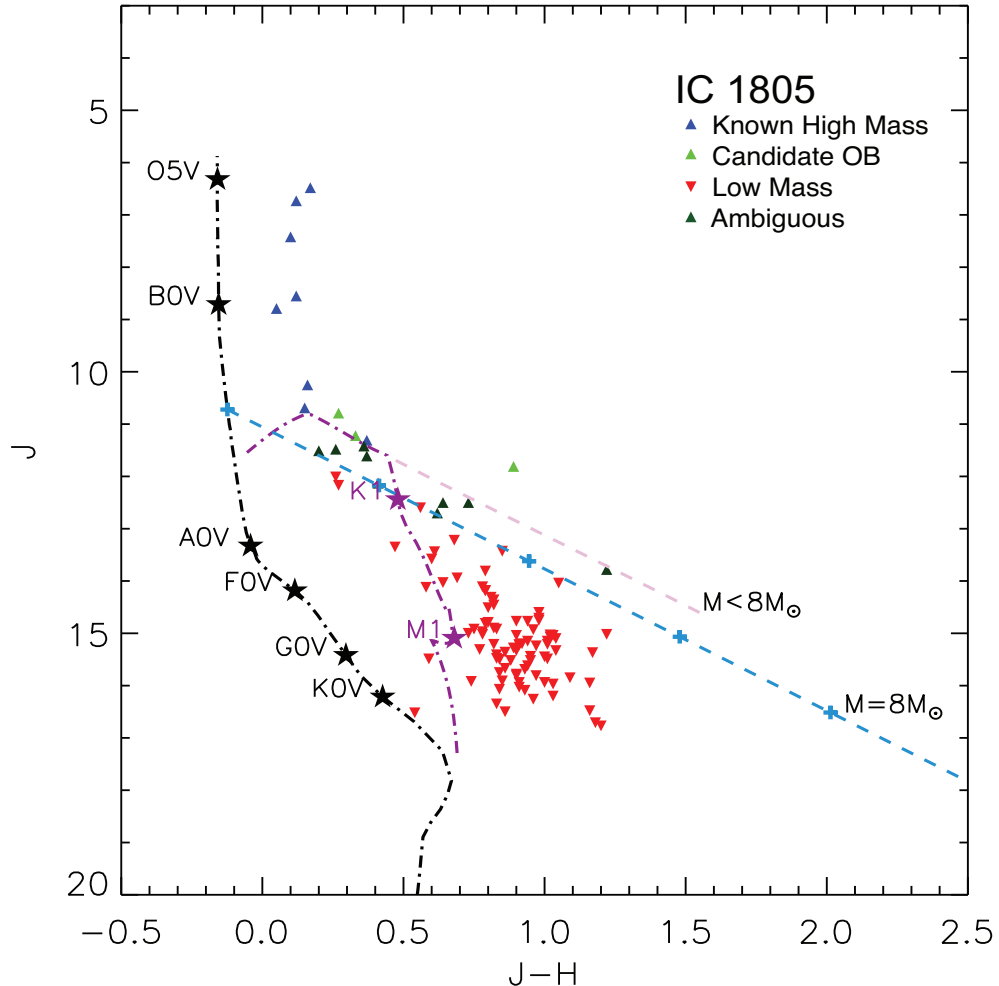


Figure 3.4: IC 1805 2MASS J vs J-H colour magnitude diagram. The blue triangles indicate the known high mass stars, the light green triangles indicate the candidate OB stars, the dark green triangles indicate the ambiguous sources and the red inverted triangles indicate low mass sources. The black dashed-dotted line is the 1 Myr main sequence isochrone (with spectral types indicated as black stars) calculated for $A_V = 0$.

The purple dashed-dotted line is the 1 Myr PMS isochrone (with spectral types indicated as purple stars). The light blue dashed line is the $8M_\odot$ reddening vector with the crosses marking every $A_V = 5$. The light purple dashed line is the reddening vector of the maximum J value of the PMS evolutionary track. Sources between this and the $8M_\odot$ reddening vector may be above or below $8M_\odot$ and are hence labelled as ambiguous sources.

3.1.1.3 Pre-Main Sequence Stars

Excluding the known high mass stars, the candidate OB stars and the extragalactic contaminants, the point sources in the FOV are most likely low mass PMS stars. As with the known high mass and candidate OB stars, some of the PMS stars are bright enough to be fit spectrally in *XSPEC*. The global results of these fits are given in graphic form in Figure 3.5. As expected, most of the brightest PMS sources in the FOV exhibit hard spectra and absorption corrected 2-8 keV $L_X \lesssim 10^{31}$ erg s⁻¹. However, one source stands out as being particularly bright with 2-8 keV $L_X \sim 10^{32}$ erg s⁻¹. This source was identified as CXO J023309.98+612459.5. Inspection of this source's lightcurve shows that it underwent a tremendous flare during the observation with at least a factor of 4 increase in photon flux at the flare's peak compared to the quiescent level, shown in Figure 3.6. The derived plasma temperatures of the sources range from 1-5 keV, with the distribution peaking at ~ 2.5 keV. The majority of these sources suffers from slight foreground absorption ($\log N_H \lesssim 22.0$ cm⁻²), similar to the high mass sources in the cluster. None of the bright PMS stars are subject to heavy absorption ($\log N_H \gtrsim 22.5$ cm⁻²). Also, the majority of these shows no sign of variability over the course of the observation with only a few variable or flaring objects. The trend in the variation of E_{median} with kT is similar to that found by Feigelson et al. (2005) with a slight increase in kT with E_{median} . In addition, a similar $E_{\text{median}}-N_H$ relation at low values of E_{median} is seen as in Feigelson et al. (2005). However, due to a lack of bright, heavily absorbed sources, their $E_{\text{median}}-N_H$ relation at higher values of E_{median} is absent. For sources with $E_{\text{median}} < 1.7$ keV, an upper limit of $\log N_H \lesssim 22.0$ cm⁻² is found.

This sample of bright PMS stars is only a fraction of the ~ 280 PMS stars in the FOV. However, despite the absence of a spectral analysis for the faint sources, much can still be derived from the data (see Table 3.1 as well as Section 3.1.1.5 for a discussion of the derivation of 2-8 keV L_X 's) about the PMS population as a whole. For this purpose it was decided to utilize 2-8 keV L_X against the median detected photon energy (E_{median}) plots. The E_{median} data are being used as they are a reliable estimator of absorbing hydrogen column (N_H , Feigelson et al., 2005). Sources with large E_{median} (and by consequence large N_H) likely have an accretion disk (Class I or II YSOs) causing the excess absorption. Following similar PMS population treatments from the literature (see Getman et al., 2006; Wang et al., 2007, for example) $E_{\text{median}} = 3$ keV (which corresponds to $\log N_H \approx 22.5$ cm⁻²) was set as the divider between lightly and heavily obscured sources. For those sources

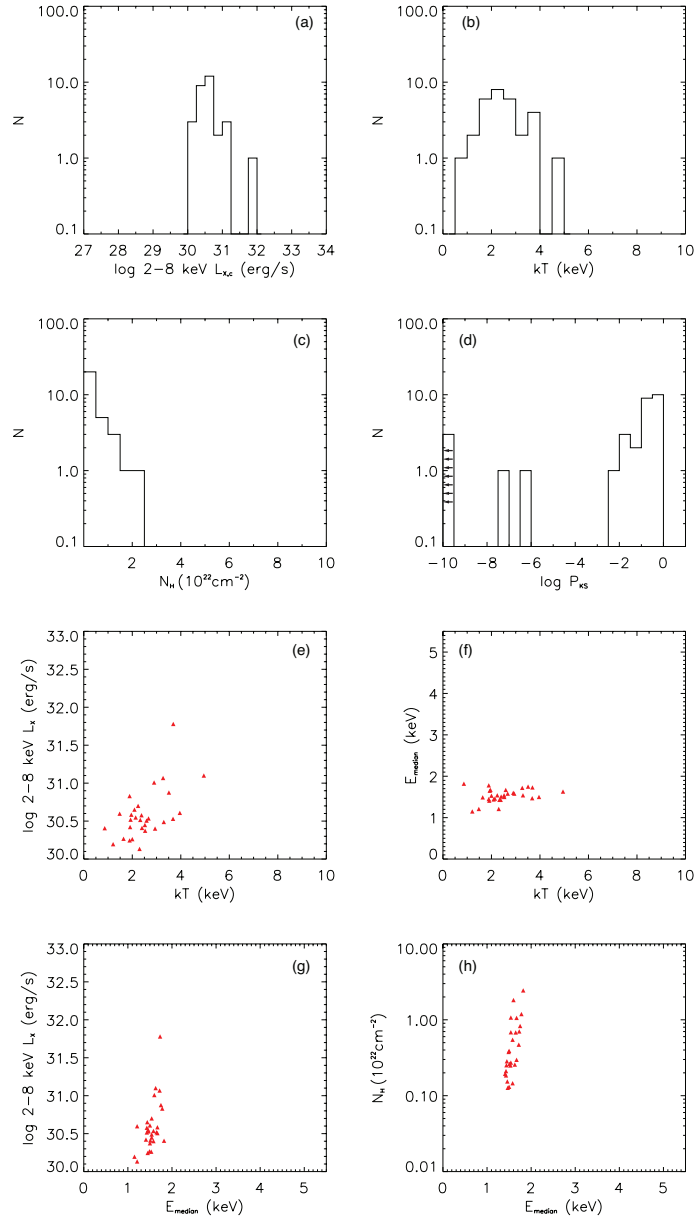


Figure 3.5: Plots of derived source parameters for the bright PMS population of IC 1805. (a) Distribution of absorption corrected 2-8 keV L_X . (b) Distribution of best fit thermal plasma temperature (kT). (c) Distribution of best fit absorbing hydrogen column (N_H). (d) Distribution of Kolmogorov-Smirnov variability statistic with $\log P_{KS} < 0.05$ indicating variability. (e) Plot of absorption corrected 2-8 keV L_X against best fit thermal plasma temperature (kT). (f) Plot of median photon energy (E_{median}) against best fit thermal plasma temperature (kT). (g) Plot of absorption corrected 2-8 keV L_X against median photon energy (E_{median}). (h) Plot of best fit absorbing hydrogen column (N_H) against median photon energy (E_{median}).

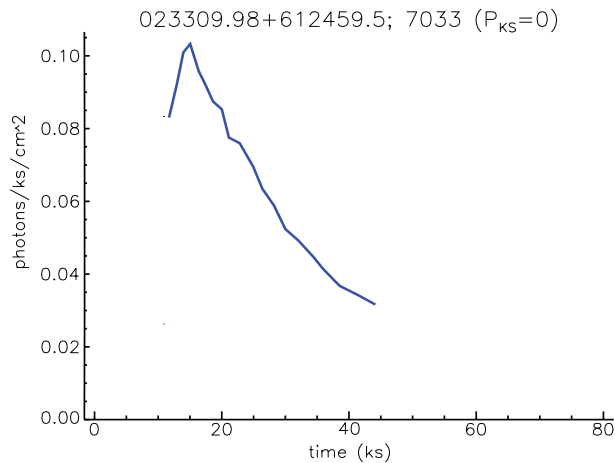


Figure 3.6: Lightcurve of the unusually bright PMS star CXO J023309.98+612459.5.

Its brightness can be explained by a large flaring event early in the observation, indicated in blue. The lightcurve does not extend to the start or end of the observation as the Kolmogorov-Smirnov test is insensitive in these regions (Broos et al., 2010).

with $E_{\text{median}} < 1.7$ keV, an upper limit of $\log N_{\text{H}} \lesssim 22.0$ cm^{-2} is inferred from Figure 3.5(h). The sources separated in this way according to absorption levels are plotted on the 2-8 keV L_{X} against E_{median} plot, shown in Figure 3.7(a). The sources were next divided according to their Kolmogorov-Smirnov variability statistic (P_{KS}). The standard variability limit of 0.05 was defined with all sources with P_{KS} below this value classified as variable and sources with $P_{\text{KS}} < 0.005$ classified as strongly variable. The resulting 2-8 keV L_{X} against E_{median} plot is shown in Figure 3.7(b).

Using Figure 3.7(a) and (b) one can draw the following conclusions about the PMS population of IC 1805:

- The distribution of sources in Figure 3.7(a) indicates that the majority of sources in the cluster suffers little or no local absorption. This implies that the majority of PMS stars in the cluster is either Class II or III YSOs.
- In addition there are 3 heavily obscured sources. These are likely either Class I or Class II YSOs viewed from an unfavourable angle.
- Figure 3.7(b) shows that the brightest PMS source CXO J023309.98+612459.5 is strongly variable, resulting from a bright flare during the observation. The other strongly variable sources scattered throughout the plot are likely due to

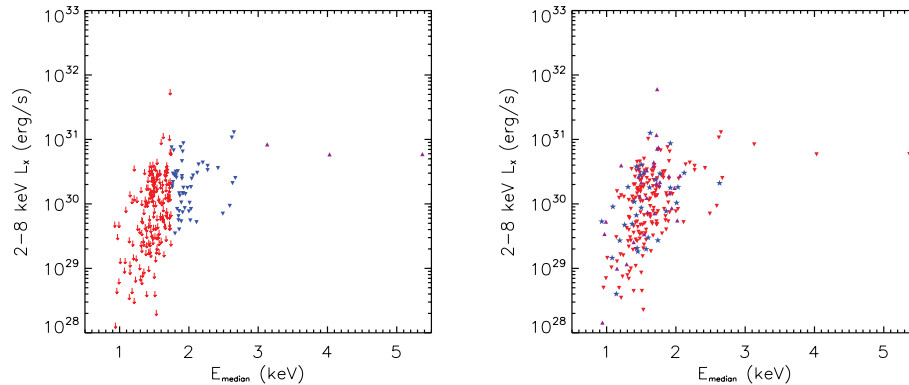


Figure 3.7: Plot of the 2-8 keV L_X against the median detected photon energy (E_{median}) for the IC 1805 PMS population separated according to E_{median} (left) and variability (right). Left: the red arrows mark $E_{\text{median}} < 1.7$ keV (indicating an upper limit of $\log N_{\text{H}} \lesssim 22.0 \text{ cm}^{-2}$), blue inverted triangles 1.7-3 keV (indicating the lightly obscured population) and purple triangles > 3 keV (indicating the heavily obscured population). Right: Inverted red triangles refer to non-variable sources, blue stars representing variable sources and the purple triangles representing strongly variable flaring sources.

less prominent flaring events. Similarly, the less variable sources are scattered throughout the plot.

- The most obscured sources show no signs of variability. Given this, and their relatively high L_X values, it is reasonable to assume that these most probably represent the high luminosity tip of the heavily obscured quiescent sources.
- The majority of the quiescent sources is localised in the lightly obscured region of the plot and exhibit a general trend to higher L_X with increasing E_{median} .

These conclusions that the IC 1805 PMS population consists mostly of Class II or III YSOs and relatively few Class I YSOs are to be expected for a cluster of the age of IC 1805. The study of [Massey et al. \(1995\)](#) showed the low mass stars ($\lesssim 3 M_{\odot}$) in the cluster to have ages of ~ 1 Myr. Assuming the PMS population is of approximately similar age, one can expect the majority of stars to be either Class II or III ([Feigelson and Montmerle, 1999](#)). It must also be noted that the classification of YSO classes here is based solely on X-ray data and uses only absorption values as an indicator of the presence of a disk or natal cloud. This is better done with deep NIR observational data which use specific tracers (e.g. - focus on infrared excess due to an accretion disk) to classify YSOs.

3.1.1.4 Diffuse Emission

As previously mentioned in the preliminary diffuse emission assessment (see Figure 3.3) there is some evidence for faint diffuse emission in the cluster centre. To obtain a better image of the diffuse emission the more detailed treatment described in Section 2.1.3 was employed. The resulting masked and adaptively smoothed image is shown in Figure 3.8.

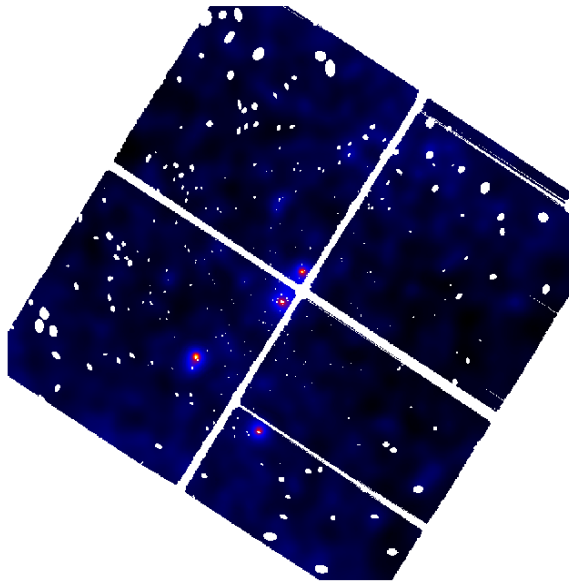


Figure 3.8: Masked and adaptively smoothed 0.5-8 keV image of IC 1805 diffuse emission. The apparently bright points are likely the unmasked wings of the PSF of the brightest sources in the FOV which are artifacts due to the selected image binning.

There is faint diffuse emission in the cluster centre and little obvious but discernible diffuse emission throughout the IC 1805 cluster. However, a spectral analysis is still required as, due to the size of the cluster in comparison to the *Chandra* ACIS-I FOV, the apparent lack of diffuse structure may simply be due to emission pervading the FOV. Without a background sky region to compare to, this cannot be disproved. Following the procedure outlined in Section 2.1.3, spectra were extracted from the entire ACIS-I FOV and the cluster core region while extracting corresponding background spectra from the appropriate ACIS ‘blank-sky’ background files. These spectra were fit in *XSPEC* with various spectral models and it was found that an absorbed thermal plasma model with $kT \sim 1$ keV yields a good fit for each of the two IC 1805 spectra. The results of these fits are given in Table 3.4

and the spectra are shown in Figure 3.9.

Table 3.4: IC 1805 Diffuse Emission X-ray Spectral Parameters

Region	N_{H} (10^{22}cm^2)	kT (keV)	Z/Z_{\odot}	χ^2/ν	$\log F_{X_{h,c}}$ ($\text{erg cm}^{-2} \text{s}^{-1}$)	$\log F_{X_{t,c}}$ ($\text{erg cm}^{-2} \text{s}^{-1}$)	$\log L_{X_{h,c}}$ (erg s^{-1})	$\log L_{X_{t,c}}$ (erg s^{-1})
all FOV	$0.32^{0.48}_{0.16}$	$1.00^{1.24}_{0.85}$	$0.07^{0.13}_{0.04}$	0.88/84	-12.83	-12.00	31.97	32.80
cluster core	$0.34^{0.57}_{0.15}$	$1.01^{1.27}_{0.82}$	$0.08^{0.16}_{0.04}$	0.98/84	-13.14	-12.31	31.66	32.49

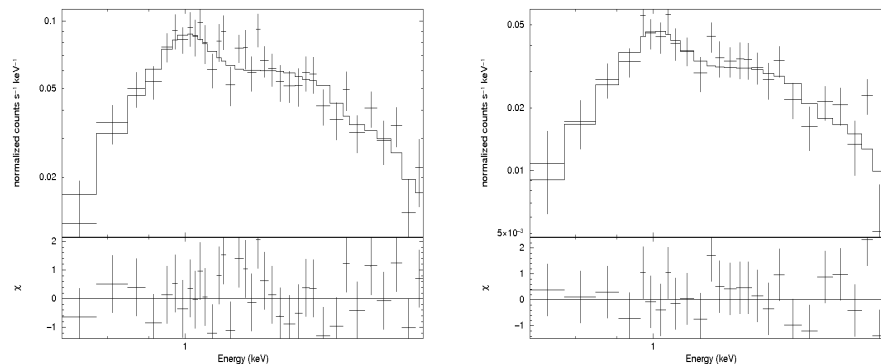


Figure 3.9: IC 1805 all FOV diffuse emission spectrum (left) and cluster core diffuse emission spectrum (right). The spectra were rebinned for plotting purposes using XSPEC’s ‘*setplot rebin*’ command. Only the 0.7-2 keV energy range is shown as the spectra approach background levels outside this range.

It is clear from the fit results in Table 3.4 that there is indeed faint diffuse emission throughout the cluster. In addition, the shape of the spectra in Figure 3.9 does not vary between the core and the total FOV spectrum which, along with the ~ 1 keV best fit thermal plasma, suggests that winds due to massive stars in the cluster are not responsible for the faint diffuse emission. Indeed, the spectral parameters and X-ray luminosities point to a more widespread source as being mostly responsible for the faint diffuse emission, probably an unresolved low mass PMS population.

3.1.1.5 XLF

To construct an XLF we require estimates for the unabsorbed X-ray luminosity for each of the sources detected in the cluster. However, only the brightest sources may be reliably fit in XSPEC leaving a substantial fraction of the cluster sources with no estimate. However, we can use outputs of the AE reduction with the equations

of Broos et al. (2010) and employ a similar treatment to Getman et al. (2010) to derive 2-8 keV X-ray luminosities for all of the cluster sources using only photometrically derived parameters. To determine a first estimate of the photometric X-ray luminosity, Equation 9 of Broos et al. (2010) was used, namely:

$$L_X \approx 4\pi d^2 F_{\text{photon}} E_{\text{median}} \quad (3.1)$$

where F_{photon} is the incident photon flux in units of photon $\text{cm}^{-2} \text{s}^{-1}$ and E_{median} is the median photon energy. Since *AE* outputs F_{photon} ¹ and E_{median} for each of the sources, their photometric X-ray luminosities can be derived. To limit the effect of foreground absorption on the derived L_X values, only the hard band is considered. Getman et al. (2010) find some systematic offset between the photometrically derived X-ray luminosity and the spectrally derived X-ray luminosities of sources bright enough for spectral fitting using this approach. Photometric X-ray luminosities were calculated for each of the IC 1805 PMS sources with spectroscopically derived L_X values. A plot of photometric L_X against spectroscopic L_X for these bright PMS sources (Figure 3.10) showed the expected offset.

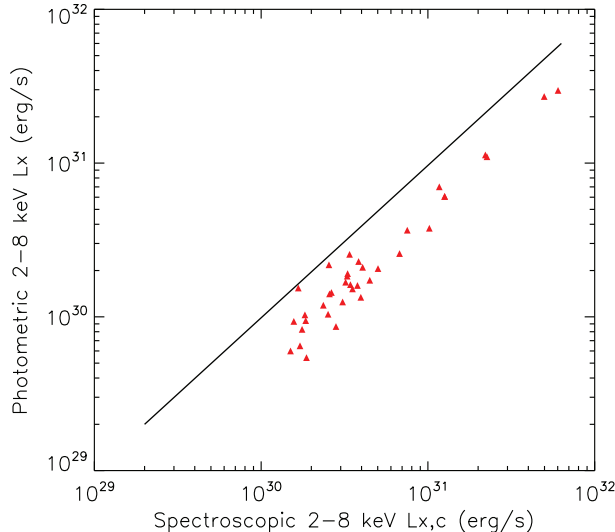


Figure 3.10: IC 1805 bright PMS star spectroscopic/photometric 2-8 keV X-ray luminosity comparison. The diagonal black line indicates a photometric/spectroscopic L_X ratio of unity.

¹*AE* actually outputs two estimates for the incident photon flux F_{photon} calculated by different means. The more statistically stable estimate via division of the net count rate in a given energy band by the detector response over that band (see Broos et al., 2010) is used in these analyses.

This systematic offset for all of the faint cluster sources was corrected using the median ratio of photometrically to spectroscopically derived L_X values in Figure 3.10¹. The faint source photometric L_X values were used in conjunction with the spectroscopically derived bright source L_X values to construct the total cluster 2-8 keV XLF for IC 1805, shown in Figure 3.11. Similarly, a 2-8 keV XLF was constructed for the PMS population which could be compared to that of the well known Orion Nebular Cluster (ONC) 2-8 keV XLF determined in the COUP, shown in Figure 3.12.

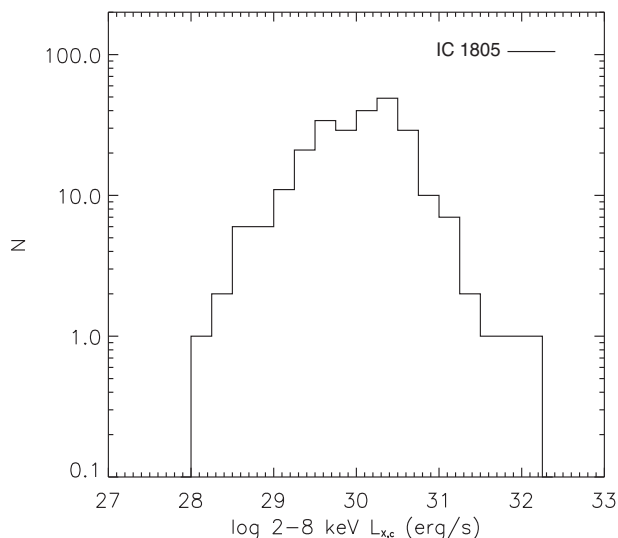


Figure 3.11: IC 1805 total cluster 2-8 keV XLF.

Figure 3.12 indicates that the observed X-ray emitting PMS population of IC 1805 is slightly smaller than that observed in the COUP. The high luminosity end of the IC 1805 and COUP low mass XLFs have approximately the same slope but the IC 1805 XLF peaks at $\log L_X = 30.3 \text{ erg s}^{-1}$ where it begins to decline as compared to the COUP XLF due to the detection limits of the observation. Using Figure 3.12 the scaling factor to match the IC 1805 XLF to that of the COUP was determined to be ~ 0.5 . Hence, given the total number of low mass X-ray sources from the COUP (~ 1500), the IC 1805 low mass X-ray emitting population in the ACIS-I FOV is estimated to be ~ 750 which is ~ 3 times larger than the detected

¹This method of correcting the offset assumes that a ‘best fit’ line through the data points runs through the origin. This is not the case however but, since the points are far from the origin, it is a good approximation.

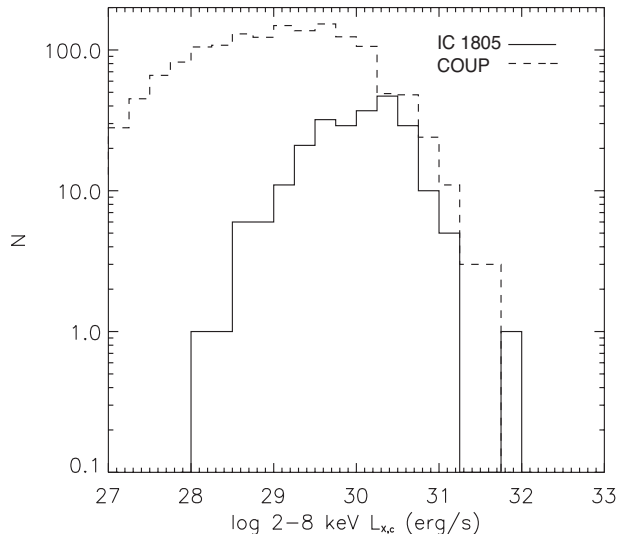


Figure 3.12: IC 1805 2-8 keV XLF (solid line) and the COUP 2-8 keV XLF (dashed line) with high mass stars removed.

population. This may seem quite low for a cluster that both [Massey et al. \(1995\)](#) and [Shi and Hu \(1999\)](#) found to contain a substantial high mass population but it must be remembered that the ACIS-I FOV covers just over 50% of the cluster area. This unresolved low mass X-ray population is likely the source of the faint diffuse emission discussed in Section 3.1.1.4. To offer a comparison to the spectrally derived unabsorbed 2-8 keV $\log L_X$ of $\sim 32.0 \text{ erg s}^{-1}$ (see Table 3.4), the part of the XLF due to the unresolved sources was integrated to determine a 2-8 keV $\log L_X$ of 32.2 erg s^{-1} (see Figure 1.6). This is very close to the observed 2-8 keV L_X and reinforces the earlier conclusion that the faint diffuse X-ray emission throughout the cluster was likely due to an unresolved low mass population.

3.1.1.6 Summary

This 78 ks *Chandra* observation of IC 1805 covered approximately 50% of the total cluster area. All of the known O stars in the FOV were detected of which one was found to be a CWB while the rest exhibit the soft spectra consistent with RDIS emission. Only the brighter B type stars in the FOV were detected, most of which exhibit moderately hard spectra, consistent with MWCS emission. A 2MASS-*Chandra* source correlation and J vs $J-H$ colour magnitude diagram analysis identified a further 3 candidate OB stars, with the brightest of these likely an early B star emitting via a MCWS. A moderate population of PMS stars was detected. The majority of

these is Class II or III YSO, with a few Class I sources also identified. Faint soft diffuse emission is found to pervade the FOV after analysis of the total FOV and cluster core diffuse spectra and is attributed to an unresolved PMS population. A 2-8 keV cluster XLF was constructed and compared to that of the COUP. Similarities at the high luminosity end of the XLFs were found, in keeping with a universal XLF/IMF correlation. Comparison of the PMS XLF to that of the COUP shows a ‘missing’ population of faint sources due to the sensitivity limit of the observation. Integration of the XLF in this ‘missing’ region yields an L_X comparable to that of the faint diffuse emission detected in the FOV, supporting the idea that this diffuse emission is due to an unresolved PMS population.

3.2 Bica 1 and Bica 2

Bica 1 and Bica 2 are quite interesting objects in that they have only recently been identified as open cluster candidates (Bica et al., 2003). They are located in the rich Cyg OB2 association which has been studied extensively in the past making their recent discovery all the more surprising. Bica et al. (2003) identified the clusters while visually inspecting the structure of the Cyg OB2 association using Digitized Sky Survey images and proceeded to use the 2MASS point source catalogue to derive the cluster parameters for each of the newly identified objects. These authors derive values of $6.6(\pm 0.2)$ and $5.6(\pm 0.2)$ for interstellar reddening (A_V) for each cluster, $1.8(\pm 0.2)$ kpc for the distance to each cluster and $1 - 4$ Myr for the age of each cluster. They also determine a projected separation of 2.3 pc of the clusters at their derived distance. This is a very small separation and indicates that these clusters may form a physical pair. Knödlseeder (2000) performed a detailed 2MASS analysis of Cyg OB2 as a whole and derived values for core radius of the association and a census of the OB population. Bica et al. (2003) note that both Bica 1 and Bica 2 lie within the Cyg OB2 core radius with Bica 1 located at the core. Given that the OB population analysis of Knödlseeder (2000) revealed 2600 (± 400) OB stars, with 120 (± 20) of these being O stars, it is reasonable to assume that many of these objects may be members of Bica 1 or Bica 2 and as such, the clusters may harbour a rich X-ray emitting population and potentially diffuse emission. (I note here that a later NIR spectroscopic study of the Cyg OB2 O star population (Comerón et al., 2002) revised the number of O stars in the population to the 90-100 range which is still a very large O star population).

Both *Chandra* and *XMM-Newton* have observed the Cyg OB2 region. *XMM-Newton* has observed the region several times with exposure times ranging from 2 - 32 ks. *Chandra* observed Cyg OB2 twice, however only one of these pointings (a deep 98 ks observation) contains the Bica 1 and Bica 2 clusters in the FOV. [Albacete Colombo et al. \(2007\)](#) use this deep *Chandra* observation to characterize the rich X-ray emitting population in the core region of Cyg OB2, in particular the low mass population which, until then, was unknown. A later study by [Wright and Drake \(2009\)](#) used this 98 ks observation with a 49 ks observation (centred northwest of the Cyg OB2 core) to analyze the broader X-ray emitting population in the region. There have yet to be studies of the diffuse emission in and around the Cyg OB2 association. It is important to note here that the X-ray population studies published in the literature thus far have focussed on Cyg OB2 as a whole and not the Bica 1 and Bica 2 clusters. As such, an analysis of the X-ray properties of the candidate cluster populations may (or may not) provide evidence that these are indeed physical clusters.



Figure 3.13: Image of Bica 1 and Bica 2 in the Cyg OB2 Association from the Palomar Sky Survey

3.2.1 Summary

The 98 ks Cyg OB2 *Chandra* dataset was aimed at the centre of the Bica 1 cluster which was sufficient to cover the entire cluster areas of Bica 1 ($R_{Cl} = 2'$) and Bica 2

($R_{CI} = 2.5'$) [Bica et al. \(2003\)](#). No background flaring periods were identified leaving the full ~ 98 ks of useable data. The *wavdetect* algorithm detected 856 sources in the FOV, 120 of which were within the Bica 1 cluster bounds with 124 within the Bica 2 cluster bounds. Foreground and extragalactic contamination simulations yield 10-20 potential foreground sources and ~ 110 -170 potential extragalactic sources in the entire FOV. Given the actual areas of the clusters and assuming the contaminants are evenly distributed throughout the FOV, this corresponds to < 2 and 5-7 Galactic and extragalactic contaminants in the Bica 1 cluster area and < 2 and 8-12 Galactic and extragalactic contaminants in the Bica 2 cluster area. Individual source data and statistics were analysed, as outlined in [2.1](#), to identify 2 and 8 candidate extragalactic sources in the Bica 1 and Bica 2 source populations respectively, roughly in line with the simulation predictions, which were removed from consideration. This left 118 Bica 1 sources and 116 Bica 2 sources, including foreground contaminants, which are all labelled as cluster sources. The adaptively smoothed image of the Cyg OB2 region revealed faint diffuse emission in both clusters which, along with the unsmoothed 0.5-8 keV ACIS-I image, is shown in [Figure 3.14](#).

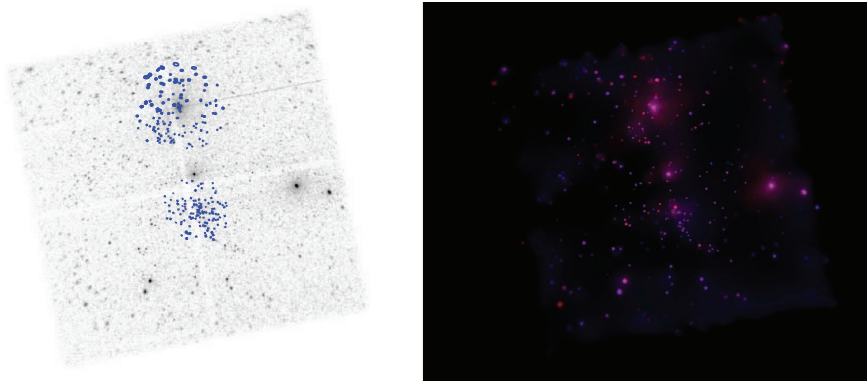


Figure 3.14: *Chandra* ACIS-I 0.5-8 keV image of Bica 1 and Bica 2 with detected sources marked in blue (left) and adaptively smoothed *Chandra* soft (0.5-2 keV, shown in red) and hard (2-8 keV, shown in blue) image.

Bica 1

High mass sources in the detected X-ray population were identified using the source lists of [Wright and Drake \(2009\)](#) and the SIMBAD database. All of the known O stars in Bica 1 were detected whereas only 1 of the 3 early B stars were detected. The spectra of each of the high mass sources with > 50 counts were fit in

XSPEC with absorbed one and two temperature thermal plasma models during the *AE* reduction and analyses procedures (results given in Table B.1). All of the known high mass sources exhibit soft spectra likely due to a RDIS emission mechanism. The brightest source (0.5-8 keV $\log L_X > 32 \text{ erg s}^{-1}$), Schulte 22, is classified in the SIMBAD database as a double star, consisting of O3I and O6V type stars. If these stars formed a physical system with a reasonable binary separation, one would expect such a system form a CWB. However, the X-ray spectrum of this source does not suggest a CWB system given the lack of significant hard emission. As such, it is likely that the these stars form an optical double rather than a physical system.

The correlated high quality 2MASS data were used to produce a J vs $J - H$ colour-magnitude diagram with the appropriate evolutionary tracks and reddening vectors (Figure B.1). This plot identifies only 2 candidate OB stars in the cluster (see Table B.2 for results of spectral fits). Only one of these sources was bright enough to be fit in *XSPEC* and was best fit with an absorbed one temperature thermal plasma model. However, the fit was not well constrained producing an extremely hard best fit thermal plasma temperature ($kT = 28.1 \text{ keV}$). This is likely not an accurate result given the derived 90% confidence interval on the result exceeds the fit parameter range of 0-64 keV. It is likely though that this source is a hard emitter and, given it's relative faintness, is likely emitting via a MCWS mechanism.

The remaining cluster sources are likely low mass PMS objects. The PMS stars with > 50 counts were fit in *XSPEC* with an absorbed thermal plasma model. The global results of these fits are given in graphic form in Figure B.2. The brightest PMS source in Bica 1 has a 2-8 keV $\log L_X < 31 \text{ erg s}^{-1}$, well within the expected range. The derived plasma temperatures of the sources range from 0.5-8 keV, peaking at $\sim 2 \text{ keV}$. The majority of these sources suffers from slight to moderate foreground absorption ($\log N_H \lesssim 22.3 \text{ cm}^{-2}$), with a small number of sources subject to quite heavy absorption ($\log N_H \gtrsim 22.5 \text{ cm}^{-2}$), possibly due to an accretion disk or natal cloud. The majority of the sources shows no sign of variability over the course of the observation, with a small number of variable sources and extremely variable, likely flaring objects. The trend in the variation of E_{median} with kT is similar to that found by Feigelson et al. (2005) with a slight increase in kT with E_{median} . There are too few lightly obscured sources to investigate the N_H - E_{median} relation of Feigelson et al. (2005) fully but most of the sources likely fall in the obscured region of the plot and show a general trend toward increasing E_{median} with increasing N_H . For

sources with $E_{\text{median}} < 1.7$ keV, an upper limit of $\log N_{\text{H}} \lesssim 22.0$ cm⁻² is found.

2-8 keV L_{X} values were calculated for the remaining PMS sources in the cluster and were used to produce the the 2-8 keV L_{X} against E_{median} plots, shown in Figure B.3. These plots indicate that the majority of the PMS sources in Bica 1 is lightly obscured, most probably Class II or Class III YSOs with 5 heavily obscured sources, likely Class I YSOs or Class II YSOs viewed from an unfavourable angle. The brightest of the heavily obscured sources are variable or flaring with a the remaining 3 showing no signs of variability. These sources likely represent the high luminosity tip of the heavily obscured source population.

Given the evident faint diffuse emission in Figure 3.14 it was deemed unnecessary to mask and adaptively smooth the image again. Spectra were extracted from the entire cluster and cluster core regions (the core radius simply defined as $R_{\text{Cl}}/2$) and fit in *XSPEC*. The spectra with the best fit model are shown in Figure B.4 with fit results given in Table B.3. Both the core and the all-FOV spectra are well fit with absorbed two temperature thermal plasma models but in both cases, the hard component plasma temperature is poorly constrained. Apart from an increase in flux, there is little difference between the core and total cluster spectra indicating no variation in diffuse emission sources throughout the cluster. Given the presence of a hard component and the number of O stars confined to the relatively small Bica 1 cluster volume (5 O stars in 5 pc³ assuming the cluster is spherically symmetric), a cluster wind may be the source of the hard diffuse emission. Assuming the model of Cantó et al. (2000, see Section 1.4.7.1) and considering the O stars to be the dominant contributors to the cluster wind, a hot component plasma temperature of ~ 11.6 keV and a 2-8 keV $\log L_{\text{X}}$ of ~ 30.8 erg s⁻¹ are derived meaning a cluster wind can account for only a fraction of the observed $\log L_{\text{X}} \sim 32.3$ erg s⁻¹.

The cluster and PMS star 2-8 keV XLFs were constructed and the PMS XLF compared to that of the COUP. Given that Bica 1 is slightly older than the ONC, the COUP data were scaled according to the scaling relation of Preibisch and Feigelson (2005). These XLFs are shown in Figure 3.15. The total cluster XLF indicates no outliers as expected. The high luminosity end of the PMS XLF shows the same slope as the COUP PMS population. Scaling the COUP population to that of Bica 1 and integrating the ‘missing’ PMS population region yields an estimate of the unresolved PMS population 2-8 keV $\log L_{\text{X}}$ of ~ 32.3 erg s⁻¹ meaning an unresolved PMS can

account for the vast majority of diffuse emission in the cluster which, given the low contribution of a cluster wind, is likely the case.

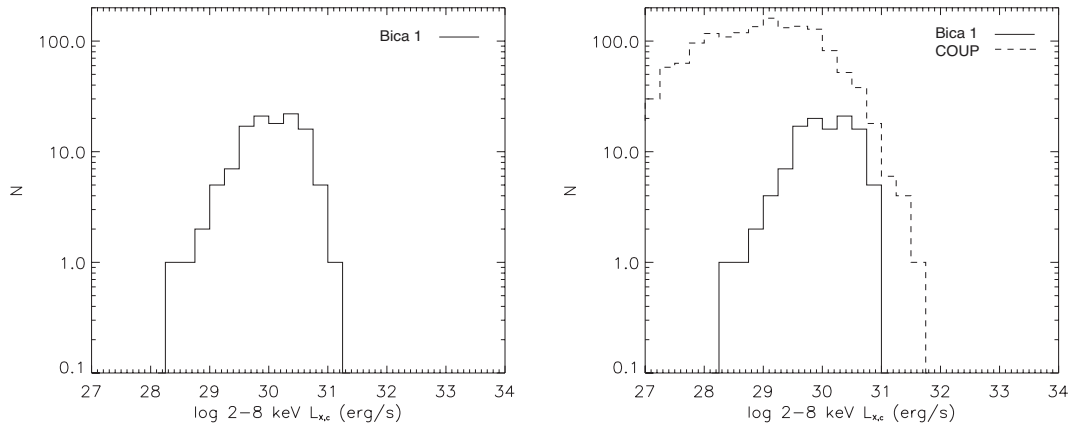


Figure 3.15: Left: Bica 1 total cluster 2-8 keV XLF. Right: Bica 1 PMS star 2-8 keV XLF (solid line) and the COUP 2-8 keV XLF (dashed line).

Bica 2

High mass sources in the detected X-ray population were identified using the source lists of [Wright and Drake \(2009\)](#) and the SIMBAD database. All of the known O stars in Bica 2 were detected whereas none of the 5 early B stars were detected. Strangely however, a B5 star was identified as an X-ray source. The spectra of each of the high mass sources with > 50 counts were fit in *XSPEC* with absorbed one and two temperature thermal plasma models during the *AE* reduction and analyses procedures (results given in Table B.4). All apart from one of the known high mass sources exhibit soft spectra likely due to a RDIS emission mechanism. The extremely bright source (0.5-8 keV $\log L_X > 34$ erg s $^{-1}$), VI Cyg 8A, exhibits the X-ray spectrum of a CWB. Indeed, this is a well known high mass binary system consisting of O6If and O5.5III(f) stars whose CWB status has long been known ([De Becker et al., 2006b](#)).

The correlated high quality 2MASS data were used to produce a J vs $J - H$ colour-magnitude diagram with the appropriate evolutionary tracks and reddening vectors (Figure B.5). This plot identifies only 1 candidate OB star in the cluster (see Table B.5). Unfortunately this source is not bright enough to spectrally derive reliable source properties in *XSPEC* and thus the nature of its X-ray emission is

unknown.

The remaining cluster sources are likely low mass PMS objects. The PMS stars with > 50 counts were fit in *XSPEC* with an absorbed thermal plasma model. The global results of these fits are given in graphic form in Figure B.6. The brightest PMS source in Bica 2 has a 2-8 keV $\log L_X < 32 \text{ erg s}^{-1}$, within the expected range. The derived plasma temperatures of the sources range from 0.1-5 keV, peaking at ~ 1 keV. All of these sources suffer from slight to moderate foreground absorption ($\log N_H \lesssim 22.3 \text{ cm}^{-2}$). About half of these sources show no signs of variability, with a small number of variable sources and a few extremely variable, likely flaring objects. The trend in the variation of E_{median} with kT is similar to that found by Feigelson et al. (2005) with a slight increase in kT with E_{median} . There are too few lightly obscured sources to investigate the N_H - E_{median} relation of Feigelson et al. (2005) fully but most of the sources likely fall in the obscured region of the plot and show a general trend toward increasing E_{median} with increasing N_H . For sources with $E_{\text{median}} < 1.7 \text{ keV}$, an upper limit of $\log N_H \lesssim 22.0 \text{ cm}^{-2}$ is found.

2-8 keV L_X values were calculated for the remaining PMS sources in the cluster and were used to produce the the 2-8 keV L_X against E_{median} plots, shown in Figure B.7. These plots indicate that the majority of the PMS sources in Bica 2 is lightly obscured, most probably Class II or Class III YSOs, with no heavily obscured sources. The brightest of these PMS sources show strong variability and likely underwent a flaring period during the observation. The absence of heavily obscured sources may result be due to a lack of Class I YSOs in the cluster or, more likely, the brightest of these are below the detection limits.

Given the evident faint diffuse emission in Figure 3.14 it was deemed unnecessary to mask and adaptively smooth the image again. Spectra were extracted from the entire cluster and cluster core regions (the core radius simply defined as $R_{Cl}/2$) and fit in *XSPEC*. The spectra with the best fit model are shown in Figure B.8 with fit results given in Table B.6. Both the core and the all-FOV spectra are well fit with absorbed two temperature thermal plasma models the temperatures of which are slightly higher for the total cluster spectrum than for the core. Given the presence of a hard component and the number of O stars confined to the relatively small Bica 2 cluster volume (10 O stars in 9 pc^3 assuming the cluster is spherically symmetric), a cluster wind may be the source of the hard diffuse emission. Assuming

the model of [Cantó et al. \(2000\)](#), see Section 1.4.7.1) and considering the O stars to be the dominant contributors to the cluster wind, a hot component plasma temperature of ~ 8.6 keV and a 2-8 keV $\log L_X$ of ~ 31.5 erg s^{-1} are derived meaning a cluster wind can only account for about a third of the observed $\log L_X \sim 32$ erg s^{-1} .

The cluster and PMS star 2-8 keV XLFs were constructed and the PMS XLF compared to that of the COUP. Given that Bica 2 is slightly older than the ONC, the COUP data were scaled according to the scaling relation of [Preibisch and Feigelson \(2005\)](#). These XLFs are shown in Figure 3.16. The total cluster XLF indicates one outlier, namely the CWB VI CYG 8A. The high luminosity end of the PMS XLF shows the same slope as the COUP PMS population. Scaling the COUP population to that of Bica 2 and integrating the ‘missing’ PMS population region yields an estimate of the unresolved PMS population 2-8 keV $\log L_X$ of ~ 31.8 erg s^{-1} meaning an unresolved PMS can account for most of diffuse emission in the cluster. Thus, the combined emission from the unresolved PMS population and the cluster wind can account for the diffuse emission in the cluster, with the unresolved population dominating.

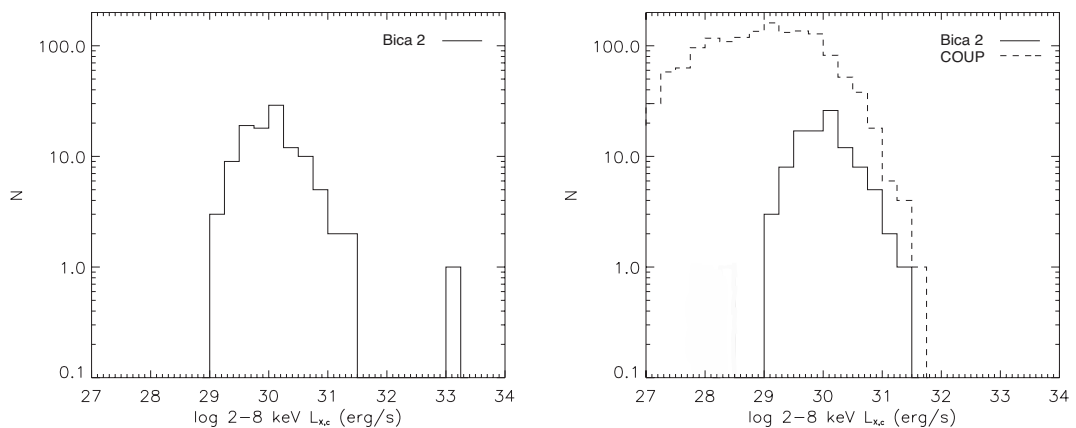


Figure 3.16: Left: Bica 2 total cluster 2-8 keV XLF. Right: Bica 2 PMS star 2-8 keV XLF (solid line) and the COUP 2-8 keV XLF (dashed line).

3.3 IC 1590

IC 1590 is a young open cluster located in the NGC 281 star forming region also known as the Pac Man Nebula ([Mirtle et al., 2008](#); [Moore, 2008](#)). This region has

long been known as a rich, active star forming region with 3 identified sites of recent and/or ongoing star formation, IC 1590 being one. Interestingly, given its location several hundred parsecs above the Galactic plane, it is thought a supernova in the region some 6 Myr ago triggered the star formation in NGC 281 (Leass et al., 2001). The IC 1590 cluster itself has had very little dedicated analysis with only one readily identifiable in the literature. This is likely due to the cluster lying behind two dust clouds one of which is in the immediate foreground of the cluster. Guetter and Turner (1997) present a photometric analysis for many of the stars in the cluster with a spectroscopic analysis of 20 of the brighter sources, including 4 O-type (which form a trapezium similar to that of the ONC), several B-type stars and a PMS population. These authors derive an age of ~ 3.5 Myr and a distance of ~ 3 kpc which are adopted for this analysis. The physical extent of the cluster is determined as $R_{Cl} = 6.6'$ however no estimate is offered for the cluster core. This total cluster radius is consistent with that from the catalogue of open cluster properties of Kharchenko et al. (2005) and thus the catalogue's core radius ($R_{Co} = 3.6'$) is adopted.

A moderately deep ~ 63 ks *Chandra* observation was performed in 2005. The pointing was not aimed directly at IC 1590 but rather at the centre of the NGC 281 star forming region. Unfortunately *Chandra* only observes some of the cluster with slightly less than half being outside the FOV. Luckily though, the O star trapezium in the core of the cluster is observed. As yet an analysis of these *Chandra* data, with respect to IC 1590 or NGC 281, have not been published in the literature. Given the presence of high mass stars in close proximity and a PMS population it is reasonable to expect a rich X-ray emitting population and potentially diffuse emission in the IC 1590 cluster.

3.3.1 Summary

The 62 ks NGC 281 *Chandra* dataset, due to the aimpoint, observed about 70% of the IC 1590 cluster. No background flaring periods were identified leaving the full ~ 62 ks of useable data. The *wavdetect* algorithm detected 310 sources in the FOV, 218 of which were within the cluster bounds. Foreground and extragalactic contamination simulations yield 3-10 potential foreground sources and ~ 90 -150 potential extragalactic sources in the entire FOV. Given the area of the cluster and assuming the contaminants are evenly distributed throughout the FOV, this corresponds to < 4 and ~ 45 -75 Galactic and extragalactic contaminants in the IC 1590



Figure 3.17: DSS Image of IC 1590.

cluster area. Individual source data and statistics were analysed, as outlined in 2.1, to identify 51 candidate extragalactic sources in the cluster source population, in line with the simulation predictions, which were removed from consideration. This left 167 sources, including foreground contaminants, which are all labelled as cluster sources. The adaptively smoothed image of the NGC 281 region revealed faint diffuse emission in the cluster which, along with the unsmoothed 0.5-8 keV ACIS-I image, is shown in Figure 3.18.

High mass sources in the detected X-ray population were identified using the SIMBAD database. All of the known O stars were detected whereas only 1 of the 2 early B stars were detected. The spectra of each of the high mass sources with > 50 counts were fit in *XSPEC* with absorbed one and two temperature thermal plasma models during the *AE* reduction and analysis procedures (results given in Table B.7). All of the known high mass sources exhibit soft spectra likely due to a RDIS emission mechanism.

The correlated high quality 2MASS data were used to produce a J vs $J - H$ colour-magnitude diagram with the appropriate evolutionary tracks and reddening vectors (Figure B.9). This plot identifies 9 candidate OB stars in the FOV (see Table B.8 for results of spectral fits). Only one of these sources was bright enough

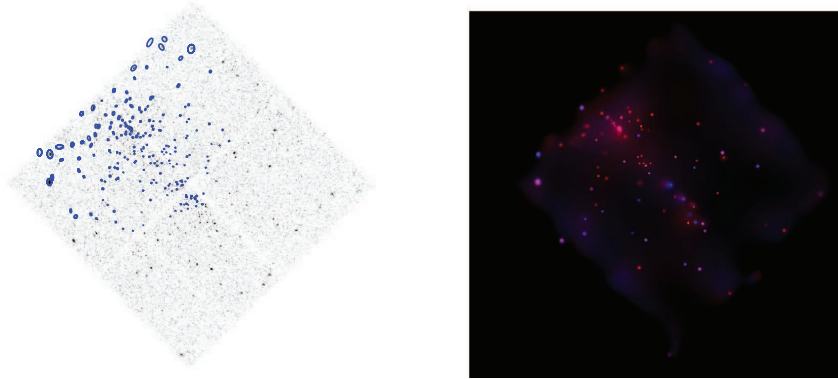


Figure 3.18: *Chandra* ACIS-I 0.5-8 keV image of IC 1590 with detected sources marked in blue (left) and adaptively smoothed *Chandra* soft (0.5-2 keV, shown in red) and hard (2-8 keV, shown in blue) image.

to be fit in *XSPEC* and was best fit with an absorbed one temperature thermal plasma model. However, the fit is formally bad with a reduced $\chi^2 > 2$. The resulting plasma temperature of $kT \sim 1.8$ keV indicates the source is likely emitting via a MCWS mechanism.

The remaining cluster sources are likely low mass PMS objects. The PMS stars with > 50 counts were fit in *XSPEC* with an absorbed thermal plasma model. The global results of these fits are given in graphic form in Figure B.10. The brightest PMS source in IC 1590 has a 2-8 keV $\log L_X \sim 31$ erg s $^{-1}$, well within the expected range. The derived plasma temperatures of the sources range from 1-4 keV, peaking at ~ 3 keV. The majority of these sources suffers from slight to moderate foreground absorption ($\log N_H \lesssim 22.3$ cm $^{-2}$), with no sources subject to heavy absorption. Also, the majority of sources shows no sign of variability over the course of the observation, with a only one variable source and 2 extremely variable, likely flaring objects. The trend in the variation of E_{median} with kT is similar to that found by Feigelson et al. (2005) with a slight increase in kT with E_{median} . There are too few heavily obscured sources to investigate the N_H - E_{median} relation of Feigelson et al. (2005) fully but most of the sources fall in the lightly obscured region of the plot and show no trend between E_{median} and N_H as expected. For sources with $E_{\text{median}} < 1.6$ keV, an upper limit of $\log N_H \lesssim 22.0$ cm $^{-2}$ is found.

2-8 keV L_X values were calculated for the remaining PMS sources in the cluster and were used to produce the the 2-8 keV L_X against E_{median} plots, shown in Figure

B.11. These plots indicate that the majority of the PMS source in IC 1590 is lightly obscured, most probably Class II or Class III YSOs with 9 heavily obscured sources, likely Class I YSOs or Class II YSOs viewed from an unfavourable angle. Five of the nine heavily obscured sources, including the two brightest, are either variable or flaring. These sources likely represent the high luminosity tip of the heavily obscured source population.

Given the evident faint diffuse emission in Figure 3.18 it was deemed unnecessary to mask and adaptively smooth the image again. Spectra were extracted from the entire cluster and cluster core regions and fit in *XSPEC* however only the total cluster spectrum had enough counts for a meaningful fit. This spectrum with the best fit model are shown in Figure B.12 with fit results given in Table B.9. The spectrum is well fit with an absorbed single temperature thermal plasma model with a soft plasma temperature yielding a 2-8 keV L_X of $\sim 2 \times 10^{32}$ erg s $^{-1}$. This suggests an unresolved PMS population as the source of the diffuse emission.

The cluster and PMS star 2-8 keV XLFs were constructed and the PMS XLF compared to that of the COUP. Given that IC 1590 is older than the ONC, the COUP data were scaled according to the scaling relation of [Preibisch and Feigelson \(2005\)](#). These XLFs are shown in Figure 3.19. The total cluster XLF indicates no outliers as expected. The high luminosity end of the PMS XLF shows the same slope as the COUP PMS population. Scaling the COUP population to that of IC 1590 and integrating the ‘missing’ PMS population region yields an estimate of the unresolved PMS population 2-8 keV L_X of $\sim 1 \times 10^{32}$ erg s $^{-1}$ meaning an unresolved PMS can account for about half the observed diffuse emission in the resolved cluster area.

3.4 NGC 1893

NGC 1893 is a massive young stellar cluster notable due to its location at the edge of the Galaxy some 11 kpc from the Galactic centre. The cluster is contained in the Aur OB2 association and associated with the HII region IC 410 and consequently is obscured. Limited optical photometric studies of the cluster have existed for many decades (see [Cuffey, 1973](#), for e.g.) but the more recent works of [Tapia et al. \(1991\)](#) and [Massey et al. \(1995\)](#) presented NIR and spectroscopic analyses

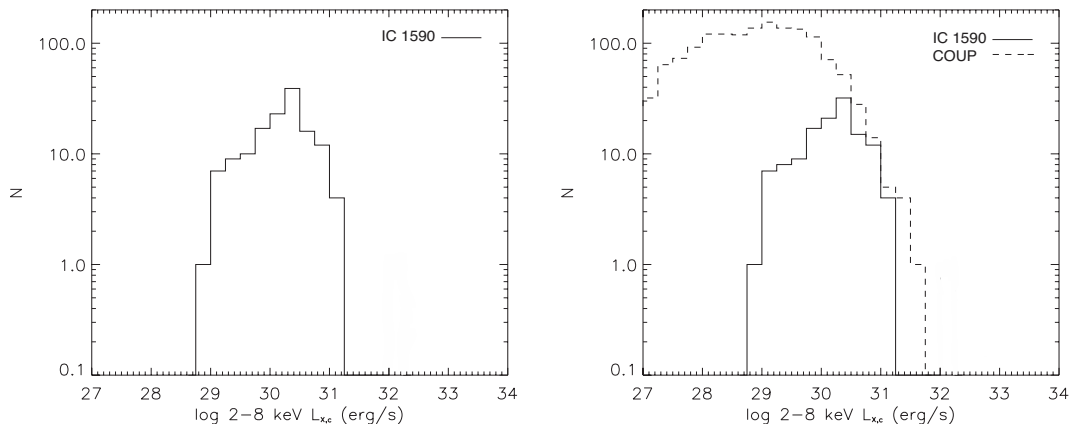


Figure 3.19: Left: IC 1590 total cluster 2-8 keV XLF. Right: IC 1590 PMS star 2-8 keV XLF (solid line) and the COUP 2-8 keV XLF (dashed line).

respectively which identified high mass stars in the cluster including several O stars. Later still, [Marco et al. \(2001\)](#) identify ~ 50 cluster stars with spectra type earlier than A0, with some PMS stars and two candidate Herbig Be stars. This implied the presence of a large PMS population, which was subsequently confirmed through observation, led to a slew of studies on the NGC 1893 stellar population (see [Marco and Negueruela, 2002](#); [Negueruela et al., 2007](#); [Sharma et al., 2007](#), etc.). Age estimates of the cluster range from about 1-4 Myr. An age of 3 Myr is adopted for this analysis based on the presence of two O5V stars in the cluster. The distance estimates to the cluster also vary somewhat, ranging between ~ 3 kpc and ~ 6 kpc ([Marco et al., 2001](#); [Massey et al., 1995](#); [Sharma et al., 2007](#)). For this analysis, a distance of 4.3 kpc, determined by [Tapia et al. \(1991\)](#), is adopted as it is at the centre of the range of distance estimates. [Sharma et al. \(2007\)](#) use various source lists to determine the extent of the cluster, the results of which vary considerably. Instead of selecting one of these estimates it was decided to adopt the total ($R_{Cl} = 12'$) and core radius ($R_{Co} = 4.8'$) from the catalogue of open cluster properties of [Kharchenko et al. \(2005\)](#).

Chandra observed NGC 1893 five times over late 2006 and early 2007 as part of a combined *Chandra-Spitzer* observing programme to investigate the prevalence of circumstellar disks in the population. The *Chandra* data were collected for a combined exposure time of ~ 440 ks. [Caramazza et al. \(2008\)](#) use these data to identify ~ 1000 sources in the FOV and perform a detailed X-ray analysis on the clusters PMS population specifically the fractions of the various classes of YSOs

in the cluster. Though this detailed analysis of the PMS X-ray sources has been published, no analysis of other cluster subpopulations such as the high mass stars or potential diffuse emission exists in the literature.



Figure 3.20: *HST* Image of NGC 1893.

3.4.1 Summary

Three *Chandra* observations of NGC 1893 that exceeded 100 ks were used for this analysis giving a total exposure time of 353 ks. Each of the observations was centered a few arcmins north of the cluster centre, however, this was sufficient to observe a substantial fraction of the cluster with only outer cluster regions lying outside the FOV. No background flaring periods were identified leaving the full ~ 353 ks of useable data. The *wavdetect* algorithm detected 797 sources in the FOV, 448 of which have a 2MASS counterpart. Foreground and extragalactic contamination simulations yield 15-30 potential foreground sources and ~ 103 -116 potential extragalactic sources in the entire FOV. Individual source data and statistics were analysed, as outlined in 2.1, to identify 110 candidate extragalactic sources in the cluster source population, in line with the simulation predictions, which were removed from consideration. This left 687 sources, including foreground contaminants, which are all labelled as cluster sources. The adaptively smoothed image of the NGC 1893 revealed bright diffuse emission in the cluster which, along with the unsmoothed 0.5-8

keV ACIS-I image, is shown in Figure 3.21.

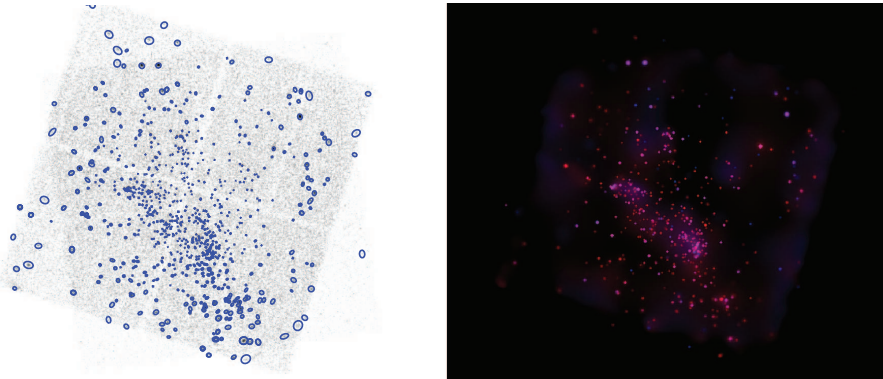


Figure 3.21: *Chandra* ACIS-I 0.5-8 keV image of NGC 1893 with detected sources marked in blue (left) and adaptively smoothed *Chandra* soft (0.5-2 keV, shown in red) and hard (2-8 keV, shown in blue) image.

High mass sources in the detected X-ray population were identified using the sourcelist of Massey et al. (1995) and the SIMBAD database. All of the known O stars were detected whereas 13 of the 18 early B stars were detected¹. The spectra of each of the high mass sources with > 50 counts were fit in *XSPEC* with absorbed one and two temperature thermal plasma models during the *AE* reduction and analyses procedures (results given in Table B.10). All apart from one of the known O stars are best fit with an absorbed one temperature thermal plasma model and show the spectral signatures of RDIS emitters. The remaining O star, namely the O4V((f)) star HD 242908, requires a two temperature thermal plasma model, with one soft and one hard thermal components, and has an X-ray luminosity that indicates a CWB system. All of the known early B-type stars exhibit moderately hard spectra and have 2-8 keV L_X values consistent with MCWS emission.

The correlated high quality 2MASS data were used to produce a J vs $J - H$ colour-magnitude diagram with the appropriate evolutionary tracks and reddening vectors (Figure B.13). This plot identifies 59 candidate OB stars in the FOV. The brightest of these sources were spectrally fit in *XSPEC* (see Tables B.11 and B.12

¹Given this very deep observation we would expect all of the early B stars to be detected, however, because the roll angles of the three observations are not the same, some of the regions in the FOV are exposed at a fraction of the on axis exposure time of 353 ks, resulting in a poorer detection limit.

for results of spectral fits). Almost all of the candidate OB stars in the cluster are well fit with thermal plasma models with plasma temperatures and derived X-ray luminosities on par with the known early B stars in the cluster. As such, if these are indeed early B-type stars, they are emitting via a MCWS mechanism.

The remaining cluster sources are likely low mass PMS objects. The PMS stars with > 50 counts were fit in *XSPEC* with an absorbed thermal plasma model. The global results of these fits are given in graphic form in Figure B.14. The brightest PMS source in NGC 1893 has a 2-8 keV $\log L_X > 32 \text{ erg s}^{-1}$, which is quite bright for a PMS star. Analysis of this source's lightcurve shows that the object underwent a period of enhanced emission in each of the three *Chandra* observations that is almost periodic in appearance, which is also suggested by its derived variability statistic of $P_{KS} = 0.028$. The derived plasma temperatures of the sources range from 0.1-10 keV, peaking at ~ 0.5 keV. The majority of these sources suffers from slight to moderate foreground absorption ($\log N_H \lesssim 22.3 \text{ cm}^{-2}$), with a few subject to heavy absorption. Many of sources shows no sign of variability over the course of the observation, however there are a large number of variable or flaring sources also identified. The trends in the variation of E_{median} with kT and E_{median} with N_H is similar to those found by Feigelson et al. (2005) with a slight increase in kT with E_{median} and increasing N_H with E_{median} above ~ 1.9 keV. For sources with $E_{\text{median}} < 1.9$ keV, an upper limit of $\log N_H \lesssim 22.3 \text{ cm}^{-2}$ is found.

2-8 keV L_X values were calculated for the remaining PMS sources in the cluster and were used to produce the the 2-8 keV L_X against E_{median} plots, shown in Figure B.15. These plots indicate that the majority of the PMS sources in NGC 1893 is lightly obscured, most probably Class II or Class III YSOs with several heavily obscured sources, likely Class I YSOs or Class II YSOs viewed from an unfavourable angle. Many of these heavily obscured sources are either variable or flaring. The rather deep observation leads to an increased number in the detection of heavily obscured sources as compared to other clusters. These sources likely represent the high luminosity end of the heavily obscured source population.

Given the obvious diffuse emission in Figure 3.21 it was deemed unnecessary to mask and adaptively smooth the image again. Spectra were extracted from the entire cluster and cluster core regions from each of the three observations and fit simultaneously in *XSPEC*. Both spectra with the best fit models are shown in Figure

B.16 with fit results given in Table B.13. The spectra are well fit with an absorbed cool thermal plasma model. There is little variation in spectral parameters of flux between the core and all-FOV spectra suggesting the same diffuse emission process throughout the cluster, likely an unresolved PMS population.

The cluster and PMS star 2-8 keV XLFs were constructed and the PMS XLF compared to that of the COUP. Given that NGC 1893 is older than the ONC, the COUP data were scaled according to the scaling relation of [Preibisch and Feigelson \(2005\)](#). These XLFs are shown in Figure 3.22. The total cluster XLF shows no outliers. This is unusual given that one of the sources, namely HD 242908, was identified as a CWB which would be expected to have a relatively high 2-8 keV L_X . As such, it is likely that HD 242908 is a wide binary system, resulting in a less luminous colliding wind zone. The high luminosity end of the PMS XLF shows the same slope as the COUP PMS population. Scaling the COUP population to that of NGC 1893 and integrating the ‘missing’ PMS population region yields an estimate of the unresolved PMS population 2-8 keV $\log L_X$ of $\sim 32.7 \text{ erg s}^{-1}$ meaning an unresolved PMS can easily account for the observed diffuse emission in the resolved cluster area.

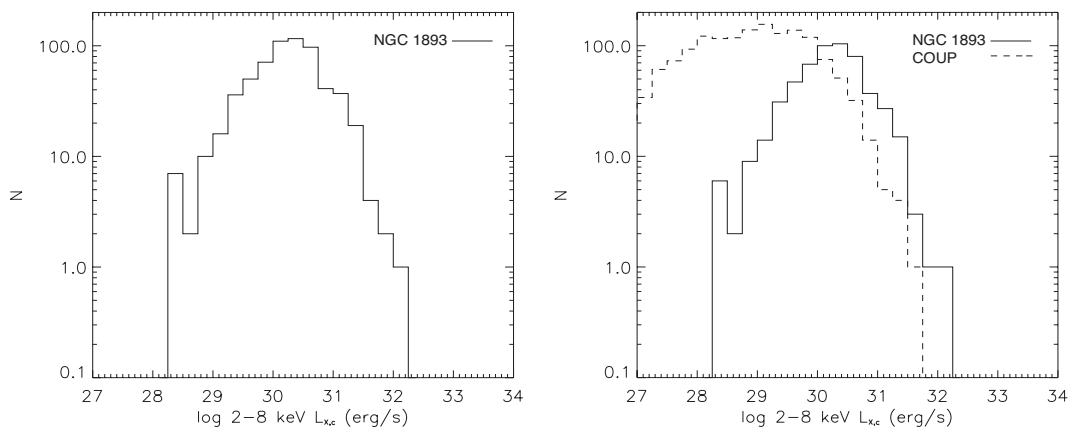


Figure 3.22: Left: NGC 1893 total cluster 2-8 keV XLF. Right: NGC 1893 PMS star 2-8 keV XLF (solid line) and the COUP 2-8 keV XLF (dashed line).

3.5 NGC 2362

NGC 2362 is a young open cluster located on the outer edge of the Orion-Cygnus arm of the Galaxy. The cluster is dominated by the quadruple τ CMa star, an

O9 supergiant and the only cluster member on the post-main sequence, and several B-type main sequence stars. The cluster has been known for some time and was long thought to consist almost entirely of early-type stars (Johnson, 1950). Later studies of the clusters stellar population have shown this not to be the case and that the mass spectrum extends much lower than the previous early-type limit (Kroupa et al., 1992). Recently the cluster has been the subject of many analyses as it suffers from low extinction meaning the stars in NGC 2362 have a low uniform reddening which make it an ideal cluster for the study of PMS stellar evolution. Moitinho et al. (2001) performed a *UBVRI* photometric analysis of the cluster focussing on the PMS population. These authors determine a cluster age of ~ 5 Myr and a distance of ~ 1.5 kpc, which have been used often in the literatures and are adopted for this analysis. Dahm (2005) performed a much more detailed analysis of the cluster population, particularly the PMS members, and derived an upper limit of $\lesssim 500 M_{\odot}$ for the cluster mass. In some of the analyses in the literature, authors attempt to determine the physical size of the cluster however these estimates, which differ somewhat, are invariably derived using a subpopulation of the cluster. Because of this, the clusters total radius ($R_{Cl} = 15'$) and core radius ($R_{Co} = 3.6'$) are adopted from the catalogue of open cluster properties of Kharchenko et al. (2005).

Chandra performed a deep ~ 100 ks observation of NGC 2362 in late 2003. Damiani et al. (2006) used these data to study the X-ray properties of the stellar population. They detect ~ 400 sources in the cluster, many of which were previously unknown PMS stars, and investigate the emission properties of the PMS sources. These data were also used by Delgado et al. (2006) who perform a multiwavelength analysis of the cluster. These authors obtain similar results to those of Damiani et al. (2006) and again focus mainly on the PMS population.

3.5.1 Summary

The 100 ks NGC 2362 *Chandra* dataset was only sufficient to resolve the central regions of the cluster area given it's rather large size on the sky. The observation event list was filtered for background flaring periods leaving ~ 96 ks of useable data. The *wavdetect* algorithm detected 449 sources in the FOV, 271 of which have 2MASS counterparts. Foreground and extragalactic contamination simulations yield 16-23 potential foreground sources and ~ 75 -84 potential extragalactic sources in the FOV. Individual source data and statistics were analysed, as outlined in Section 2.1, to

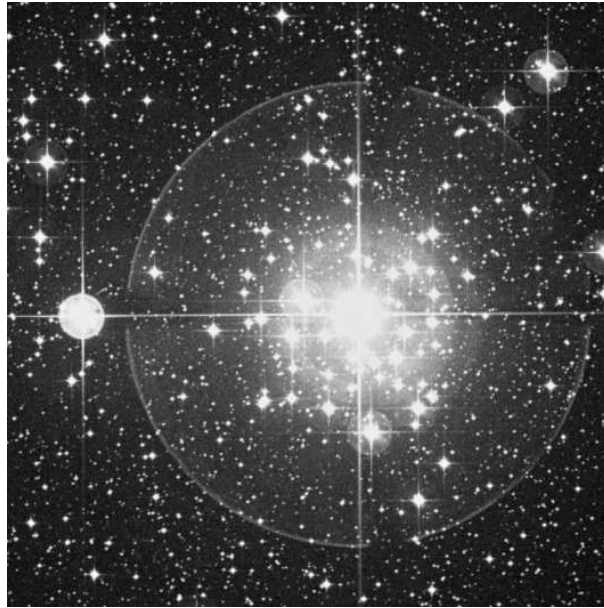


Figure 3.23: DSS Image of NGC 2362.

identify 56 candidate extragalactic sources in the cluster source population, lower than the simulation predictions. This implies a further ~ 20 extragalactic sources may be contaminating the NGC 2362 cluster population. Without further information however, there is no way to identify these sources and thus only the 56 candidate extragalactic sources were removed from consideration. This left 393 sources, including foreground contaminants, which are all labelled as cluster sources. The adaptively smoothed image of the NGC 2362 region showed no evidence of diffuse emission in the cluster which, along with the unsmoothed 0.5-8 keV ACIS-I image, is shown in Figure 3.24.

High mass sources in the detected X-ray population were identified using the SIMBAD database. The one known O star in NGC 2362 was detected whereas only 5 of the 9 early B stars were detected. The spectra of each of the high mass sources with > 50 counts were fit in *XSPEC* with absorbed one and two temperature thermal plasma models during the *AE* reduction and analyses procedures (results given in Table B.14). All of the known early B-type stars exhibit soft spectra likely due to a RDIS emission mechanism. The spectrum of the brightest source τ CMa, an O9Ib star, has a somewhat more complex spectrum with both a one and two temperature thermal plasma models giving poor fits. This is unsurprising however as τ CMa is a well known multiple star with at least 3 components of which, one is a known

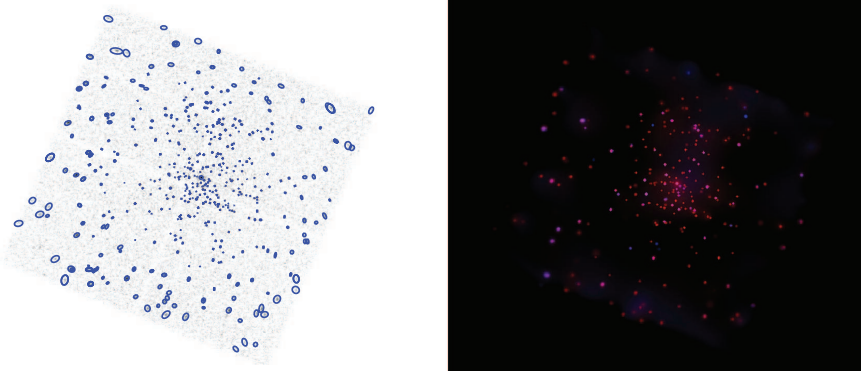


Figure 3.24: *Chandra* ACIS-I 0.5-8 keV image of NGC 2362 with detected sources marked in blue (left) and adaptively smoothed *Chandra* soft (0.5-2 keV, shown in red) and hard (2-8 keV, shown in blue) image.

YSO. This source (and potentially the other object(s) in this system) is likely emitting X-rays. As such, this(these) star(s) may be contaminating the O supergiant X-ray spectrum of τ CMa. The derived spectral parameters from the two temperature thermal plasma of this source are shown in Table B.14 for descriptive purposes.

The correlated high quality 2MASS data were used to produce a J vs $J - H$ colour-magnitude diagram with the appropriate evolutionary tracks and reddening vectors (Figure B.9). This plot identifies 3 candidate OB stars in the FOV (see Table B.15 for results of spectral fits). Two of these sources were bright enough to be fit in *XSPEC* and were best fit with an absorbed one temperature thermal plasma model. Both these sources exhibit soft X-ray spectra with plasma temperatures and X-ray luminosities in line with the known early B-type stars in the cluster. As such, these sources are likely emitting via a RDIS mechanism.

The remaining cluster sources are likely low mass PMS objects. The PMS stars with > 50 counts were fit in *XSPEC* with an absorbed thermal plasma model. The global results of these fits are given in graphic form in Figure B.18. The brightest PMS source in NGC 2362 has a 2-8 keV $\log L_X \sim 32 \text{ erg s}^{-1}$, within the expected range. The derived plasma temperatures of the sources range from 0.1-5 keV, peaking at ~ 1 keV. The majority of these sources suffers from slight to moderate foreground absorption ($\log N_H \lesssim 22.3 \text{ cm}^{-2}$), with no sources subject to heavy absorption. Many of the sources shows no sign of variability over the course of the observation, with a small number of variable and several extremely variable, likely

flaring objects. The trend in the variation of E_{median} with kT is similar to that found by Feigelson et al. (2005) with a slight increase in kT with E_{median} , as is the trend in increasing N_{H} with E_{median} above a threshold level. For sources with $E_{\text{median}} < 1.4$ keV, an upper limit of $\log N_{\text{H}} \lesssim 21.9 \text{ cm}^{-2}$ is found.

2-8 keV L_{X} values were calculated for the remaining PMS sources in the cluster and were used to produce the the 2-8 keV L_{X} against E_{median} plots, shown in Figure B.19. These plots indicate that the majority of the PMS source in NGC 2362 is lightly obscured, most probably Class II or Class III YSOs with 3 heavily obscured sources, likely Class I YSOs or Class II YSOs viewed from an unfavourable angle. Two of the three heavily obscured sources show signs of variability. These sources likely represent the high luminosity tip of the heavily obscured source population which, given the age of NGC 2362, is likely relatively small in comparison to other programme clusters.

There is little evidence for diffuse emission in the cluster centre (see Figure 3.24) however there may still be faint diffuse emission throughout the FOV. To obtain a better image of the diffuse emission a point source masked and adaptively smoothed image, shown in Figure 3.25, was created.

Figure 3.25 shows faint diffuse emission in the cluster core. Spectra were extracted from the entire FOV and cluster core region and fit in *XSPEC*. This spectrum with the best fit model are shown in Figure B.20 with fit results given in Table B.16. The spectra are well fit with an absorbed cool thermal plasma model. There is little variation in spectral parameters of flux between the core and all-FOV spectra suggestion the same diffuse emission process throughout the cluster, likely an unresolved PMS population, with a 2-8 keV $\log L_{\text{X}}$ of $\sim 30.6 \text{ erg s}^{-1}$ derived for the all-FOV diffuse emission.

The cluster and PMS star 2-8 keV XLFs were constructed and the PMS XLF compared to that of the COUP. Given that NGC 2362 is older than the ONC, the COUP data were scaled according to the scaling relation of Preibisch and Feigelson (2005). These XLFs are shown in Figure 3.26. The total cluster XLF indicates no outliers as expected. The high luminosity end of the PMS XLF shows the same slope as the COUP PMS population. Scaling the COUP population to that of NGC 2362 and integrating the ‘missing’ PMS population region yields an estimate of the

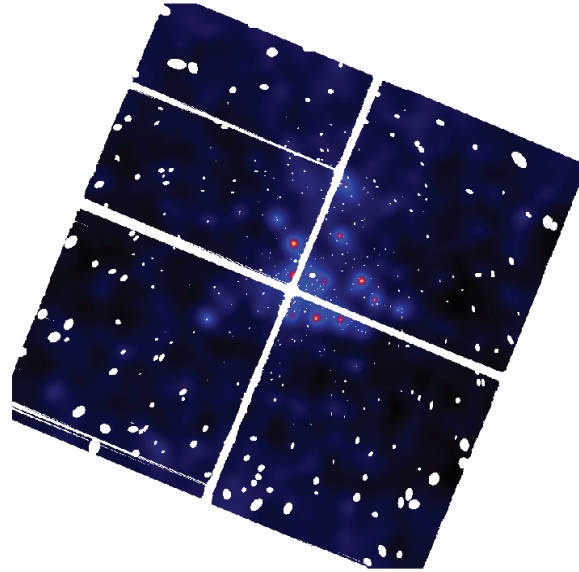


Figure 3.25: Masked and adaptively smoothed 0.5-8 keV image of NGC 2362 diffuse emission. The apparently bright points are likely the unmasked wings of the PSF of the brightest sources in the FOV which are artifacts due to the selected image binning.

unresolved PMS population 2-8 keV $\log L_X$ of $\sim 30.8 \text{ erg s}^{-1}$ meaning an unresolved PMS can easily account for the observed diffuse emission in the resolved cluster area.

3.6 NGC 3603

NGC 3603 is a giant HII region located in the Carina spiral arm and is famous for being the most luminous optically visible HII region in the Galaxy (Nürnberg, 2003). At the heart of this giant HII region is the massive young central cluster also commonly referred to as NGC 3603. The NGC 3603 cluster has been the subject of many studies over the years not only because of its size and stellar population but in particular the fact that it suffers from low foreground extinction ($A_V = 4.5$, Stolte et al., 2004, and references therein) making it easy to observe the stellar population in all wavebands down to low masses. There have been several studies of the stellar content of the NGC 3603 cluster which have identified a large high mass stellar population consisting of WRs and early and late O stars at various stages of evolution (see Melena et al., 2008; Moffat et al., 1994, for example). In addition Stolte et al. (2004) and Sung and Bessell (2004) identify a rich pre-main sequence

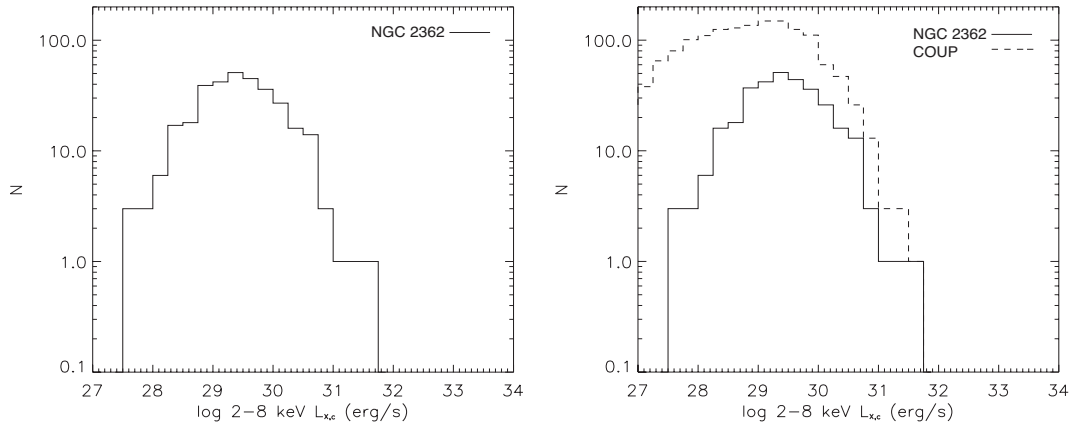


Figure 3.26: Left: NGC 2362 total cluster 2-8 keV XLF. Right: NGC 2362 PMS star 2-8 keV XLF (solid line) and the COUP 2-8 keV XLF (dashed line).

in the cluster. As such, the age estimates for the cluster range from 1-4 Myr but is mostly quoted at ~ 1 Myr. Distance estimates to the cluster vary between 6-10 kpc but as noted by [Melena et al. \(2008\)](#), this variation arises due to the uncertain reddening correction. The most recent distance estimate is 7.6 kpc ([Melena et al., 2008](#)).

Chandra observed the NGC 3603 cluster for 50 ks in its first year of observations. [Moffat et al. \(2002\)](#) presented the first analysis of this observational data. They identify almost 400 sources in the FOV, at least 40 of which are associated with optically identified WRs and OB stars, most of the remaining sources likely being PMS stars. The three WR stars in the cluster were found to be anomalously bright in X-rays which the authors indicate may be due to a colliding wind emission mechanism. In addition, these authors identify weak diffuse emission in the centre of the cluster which they attribute to a cluster wind. [Sung and Bessell \(2004\)](#) also use this dataset to determine the X-ray emission from the PMS population in the cluster and highlight the problem of crowding in the cluster core. The rich X-ray emitting stellar population and diffuse emission present in the NGC 3603 cluster make it very suited for study in this project.

3.6.1 Summary

The 50 ks NGC 3603 *Chandra* dataset was sufficient to resolve the entire cluster area. The observation event list was filtered for background flaring periods leaving ~ 48 ks of useable data. The *wavdetect* algorithm detected 352 sources in the FOV, 165 of which are within the cluster bounds. 57 of these source were found to



Figure 3.27: *HST* Image of NGC 3603.

have 2MASS counterparts. Foreground and extragalactic contamination simulations yield 2-8 potential foreground sources and ~ 90 -103 potential extragalactic sources in the FOV. Given the actual area of the cluster and assuming the contaminants are evenly distributed throughout the FOV, this corresponds to 0-1 Galactic and 15-18 extragalactic contaminants in the NGC 3603 cluster area. Individual source data and statistics were analysed, as outlined in 2.1, to identify 39 candidate extragalactic sources in the cluster source population, higher than the simulation predictions. This implies some ~ 20 candidate extragalactic sources may actually be members NGC 3603 cluster population. Without further information however, there is no way to identify these sources and thus the 39 candidate extragalactic sources were removed from consideration. This left 126 sources, including foreground contaminants, which are all labelled as cluster sources. The adaptively smoothed image of the NGC 3603 region showed obvious diffuse emission in the cluster which, along with the unsmoothed 0.5-8 keV ACIS-I image, is shown in Figure 3.28.

High mass sources in the detected X-ray population were identified using the source list of Melena et al. (2008) and the SIMBAD database. Unfortunately, given the incredibly rich population high mass stars, their location in the core and the distance of NGC 3603, source crowding is a serious issue. Melena et al. (2008) identify ~ 50 main sequence and evolved O stars stars in the cluster core. Only

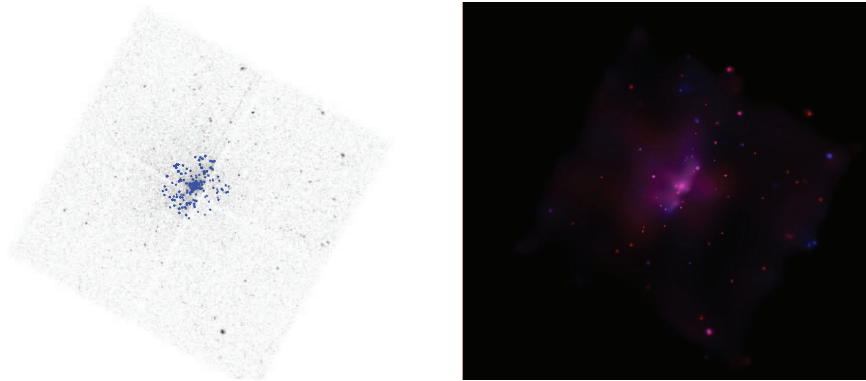


Figure 3.28: *Chandra* ACIS-I 0.5-8 keV image of NGC 3603 with detected sources marked in blue (left) and adaptively smoothed *Chandra* soft (0.5-2 keV, shown in red) and hard (2-8 keV, shown in blue) image.

18 X-ray sources were matched to this population with some sources consisting of up to 4 known high mass stars. In addition, two extremely bright sources were detected in the heart of the cluster which are almost 2 orders of magnitude brighter than surrounding cluster sources. These effectively drown the emission from less bright sources in the vicinity resulting in some non-detections. Stars with spectral type as early as O3 were not detected for this reason. Unfortunately there is little that can be done about this. Image reconstruction algorithms may uncover these as contributing X-ray sources hidden in the diffuse emission but this will not allow any meaningful spectral information to be derived. Many of the later O stars were not detected simply because they fall below the detection threshold of the observation. The spectra of each of the high mass sources with > 50 counts were, nevertheless, fit in *XSPEC* with absorbed one and two temperature thermal plasma models during the *AE* reduction and analyses procedures (results given in Table B.17). Of the single known high mass stars 4 show spectra consistent with RDIS emission mechanisms. A further 3, namely Sh 49, Sh 47 and Sh 22, show moderately hard and bright spectra and are likely relatively low luminosity CWBs. Source CXO J11150727611538.3 was found to consist of 4 very high mass sources including 2 WRs. The spectrum of this source was well fit with an absorbed two temperature thermal plasma corrected for photon pileup. The derived 0.5-8 keV L_X is quite bright and it is very likely that one or more of these are CWB systems. The remaining source is the so called NGC 3603 C, another WR, whose derived L_X value is extraordinarily high. This is almost definitely a close CWB system.

The correlated high quality 2MASS data were used to produce a J vs $J - H$ colour-magnitude diagram with the appropriate evolutionary tracks and reddening vectors (Figure B.9). This plot identifies 2 candidate OB stars in the FOV (see Table B.18 for results of spectral fits). As well as being in the very high mass region of the 2MASS colour-magnitude diagram, they are very bright in X-rays (also reported by Sung and Bessell, 2004), yet no spectral types exist for these sources. Indeed, for many of the optical or IR surveys of the clusters (see Melena et al., 2008, for example) observations have focussed primarily on the centre of the cluster leaving the outer regions largely unexplored. One of these sources is well fit with absorbed hot thermal plasma models and have 0.5-8 keV L_X values well in excess of 10^{32} erg s $^{-1}$, consistent with CWB emission or possibly a WR. The second source is the second brightest detected in the cluster. It's spectrum is well fit with a two temperature thermal plasma with an $L_X > 10^{34}$ erg s $^{-1}$. As such, this source is almost certainly a massive CWB system.

It is unclear as to the nature of the remaining cluster sources. Many of them are likely bright PMS stars but it is just as likely that, particularly in the outer cluster regions, the sources are as yet unidentified O-type or early B-type stars. Thus, for the remainder of the analysis, I will refer to them simply as 'unidentified' cluster sources. The unidentified stars with > 50 counts were fit in *XSPEC* with an absorbed thermal plasma model. The global results of these fits are given in graphic form in Figure B.22. Only 3 sources satisfied this brightness criteria. Two of these sources exhibit soft spectra with X-ray luminosity values of 2-8 keV $\log L_X \sim 32$ erg s $^{-1}$. In addition, these sources show no signs of variability. As such, it is entirely possible that these are early O-type stars. The remaining source has about the same derived X-ray luminosity is well fit with a very hot thermal plasma model has a P_{KS} value consistent with a flaring source. Indeed, inspection of the lightcurve reveals the source underwent a strong flaring event, increasing to almost 5 times it's quiescent count rate, during the observation. Because there is likely only one bright PMS star in the cluster, the relations of Feigelson et al. (2005) cannot be investigated. An upper limit of $\log N_H \lesssim 22.2$ cm $^{-2}$ is set for sources with $E_{\text{median}} < 1.8$ keV, consistent with similar programme clusters.

2-8 keV L_X values were calculated for the remaining unidentified sources in the cluster and were used to produce the the 2-8 keV L_X against E_{median} plots, shown in Figure B.23. These plots consolidate the earlier conclusion that many of these

sources are likely as yet unidentified massive stars. Compared to similar plots for the other programme clusters, the peak luminosity ‘plateau’ is located at about the 10^{32} erg s⁻¹ level. In addition, many of the sources on or near this level show no signs of variability, consistent with high mass star emission. There can be no doubt however that PMS sources also occupy this region of the plot with several moderate to highly absorbed sources showing signs of variability, and in some cases flaring.

Figure 3.28 shows diffuse emission in the cluster. Spectra were extracted from the entire FOV and cluster core region and fit in *XSPEC*. These spectra with the best fit models are shown in Figure B.24 with fit results given in Table B.19. The spectra are well fit with an absorbed two temperature thermal plasma model. There is little variation in spectral parameters or flux between the core and all-FOV spectra suggesting the same diffuse emission processes throughout the cluster which, given the rich high mass stellar population, may be a cluster wind. Assuming the model of Cantó et al. (2000, see Section 1.4.7.1) and considering the all of the known high mass stars to be contributing to the cluster wind, a hot component plasma temperature of ~ 9 keV and a 2-8 keV $\log L_X$ of ~ 32.3 erg s⁻¹ are derived for the diffuse emission in the core where the all of the known high mass stars reside. The determined X-ray luminosity is significantly smaller than the observed $\log L_X \sim 33.8$ erg s⁻¹ for the core, meaning this cluster wind may only account for a fraction of the observed diffuse emission in NGC 3603. However, it must be noted that this value is likely underestimated given only the brightest stars in core with known spectral types are considered. Even in the source list of Melena et al. (2008), spectral types are derived for only 38 of the 50 brightest sources. In addition, this does not include the multitude of late O-type stars yet to be identified in the cluster.

The cluster and unidentified source 2-8 keV XLFs were constructed and the unidentified source XLF compared to that of the PMS XLF of the similarly aged COUP. Though this may not be explicitly correct, it can offer an estimate to the contribution of an unresolved unidentified source population. These XLFs are shown in Figure 3.29. The total cluster XLF indicates several outliers which consist of the CWB candidates and the multiple source CXO J 11150727611538.3. The high luminosity end of the unidentified source XLF shows roughly the same slope as the COUP PMS population. Scaling the COUP PMS population to that of the NGC 3603 unidentified source population and integrating the ‘missing’ unidentified source population region yields an estimate of the unresolved population 2-8 keV $\log L_X$

of $\sim 34 \text{ erg s}^{-1}$ meaning an unresolved population can account for about half of the observed diffuse emission in cluster. It is very likely that both an unresolved population and a cluster wind are responsible for the diffuse emission with the unresolved sources dominating, though it is noted that the cluster wind estimate is likely underestimated.

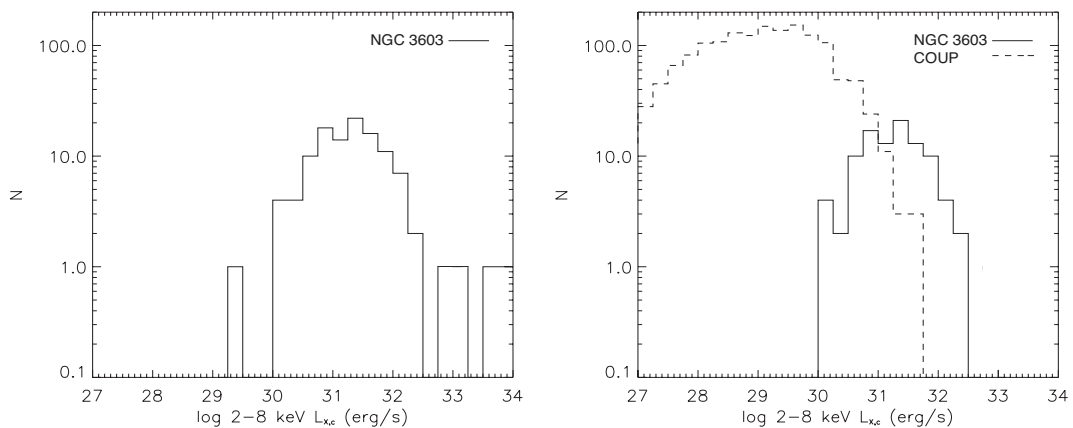


Figure 3.29: Left: NGC 3603 total cluster 2-8 keV XLF. Right: NGC 3603 unidentified source 2-8 keV XLF (solid line) and the COUP 2-8 keV XLF (dashed line).

3.7 NGC 6611

NGC 6611 is a young open cluster embedded in the HII region M 16, better known as the Eagle Nebula. Hillenbrand et al. (1993) found NGC 6611 to contain a large population of PMS stars along with a large number of massive stars, over 50 of which are of spectral type B5 or earlier. A more recent study of the massive stellar content of NGC 6611 was carried out by Dufton et al. (2006) who supplement and refine the massive stellar parameters. Winds from these massive stars are responsible for exciting and shaping the Eagle Nebula which has given rise to nebulosity features such as the now famous “Pillars of Creation”. Given the identified stellar population, age estimates for stars in the cluster are typically quoted in the 1-6 Myr range (Bonatto et al., 2006b; Hillenbrand et al., 1993; Martayan et al., 2008), however Guarcello et al. (2007) identify stars with ages up to 3 Myr and the youngest stars having ages of 0.1 Myr. Distance estimates to the cluster are somewhat more consistent with most being $\approx 2 \text{ kpc}$ (Belikov et al., 1999; Bonatto et al., 2006b; Guarcello et al.,

2007; Hillenbrand et al., 1993).

Chandra has performed a 78 ks observation centered on the NGC 6611 cluster. Linsky et al. (2007) present an analysis of these data which discussed the Young Stellar Object (YSO) population in and near the Pillars of Creation. Guarcello et al. (2010) use this same observation along with two additional observations of different parts of M 16 to assess the chronology of star formation in M 16 and its relation to the presence of the massive stars in NGC 6611. Surprisingly no other analysis of the X-ray properties of the cluster exists in the literature to date. Given the populations of OB and PMS stars, it is reasonable to assume that cluster exhibits diffuse emission in addition to the a rich X-ray emitting population.

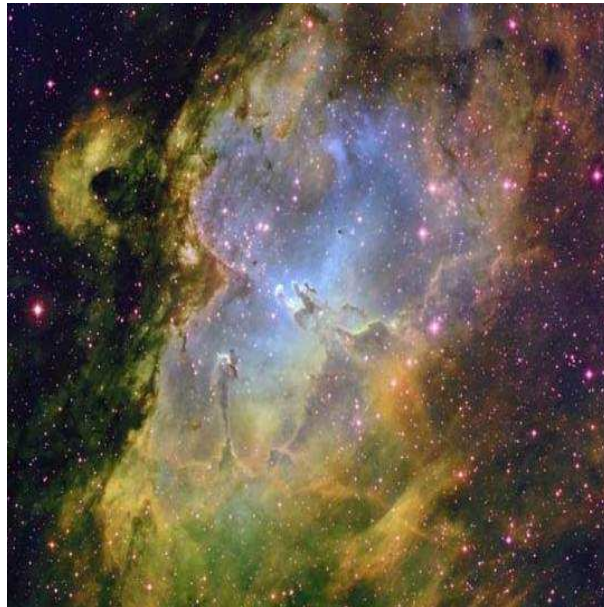


Figure 3.30: *HST* Image of M 16 with NGC 6611 located in the centre of the nebula.

3.7.1 Summary

The 78 ks NGC 6611 *Chandra* dataset was aimed at the centre of the cluster. The 17'x17' ACIS-I FOV was only sufficient to cover $\sim 50\%$ of the entire cluster area ($R_{Cl} = 13.2'$) but was enough to resolve the cluster core ($R_{Co} = 4.8'$). Background flaring periods were removed leaving ~ 76 ks of useable data. The *wavdetect* algorithm detected 893 sources in the FOV, 620 of which were found to have 2MASS counterparts. Foreground and extragalactic contamination simulations yield 5-12

potential foreground sources and 40-56 potential extragalactic sources in the FOV. Individual source data and statistics were analysed, as outlined in 2.1, to identify 51 candidate extragalactic sources in the FOV, in line with the simulation predictions, which were removed from consideration. This left 842 sources in the FOV including, including foreground contaminants, which are all labelled as cluster sources. The adaptively smoothed image of the cluster revealed bright diffuse emission throughout the cluster core which, along with the unsmoothed 0.5-8 keV ACIS-I image, is shown in Figure 3.31.

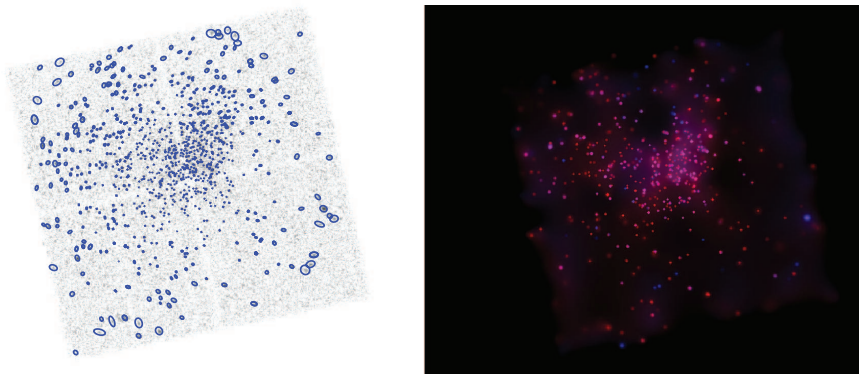


Figure 3.31: *Chandra* 17'×17' ACIS-I 0.5-8 keV image of NGC 6611 with detected sources marked in blue (left) and adaptively smoothed *Chandra* soft (0.5-2 keV, shown in red) and hard (2-8 keV, shown in blue) image.

High mass sources in the detected X-ray population were identified using the source lists of [Dufton et al. \(2006\)](#) and the SIMBAD database. All of the known O stars in the FOV were detected whereas only 16 of the 22 early B stars were detected. The spectra of each of the high mass sources with > 50 counts were fit in *XSPEC* with absorbed one and two temperature thermal plasma models during the *AE* reduction and analyses procedures (results given in Table B.20). All of the known O stars and two of the early B stars exhibit soft spectra, in keeping with a RDIS emission mechanism. The remaining early B-type stars are well fit by moderately hard thermal plasma models. Given the relatively low L_X values of these sources, it is likely that they are MCWS emitters.

The correlated high quality 2MASS data were used to produce a J vs $J - H$ colour-magnitude diagram with the appropriate evolutionary tracks and reddening vectors (Figure B.25). This plot identifies 38 candidate OB stars in the FOV (see

Tables B.21 and B.22 for results of spectral fits). All of the bright candidate OB sources were best fit with an absorbed one temperature thermal plasma model, all having derived hard kT values and all with $L_X < 10^{32}$ erg s $^{-1}$. If indeed these are OB stars, they have the signatures of MCWS emission.

The remaining cluster sources are likely low mass PMS objects. The PMS stars with > 50 counts were fit in *XSPEC* with an absorbed thermal plasma model. The global results of these fits are given in graphic form in Figure B.26. The brightest PMS source in NGC 6611 has a 2-8 keV $\log L_X < 32$ erg s $^{-1}$, within the expected range. The derived plasma temperatures of the sources range from 1-10 keV, peaking at ~ 2 keV. The majority of these sources suffers from slight foreground absorption ($\log N_H \lesssim 22.0$ cm $^{-2}$), with a few sources subject to quite heavy absorption ($\log N_H \gtrsim 22.5$ cm $^{-2}$), possibly due to an accretion disk or natal cloud. Similarly, the majority of the sources shows no sign of variability over the course of the observation. However, there is a sizable fraction of variable sources with a few extremely variable, likely flaring objects. Trends in the variation of E_{median} with kT and N_H are similar to those found by Feigelson et al. (2005) with a slight increase in kT with E_{median} and increasing N_H with E_{median} above ~ 1.7 keV. For sources with $E_{\text{median}} < 1.7$ keV, an upper limit of $\log N_H \lesssim 22.0$ cm $^{-2}$ is found.

2-8 keV L_X values were calculated for the remaining PMS sources in the cluster and were used to produce the the 2-8 keV L_X against E_{median} plots, shown in Figure B.27. These plots indicate that the majority of the PMS source in NGC 6611 is lightly obscured, most probably Class II or Class III YSOs with > 20 heavily obscured sources, likely Class I YSOs or Class II YSOs viewed from an unfavourable angle. Many of these heavily obscured sources are variable or flaring with a few quiescent objects. These likely represent the high luminosity tip of the heavily obscured source population.

Given the obvious diffuse emission in Figure 3.31 it was deemed unnecessary to mask and adaptively smooth the image again. Spectra were extracted from the cluster core region and the entire FOV and fit in *XSPEC*. The spectra with the best fit models are shown in Figure B.28 with fit results given in Table B.23. Both the core and the all-FOV spectra are best fit with absorbed two temperature thermal plasma models. There is a noticeable increase in the hard component kT from the

core to the all-FOV spectrum. This may be due to hard emission in the cluster being localized in the core causing its brightness in relation to the soft emission to be lessened by the cluster wide soft emission resulting in a poorly constrained hard fit component. If this is the case it is likely that some of the hard emission in the core of NGC 6611 is due to a cluster wind. Assuming the model of [Cantó et al. \(2000](#), see Section 1.4.7.1) and considering the O stars to be the dominant contributors to the cluster wind, a hot component plasma temperature of ~ 9.5 keV and a 2-8 keV $\log L_X$ of ~ 30 erg s $^{-1}$ are derived meaning a cluster wind can only account for a fraction of the observed diffuse emission.

The cluster and PMS star 2-8 keV XLFs were constructed and the PMS XLF compared to that of the COUP. Given that NGC 6611 is slightly older than the ONC, the COUP data were scaled according to the scaling relation of [Preibisch and Feigelson \(2005\)](#). These XLFs are shown in Figure 3.32. The total cluster XLF shows no high luminosity outliers as expected. The high luminosity end of the PMS XLF shows the same slope as the COUP PMS population. Scaling the COUP population to that of NGC 6611 and integrating the ‘missing’ PMS population region yields an estimate of the unresolved PMS population 2-8 keV $\log L_X$ of ~ 32.9 erg s $^{-1}$. Thus the unresolved PMS population can account for the majority of the diffuse emission in the FOV of $\log L_X \sim 33$ erg s $^{-1}$.

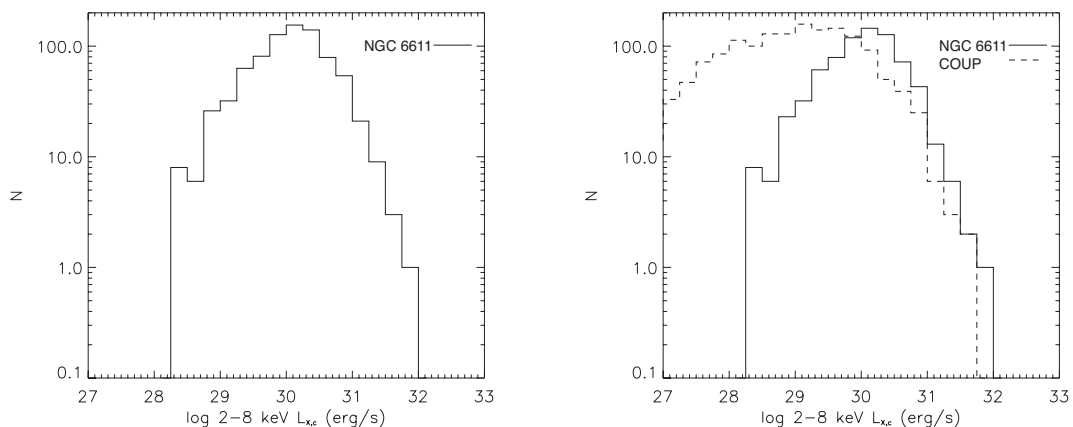


Figure 3.32: Left: NGC 6611 total cluster 2-8 keV XLF. Right: NGC 6611 PMS star 2-8 keV XLF (solid line) and the COUP 2-8 keV XLF (dashed line).

3.8 NGC 6618

NGC 6618 is the central exciting cluster of M 17, one of the brightest giant HII regions known, located at the northeast edge of one of the largest giant molecular clouds in the Galaxy (Elmegreen et al., 1979). The cluster itself has been known for some time but because it suffers from substantial absorption due to the obscuring material of the molecular cloud ($A_V \sim 8$, Hanson et al., 1997), studies of the stellar content were limited until recent observations in the IR and X-ray bands. Lada et al. (1991) performed a NIR survey of the cluster region and identified 100 stars earlier than B9 including 14 O stars and 34 B0-B3 stars (numbers quoted account for refined spectral types in more recent studies). Broos et al. (2007) used a *Chandra* observation to identify a further 100 candidate OB stars in the M 17 region, some of which are associated with the NGC 6618 cluster. In addition to the high mass population, rich PMS and protostellar populations have also been identified in the cluster (Broos et al., 2007; Hoffmeister et al., 2008, and references therein). The cluster is thought to be ~ 1 Myr given the absence of evolved high mass stars but age estimates based on main sequence and PMS evolutionary tracks range from 0.5-3 Myr (Hoffmeister et al., 2008; Jiang et al., 2002). Distance estimates range from 1.3 kpc (Hanson et al., 1997) to 2.4 kpc (Russeil, 2003) with recent thorough studies of the region by Nielbock et al. (2001) and Povich et al. (2007) yielding a distance of 1.6 kpc.

Chandra has observed M 17 several times since its launch whereas *XMM-Newton* has observed the region once, the analysis of which has yet to be reported. As already mentioned, Broos et al. (2007) used a 40 ks *Chandra* observation to characterize the X-ray emitting point sources in the M 17 region, including NGC 6618. They detected all of the known O stars, over half the known B stars, ~ 100 candidate OB star, a PMS population and a protostellar population. In addition they classified some of the high mass cluster sources as being members of colliding wind binary systems. Townsley et al. (2003) use this same observational data to analyse the diffuse X-ray emission throughout the M17 region. These authors find a very complex diffuse emission morphology and attribute the emission to a thermalized cluster wind. Since these publications, *Chandra* has performed a very deep observation of the M17 region lasting 151 ks. Given the studies of Broos et al. (2007) and Townsley et al. (2003) have identified rich X-ray emitting point source populations and diffuse emission using a substantially shorter 40 ks observation, it is reasonable to assume that the

deeper observation will greatly add to the known X-ray properties of the cluster and is such is ideal for study in this project.



Figure 3.33: 2MASS Image of NGC 6618.

3.8.1 Summary

The 151 ks NGC 6618 *Chandra* dataset was aimed at the centre of the cluster. The 17'x17' ACIS-I FOV was only sufficient to cover $\sim 50\%$ of the entire cluster area ($R_{Cl} = 13.2'$) but was enough to resolve the cluster core ($R_{Co} = 4.8'$). However, two other stellar populations are known in the field, namely the M 17 North Cloud (M 17 N) and the Kleinmann-Wright Object (KWO)¹ cluster region. Any source falling within the bounds of these stellar populations were removed from consideration as, without further information, there is no way to identify which population they actually belong to. No background flaring periods were identified leaving the full ~ 151 ks of useable data. The *wavdetect* algorithm detected 1068 sources in the FOV with 57 of these falling in the bounds of M 17 N or the KWO cluster. 2MASS counterparts were identified for 408 of the remaining sources. Foreground and extragalactic contamination simulations yield 21-35 potential foreground sources and 50-70 potential extragalactic sources in the FOV. Individual source data and

¹The Kleinmann-Wright Object is an usual double B star system in which one of the stars is a Herbig Be star (Chini et al., 2004)

statistics were analysed, as outlined in 2.1, to identify 107 candidate extragalactic sources in the FOV. This implies as many as 47 of the identified extragalactic sources may actually be members of the NGC 6618 cluster population. Without further information however, there is no way to identify these sources and thus only all 107 candidate extragalactic sources were removed from consideration. This left 904 sources in the FOV, including foreground contaminants, which are all labelled as cluster sources. The adaptively smoothed image of the cluster revealed bright diffuse emission throughout the cluster in addition to a stream of soft diffuse emission eastward of the cluster which, along with the unsmoothed 0.5-8 keV ACIS-I image, is shown in Figure 3.34.

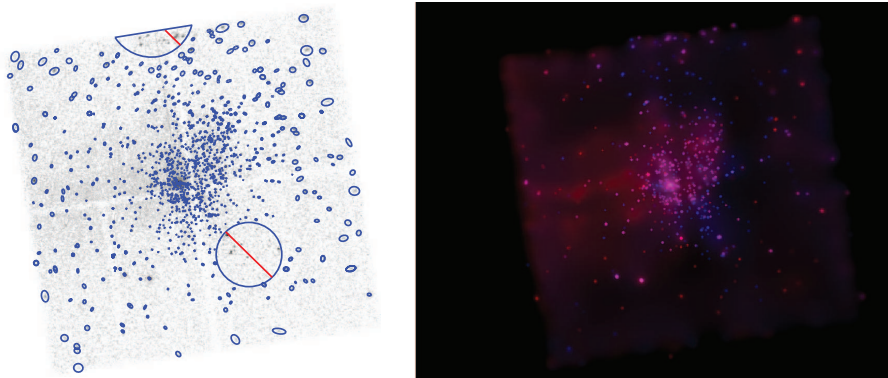


Figure 3.34: *Chandra* ACIS-I 0.5-8 keV image of NGC 6618 with detected sources marked in blue (left) and adaptively smoothed *Chandra* soft (0.5-2 keV, shown in red) and hard (2-8 keV, shown in blue) image. The M17 N and KWO cluster regions are identified in the north and southwest of the left image respectively.

High mass sources in the detected X-ray population were identified using the source lists of Hoffmeister et al. (2008) and the SIMBAD database. All of the known O stars in the FOV were detected whereas only 18 of the 44 early B stars were detected. The spectra of each of the high mass sources with > 50 counts were fit in *XSPEC* with absorbed one and two temperature thermal plasma models during the *AE* reduction and analyses procedures (results given in Table B.24). The results of the spectral fits show that three different X-ray emission processes are at work in the high mass sources of NGC 6618. Three sources stand out as being likely CWB systems, namely CEN 1a, CEN 1b and CEN 2, each of which are well fit with two temperature thermal plasma models and have derived values of $0.5-8 \text{ keV } \log L_X > 32 \text{ erg s}^{-1}$. Many of the remaining known high mass stars, in particular

the mid-late O-type and early B-type stars, are well fit with hard thermal plasma models and have L_X values consistent with MCWS emission. Unsurprising given the extreme youth of this cluster. The remaining known high mass sources are well fit with soft thermal plasma models and have L_X values consistent with RDIS emission.

The correlated high quality 2MASS data were used to produce a J vs $J - H$ colour-magnitude diagram with the appropriate evolutionary tracks and reddening vectors (Figure B.29). This plot identifies 14 candidate OB stars in the FOV (see Table B.25 for results of spectral fits). Almost all of the candidate OB sources were best fit with a hard one temperature thermal plasma model, most having derived hard kT values and all with $L_X < 10^{32}$ erg s $^{-1}$. If indeed these are OB stars, they derived parameters consistent with MCWS emission. Only one of the candidate OB stars is well fit with a cool thermal plasma model and has L_X values consistent with RDIS emission.

The remaining cluster sources are likely low mass PMS objects. The PMS stars with > 50 counts were fit in *XSPEC* with an absorbed thermal plasma model. The global results of these fits are given in graphic form in Figure B.30. The brightest PMS source in NGC 6618 has a 2-8 keV $\log L_X < 32$ erg s $^{-1}$, within the expected range. The derived plasma temperatures of the sources range from 0.1-10 keV, peaking at ~ 3 keV. Many of these sources suffer from slight foreground absorption ($\log N_H \lesssim 22.0$ cm $^{-2}$) however several sources are subject to quite heavy absorption ($\log N_H \gtrsim 22.5$ cm $^{-2}$), possibly due to an accretion disk or natal cloud. Similarly, many sources shows no sign of variability over the course of the observation. However, there is a sizable fraction of variable sources with a few extremely variable, likely flaring objects. Trends in the variation of E_{median} with kT and N_H are similar to those found by Feigelson et al. (2005) with a slight increase in kT with E_{median} and increasing N_H with E_{median} above ~ 1.6 keV. For sources with $E_{\text{median}} < 1.6$ keV, an upper limit of $\log N_H \lesssim 22.0$ cm $^{-2}$ is found.

2-8 keV L_X values were calculated for the remaining PMS sources in the cluster and were used to produce the 2-8 keV L_X against E_{median} plots, shown in Figure B.31. These plots indicate that the majority of the PMS source in NGC 6618 is lightly obscured, most probably Class II or Class III YSOs with a substantial amount of heavily obscured sources, likely Class I YSOs or Class II YSOs viewed from an unfavourable angle. Many of these heavily obscured sources are variable or

flaring with a few quiescent objects. These likely represent the high luminosity end of the heavily obscured source population.

Given the obvious diffuse emission in Figure 3.34 it was deemed unnecessary to mask and adaptively smooth the image again. Spectra were extracted from the cluster core region and the entire FOV and fit in *XSPEC*. The spectra with the best fit models are shown in Figure B.32 with fit results given in Table B.26. Due to the stream of soft diffuse emission from the cluster core, a three temperature thermal plasma was required for an acceptable fit to the all-FOV spectrum. The soft region of the spectrum is best fit with 0.15 keV and 0.58 keV thermal plasmas, in addition to a much harder 10 keV plasma to account for the relatively faint hard emission. The core region is somewhat different however with only a two temperature thermal plasma model required with soft and hard plasma components. Given the number of high mass stars in the region, a cluster wind may be partly responsible for the diffuse emission, particularly in the core. Assuming the model of Cantó et al. (2000, see Section 1.4.7.1) and considering the O stars to be the dominant contributors to the cluster wind, a hot component plasma temperature of ~ 10.5 keV and a 2-8 keV $\log L_X$ of ~ 30.7 erg s^{-1} are derived meaning a cluster wind can only account for a fraction of the observed $\log L_X \sim 32.5$ erg s^{-1} in the core. It is noted that the bright stream of soft diffuse emission seen in the FOV has little contribution to the hard band 2-8 keV L_X values discussed here.

The cluster and PMS star 2-8 keV XLFs were constructed and the PMS XLF compared to that of the similarly aged COUP. These XLFs are shown in Figure 3.35. The total cluster XLF shows two high luminosity outliers, namely the two brightest CWB candidates. The high luminosity end of the PMS XLF shows the same slope as the COUP PMS population. Scaling the COUP population to that of NGC 6611 and integrating the ‘missing’ PMS population region yields an estimate of the unresolved PMS population 2-8 keV $\log L_X$ of ~ 33 erg s^{-1} . Thus the unresolved PMS population can account for the majority of the hard diffuse emission in the FOV of 2-8 keV $\log L_X \sim 33.3$ erg s^{-1} .

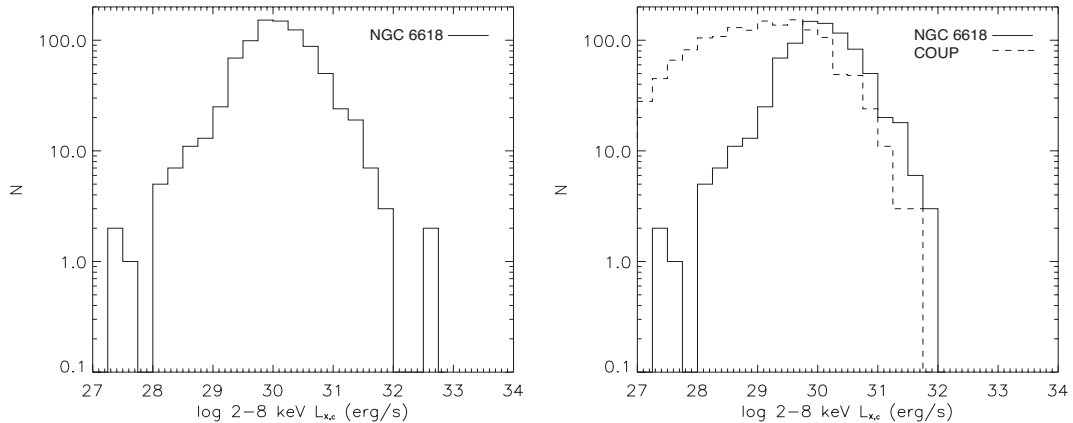


Figure 3.35: Left: NGC 6618 total cluster 2-8 keV XLF. Right: NGC 6618 PMS star 2-8 keV XLF (solid line) and the COUP 2-8 keV XLF (dashed line).

3.9 Trumpler 14

Trumpler 14 (Tr14) is a young massive star cluster located in the Great Carina Nebula, one of the most active star forming regions in the Galaxy. The cluster suffers from relatively low optical extinction ($A_V \approx 2.6$, [Ascenso et al., 2007b](#)) and this, coupled with its moderate distance (~ 2.8 kpc, [Tapia et al., 2003](#)), have made Tr14 one of the most studied clusters in the Galaxy. [Massey and Johnson \(1993\)](#) and [Vazquez et al. \(1996\)](#) performed studies on the stellar content of the cluster and identified some 13 O type and 18 B type stars in the population with one of the O stars later being classified as a rare O2If* star ([Walborn et al., 2002](#)). Even with this high mass population, [Ascenso et al. \(2007b\)](#) find that the cluster is less dense than other clusters of similar size and stellar content. In addition to the high mass population, [DeGioia-Eastwood et al. \(2001\)](#) and later [Sanchawala et al. \(2007b\)](#), identify a PMS population. The presence of high mass and PMS population indicate an age of 1-5 Myr which is confirmed by several authors (eg. - [Ascenso et al., 2007b](#); [DeGioia-Eastwood et al., 2001](#); [Tapia et al., 2003](#)). An age of 1 Myr is adopted for this analysis. [Tapia et al. \(2003\)](#) use the distribution of stars in the V band to determine a cluster radius of $\sim 4.5'$, which is adopted for this analysis.

Both *Chandra* and *XMM-Newton* have obtained moderately deep observations of Tr14. [Townesley \(2006\)](#) use a 60 ks *Chandra* observation centered on the cluster to identify ~ 1600 point sources in the FOV embedded in large scale diffuse emission. These authors identify the brightest point sources as being coincident with the known

O type stars in the cluster, some of which show hard spectral emission, consistent with CWB or MCWS emission. They also note that the diffuse emission in the region is soft and seemingly not associated with the massive stars in the cluster. While not completely disregarding some contribution from the massive stellar winds, these authors favour one or more cavity supernovae not associated with the cluster as being responsible for the diffuse emission. [Albacete Colombo et al. \(2003\)](#) used a 44 ks *XMM-Newton* observation, centered on η Carinae (located in the nearby Trumpler 16 cluster, see Section 3.10) to identify 80 point sources in the FOV with those in the northwest associated with Tr14. These authors proceeded to derive spectral properties for these sources. Unfortunately, due to the large off-axis angle of Tr14, only a limited cluster analysis could be performed and hence, the analysis presented focuses on the global properties of the sources in the Carina region rather than on the cluster itself. It is clear from the literature that Tr14 contains a very rich and varied stellar content and X-ray emitting population and as such is ideal for study in this project.



Figure 3.36: 2MASS Image of Trumpler 14.

3.9.1 Summary

The 60 ks Tr14 *Chandra* dataset was aimed at the centre of the cluster and was sufficient to cover the entire cluster area. No background flaring periods were iden-

tified leaving the full ~ 60 ks of useable data. The *wavdetect* algorithm detected 1154 sources in the FOV, 868 of which fall within the cluster bounds. 2MASS counterparts were identified for 562 of these sources. Foreground and extragalactic contamination simulations yield 15-22 potential foreground sources and 70-80 potential extragalactic sources in the FOV. Assuming the contaminants are distributed evenly across the FOV, this corresponds to 4-6 and 19-22 Galactic and extragalactic contaminants in the cluster area. Individual source data and statistics were analysed, as outlined in 2.1, to identify 27 candidate extragalactic sources in the cluster. This implies a few of the identified extragalactic sources may actually be members of the Tr14 cluster population. Without further information however, there is no way to identify these sources and thus all 27 candidate extragalactic sources were removed from consideration. This left 841 sources in the cluster bounds including, including foreground contaminants, which are all labelled as cluster sources. The adaptively smoothed image revealed bright diffuse emission throughout the cluster in addition to a region of soft diffuse emission in the southeast of the FOV which, along with the unsmoothed 0.5-8 keV ACIS-I image, is shown in Figure 3.37.

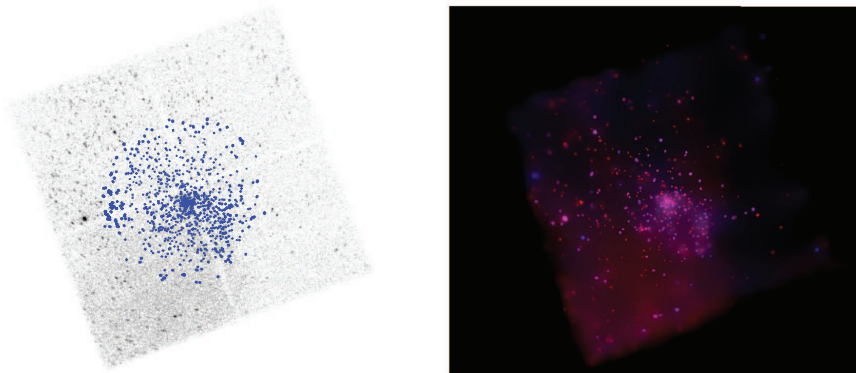


Figure 3.37: *Chandra* ACIS-I 0.5-8 keV image of Trumpler 14 with detected sources marked in blue (left) and adaptively smoothed *Chandra* soft (0.5-2 keV, shown in red) and hard (2-8 keV, shown in blue).

High mass sources in the detected X-ray population were identified using the source lists of [Massey and Johnson \(1993\)](#) and the SIMBAD database. All of the known O stars in the FOV were detected whereas only 5 of the 18 early B stars were detected. The spectra of each of the high mass sources with > 50 counts were fit in *XSPEC* with absorbed one and two temperature thermal plasma models during the *AE* reduction and analyses procedures (results given in Table B.27). In general

the known high mass sources exhibit soft spectra, in keeping with a RDIS emission mechanism. The one early B-type star bright enough to be spectrally fit shows the spectral signatures of MCWS emission. One source, namely HD 93129 A, which is a very rare O2I star, requires a two temperature thermal plasma model for an acceptable fit. This, coupled with its derived 0.5-8 keV $\log L_X$ of $\sim 33.2 \text{ erg s}^{-1}$ suggests that HD 93129 A is a CWB system. Indeed this system is has already been confirmed as a CWB through radio observations (Benaglia and Koribalski, 2004).

The correlated high quality 2MASS data were used to produce a J vs $J - H$ colour-magnitude diagram with the appropriate evolutionary tracks and reddening vectors (Figure B.33). This plot identifies 12 candidate OB stars in the FOV (see Table B.28 for results of spectral fits). Five of the candidate OB sources were bright enough to be fit in *XSPEC*. Three of these are best fit with an absorbed one temperature thermal plasma model having derived hard kT values and all with $\log L_X < 32 \text{ erg s}^{-1}$, the signatures of MCWS emission. The remaining bright candidate OB stars are well fit with a cool thermal plasma model and have L_X values consistent with RDIS emission.

The remaining cluster sources are likely low mass PMS objects. The PMS stars with > 50 counts were fit in *XSPEC* with an absorbed thermal plasma model. The global results of these fits are given in graphic form in Figure B.34. The brightest PMS source in Tr14 has a 2-8 keV $\log L_X < 32 \text{ erg s}^{-1}$, within the expected range. The derived plasma temperatures of the sources range from 0.1-9 keV, peaking at ~ 2 keV. Many of these sources suffers from slight foreground absorption ($\log N_H \lesssim 22.0 \text{ cm}^{-2}$) with a couple of sources subject to heavy absorption ($\log N_H \gtrsim 22.5 \text{ cm}^{-2}$), possibly due to an accretion disk or natal cloud. Similarly, many sources shows no sign of variability over the course of the observation with several variable sources and a few extremely variable, likely flaring objects. Trends in the variation of E_{median} with kT and N_H are similar to those found by Feigelson et al. (2005) with a slight increase in kT with E_{median} and increasing N_H with E_{median} above $\sim 1.8 \text{ keV}$. For sources with $E_{\text{median}} < 1.8 \text{ keV}$, an upper limit of $\log N_H \lesssim 22.2 \text{ cm}^{-2}$ is found.

2-8 keV L_X values were calculated for the remaining PMS sources in the cluster and were used to produce the the 2-8 keV L_X against E_{median} plots, shown in Figure B.35. These plots indicate that the majority of the PMS sources in Tr14 is lightly obscured, most probably Class II or Class III YSOs with about 12 heavily obscured

sources, likely Class I YSOs or Class II YSOs viewed from an unfavourable angle. Most of these sources show no signs of variability with a few variable sources. These likely represent the high luminosity tip of the heavily obscured source population.

Given the obvious diffuse emission in Figure 3.37 it was deemed unnecessary to mask and adaptively smooth the image again. Spectra were extracted from the cluster core and cluster regions and fit in *XSPEC*. The spectra with the best fit model are shown in Figure B.36 with fit results given in Table B.29. Due to the region of soft diffuse emission in the southwest of the FOV, a three temperature thermal plasma was required for an acceptable fit to the total cluster spectrum. The soft region of the spectrum is best fit with 0.18 keV and 0.74 keV thermal plasmas, in addition to a harder 3.83 keV plasma to account for the relatively faint hard emission. Given Townsley (2006) indicate that the region of soft diffuse emission is not associated with the cluster, it is not discussed further here. The core region does not required the very soft component with a two temperature thermal plasma model with soft and hard plasma components yielding a good fit. Given the number of high mass stars in the region, a cluster wind may contribute to the hard diffuse emission, particularly in the core. Assuming the model of Cantó et al. (2000, see Section 1.4.7.1) and considering the O stars to be the dominant contributors to the cluster wind, a hot component plasma temperature of ~ 12 keV and a 2-8 keV $\log L_X$ of ~ 31.3 erg s $^{-1}$ are derived meaning a cluster wind can only account for a fraction of the observed diffuse emission in the core. It is noted here that the bright region of soft diffuse emission seen in the FOV has little contribution to the hard band 2-8 keV L_X values discussed here.

The cluster and PMS star 2-8 keV XLFs were constructed and the PMS XLF compared to that of the similarly aged COUP. These XLFs are shown in Figure 3.38. The high luminosity end of the PMS XLF shows the same slope as the COUP PMS population. Scaling the COUP population to that of Tr14 and integrating the ‘missing’ PMS population region yields an estimate of the unresolved PMS population 2-8 keV $\log L_X$ of ~ 33 erg s $^{-1}$. Thus the unresolved PMS population can account for all of the hard diffuse emission in the cluster of 2-8 keV $\log L_X \sim 33$ erg s $^{-1}$.

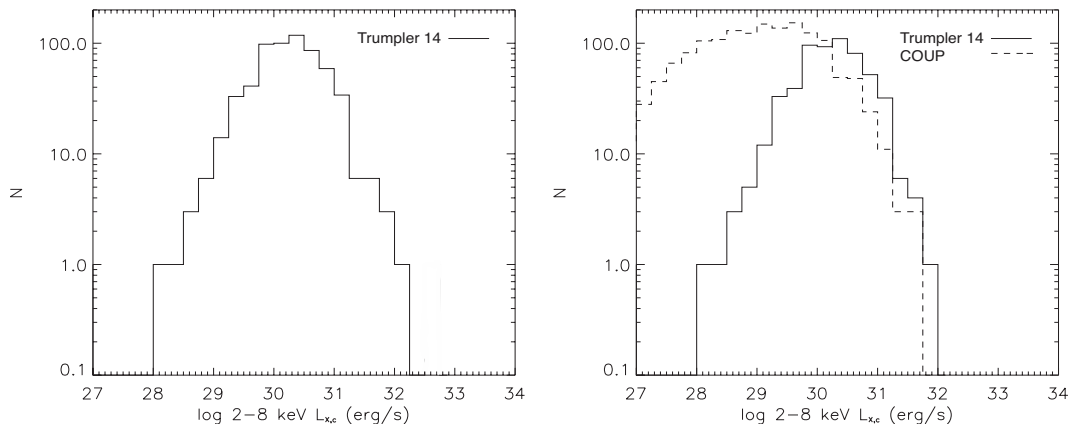


Figure 3.38: Left: Trumpler 14 total cluster 2-8 keV XLF. Right: Trumpler 14 PMS star 2-8 keV XLF (solid line) and the COUP 2-8 keV XLF (dashed line).

3.10 Trumpler 16

Trumpler 16 (Tr16) is a young massive star cluster located in the Great Carina Nebula, one of the most active star forming regions in the Galaxy. The cluster well known as it harbours the enigmatic η Carinae, a LBV in a high mass binary system. However, the cluster is also known to host many more massive stars with population studies revealing many O stars including 2 O3V stars (see [DeGioia-Eastwood et al., 2001](#); [Massey and Johnson, 1993](#); [Tapia et al., 2003](#), for example). More recent IR surveys of the cluster have revealed a rich PMS population ([Albacete-Colombo et al., 2008](#); [Sanchawala et al., 2007a,b](#)). Many of the existing studies of the Tr16 derive a cluster distance of between 2-3 kpc. For this analysis, the most common distance of 2.5 kpc is adopted. Similarly age estimates range from 1-5 Myr depending the subpopulation, with the detected high mass sources suggesting a cluster age of about 4 Myr ([DeGioia-Eastwood et al., 2001](#); [Sanchawala et al., 2007b](#), for example) while estimates from the low mass population suggest an age of 1-3 Myr ([Sanchawala et al., 2007b](#)). An cluster age of 4 Myr is adopted for this analysis, consistent with the age determined from the high mass stars in the cluster. [Tapia et al. \(2003\)](#) use the distribution of stars in the V band to determine a cluster radius of $\sim 5.5'$, which is adopted for this analysis. This value is in reasonable agreement with the estimate from the catalogue of open cluster properties of [Kharchenko et al. \(2005\)](#) and thus the catalogue's core radius ($R_{Cl}=3.6'$) is adopted.

Both *Chandra* and *XMM-Newton* have observed Tr16, primarily due to the pres-

ence of η Carinae. Most recently [Albacete-Colombo et al. \(2008\)](#) used a 90 ks *Chandra* observation of the cluster to survey the low mass stars in the region, identifying over 1000 sources in and around the cluster. Though these authors focus primarily on the low mass population, they also characterize the X-ray emission from the high mass sources. Previous studies also utilize this observational data with [Sanchawala et al. \(2007a\)](#) performing a multiwavelength survey of the region and the studies of [Evans et al. \(2003\)](#) and [Evans et al. \(2004\)](#) focussing on the bright high mass sources in and around Tr16. [Albacete Colombo et al. \(2003\)](#) used a 44 ks XMM-Newton observation, centered on η Carinae to identify 80 point sources in the FOV and perform an X-ray photometric analysis of the detected population as well as spectral analysis for the brightest high mass sources. Only X-ray studies of the cluster as a whole are mentioned here. There is also a vast number of X-ray studies which use *Chandra* and *XMM-Newton* to analyze the X-ray emission from η Carinae available in the literature (for example [Corcoran et al., 2010](#); [Hamaguchi et al., 2007](#); [Henley et al., 2008](#); [Leyder et al., 2008](#), to name but a few).



Figure 3.39: *HST* Image of Trumpler 16.

3.10.1 Summary

The 90 ks Tr 16 *Chandra* dataset was aimed slightly to the west of the cluster but was sufficient to cover the entire cluster area. No background flaring periods were

identified leaving the full ~ 90 ks of useable data. The *wavdetect* algorithm detected 895 sources in the FOV, 549 of which fall within the cluster bounds. 2MASS counterparts were identified for 326 of these sources. Foreground and extragalactic contamination simulations yield 20-27 potential foreground sources and 75-85 potential extragalactic sources in the FOV. Assuming the contaminants are distributed evenly across the FOV, this corresponds to 6-9 and 25-28 Galactic and extragalactic contaminants in the cluster area. Individual source data and statistics were analysed, as outlined in 2.1, to identify 25 candidate extragalactic sources in the cluster which were removed from consideration. This left 524 sources in the cluster area including, including foreground contaminants, which are all labelled as cluster sources. The adaptively smoothed image of the cluster revealed soft diffuse emission throughout the cluster in addition to localised hard diffuse emission surrounding η Carinae which, along with the unsmoothed 0.5-8 keV ACIS-I image, is shown in Figure 3.40.

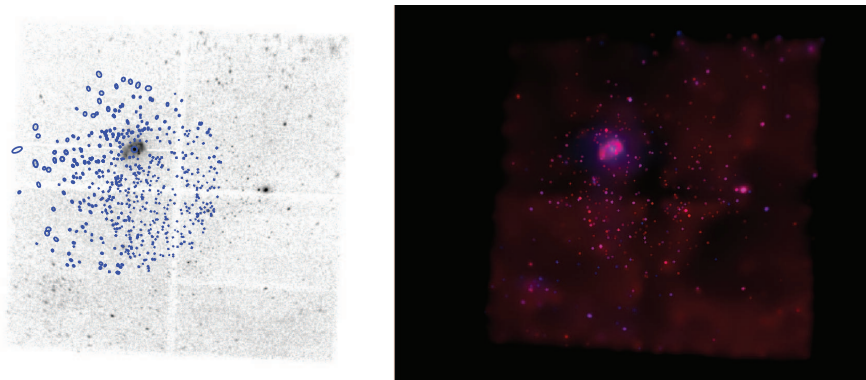


Figure 3.40: *Chandra* ACIS-I 0.5-8 keV image of Trumpler 16 with detected sources marked in blue (left) and adaptively smoothed *Chandra* soft (0.5-2 keV, shown in red) and hard (2-8 keV, shown in blue).

High mass sources in the detected X-ray population were identified using the source lists of [Massey and Johnson \(1993\)](#) and the SIMBAD database. All of the known O stars in the FOV were detected whereas only 4 of the 20 early B stars were detected. The spectra of each of the high mass sources with > 50 counts were fit in *XSPEC* with absorbed one and two temperature thermal plasma models during the *AE* reduction and analyses procedures (results given in Table B.30). In general the known high mass sources exhibit soft spectra, signifying a RDIS emission mechanism. One of the early B-type stars is best fit with a hard thermal plasma model

indicating a MCWS emission. One source, namely MJ 496, an O8.5V star, requires a two temperature thermal plasma model for an acceptable fit. This, coupled with its derived 0.5-8 keV L_X value of $> 10^{32}$ erg s $^{-1}$ suggests that MJ 496 is a CWB system. One source with no spectral fit is the incredible bright η Carinae which is a known CWB consisting of an LBV and probably an evolved O star [Verner et al. \(2005\)](#). This remarkable source has a multitude of publications dedicated to the study of its X-ray emission. Its spectrum is so complex that attempts at fitting with simplistic absorbed one or two thermal plasma models fail to yield acceptable fits. Several authors have determined best fits to η Carinae in various observations (see [Leutenegger et al., 2003](#); [Seward et al., 2001](#), for example), with the best fits usually consisting of two temperature models with the addition of spectral lines. η Carinae is also known to vary substantially on both long and short timescales ([Moffat and Corcoran, 2009](#), and references therein) and as such, this 90 ks observation is only a snapshot of in this periodic emission. In addition, the η Carinae spectrum, extracted in this observation suffers from quite serious photon pileup further complicating a spectral analysis. For these reasons it was decided not to fit the spectrum. However, lower L_X limits for this source were estimate which are consistent with values quoted in the literature.

The correlated high quality 2MASS data were used to produce a J vs $J - H$ colour-magnitude diagram with the appropriate evolutionary tracks and reddening vectors (Figure [B.37](#)). This plot identifies 19 candidate OB stars in the FOV (see Table [B.31](#) for results of spectral fits). Eight of the candidate OB sources were bright enough to be fit in *XSPEC*. All apart from one of these are best fit with an absorbed one temperature thermal plasma model having derived hard kT values and all with $L_X < 10^{32}$ erg s $^{-1}$, the signatures of MCWS emission. The remaining bright candidate OB star is well fit with a cool thermal plasma model and has an L_X value consistent with RDIS emission.

The remaining cluster sources are likely low mass PMS objects. The PMS stars with > 50 counts were fit in *XSPEC* with an absorbed thermal plasma model. The global results of these fits are given in graphic form in Figure [B.38](#). The brightest PMS source in Tr 16 has a 2-8 keV $\log L_X < 32$ erg s $^{-1}$, within the expected range. The derived plasma temperatures of the sources range from 0.1-7.5 keV, peaking at ~ 2 keV. Many of these sources suffers from slight foreground absorption ($\log N_H \lesssim 22.5$ cm $^{-2}$) with no sources subject to heavy absorption ($\log N_H \gtrsim 22.5$ cm $^{-2}$).

Most sources shows no sign of variability over the course of the observation with some variable sources and a several extremely variable, likely flaring objects. Trends in the variation of E_{median} with kT and N_{H} are similar to those found by Feigelson et al. (2005) with a slight increase in kT with E_{median} and increasing N_{H} with E_{median} above ~ 1.8 keV, though not many sources fall in this region of the plot. For sources with $E_{\text{median}} < 1.8$ keV, an upper limit of $\log N_{\text{H}} \lesssim 22.2$ cm $^{-2}$ is found.

2-8 keV L_{X} values were calculated for the remaining PMS sources in the cluster and were used to produce the the 2-8 keV L_{X} against E_{median} plots, shown in Figure B.39. These plots indicate that the vast majority of the PMS source in Tr 16 is lightly obscured, most probably Class II or Class III YSOs with only 2 heavily obscured sources, likely Class I YSOs or Class II YSOs viewed from an unfavourable angle. Most of these sources show no signs of variability, however, many sources, including several of the brightest sources and the heavily obscured sources, show signs of strong variability. These heavily obscured sources likely represent the high luminosity tip of the heavily obscured source population.

Given the obvious diffuse emission in Figure 3.40 it was deemed unnecessary to mask and adaptively smooth the image again. Spectra were extracted from the cluster core and cluster regions and fit in *XSPEC*. For each of the spectra, the entire η Carinae region (i.e.- including the homunculus) was masked. The spectra with the best fit model are shown in Figure B.40 with fit results given in Table B.32. Both spectra are well fit with three temperature thermal plasmas with two soft and one hard component. However, in both the total cluster and cluster core spectra, the hard component plasma temperature very high and not well constrained. Interestingly, the soft diffuse emission that pervades the region may not be associated with the cluster. Given Tr16 is very close to southeast of Tr14 and that the Tr14 observation showed a region of bright diffuse emission extending southeastward, the soft diffuse emission in the Tr16 observation is likely an extension of the emission in the Tr14 observation. Indeed, the temperature of the very soft component in the best fit to the Tr16 soft diffuse emission in both the core and total cluster spectra is in reasonable agreement with that of the very soft component in the Tr14 emission. As such, this very soft component is likely not associated with Tr16 and is not discussed further. Given the number of massive stars in Tr16, in particular η Carinae, it is likely a cluster wind contributes to the observed emission in the cluster. Assuming the model of Cantó et al. (2000, see Section 1.4.7.1), considering

the O stars and η Carinae¹ to be the dominant contributors to the cluster wind, a hot component plasma temperature of ~ 4 keV and a 2-8 keV $\log L_X$ of ~ 33.7 erg s⁻¹ are derived meaning a cluster wind can easily account for the observed diffuse emission in the core. The dominant contributor to the cluster wind by far is η Carinae. Its significant mass loss supplies the required material to push the cluster wind's L_X so high. However, it must be noted that not all of the material shed by η Carinae would be available to fuel a cluster wind, with some of its wind likely impeded by that of its companion. As such, the derived cluster wind $\log L_X \sim 33.7$ erg s⁻¹ represents an upper limit. It is noted here that the soft diffuse emission seen in the FOV has little contribution to the hard band 2-8 keV L_X values discussed here.

The cluster and PMS star 2-8 keV XLFs were constructed and the PMS XLF compared to that of the similarly aged COUP. Given that Tr16 is older than the ONC, the COUP data were scaled according to the scaling relation of [Preibisch and Feigelson \(2005\)](#). These XLFs are shown in [Figure 3.41](#). The total cluster XLF shows one high luminosity outlier, namely η Carinae. The high luminosity end of the PMS XLF shows the same slope as the COUP PMS population. Scaling the COUP population to that of Tr 16 and integrating the 'missing' PMS population region yields an estimate of the unresolved PMS population 2-8 keV $\log L_X \sim 32.9$ erg s⁻¹. Thus the unresolved PMS population can account for about half of the hard diffuse emission in the cluster of $\log L_X \sim 33.3$ erg s⁻¹. Overall, these results suggest that an unresolved PMS population constitutes about half of the observed hard diffuse emission in the cluster, with the cluster wind responsible for the remaining emission.

3.11 Westerlund 1

Westerlund 1 (Wd1) was discovered in the early sixties and was initially classified as an open cluster ([Westerlund, 1961](#)). The cluster suffers from significant reddening ($A_V \approx 12.9$ mag, [Piatti et al., 1998](#)) and, because of this, only recently detailed photometric and spectroscopic analyses have been performed ([Clark and Negueruela, 2002, 2004](#); [Clark et al., 2005](#); [Negueruela and Clark, 2005](#)). [Clark et al. \(2005\)](#) found a rich population of evolved OB stars, including over 20 WRs, and, using a standard Kroupa ([Kroupa, 2001](#)) initial mass function (IMF), inferred a cluster mass

¹Physical wind properties for η Carinae of $v = 500$ km s⁻¹ and $\dot{M} = 1 \times 10^3 M_\odot$ yr⁻¹ adopted from [Hillier et al. \(2001\)](#)

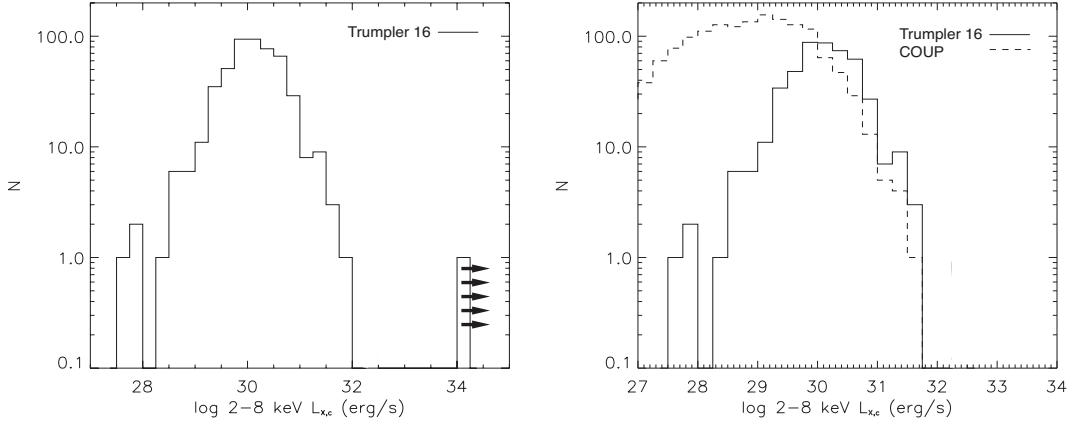


Figure 3.41: Left: Trumpler 16 total cluster 2-8 keV XLF. The black arrows indicate a lower limit as to the L_X of η Carinae. Right: Trumpler 16 PMS star 2-8 keV XLF (solid line) and the COUP 2-8 keV XLF (dashed line).

of $\gtrsim 10^5 M_\odot$. This is at the lower limit of the SSC mass range and certainly made Wd1 the most massive young cluster in the Galaxy. A more recent deep IR study, however, revises this mass estimate somewhat downwards to $\approx 4.5 \times 10^4 M_\odot$ (Brandner et al., 2008). Although this is still bigger than any other known Galactic open cluster, it is smaller than extragalactic SSCs. In addition Brandner et al. (2008) revised previous estimates of age and distance to 3.6 ± 0.7 Myr and 3.55 ± 0.17 kpc respectively, which are adopted for this analysis. Unlike all of the other programme clusters, Wd1 is known to contain at least one post-supernova object, namely the well known magnetar CXOU J164710.2-455216 (Muno et al., 2006a, 2007). Though this is the only known post supernova object, a further 10^2 SNae are thought to have occurred in the cluster already based on the clusters age and extrapolation of its IMF (Clark et al., 2008; Muno et al., 2006b). A recent study of Negueruela et al. (2010) focussed on the OB supergiants in the cluster, increasing the number to over 50.

Both *Chandra* and *XMM-Newton* have observed Wd1. A series of four papers on the X-ray properties of Wd1 (point sources and diffuse emission) has been published which analyzes data from a joint *Chandra/XMM-Newton* observation programme (Clark et al., 2008; Muno et al., 2006a, 2007, 2006b). Clark et al. (2008) performed an analysis of the X-ray point source population. These authors identify many of the known high mass stars in the cluster, including many of the WRs. Muno et al. (2006b) used the same *Chandra* data to assess the diffuse emission in the cluster

finding bright emission throughout the cluster dominated by a hard component and discuss both thermal and non-thermal origins for the emission.



Figure 3.42: 2MASS Image of Westerlund 1.

3.11.1 Summary

The combined 60 ks Wd 1 *Chandra* observations were centered on the cluster and was sufficient to cover the entire cluster area. Background flaring periods were identified and removed leaving ~ 57 ks of useable data. The *wavdetect* algorithm detected 231 sources in the FOV, 159 of which fall within the cluster bounds. 2MASS counterparts were identified for 31 of these sources. Foreground and extragalactic contamination simulations yield 6-17 potential foreground sources and 22-35 potential extragalactic sources in the FOV. Assuming the contaminants are distributed evenly across the FOV, this corresponds to < 5 and 10-18 Galactic and extragalactic contaminants in the cluster area. Individual source data and statistics were analysed, as outlined in 2.1, to identify 29 candidate extragalactic sources in the cluster. This implies as many as 10 of the identified extragalactic sources may actually be members of the Wd1 cluster population. Without further information however, there is no way to identify these sources and thus only all 29 candidate extragalactic sources were removed from consideration. This left 130 sources in the FOV including, including

foreground contaminants¹ which are all labelled as cluster sources. The adaptively smoothed image revealed bright diffuse emission throughout the cluster which, along with the unsmoothed 0.5-8 keV ACIS-S image, is shown in Figure 3.43.

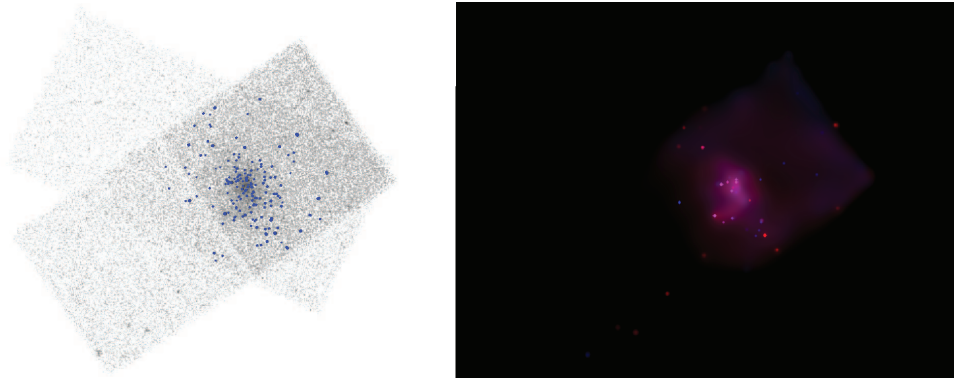


Figure 3.43: *Chandra* ACIS-S 0.5-8 keV image of Westerlund 1 with detected sources marked in blue (left) and adaptively smoothed *Chandra* soft (0.5-2 keV, shown in red) and hard (2-8 keV, shown in blue) image.

High mass sources in the detected X-ray population were identified using the source lists of [Clark et al. \(2005\)](#); [Negueruela et al. \(2010\)](#) and the SIMBAD database. Due to its size and age, Wd1 contains a zoo of evolved massive stars. There are some 25 known WRs and over 50 supergiants in the cluster, of which 11 of the WRs and 23 of the supergiants are detected. Unfortunately, the limiting detection threshold flux falls in the region of the emission from the evolved population. In addition, due to the high absorbing hydrogen column in the direction of Wd1, soft sources suffer from substantial absorption which affects their detectability, resulting in many non-detections. The majority of the detected sources have insufficient counts for a spectral analysis. The spectra of each of the high mass sources with > 50 counts were fit in *XSPEC* with absorbed one and two temperature thermal plasma models during the *AE* reduction and analysis procedures (results given in Tables [B.33](#) and [B.34](#)). Interpretation of the results of these spectral fits is somewhat of a problem in Wd1 due to its high foreground absorption. Only one of the detected supergiants in the cluster, namely W30a, was bright enough for spectral fitting. The spectrum is well fit with an absorbed moderately hard thermal plasma model. We would expect a late O supergiant to have a soft spectrum. As such, it is likely that this is a

¹One extremely bright foreground source, namely HD 151098, was identified and removed from the analysis.

CWB, a conclusion which is strengthened by the derived L_X value of $> 10^{32}$ erg s $^{-1}$. One source, namely W53, is a known high mass star that has yet to be spectrally classified. This source exhibits a soft spectrum and its L_X value suggests that it is a single high mass star, likely a late O or early B supergiant given the amount present in the cluster. If this is the case, it is the brightest single non-WR X-ray emitter in the stellar population. An obvious CWB candidate is a rare sgB[e] star W9. It is well fit with an absorbed two temperature thermal plasma model and, though the hard component is poorly constrained, is one of the brightest sources in the cluster. The remaining bright high mass sources are all WR stars. Single WR of nitrogen class (WN) stars are known to be well fit with two temperature thermal plasma models and L_X values in the $10^{31} - 10^{33}$ erg s $^{-1}$ range (Skinner et al., 2010). In the Wd1 WN sample, the brighter sources are well fit with a two temperature model with soft and hard components, whereas the less bright sources are well fit with single temperature models with hard components only. For these latter sources, it is likely that much of the soft component is absorbed and is consequently missed in the spectral fitting process. With regard to the brighter sources, the two temperature nature of their spectra makes it difficult to determine whether or not they are CWB systems. However, based on the WN analysis of Skinner et al. (2010) who suggest the only source with $L_X > 10^{33}$ erg s $^{-1}$ is in fact a binary system, this lower limit to WN CWB systems used to identify WR A and WR B as candidate CWBs. The remaining WR stars are the carbon rich WR (WC) stars WR E and WR F. This is unusual as single WC stars are known to be very weak X-ray emitters with little, if any, X-ray detections (Skinner et al., 2010, and references therein). As such, these sources may be binary systems. Though WR F is a modestly bright source and could be a CWB, WR E is very weak and it is hard to assign CWB status to this source and as such, it may be one of the first X-ray detections of a single WC star.

The correlated high quality 2MASS data were used to produce a J vs $J - H$ colour-magnitude diagram with the appropriate evolutionary tracks and reddening vectors (Figure B.41). This plot identifies 1 candidate OB star in the FOV however it was not sufficiently bright to perform a reliable spectral fit in *XSPEC* (see Table B.35) and thus, the nature of the X-ray emission from this object is unknown.

It is unclear as to the nature of the remaining cluster sources. Many of them are likely bright PMS stars but it is just as likely that the sources are as yet unidentified late O-type or early B-type stars. Thus, for the remainder of the analysis, I will

refer to them simply as ‘unidentified’ cluster sources. The unidentified stars with > 50 counts were fit in *XSPEC* with an absorbed thermal plasma model. Only two sources satisfied this brightness criteria whose fit results are given in graphic form in Figure B.42. One of the sources exhibits a soft spectrum and low absorption and is likely an unidentified massive star. The second source on the other hand is heavily absorbed and could be a bright Class I YSO. Because there is likely only one bright PMS star in the cluster, the relations of Feigelson et al. (2005) cannot be investigated. An upper limit of $\log N_{\text{H}} \lesssim 22.2 \text{ cm}^{-2}$ is set for sources with $E_{\text{median}} < 1.8 \text{ keV}$, consistent with similar programme clusters.

2-8 keV L_{X} values were calculated for the remaining unidentified sources in the cluster and were used to produce the the 2-8 keV L_{X} against E_{median} plots, shown in Figure B.43. These plots indicate that the majority of the unidentified sources in Wd1 is lightly obscured with about 15 heavily obscured sources. Most of the less bright sources show no signs of variability with a few variable sources. However, almost all of the brighter sources are either variable or flaring. This suggests that most of these are PMS sources. In addition, late O and early B supergiants, which dominate the upper Wd1 HR diagram, are expected to have soft spectra with little emission in the 2-8 keV band. As such, these stars would be confined to the lower regions of the plots in Figure B.43. If indeed these are mostly PMS sources, the data suggests that most are Class II or Class III YSOs with a few Class I YSOs or Class II YSOs viewed from an unfavourable angle.

Given the obvious diffuse emission in Figure 3.43 it was deemed unnecessary to mask and adaptively smooth the image again. Spectra were extracted from the cluster core and total cluster regions for each observation and simultaneously fit in *XSPEC*. The spectra with the best fit model are shown in Figure B.44 with fit results given in Table B.36. Both the total cluster and cluster core spectra require two temperature thermal plasmas for an acceptable fit. There is very little variation in the derived total cluster and cluster core spectra parameters suggesting the emission mechanisms responsible for the emission throughout the cluster are the same. Given the number of WR stars in the region, a cluster wind will definitely contribute to the diffuse emission, particularly in the core. Assuming the model of Cantó et al. (2000, see Section 1.4.7.1) and considering the WR stars to be the dominant contributors to the cluster wind, a hot component plasma temperature of 3.7 keV and a 2-8 keV $\log L_{\text{X}}$ of $\sim 34 \text{ erg s}^{-1}$ are derived meaning a cluster wind can easily account for all

of the observed hard diffuse emission in the core.

The cluster and unidentified source 2-8 keV XLFs were constructed and the unidentified source XLF compared to the PMS XLF of the COUP to obtain an estimate of the contribution of an unresolved population to the diffuse emission. Given that Wd1 is older than the ONC, the COUP data were scaled according to the scaling relation of [Preibisch and Feigelson \(2005\)](#). These XLFs are shown in [Figure 3.44](#). The total cluster XLF shows no high luminosity outliers, unsurprising given the large number of luminous sources. The high luminosity end of the unidentified source XLF shows roughly the same slope as the COUP PMS population. Scaling the COUP population to that of Wd1 and integrating the ‘missing’ population region yields an estimate of the unresolved population 2-8 keV $\log L_X$ of $\sim 33 \text{ erg s}^{-1}$. Thus the unresolved PMS population can account for only a fraction of the hard diffuse emission in the FOV of $\log L_X \sim 34 \text{ erg s}^{-1}$. Interestingly, if indeed the high 2-8 keV luminosity sources in the unidentified population are actually PMS sources (as suggested above), the Wd1 PMS population derived from scaling of the COUP XLF, is surprisingly small. [Brandner et al. \(2008\)](#) extrapolate the observed intermediate mass population to lower masses and determine $\sim 10^5$ stars in the PMS mass range. Comparing the total Wd1 PMS population (both resolved and unresolved) to that of the COUP infers ~ 2000 sources down to $0.1 M_\odot$, which is substantially smaller than the number determined by [Brandner et al. \(2008\)](#) and may indicate the cluster IMF is truncated at the lower masses. If this is the case, their derived cluster mass of $\approx 4.5 \times 10^4 M_\odot$ may be overestimated.

One source that has not been discussed or included in the analysis thus far is the well known magnetar CXOU J164710.2-455216 which has been discussed in great detail in the literature ([Muno et al., 2006a, 2007](#)) and is this only briefly described here. The source in it’s quiescent state is well fit with an absorbed soft black body model ([Clark et al., 2008; Muno et al., 2007](#)), which is verified in this analysis. An absorption corrected 0.5-8 keV $\log L_X \sim 32.7 \text{ erg s}^{-1}$ is derived, which differs slightly from the previous analyses due to a different assumed cluster distance.

3.12 Westerlund 2

Westerlund 2 (Wd2) is a massive stellar cluster located in the giant HII complex RCW 49. The cluster was discovered in the early sixties ([Westerlund, 1961](#)) and for

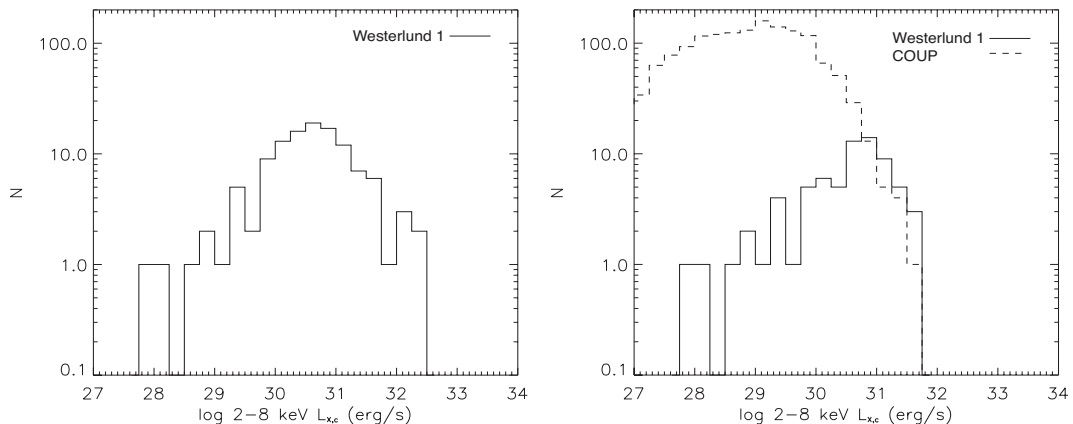


Figure 3.44: Left: Westerlund 1 total cluster 2-8 keV XLF. Right: Westerlund 1 unidentified source 2-8 keV XLF (solid line) and the COUP 2-8 keV XLF (dashed line).

many years went largely unnoticed. Only recently has the cluster been the subject of intense study due to the presence of the very high mass binary system WR20a, which is a double WR system and possibly the most massive binary in the Galaxy, and extended γ -ray emission (Aharonian et al., 2007) in the region. Early spectroscopic studies of the cluster revealed several mid O-type stars in the cluster as well as two WR stars (see Moffat et al., 1991, for example). A more recent combined photometric and spectroscopic survey by Rauw et al. (2007) assigned spectral types as early as O3V to stars in the core of the cluster though suggest that many more O-type stars were likely missed due to high foreground absorption in the region. In the intervening years, several photometric surveys of the cluster were performed to derive cluster parameters such as age and distance (see Ascenso et al., 2007a; Carraro and Munari, 2004; Piatti et al., 1998, for example). Age estimates from the various photometric and spectroscopic analyses are somewhat consistent ranging from 2-3 Myr given the high mass stellar population. An age of 2.5 Myr is adopted for this analysis. Unfortunately, the distance to the cluster is much more controversial with estimates ranging from 2-8 kpc. This is due to Wd2 lying tangential to the Carina spiral arm resulting a large range of possible kinematic distances, the so called kinematic distance ambiguity. In this analysis, an adopted distance of 4.2 kpc is selected following the reasoning of Tsujimoto et al. (2007) who adopt the distance of Churchwell et al. (2004) as a compromise since the estimate lies roughly in the centre of the range of distances in the literature. A cluster radius of $\sim 4'$ is adopted from the NIR survey of Ascenso et al. (2007a). Unfortunately there is no Wd2 entry in the catalogue of open cluster properties of Kharchenko et al. (2005) and thus a

simplistic core radius of $R_{Co}=R_{Cl}/2$ is adopted.

Chandra has observed the Wd2 region on three occasions. [Tsujiimoto et al. \(2007\)](#) use the first of these, a 40 ks observation, to assess the X-ray emitting population in the region, detecting emission from the known massive stars (some of which are likely CWB systems), several candidate massive stars and a PMS population. [Townesley \(2006\)](#) use these same data to perform an analysis of the diffuse emission in the Wd2 region. These authors find diffuse emission to pervade the cluster core that is well fit with a two component model. They do not, however, discuss potential sources for this emission. [Nazé et al. \(2008\)](#) use these data with a further two 50 ks observations to perform a deeper analysis of the cluster population, assessing emission from high mass stars as well as bright, flaring PMS sources and discuss the observed diffuse X-ray emission in relation to the extended γ -ray emission ([Aharonian et al., 2007](#)). These authors find that it is unlikely that the γ -ray emission is related to the diffuse X-ray emission seen in the cluster.



Figure 3.45: *Spitzer* Image of Westerlund 2.

3.12.1 Summary

The combined 140 ks Wd 2 *Chandra* observations were centered on the cluster and were sufficient to cover the entire cluster area. Background flaring periods were identified and removed leaving ~ 136 ks of useable data. The *wavdetect* algorithm detected 588 sources in the FOV, 399 of which fall within the cluster bounds. 2MASS counterparts were identified for 196 of these sources. Foreground and extragalactic contamination simulations yield 23-35 potential foreground sources and 110-135 potential extragalactic sources in the FOV. Assuming the contaminants are distributed evenly across the FOV, this corresponds to 4-6 and 20-25 Galactic and extragalactic contaminants in the cluster area. Individual source data and statistics were analysed, as outlined in 2.1, to identify 56 candidate extragalactic sources in the cluster. This implies as many as 30 of the identified extragalactic sources may actually be members of the Wd2 cluster population. Without further information however, there is no way to identify these sources and thus only all 56 candidate extragalactic sources were removed from consideration. This left 343 sources in the cluster area, including foreground contaminants which are all labelled as cluster sources. The adaptively smoothed image of the cluster revealed bright diffuse emission which, along with the unsmoothed 0.5-8 keV ACIS-I image, is shown in Figure 3.46.

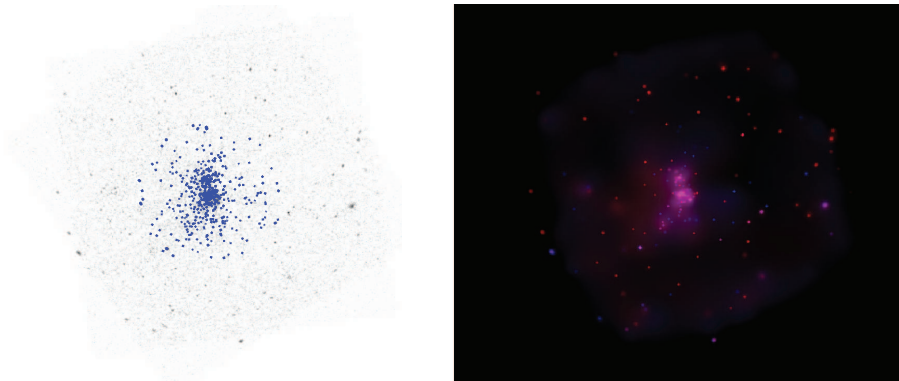


Figure 3.46: *Chandra* ACIS-I 0.5-8 keV image of Westerlund 2 with detected sources marked in blue (left) and adaptively smoothed *Chandra* soft (0.5-2 keV, shown in red) and hard (2-8 keV, shown in blue) image.

High mass sources in the detected X-ray population were identified using the source lists of [Rauw et al. \(2007\)](#) and the SIMBAD database. All of the known O

stars and WRs in the FOV were detected. As yet no B stars have been spectroscopically identified in the cluster. The spectra of each of the high mass sources with > 50 counts were fit in *XSPEC* with absorbed one and two temperature thermal plasma models during the *AE* reduction and analysis procedures (results given in Table B.37). All of the known high mass sources well fit with a one temperature thermal plasma model exhibit soft spectra, in keeping with a RDIS emission mechanism. The remaining O stars, namely MSP 167, MSP 183 and MSP 188, are best fit with two temperature thermal plasma models and have derived 0.5-8 keV L_X values $> 10^{33}$ erg s $^{-1}$ suggesting that these sources are CWB systems. Both of the WR systems in the cluster are best fit with two temperature thermal plasma models and have derived 0.5-8 keV L_X values well in excess of 10^{33} erg s $^{-1}$ indicating both are CWB systems.

The correlated high quality 2MASS data were used to produce a J vs $J - H$ colour-magnitude diagram with the appropriate evolutionary tracks and reddening vectors (Figure B.45). This plot identifies 2 candidate OB stars in the FOV (see Table B.38 for results of spectral fits). Both candidates were bright enough to be fit in *XSPEC*. One of the sources is best fit with an absorbed one temperature thermal plasma model having a derived hard kT value and $L_X < 10^{32}$ erg s $^{-1}$, the signatures of MCWS emission. The remaining bright candidate OB star is well fit with a cool thermal plasma model and has L_X values consistent with RDIS emission, suggesting it is a single OB star.

It is unclear as to the nature of the remaining cluster sources. Many of them are likely bright PMS stars but it is just as likely that, particularly in the outer cluster regions, the sources are as yet unidentified O-type or early B-type stars. Thus, for the remainder of the analysis, I will refer to them simply as ‘unidentified’ cluster sources. The unidentified stars with > 50 counts were fit in *XSPEC* with an absorbed thermal plasma model. The global results of these fits are given in graphic form in Figure B.46. The brightest unidentified source in Wd2 has a 2-8 keV $\log L_X < 32$ erg s $^{-1}$. The derived plasma temperatures of the sources range from 0.1-9 keV, peaking at ~ 3 keV. Many of these sources suffer from slight foreground absorption ($\log N_H \lesssim 22.5$ cm $^{-2}$) with no sources subject to heavy absorption ($\log N_H \gtrsim 22.5$ cm $^{-2}$). About half of these sources show no sign of variability over the course of the observation with the remaining sources either variable or extremely variable, likely flaring objects. Trends in the variation of E_{median} with kT and N_H are similar to

those found by Feigelson et al. (2005) with a slight increase in kT with E_{median} and increasing N_{H} with E_{median} above ~ 2 keV. Due to a lack of sources below $E_{\text{median}} = 2$ keV, an upper limit of $\log N_{\text{H}} \lesssim 22.2 \text{ cm}^{-2}$ is set for sources with $E_{\text{median}} < 1.8$ keV, consistent with similar programme clusters. These results show that some of the sources exhibit soft thermal spectra and have L_{X} values consistent with RDIS emission in massive stars.

2-8 keV L_{X} values were calculated for the remaining unidentified sources in the cluster and were used to produce the the 2-8 keV L_{X} against E_{median} plots, shown in Figure B.47. These plots indicate that the majority of the unidentified sources in Wd2 is lightly obscured with several heavily obscured sources, likely Class I YSOs or Class II YSOs viewed from an unfavourable angle. Most of these sources show no signs of variability with the remaining sources (including the brightest and most absorbed sources) being either variable or strongly variable. The heavily absorbed sources likely represent the high luminosity end of the heavily obscured source population.

Given the obvious diffuse emission in Figure 3.46 it was deemed unnecessary to mask and adaptively smooth the image again. Spectra were extracted from the cluster core and the total cluster regions from each of the observational datasets and simultaneously fit in *XSPEC*. The spectra with the best fit model are shown in Figure B.48 with fit results given in Table B.39. Both the total cluster and cluster core spectra are well fit with absorbed two temperature thermal plasma models. There is little variation from the core to the total cluster spectrum apart from an increase in flux suggesting similar emission processes throughout the cluster. Given the number of O-type stars in the cluster and the 3 WR stars, a cluster wind likely contributes to the diffuse emission. Assuming the model of Cantó et al. (2000, see Section 1.4.7.1) and considering the known O stars and WRs to be the dominant contributors to the cluster wind, a hot component plasma temperature of ~ 9.6 keV and a 2-8 keV $\log L_{\text{X}}$ of $\sim 31 \text{ erg s}^{-1}$ are derived meaning a cluster wind can only account for a fraction of the observed diffuse emission in the core. It is noted here that this model only includes the known high mass stars. It is likely that there are more unidentified high mass stars contributing to the cluster wind and thus this estimate represents a lower limit to the emission.

The cluster and unidentified source 2-8 keV XLFs were constructed and the unidentified XLF compared to the PMS XLF of the COUP. Given that Wd2 is older than the ONC, the COUP data were scaled according to the scaling relation of [Preibisch and Feigelson \(2005\)](#). These XLFs are shown in Figure 3.47. The total cluster XLF shows several high luminosity outliers which is unsurprising given the number of likely CWBs in the cluster. The high luminosity end of the unidentified source XLF shows a different slope to the COUP PMS population. This is likely due to the assumptions of the distance to Wd2, which as already mentioned, is still somewhat controversial. This makes scaling the COUP population to that of Wd2 somewhat difficult. However, it is clear that the stellar population of Wd2 is substantially bigger than that of the ONC. A very rough scaling of the COUP population to that of Wd2 was performed. Integrating the ‘missing’ unidentified source population region yields an estimate of the unresolved population 2-8 keV $L_X \sim 33 - 34 \text{ erg s}^{-1}$. Thus the unresolved population is likely the source of most of the hard diffuse emission in the cluster of $\log L_X \sim 33.6 \text{ erg s}^{-1}$.

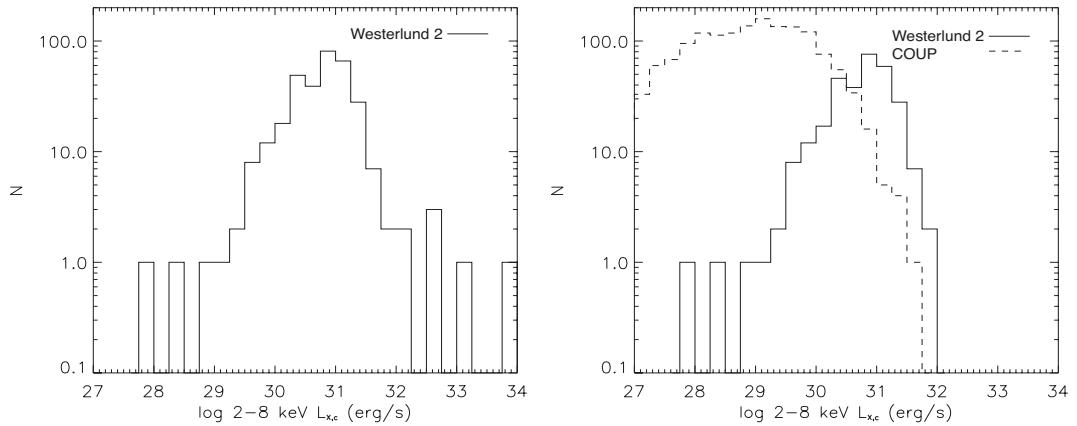


Figure 3.47: Left: Westerlund 2 total cluster 2-8 keV XLF. Right: Westerlund 2 unidentified source 2-8 keV XLF (solid line) and the COUP 2-8 keV XLF (dashed line).

Chapter 4

Diffuse Thermal X-ray Emission in the Core of Westerlund 1

Data reduction and analysis in this project were carried out with specific goals in mind, namely the characterisation of the X-ray emitting populations of the programme clusters. However, on occasion, additional research avenues presented themselves and, where time allowed, these were investigated to the full with a view to publication. In this chapter, one of those results is presented, namely the identification of hard thermal X-ray emission in the core of Westerlund 1 using *XMM-Newton* observational data, which is an adapted version of the scientific paper submitted for publication.

4.1 Introduction

Refer to Section 3.11 for a brief introduction and description of Wd1. As noted in that section, a series of four papers on the X-ray properties of Wd1 (point sources and diffuse emission) has been published which analyzes data from a joint *Chandra/XMM-Newton* observation programme (Clark et al., 2008; Munro et al., 2006a, 2007, 2006b). Munro et al. (2006b), henceforth MU06, used the *Chandra* data to perform a diffuse emission analysis and found that the emission throughout the cluster is dominated by a hard component. These authors were unable to identify the nature of this emission due to the absence of hard emission lines and discussed both thermal and non-thermal origins for the hard component. However, to date, no diffuse emission analysis had been performed using the *XMM-Newton* observational data. As yet these data have only been used in an analysis of the well known

magnetar CXOU J164710.2-455216 (Muno et al., 2006a, 2007) in the cluster. It is reasonable to assume that an analysis of the Wd1 diffuse emission using the *XMM-Newton* observation data may allow the identification of hard emission lines that are undetected by Chandra given the larger throughput and sensitivity to diffuse emission of *XMM-Newton* and the comparable exposure times of the *XMM-Newton* and *Chandra* observations.

4.2 Observations and Analysis

XMM-Newton observed Wd1 on 16 September 2006 for ~ 48 ks (Obs. ID 0404340101, Revolution 1240). The event files were processed using the *XMM-Newton* Science Analysis Software (*SAS*, Version 7.1.0) meta-tasks *emproc* and *epproc*. The data were then filtered for good grades¹ in the energy band 0.3-10 keV (the energy range at which all 3 of the EPIC instruments are most sensitive) and images for each of the three EPIC cameras, namely the PN, MOS1 and MOS2, were created. The PN and MOS2 images were found to contain single reflection artifacts which are due to X-rays from a source outside the field of view (20'-80' off-axis) reaching the sensitive area of the focal plane detectors by single reflection from the rear end of the hyperboloid component of the *XMM-Newton* mirror shells². This object was identified as the low mass X-ray binary 4U 1642-45. Images from the three EPIC instruments were combined to produce the false colour image shown in Figure 4.1.

4.2.1 Point Sources

Point source detection was performed over three standard *XMM-Newton* energy bands (0.5-2 keV, 2-4.5 keV and 4.5-7.5 keV) on the three EPIC images using the *SAS* meta-task *edetect-chain*. In total, 90 sources with a minimum maximum-likelihood detection threshold of 10 were found; 7 of these are associated with the reflection and were thus ignored. A further 8 sources were removed after visual inspection showed them likely to be spurious, leaving 75 source detections in the field. By correlation with the comprehensive *Chandra* source list in Clark et al. (2008), 4 of our *XMM-Newton* sources appear to have high mass X-ray emitting counterparts in the cluster with a further 8 having Pre-main Sequence (PMS) counterparts. One source was found to have no counterpart in the source list of Clark et al. (2008) or

¹See Section A.1 for a discussion of grade filtering.

²See http://xmm.esa.int/external/xmm_user_support/documentation/uhb/node23.html

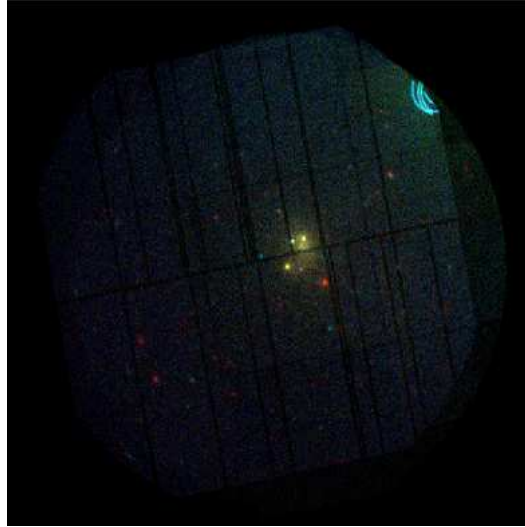


Figure 4.1: Combined MOS/PN false colour image of Westerlund 1 with red, green and blue corresponding to the 0.3-2 keV, 2-4.5 keV and 4.5-10 keV energy bands, respectively. The FOV is approximately 30' in diameter. Both the Wd1 cluster diffuse emission and several point sources are seen at the centre of the FOV. The X-ray binary 4U 1642-45 reflection is seen in the upper right of the image.

in the SIMBAD database and is likely a newly detected flaring PMS star. Table 4.1 gives our detected cluster sources and their corresponding *Chandra* designations, along with spectrally derived source parameters.

4.2.2 Diffuse Analysis

It is obvious from Figure 4.1 not only that the reflections could contaminate the diffuse emission in Wd1 but also that they are more prominent in the harder energies which are of particular interest to our analysis. To address this various analysis techniques were considered including the *XMM-Newton* Extended Source Analysis Software (*ESAS*) and ‘blank sky’ background event files but found that none could adequately account for the reflection emission. Instead it was decided to adopt the more traditional method of background extraction from regions within the FOV. By defining background regions that are as contaminated by the reflection as the cluster, the contribution of the reflection to the cluster spectra can be reduced. It was decided not to use the PN data for the diffuse emission analysis as detector gaps mask some of the Wd1 cluster core. Therefore, the following analysis is based on the MOS data only. To assess first the diffuse emission in the FOV of the MOS

Table 4.1: Westerlund 1 *XMM-Newton* Point Sources.

High Mass Stars												
No.	Chandra Source (CXO J)	Opt. ID	Sp Type	X-ray Type (a)	MOS Net Counts (b)	Model (c)	N_H (10^{22} cm^{-2})	kT (keV)	kT_2 (keV)	χ^2/ν	F_X^{unabs} ($10^{-12} \text{ erg cm}^{-2} \text{ s}^{-1}$) (d)	L_X^{unabs} ($10^{33} \text{ erg s}^{-1}$) (d)
1	164704.1-455039	W 30	<i>O9-B0.5Ia</i>	<i>CWB</i>								
	164704.1-455031	W 9	<i>sgB[e]</i>	<i>CWB</i>	2157	2T	2.5	0.7	2.9	2.170	4.37	6.59
	164705.1-455041	W 27	<i>OB SG</i>	<i>RDIS</i>								
2	164705.0-455225	WR F	<i>WC9d</i>	<i>CWB</i>	509	1T	$0.77_{0.29}^{1.26}$	$4.72_{2.93}^{12.90}$	–	0.909	0.23	0.26
3	164708.3-455045	WR A	<i>WN7b</i>	<i>CWB</i>	988	1T	$2.37_{2.05}^{2.85}$	$1.48_{1.17}^{1.78}$	–	1.967	0.89	1.34
4	164710.2-455217	–	–	<i>Magnetar</i>	1708	BB	$0.90_{0.76}^{1.07}$	$0.63_{0.60}^{0.66}$	–	1.084	0.36	0.54
Pre-Main Sequence Stars												
No.	Chandra Source (CXO J)	Opt. ID	Sp Type	X-ray Type (a)	MOS Net Counts (b)	Model (c)	N_H (10^{22} cm^{-2})	kT (keV)	kT_2 (keV)	χ^2/ν	F_X^{unabs} ($10^{-12} \text{ erg cm}^{-2} \text{ s}^{-1}$) (d)	L_X^{unabs} ($10^{33} \text{ erg s}^{-1}$) (d)
5	164640.8-454834	–	–	<i>PMS Flare</i>	34	–	–	–	–	–	–	–
6	164648.8-455307	–	–	<i>PMS Flare</i>	39	1T	$1.36_{0.55}^{2.70}$	$0.86_{0.25}^{2.71}$	–	0.959	0.04	0.05
7	–	–	–	<i>PMS Flare</i>	62	1T	$0.76_{0.50}^{1.36}$	$4.07_{2.18}^{7.08}$	–	1.992	0.01	0.02
8	164652.6-455357	–	–	<i>PMS Flare</i>	210	1T	$0.51_{0.32}^{0.84}$	$7.64_{3.22}^{--}$	–	1.057	0.06	0.09
9	164703.2-455157	–	–	<i>PMS Flare</i>	397	1T	$1.28_{0.65}^{1.96}$	$2.49_{1.69}^{4.90}$	–	0.954	0.12	0.19
10	164712.8-455435	–	–	<i>PMS Flare</i>	40	–	–	–	–	–	–	–
11	164713.6-454857	–	–	<i>PMS Flare</i>	62	–	–	–	–	–	–	–
12	164718.7-454758	–	–	<i>PMS Flare</i>	66	–	–	–	–	–	–	–
13	164720.1-455138	–	–	<i>PMS Flare</i>	19	–	–	–	–	–	–	–

In this table the *Chandra* designation, optical ID and spectral types are adopted from Clark et al. (2008) and references therein. Notice that Source 1 encompasses W 30, W 9 and W 27 which are unresolved by *XMM-Newton*. No counterpart for Source 7 was found in the analysis of Clark et al. (2008) or in the SIMBAD database.

(a) - X-ray type adopted from Clark et al. (2008). PMS = Pre-Main Sequence, CWB = Colliding Wind Binary, RDIS = Radiatively Driven Instability Shocks in stellar winds. (b) - Combined MOS net counts. PN counts omitted due to some sources lying on detector gaps. (c) - Best fit X-ray spectral model each of which was convolved with an absorbing hydrogen column. Only those sources with > 100 combined MOS and PN net counts were spectrally analysed. All spectral fits were performed in *XSPEC* 12.3.1. 1T = one temperature thermal plasma, 2T = two temperature thermal plasma, BB = black body. The spectrum of Source 2 is approximated by a 2T thermal plasma model however the true spectrum is likely described by a more complex model given it is an amalgam of several unresolved bright sources. In addition, Sources 3 and 4 are likely described by a 2T thermal plasma model however the soft components are poorly constrained and thus only the 1T approximation is given. (d) - Absorption corrected X-ray fluxes and luminosities quoted in the 0.5-8 keV energy range.

4.2 Observations and Analysis

cameras non-background subtracted image of the emission were created using *ESAS* (Version 2)¹. To exclude the point sources from the image a source mask was created to exclude not only the point sources detected in this *XMM-Newton* analysis but also those detected by [Clark et al. \(2008\)](#)², using 30" and 10" diameter exclusion regions respectively. The resulting image is shown in Figure 4.2.

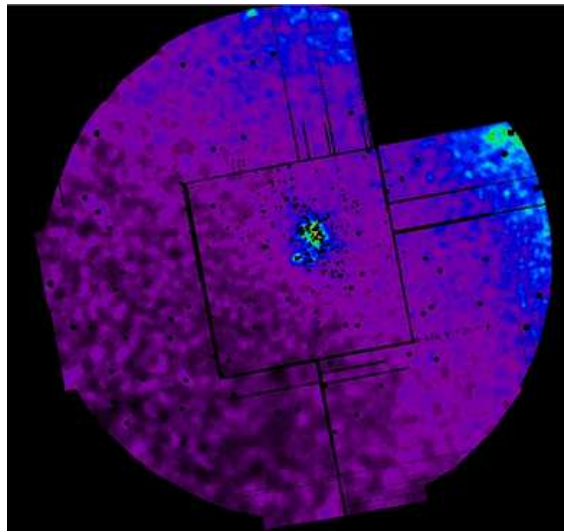


Figure 4.2: Smoothed, non-background subtracted, combined MOS1/MOS2 image with the CCDs most affected by the reflection omitted. Again the FOV is approximately 30' in diameter.

Figure 4.2 clearly shows that the diffuse emission in the FOV is dominated by the reflection. Extracting background spectra from within the FOV would mean that any contributing sources of background photons will be contained in these spectra, including the reflection itself. Hence, each contaminant was first assessed as some of these can vary across the FOV. The *ESAS* manual identifies 4 sources of background contamination. These are Solar Wind Charge Exchange (SWCE) contamination, instrumental fluorescence lines, residual soft proton contamination and the cosmic background. In the case of this observation, the SWCE and one instrumental fluorescence line can largely be ignored as they only significantly contaminate spectra below 1.5 keV (given the absorbing hydrogen column in the direction of Wd1, any emission below this energy is likely foreground emission). The second fluorescence

¹Software available at http://xmm2.esac.esa.int/external/xmm_sw_cal/\background/epic_esas.shtml

²Electronic catalogue accessed via the Vizier service

line ($E = 1.75$ keV) may contaminate the spectra especially in larger extraction regions. Soft proton contamination blights almost all observations. Periods of high contamination are screened out in the data reduction process but residual contamination can still affect the observational data. However, it is assumed that the level of contamination is constant across the FOV and hence should be contained in the backgrounds. Similarly it is assumed that the cosmic background is constant across the FOV and is also contained in the backgrounds. The final source of contamination, unique to this observation, is the 4U 1642-45 reflection. This can be compensated for by the selection of appropriate background regions that are equally contaminated as the cluster, determined using Figure 4.2.

The cluster core coordinates determined by MU06 as $\alpha_0 = 16\ 47\ 04.3$, $\delta_0 = -45\ 50\ 59$ were adopted and spectra extracted from the central 1' radius region and three annuli extending out from the core (1'-2', 2'-3.5', 3.5'-5') with the XMM-Newton and Chandra point sources masked. As any X-ray photons detected below 1.5 keV are likely foreground emission and because of the two instrumental fluorescence lines at 1.49 keV and 1.75 keV, we have restricted our spectral analysis to the 2-8 keV energy band which conforms to the standard *Chandra* hard band as used by MU06. The MOS 1 and MOS 2 spectra and ancillary files for each annulus were combined¹ and the resulting spectra were adaptively binned so that each bin has a S/N of 5. MU06 found that the cluster diffuse emission spectra are well fit with either an absorbed two-temperature thermal plasma model (the harder thermal component with sub-solar abundance to explain the lack of hard emission lines) or an absorbed thermal plasma plus power law model. Hence, the combined MOS spectra were fit in *XSPEC*² with these models. The results of both model fits for each extraction region are presented in Table 4.2. The abundance parameter of the cool thermal component in the fits was poorly constrained due to the majority of this emission falling below 1.5 keV, however it was fixed at $2 Z_\odot$ to be consistent with MU06.

The fit results are in general agreement with those of MU06. The outer annulus exhibits only a hard component adequately fit by either an absorbed thermal plasma or absorbed power law model. There is little difference between the absorbed two temperature thermal plasma and absorbed thermal plasma plus power law models

¹Following the procedure found at http://xmm.esa.int/sas/current/documentation/threads/epic_merging.shtml

²*XSPEC* Version 12.3.1 was used for all spectral fits in this analysis.

in the inner annuli with the same absence of hard emission lines found by MU06. This is somewhat surprising as, for a cluster such as Wd1 with a large, centrally located WR population, the hard diffuse emission is expected to be thermal in origin due mostly to a thermalized cluster wind (Oskinova, 2005). To assess this further MOS spectra from the inner 2' radius region were extracted, combined and adaptively binned so that each bin has a S/N of 3 to make any possible weak and narrow emission lines more obvious. The resulting combined MOS spectrum is shown in Figure 4.3.

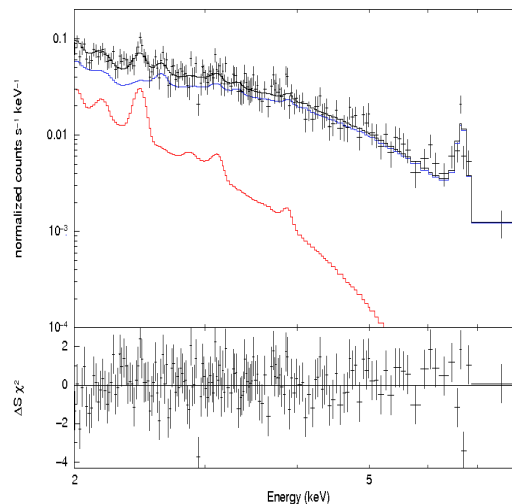


Figure 4.3: Combined MOS inner 2' spectrum binned with S/N=3 and fit with an absorbed two temperature thermal plasma model. The blue and red lines indicate the individual thermal components of the model, representing the hard and soft components respectively.

With these choices of extraction region and spectral binning, the He-like Fe 6.7 keV line, which is used as a diagnostic for thermal diffuse hard emission, is now seen in the combined MOS spectrum. A conservative estimate of the significance of this emission line was determined using the F-test probability for the addition of a 6.7 keV Gaussian line to a power law fit of the combined MOS spectrum in the 4-8 keV range (in view of an absence of other emission lines). This yields an F-test probability of 7.6×10^{-6} ($\sim 4.3\sigma$). The 2-8 keV core MOS spectra were fit

4.2 Observations and Analysis

Table 4.2: Diffuse Spectral Fits.

Original extraction region spectral fits								
Two temperature thermal plasma								
Region	N_{H} (10^{22} cm^{-2})	kT_1 (keV)	$(Z/Z_{\odot})_1$ ^a	kT_2 (keV)	$(Z/Z_{\odot})_2$	χ^2/ν	$F_{\text{X}}^{\text{unabs } b}$ ($10^{-12} \text{ erg cm}^{-2} \text{ s}^{-1}$)	$L_{\text{X}}^{\text{unabs } b}$ ($10^{33} \text{ erg s}^{-1}$)
<1'	$2.03_{1.88}^{2.19}$	$0.62_{0.49}^{0.78}$	2	$3.43_{2.73}^{4.60}$	$0.40_{0.32}^{0.51}$	0.758	0.41	0.62
1'-2'	$1.73_{1.57}^{1.88}$	$0.60_{0.46}^{0.74}$	2	$2.86_{2.46}^{3.31}$	$0.16_{0.10}^{0.35}$	1.203	0.75	1.12
2'-3.5'	$2.80_{2.57}^{3.07}$	$0.81_{0.68}^{0.93}$	2	$5.21_{3.56}^{9.66}$	$0.50_{0.32}^{0.51}$	1.111	1.16	1.75
3.5'-5' ^c	2.4	–	–	3.4	0.2	1.078	1.36	2.05
Thermal plasma plus power law								
Region	N_{H} (10^{22} cm^{-2})	kT (keV)	Z/Z_{\odot} ^a	Γ	–	χ^2/ν	$F_{\text{X}}^{\text{unabs } b}$ ($10^{-12} \text{ erg cm}^{-2} \text{ s}^{-1}$)	$L_{\text{X}}^{\text{unabs } b}$ ($10^{33} \text{ erg s}^{-1}$)
<1'	$2.05_{1.88}^{2.19}$	$0.73_{0.57}^{0.86}$	2	$2.19_{1.82}^{2.38}$	–	0.848	0.43	0.65
1'-2'	$1.81_{1.68}^{1.95}$	$0.72_{0.52}^{0.87}$	2	$2.40_{2.25}^{2.55}$	–	1.249	0.78	1.17
2'-3.5'	$2.97_{2.70}^{3.26}$	$0.83_{0.70}^{0.93}$	2	$2.00_{1.68}^{2.27}$	–	1.107	1.10	1.66
3.5'-5' ^c	2.8	–	–	2.3	–	1.034	1.65	2.49
Core spectral fit with refined binning								
Two temperature thermal plasma								
Region	N_{H} (10^{22} cm^{-2})	kT_1 (keV)	$(Z/Z_{\odot})_1$ ^a	kT_2	$(Z/Z_{\odot})_2$	χ^2/ν	$F_{\text{X}}^{\text{unabs}}$ ($10^{-12} \text{ erg cm}^{-2} \text{ s}^{-1}$)	$L_{\text{X}}^{\text{unabs } b}$ ($10^{33} \text{ erg s}^{-1}$)
<2'	$2.03_{1.88}^{2.14}$	$0.68_{0.55}^{0.80}$	2	$3.07_{2.69}^{3.67}$	$0.62_{0.40}^{0.89}$	0.971	1.71	2.56

^a $(Z/Z_{\odot})_1$ for both models is fixed at 2.

^bAbsorption corrected X-ray fluxes and luminosities quoted in the 2-8 keV energy range, consistent with the analysis of MU06.

^cIn the outermost annulus, the reflection emission becomes a significant part of the background subtracted spectrum. Since we cannot adequately account for this in *XSPEC* the spectral parameters listed above for this region are less reliable. In addition, as MU06, we find that the diffuse X-ray emission in this region of the cluster consists only of a hard component.

simultaneously in *XSPEC* with various combinations of thermal and non-thermal models and it was found that the data are best fit with an absorbed two temperature thermal plasma model as this can account for the He-like Fe 6.7 keV line and the softer emission lines below 3 keV due to He-like S and He-like Si. The results of the core two temperature thermal plasma fit are also given in Table 4.2. The fact that the line is accounted for by this model demonstrates that, at least in the inner 2' radius region, the hard component is predominantly thermal in origin. A similar treatment was applied to both the outer extraction annuli, however this failed to reveal any line emission in the hard continuum so it is still debatable as to whether thermal or non-thermal processes are responsible for the hard emission in these regions.

4.3 Discussion

4.3.1 Origin of 6.7 keV Emission Line

To confirm that the emission line at 6.7 keV is a feature of the cluster diffuse emission other potential sources for this line must be ruled out, such as point source contamination, the reflection, cosmological background and those other contributions mentioned above.

4.3.1.1 Point Source Contamination

Although exclusion regions were defined to mask the point sources it is possible that these masks did not completely exclude point source photons at the extreme edges of the wings of their PSFs. To verify that the emission line is not the result of point source contamination, combined point source spectra for those sources that lie within the 2' radius circle centered on the cluster core were extracted for each MOS camera. The resulting spectra were combined and this spectrum adaptively binned so that each bin has a S/N of 3, shown in Figure 4.4.

Inspection of the 6.7 keV region of the combined MOS spectrum in Figure 4.4 shows line emission centered at ~ 6.7 keV with a significance of 5.1σ . To assess the strength of this line in comparison to the diffuse emission line, the X-ray flux in the 6.6 keV - 6.8 keV range for the combined MOS diffuse spectrum and the combined MOS point source spectrum was determined. It was found that the combined MOS point source spectral line flux of 5.73×10^{-14} erg cm $^{-2}$ s $^{-1}$ is just over half the

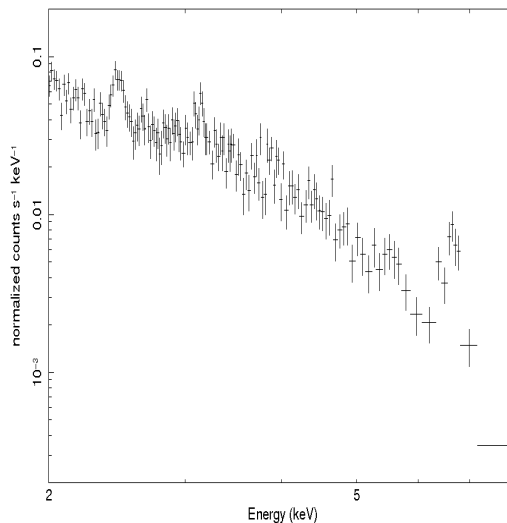


Figure 4.4: Combined MOS spectrum of sources within a 2' region centered on the cluster core.

strength of the combined MOS diffuse emission line flux of $1.02 \times 10^{-13} \text{ erg cm}^{-2} \text{ s}^{-1}$. However, the point source extraction regions occupy $\sim 25\%$ of the cluster core area which is one third of the diffuse emission extraction region. As such one third of the combined diffuse emission flux in the 6.6 keV - 6.8 keV range is likely contained in the combined point source spectral line flux, meaning the flux due to point sources only may be as low as $2.33 \times 10^{-14} \text{ erg cm}^{-2} \text{ s}^{-1}$. If the emission line in the diffuse spectrum were a result of point source contamination one would expect the line in the point source spectrum to be significantly larger than that in the diffuse spectrum given that the vast majority of these photons was in fact masked out when creating the diffuse spectrum. For this reason, point source contamination is ruled out.

4.3.1.2 Reflection

To reduce the contribution of the reflection to the diffuse spectra, background regions as much contaminated by the reflection as the cluster were selected. However, this is not a perfect solution and contamination by the reflection has to be investigated. To assess if contamination by the reflection is the source of the emission line, spectra for those regions most affected by the reflection (but without the reflection hyperbolas) were extracted and combined. A new combined MOS background spectrum was created from regions devoid of point sources on the opposite side of the FOV where the contamination from the reflection is at a minimum (i.e. - mainly

the regular background contaminants present) and subtract this from the combined MOS reflection spectrum. The resulting spectrum was again binned so that each bin has a S/N of 3, shown in Figure 4.5.

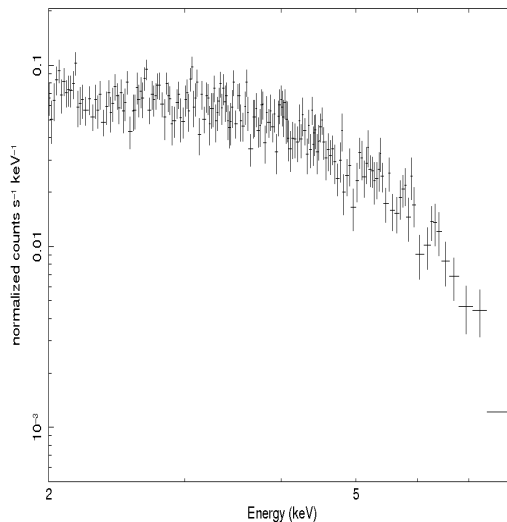


Figure 4.5: Combined MOS background subtracted reflection spectrum, extracted from those regions most contaminated by the out of FOV source.

Figure 4.5 shows no significant emission at or around 6.7 keV so we can safely assume that contamination by the reflection is not responsible for the line.

4.3.1.3 Instrumental Background

The instrumental background comprises the soft proton background, instrumental fluorescence lines and particle background. From the *ESAS* method, it is seen that the soft proton contamination is well modeled as a power law (or broken power law). Hence soft proton contamination cannot be responsible for the emission line. Similarly the instrumental fluorescence lines are modeled as Gaussian peaks at 1.49 keV and 1.75 keV and thus are not the source of the line at 6.7 keV. Moreover, the particle background contribution is simply too low to cause the emission line (Kuntz and Snowden, 2008).

4.3.1.4 Cosmic Background

When extracting the backgrounds we assume that the cosmic background emission is constant across the FOV and thus contained in the backgrounds. To assess the contribution of the cosmic background, the combined MOS background extracted for use with the reflection spectrum in Section 4.3.1.2 was utilized. The combined background spectrum was binned so that each bin contains 30 counts, shown in Figure 4.6. No significant emission lines at or around the 6.7 keV region are seen so one can assume that the diffuse emission line is not from the cosmic background.

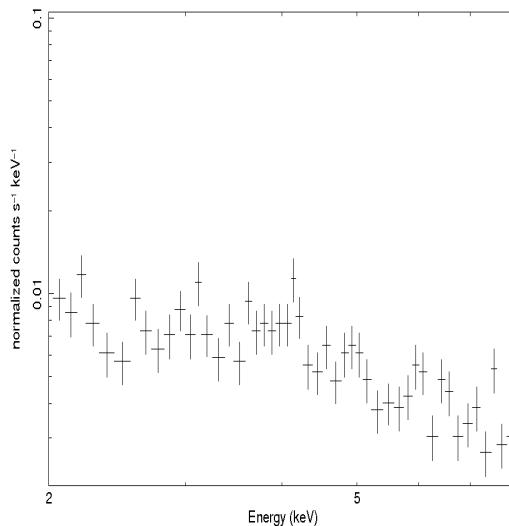


Figure 4.6: Combined MOS cosmic background spectrum, extracted from those regions least contaminated by the reflection.

4.3.2 Sources of Hard Emission

Having demonstrated that the 6.7 keV line is a feature of the cluster diffuse emission and hence that the diffuse emission within 2' of the cluster core is mostly thermal in origin, possible sources for this component are now addressed. There are three potential sources of thermal emission in the core of a cluster as large as and with the age of Wd1. These are a thermalized cluster wind, Supernova Remnants (SNRs) and unresolved PMS stars.

4.3.2.1 Cluster Wind

A cluster as large as Wd1 is expected, and is indeed found by [Clark et al. \(2005\)](#), to contain many massive stars in the cluster core. These massive stars are the source of large amounts of energy and mass being ejected into the cluster volume via stellar winds. The winds collide and thermalize, filling the cluster core volume with a hot, shocked plasma. After some time, the outflow from these thermalized winds becomes stationary and a steady state cluster wind ensues ([Cantó et al., 2000](#), and references therein). The temperature of this hot, diffuse plasma throughout the core is sufficiently high to radiate at X-ray energies and hence is potentially responsible for the diffuse hard emission in Wd1. MU06 make use of the equations of [Cantó et al. \(2000\)](#) for the central hydrogen density and temperature, namely:

$$\left(\frac{n_0}{\text{cm}^{-3}}\right) = 0.1N \left(\frac{\dot{M}}{10^{-5}M_{\odot} \text{ yr}^{-1}}\right) \left(\frac{v_w}{10^3 \text{ km s}^{-1}}\right)^{-1} \left(\frac{R_C}{\text{pc}}\right)^{-2} \quad (4.1)$$

$$\left(\frac{T_0}{\text{K}}\right) = 1.55 \times 10^7 \left(\frac{v_w}{10^3 \text{ km s}^{-1}}\right)^2 \quad (4.2)$$

where N is the number of stars contributing to the thermalized cluster wind, \dot{M} is the average mass loss rate per star, v_w is a weighted average wind velocity of the stars and R_C is the radius of the region containing the stars. To enable direct comparison of results a similar treatment as performed by MU06 was applied. In the analysis of MU06 only the WR stars are considered as the contributors to the cluster wind and from Equation 1 an emission measure ($K_{\text{EM}} = \frac{4}{3}\pi R_C^3 n_0^2$) is calculated before using a standard thermal plasma model in *XSPEC* to extract fluxes. This treatment differs slightly from that of MU06 in two ways. First, the value of R_C is set at 2 pc ($\approx 2'$ at 3.55 kpc) which is the core extraction region in the analysis above. This is an acceptable value as [Cantó et al. \(2000\)](#) state that the value of R_C needs only be approximate to the distance from the cluster centre to the outermost star, i.e. - all the stars considered to contribute to the cluster wind are inside R_C (see also Figure 4.7). Second, rather than assign typical values for \dot{M} and v_w for WRs in general, the known spectral types of the WRs in the cluster core ([Crowther et al., 2006](#)) are used along with general physical and wind properties of WRs ([Crowther, 2007](#)) to estimate the more accurate mean values of $\dot{M} = 1.4 \times 10^{-5} M_{\odot} \text{ yr}^{-1}$ and $v_w = 1320 \text{ km s}^{-1}$ for the 21 WRs within 2 pc of the cluster centre. Inputting these values into Equations 1 and 2 yields $n_0 = 0.5 \text{ cm}^{-3}$ and $kT_0 = 3.7 \text{ keV}$. K_{EM} was then calculated

and the appropriate values were fed into the APEC spectral model (Smith et al., 2001) in *XSPEC* which gives an unabsorbed X-ray luminosity (L_X^{unabs}) in the 2-8 keV energy range of $\sim 2 \times 10^{33}$ erg s $^{-1}$. Extracting the observed high temperature value from the two temperature fit above yields an L_X^{unabs} of 1.7×10^{33} erg s $^{-1}$. Hence, the predicted value is in excellent agreement with the observed value. Thus, a thermalized cluster wind can account for the hard thermal emission in the core of Wd1. This result differs from that of MU06, who found that the hard emission in the cluster core is approximately half of their predicted value. The discrepancy results mainly from the setting of $R_C = 4$ pc ($\approx 3'$ at their adopted distance of 5 kpc) in their calculations. The smaller R_C value used in this analysis reduces the emission measure and hence the derived L_X^{unabs} .

Stevens and Hartwell (2003) used the model of Cantó et al. (2000) to predict the properties of the cluster wind for some Galactic and Magellanic Cloud clusters and compared them to observation. They found that, in all cases bar one, the predicted kT_0 values are much larger than observed and that the predicted X-ray luminosities are much less than observed. The results presented here are somewhat at odds with those of Stevens & Hartwell in that the predicted values of kT_0 and L_X^{unabs} are quite close to those observed. The difference in kT_0 can be explained by the adopted v_w value. For the determination of kT_0 only the WRs in the cluster are considered (given that the early O stars have already evolved off the main sequence), which have lower wind velocities than the early O stars in the clusters studied by Stevens & Hartwell, thus keeping kT_0 down. A possible explanation for their difference in L_X^{unabs} (and to some extent also kT_0) values is that in all bar the same one cluster, Stevens & Hartwell fit the diffuse spectra with a single temperature model. This may underestimate any cool thermal component that is present in the diffuse spectra of the clusters (and the observed kT value will be an amalgam of the hot and cool component kT values). If a cool component has been underestimated, this will dramatically affect the observationally derived L_X^{unabs} given that the unabsorbed cool component will greatly add to the overall L_X^{unabs} . Since a cool thermal component is seen in Wd1 and the analysis is restricted to the harder thermal component only, our results are close to those predicted. One must be aware however that the model used in this analysis does not incorporate the thermalization efficiency and mass loading of the cluster wind described by Stevens & Hartwell. In practice, the adopted model assumes no mass loading and a thermalization efficiency of 1 (i.e. - no radiative losses in the conversion of the stellar wind energies to the cluster wind). This may

be simplistic and it is noted here that a change in either parameter would serve to increase the predicted overall X-ray luminosity (i.e. - not restricted to the hard energy band) and reduce the kT_0 value.

4.3.2.2 Supernova Remnants

SNRs emit X-rays through thermal and/or non-thermal processes. Since the hard emission in the core of Wd1 has been identified as predominantly thermal, we address only the thermal emission mechanisms (i.e. - the SNR interaction with its surroundings). In order to assess whether SNRs contribute to the hard thermal emission, the number of potential SNRs present must first be determined. Several of the previous analyses of Wd1 (MU06; Brandner et al., 2008; Clark et al., 2008, etc.) use the stellar population to extrapolate the cluster IMF to higher masses and determine that the cluster initially contained $\sim 10^2$ stars with $M > 50M_\odot$. Given the age of Wd1 we can assume that all these stars have already been lost to Supernovae (SNaE). However, apart from the magnetar, no evidence of post SN objects (SNRs, compact objects or X-ray binaries) was found in the analyses of either MU06 or Clark et al. (2008). Possible reasons for the absence of the discrete objects are beyond the scope of this analysis, instead only the potential contribution of the SNRs to the diffuse emission in the cluster core is addressed. SNRs are expected to emit X-rays when the shock front interacts with the surrounding ISM, but in the Wd1 region winds from the massive stars have cleared away the ISM so we cannot expect to observe emission from this process (MU06 and references therein). However, SNRs can also interact with the stellar winds of nearby massive stars in the cluster (Velázquez et al., 2003). Indeed, the interaction of a SNR with a single stellar wind was shown by Velázquez et al. to be X-ray bright ($L_X^{\text{unabs}} \sim 10^{34} \text{erg s}^{-1}$ in the 0.3-10 keV energy range) throughout the lifetime of the SNR ($\sim 10^4 \text{yr}$) with a star-SNR separation of ~ 10 pc. Given that in the core of Wd1 the largest possible star-SNR separation is 4 pc, any star-SNR interaction region would be expected to be even brighter than this. Furthermore, the number of interaction regions due to multiple massive stars would serve to increase the expected overall luminosity. Assuming that a star-SNR interaction region in Wd1 has a 0.3-10 keV $L_X^{\text{unabs}} = 10^{34} \text{erg s}^{-1}$ (which is undoubtedly an underestimate) and that there is a number of massive stars in the core of 20, a single SNR in the cluster would be expected to have at least a 0.3-10 keV $L_X^{\text{unabs}} \sim 10^{35} \text{erg s}^{-1}$. To compare this to the 2-8 keV L_X^{unabs} of the observed

hard component diffuse emission, WebPIMMs¹ was used to convert the observed flux from the 2-8 keV to the 0.3-10 keV energy range, assuming a thermal plasma model with our observed hard component $kT = 3.07$ keV and derive a 0.3-10 keV $L_X^{\text{unabs}} \approx 3 \times 10^{33} \text{erg s}^{-1}$. Thus, the conservative lower limit of $L_X^{\text{unabs}} \sim 10^{35} \text{erg s}^{-1}$ for a single SNR is already two orders of magnitude higher than the observed luminosity of the diffuse emission in the core. Hence, at the current epoch, there is little evidence for SNRs in the cluster and thus these are unlikely to be the cause of the diffuse emission.

4.3.2.3 Unresolved Pre-Main Sequence Stars

In their *Chandra* point source analysis, Clark et al. (2008) identified not only the X-ray emitting high mass population but also a number of PMS stars down to a limiting luminosity of $\sim 10^{31} \text{erg s}^{-1}$. These sources represent the most luminous members of the PMS population and were masked in the spectral analysis above. However, the remaining unresolved PMS population could contribute significantly to the diffuse emission in the cluster. In Wd1, only stars with $M \lesssim 3M_\odot$ have yet to evolve onto the Zero Age Main Sequence (ZAMS) (Brandner et al., 2008). The objects in the $3.2 - 1.7M_\odot$ mass range are becoming stars of spectral type A, which are not established X-ray emitters. For an estimate of the unresolved PMS stars we will assume these objects to be X-ray emitters for $M < 1.5M_\odot$, which is in line with the upper mass limit for low mass PMS stars with X-ray emission due to magnetic reconnection events adopted by Clark et al. (2008). Whereas these authors assume a ratio between high luminosity and low (unresolved) luminosity PMS X-ray emitters for Wd1 as for the Chandra Orion Ultradeep Project (COUP, Getman et al., 2005) sources, knowledge on the actual Wd1 (pre-)stellar population as given by Brandner et al. (2008) is employed here. The reason is that the procedure of Clark et al. (2008) involves propagating a high/low luminosity object ratio of 2/1614 for the COUP sources to a larger number of high luminosity Wd1 sources (viz. 45). This may however not be totally reliable due to the inherent inaccuracy of magnifying uncertainties attached to only 2 high luminosity COUP sources.

Information on the (pre-)stellar population of Wd1 is contained in Brandner et al. (2008, their Table 6). In there, the numbers of object are specified for a few annuli around the cluster centre and for several mass intervals. Observed numbers in

¹Found at heasarc.nasa.gov/Tools/w3pimms.html

the mass interval $3.4 - 30M_{\odot}$, corrected for incompleteness, are used for normalising the mass function, which has a different slope in each of the annuli for masses $M > 0.5M_{\odot}$ (as determined from their photometry), while each time having the same, shallower slope for masses in the interval $0.08 - 0.5M_{\odot}$. For the unresolved Wd1 PMS population we select the mass range $0.08 - 1.5M_{\odot}$, include objects within $2'$ from the cluster centre (in order to compare with our observed diffuse 2-8 keV X-ray luminosity for the cluster core), and require continuity for the stellar mass function from high mass ($> 0.5M_{\odot}$) to low mass ($0.08 - 0.5M_{\odot}$) objects. This yields a number of low mass PMS objects in Wd1 of nearly 44000. Each of the PMS objects is assigned an X-ray luminosity, L_X , dependent on the mass of the object, working in $0.1M_{\odot}$ intervals. The mass-dependent L_X , valid for the age of Wd1, is taken from [Flaccomio et al. \(2003\)](#), their Figure 10) and has been transformed from their 0.1-4.0 keV interval to the 2.0-8.0 keV interval used in this article, with the help of the WebPIMMS tool. The X-ray band transformation is for a Raymond-Smith model spectrum for which a characteristic energy kT is required (considering one temperature spectra for simplicity). The comparably young cluster Trumpler 16 features a median kT around 1.5 keV ([Albacete-Colombo et al., 2008](#)). However, plots of $\log L_X$ against (single) kT for COUP sources, for which much deeper data are available, suggest that for low luminosity X-ray sources the values for kT decrease, to around 1 keV. If $kT \approx 1.5$ keV is adopted for the Wd1 PMS objects, their combined 2-8 keV luminosity is $1.1 \times 10^{33} \text{erg s}^{-1}$. But, if the diffuse emission would come from unresolved, low luminosity PMS sources their typical kT could be lower. For sources with $kT \sim 1$ keV the combined 2-8 keV PMS luminosity becomes $4.6 \times 10^{32} \text{erg s}^{-1}$. In reality their 2-8 keV luminosity may be lower still if individual PMS objects have strong circumstellar absorption, if the lower X-ray luminosities found for Weak line T Tauri Stars - compared to Classical T Tauri Stars - are taken into account, and if not all inferred PMS objects would actually be X-ray sources. Thus the PMS object X-ray luminosity of $L_X \lesssim 10^{33} \text{erg s}^{-1}$ is expected, which is less than half of the observed $2.56 \times 10^{33} \text{erg s}^{-1}$ for the total diffuse 2-8 keV emission.

4.4 Conclusions

The above analysis and discussion of the until now unexploited *XMM-Newton* diffuse emission data for Wd1 have demonstrated a Fe 6.7 keV emission line, indicating that the hard X-ray component in the inner $2'$ radius region of the cluster is predominantly thermal in origin. The most likely explanation for this diffuse component is

a thermalized cluster wind. An estimated value for the 2-8 keV X-ray luminosity produced by a cluster wind in Wd1 ($2 \times 10^{33} \text{erg s}^{-1}$) is close to the observationally determined value for this luminosity ($1.7 \times 10^{33} \text{erg s}^{-1}$). The conclusion that the cluster wind is the likely cause of the diffuse emission is also in line with the model predictions of [Oskinova \(2005\)](#).

We note further that the morphology of the Wd1 diffuse X-ray emission (see [Figure 4.7](#)) resembles the distribution of the massive stars in the cluster, in particular in showing a noticeable extension to the SE. When the less massive stars are considered, such as those down to $0.8M_{\odot}$ ([Brandner et al. 2008](#); see also their [Figure 1](#)), the cluster shows a smoother, roughly N-S elongated distribution. In addition, the radial dependence of the mass distribution determined by [Brandner et al. \(2008\)](#) decreases steeper than the radial distribution of the diffuse X-ray emission. These qualitative considerations are not in support of a stellar origin for the diffuse emission.

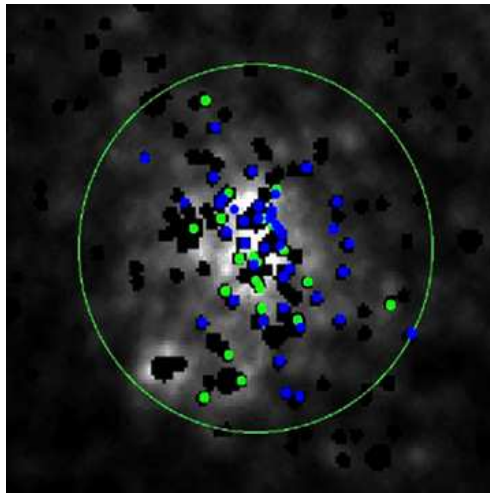


Figure 4.7: Distribution of massive stars in the cluster core in relation to the diffuse emission. Wolf-Rayets are indicated by the filled green circles whereas main sequence and evolved OB stars are indicated by filled blue circles. The large circle indicates the 2'' core radius and the black areas indicate areas where point sources were masked. It is clear that the diffuse emission resembles the distribution of the massive stars in the cluster core.

While the PMS objects are less likely as the main cause of the Wd1 diffuse emission, they could nevertheless still make a contribution to the diffuse component.

Although based on a somewhat different analysis, also [Muno et al. \(2006b\)](#) estimate that $\lesssim 30\%$ of the diffuse component could be attributed to PMS objects. For future studies it will be important to establish what contribution the PMS objects could make to the X-ray emission of young star clusters, as dependent on typical X-ray luminosity levels, circumstellar absorption and incidence of X-ray emission among the PMS objects, which currently is not well determined.

Chapter 5

Results

Chapter 3 described the characterisation of the X-ray emitting populations of the young Galactic star clusters selected for study in this project. In the forthcoming section I will describe general results from this process, in particular with regard to cluster sub-populations. Following this I will present the results of the project with respect to the goals described in Section 1.3, namely investigation of the model predictions of Oskinova (2005) across the range of cluster size and ages and testing the universality of the IMF using the XLFs of the clusters.

5.1 General Results of the Sub-Populations

5.1.1 Massive Stars

Overall, some 233 massive stars with spectral type earlier than B3 were detected in the clusters. These sources constitute individual massive OB stars emitting via RDIS and/or MCWS emission mechanisms, WRs, LBVs, CWBs as well as optical double/multiple systems. In this section I will describe the general results from this sample, focussing on those sources for which were bright enough to be spectrally fit in *XSPEC* (~ 140 sources). Prior to discussing each individual sub-population, we can first create the 0.5-8 keV and 2-8 keV L_X/L_{bol} diagrams for the entire sample of high mass stars and systems. L_{bol} values are assigned to the various spectral types using the calibrations of Martins et al. (2005) for O stars, Crowther (2007) for WRs and Kaler (1997) for the B stars. The resulting L_X/L_{bol} diagrams are shown in Figure 5.1.

5.1 General Results of the Sub-Populations

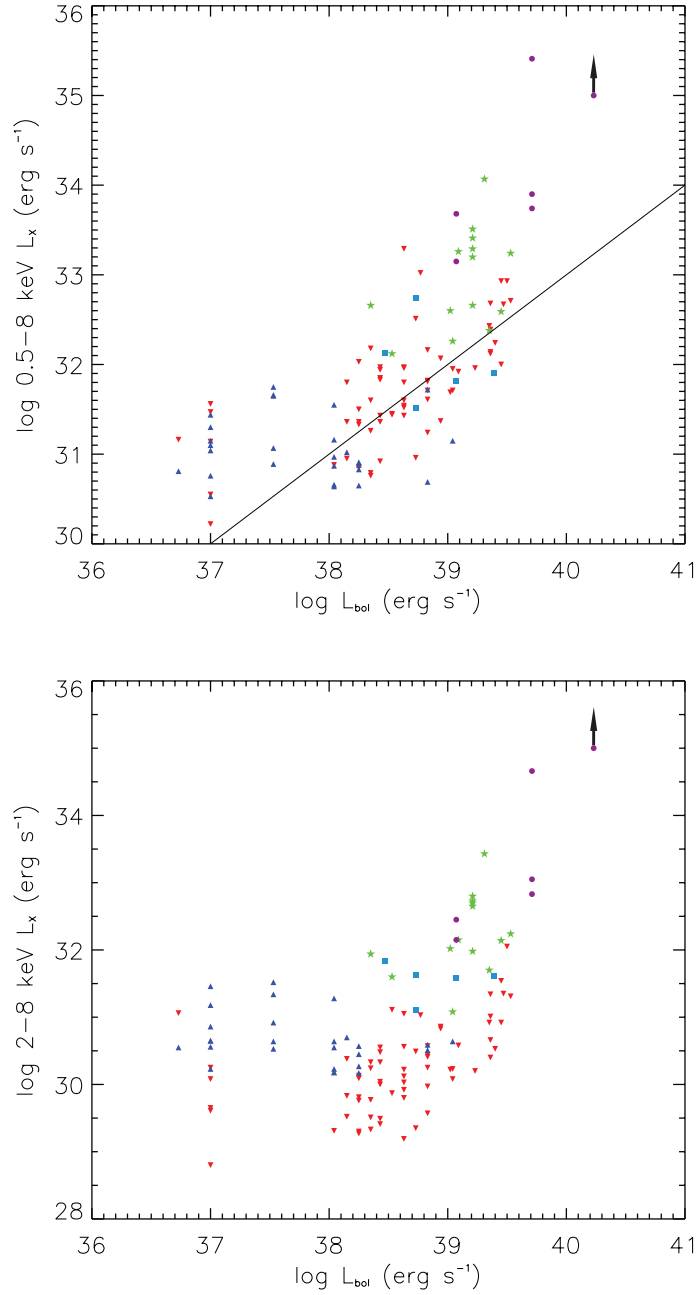


Figure 5.1: 0.5-8 keV L_X/L_{bol} diagram (top) and 2-8 keV L_X/L_{bol} diagram (bottom).

The various symbols represent the various emission types. Red inverted triangles represent the RDIS emitters, blue triangles the MCWS emitters, light blue square the WRs, green stars the O star CWBs and the purple circles the WR/LBV CWBs. The black line in the 0.5-8 keV L_X/L_{bol} diagram indicates the canonical $L_X/L_{bol} = 10^{-7}$ relation for stars emitting via shocks in their stellar winds. The arrow on the bright source η Carinae indicates a lower limit to the X-ray luminosity.

5.1 General Results of the Sub-Populations

The RDIS emitters agree well with the canonical $L_X/L_{bol} = 10^{-7}$ relation in the 0.5-8 keV L_X/L_{bol} diagram. Interestingly, a separate L_X/L_{bol} relation is evident for the CWBs in each L_X/L_{bol} diagram. These relations are investigated further in the following sections.

5.1.1.1 Radiatively Driven Instability Shock Emitters

Those sources with spectral parameters and derived luminosities consistent with RDIS emission were extracted from the sample of massive star detections. Table 5.1 offers general parameters of these sources, separated by spectral type, which are visualized in Figures 5.2 and 5.3. From Figure 5.2, there is no obvious variation in kT with spectral type with the derived values being roughly constant across the mass spectrum. A decrease in L_X values is seen moving from early O into the later O and early B type stars, which is to be expected given these lower mass stars have weaker winds. Using Figure 5.1, the actual L_X/L_{bol} ratio for the total and hard L_X bands were determined to be $\sim -6.85(\pm 0.54)$ and $\sim -8.33(\pm 0.64)$ respectively, consistent with estimates from other studies. For example, Nazé (2009) use the 2XMMi Serendipitous Source Catalogue to derive these L_X/L_{bol} relations for the catalogued massive stars and the results presented here are consistent with those of this less deep survey analysis.

5.1 General Results of the Sub-Populations

Table 5.1: RDIS X-ray Emitting Properties of the Various Spectral Types

Sp. Type	No. of Sources	kT (keV)	$\log L_{X_{h,c}}$ (erg s ⁻¹)	$\log L_{X_{t,c}}$ (erg s ⁻¹)
Class I				
O3I	1	0.61 (±0.06)	31.31(-)	32.71(-)
O3.5I	1	0.98 (±0.58)	32.05(-)	32.93(-)
O4I	1	0.65 (±0.05)	31.35(-)	32.67(-)
O5I	1	0.48 (±0.10)	30.53(-)	32.24(-)
Class III				
O3III	2	0.71 (±0.46)	31.23 (±0.44)	32.47 (±0.66)
O4III	1	0.64 (±0.05)	30.92(-)	32.43(-)
O6III	1	0.64 (±0.08)	30.58(-)	31.92(-)
O6.5III	1	0.55 (±0.20)	30.22(-)	31.69(-)
O8.5III	1	0.46 (±0.21)	31.03(-)	32.82(-)
O9.7III	1	0.43 (±0.16)	28.96(-)	31.04(-)
Class V				
O3V	4	0.58 (±0.14)	30.85(±0.41)	32.33(±0.26)
O3.5V	1	0.52 (±0.18)	30.2(-)	31.96(-)
O5V	2	0.5 (±0.11)	30.11(±0.11)	31.83(±0.17)
O5.5V	3	0.71 (±0.78)	30.85(±0.02)	31.72(±0.5)
O6V	7	0.6 (±0.15)	30.24(±0.35)	31.74(±0.28)
O6.5V	2	0.46 (±0.15)	29.92(±0.81)	31.74(±1.1)
O7V	8	0.51 (±0.17)	30.11(±0.55)	31.89(±0.6)
O7.5	2	0.59 (±0.06)	30.49(±0.88)	31.45(±0.01)
O8V	7	0.53 (±0.24)	30.04(±0.45)	31.61(±0.39)
O8.5V	5	0.59 (±0.24)	29.84(±0.44)	31.32(±0.59)
O9V	6	0.56 (±0.07)	29.73(±0.37)	31.32(±0.44)
O9.5V	3	0.53 (±0.45)	29.91(±0.44)	31.37(±0.43)
B0V	1	0.64 (±0.28)	29.31(-)	30.88(-)
B2V	3	0.64 (±1.57)	29.57(±0.73)	31.08(±0.75)
Transitional				
O5.5V-III	2	0.46 (±0.14)	30.77(±0.49)	32.76(±0.38)
O6V-III	1	0.88 (±0.23)	31.09(-)	32.18(-)

5.1.1.2 Magnetically Confined Wind Shock Emitters

One result from the analysis of the programme clusters is that the majority of the detected early B-type stars seem to be MCWS emitters. Out of the 26 stars with spectral type B0-B3, 19 of these, as well as several late O-type stars, have

5.1 General Results of the Sub-Populations

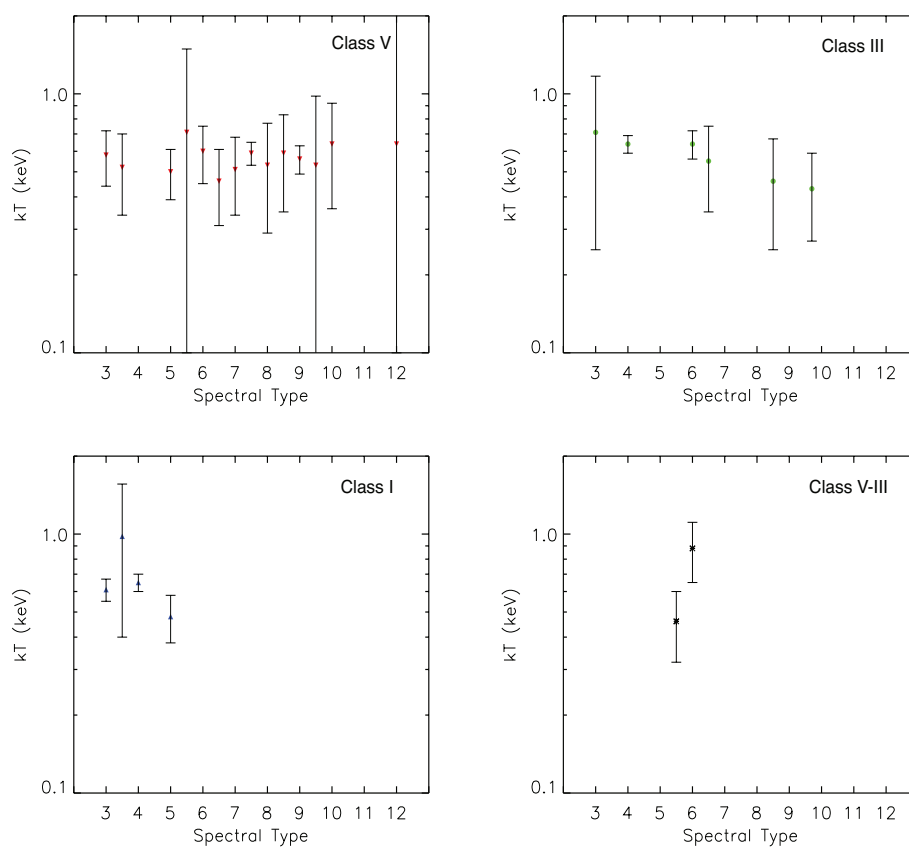


Figure 5.2: Plots of derived kT values for the various spectral types and luminosity classes, where spectral type 3 corresponds to O3, 4 to O4, 10 to B0, etc., emitting via RDIS.

5.1 General Results of the Sub-Populations

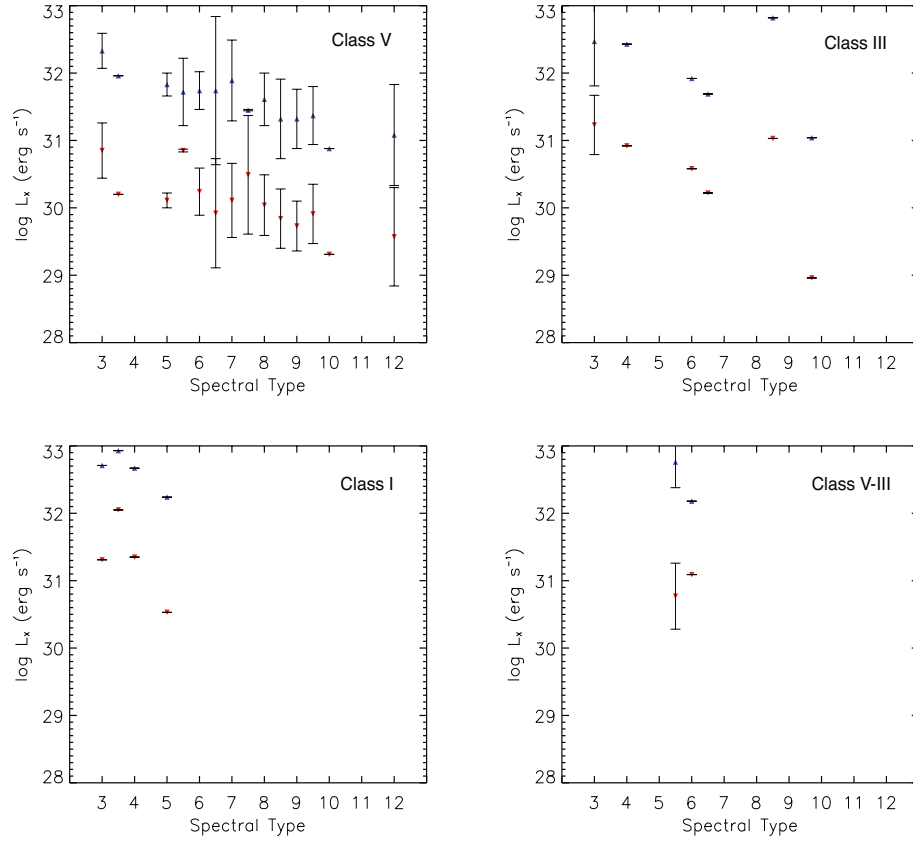


Figure 5.3: Plots of derived L_X values for the various spectral types and luminosity classes, where spectral type 3 corresponds to O3, 4 to O4, 10 to B0, etc., emitting via RDIS. The blue triangles represent the derived total band 0.5-8 keV L_X , whereas the red inverted triangles represent the hard band 2-8 keV L_X . Points without errors refer to spectral bins containing only one source.

5.1 General Results of the Sub-Populations

hard derived thermal plasma temperatures consistent with this emission mechanism. MCWS emission is regularly mentioned in cluster analyses from the literature as being responsible for relatively low luminosity hard sources and thus, are quite common. Detailed analyses of these sources are normally performed through high resolution X-ray spectroscopy and thus restricted to nearby objects. [Schulz et al. \(2003\)](#) suggest that OB stars likely retain some magnetic field when entering the main sequence which is lost as the star ages. If this is the case, it is likely that many of the late O and early B stars in the youngest programme clusters do indeed have a magnetic field which is responsible for the observed emission. These authors analyze three very young massive stars of the Orion trapezium, two B0.5V stars and one O6.5V star, and determine that a MCWS is responsible for the observed X-ray emission in all three cases, ruling out other possibilities such as unresolved PMS companions. All apart from 4 of the apparent MCWS emitting stars in the programme cluster analyses above are located in very young clusters with ages $\lesssim 1.5$ Myr. This suggests that the MCWS mechanism does indeed play an important role in X-ray emission from the youngest OB stars in the sample. [Nazé \(2009\)](#) show that many of the early B stars in the 2XMMi Serendipitous Source Catalogue require moderately hard thermal components to achieve acceptable spectral fits. This author also infers the presence of magnetic phenomena to explain these results however, the age estimates for the stars are not given and so it is unclear whether these stars are young or not. As such this analysis represents one of the first correlations of the frequency of MCWS mechanism in OB stars of known age. The L_X/L_{bol} relation for the MCWS sources shows relatively little correlation. The observed L_X values are dispersed across a wide range of L_{bol} values. Because of this, no L_X/L_{bol} correlation is derived.

5.1.2 Colliding Wind Binaries

All of the detected CWBs are shown in Table [5.2](#). These sources are separated into two categories, those CWBs where the primary is an O star and those where the primary is a WR or LBV (I also include the unusual sgB[e] source W9 in this category). Also included are the two candidate CWBs detected in NGC 3603, which we will call NGC 3603 U1 and U2, for which no spectral type has been assigned to the primary but whose X-ray spectra and L_X values are consistent with other detected CWBs in the programme clusters. A dedicated study of these sources at other wavelengths is certainly warranted as, particularly for NGC 3603 U2, one of the

5.1 General Results of the Sub-Populations

stars is very likely a WR given its derived luminosity is comparable to known WR CWBs. It is difficult to compare CWB systems as, not only will the spectral types of the component stars affect the spectral parameters, but binary system parameters such as their separation, and observational issues, such as the viewing angle, can also have an effect. However, both the 0.5-8 keV and 2-8 keV L_X/L_{bol} diagrams (see Figure 5.1) indicate some correlation between the bolometric luminosity of the primary and the observed X-ray luminosity. This is a results also in various surveys of O stars populations (see Nazé, 2009; Sana et al., 2006, for example). The reasons for this observed correlation are unclear but Nazé (2009) suggest that radiative inhibition, where the radiation of one component decelerates the wind originating in its companion is responsible. Using the Figure 5.1, values of $-5.99(\pm 0.63)$ and $-6.77(\pm 0.64)$ for the 0.5-8 keV and 2-8 keV energy bands respectively are derived for the L_X/L_{bol} relation of the CWB sample, approximately consistent with that of Nazé (2009) who utilize the less deep survey data for this derivation.¹

¹These estimates omit η Carinae, due to uncertain L_X values, and W9 as no L_{bol} value could be found for this unusual source.

5.1 General Results of the Sub-Populations

Table 5.2: Detected Colliding Wind Binaries

O Star CWBs							
Name	Sp. Type	Counts	N_{H} (cm^{-2})	kT (keV)	kT_2 (keV)	$\log L_{X_{h,c}}$ (erg s^{-1})	$\log L_{X_{t,c}}$ (erg s^{-1})
HD 93129 A	O2If*	4421	$0.81^{0.87}_{0.74}$	$0.58^{0.61}_{0.55}$	$2.46^{2.78}_{2.18}$	32.24	33.24
Sh 22	O3III(f)	238	$0.45^{0.69}_{0.29}$	$1.89^{2.42}_{1.49}$	—	32.14	32.59
HD 15558	O4III(f)	2904	$0.32^{0.37}_{0.28}$	$1.24^{1.29}_{1.19}$	—	31.70	32.38
Sh 47	O4V	426	$0.99^{1.39}_{0.78}$	$1.38^{1.64}_{1.08}$	—	32.80	33.41
CEN 1b	O4V	11781	$2.3^{2.39}_{2.21}$	$0.93^{1.05}_{0.8}$	$3.05^{3.39}_{2.65}$	32.70	33.29
CEN 1a	O4V	12323	$1.94^{2.02}_{1.85}$	$0.9^{0.99}_{0.79}$	$5.2^{5.58}_{4.83}$	32.65	33.20
MSP 183	O4V	2110	$1.48^{1.8}_{1.21}$	$0.38^{0.59}_{0.24}$	$3.06^{3.62}_{2.64}$	32.73	33.51
MSP 188	O4V-III	1413	$1.23^{1.43}_{0.95}$	$0.65^{0.85}_{0.5}$	$2.8^{2.96}_{2.02}$	32.17	33.02
HD 242908	O4V((f))	4976	$0.21^{0.25}_{0.16}$	$0.6^{0.64}_{0.57}$	$6.17^{3.55}_{2.13}$	31.98	32.66
CEN 2	O5V	1866	$0.95^{1.06}_{0.79}$	$0.61^{0.67}_{0.55}$	$3.78^{9.52}_{2.2}$	31.08	32.26
VI CYG 8A	O6If + O5.5III(f)	38195	$1.18^{1.33}_{1.22}$	$0.72^{0.75}_{0.63}$	$2.07^{2.13}_{2.01}$	33.43	34.07
MSP 167	O6III	777	$1.92^{2.14}_{1.69}$	$0.54^{0.61}_{0.44}$	$2.8^{5.14}_{2.23}$	32.15	33.26
Sh 49	O7.5V	52	$1.08^{2.22}_{0.47}$	$1.59^{3.07}_{0.86}$	—	31.60	32.12
MJ 496	O8.5V	1816	$0.91^{1.07}_{0.68}$	$0.74^{0.85}_{0.62}$	$2.04^{2.38}_{1.78}$	31.94	32.66
W 30a	O9-B0.5Ia	477	$2.51^{3.18}_{2.12}$	$1.42^{1.72}_{1.05}$	—	32.02	32.60
WR/LBV CWBs							
Name	Sp. Type	Counts	N_{H} (cm^{-2})	kT (keV)	kT_2 (keV)	$\log L_{X_{h,c}}$ (erg s^{-1})	$\log L_{X_{t,c}}$ (erg s^{-1})
NGC3603 C	WN6+abs	7320	$1.34^{1.43}_{1.24}$	$0.66^{0.8}_{0.57}$	$1.85^{2.09}_{1.72}$	34.66	35.41
η Car	LBV	29603	—	—	—	> 35.00	> 35.00
W 9	sgB[e]	394	$4.28^{5.5}_{3.72}$	$0.71^{0.89}_{0.45}$	64	32.35	33.59
WR A	WN7b	642	$3.53^{4.38}_{3.81}$	$0.28^{0.34}_{0.23}$	$3.68^{5.69}_{2.77}$	32.45	33.68
WR B	WN7o	228	$4.65^{5.4}_{2.98}$	$0.5^{1.54}_{0.13}$	$2.87^{3.17}_{0.17}$	32.15	33.15
WR 20b	WN6ha	1504	$4.02^{4.9}_{3.37}$	$0.38^{0.5}_{0.28}$	$5.34^{7.94}_{3.77}$	32.83	33.74
WR 20a	WN6ha+WN6ha	4123	$2.33^{2.56}_{2.16}$	$0.42^{0.49}_{0.33}$	$2.76^{3.16}_{3.12}$	33.05	33.90
WR F	WC9d	99	4.19	3.26	—	31.84	32.13
Candidate CWBs							
Name	Sp. Type	Counts	N_{H} (cm^{-2})	kT (keV)	kT_2 (keV)	$\log L_{X_{h,c}}$ (erg s^{-1})	$\log L_{X_{t,c}}$ (erg s^{-1})
NGC 3603 U1	—	892	$1.23^{1.43}_{1.04}$	$2.09^{2.57}_{1.78}$	—	31.75	32.55
NGC 3603 U2	—	3880	$1.96^{2.10}_{1.81}$	$0.71^{0.84}_{0.56}$	$4.97^{7.24}_{3.99}$	32.92	34.53

5.1.3 PMS Stars

Overall, there is quite a large sample of PMS stars in the programme clusters. Though the majority have too few photon counts to derive spectral parameters, there are still a great number (~ 1000) for which such an analysis can be performed.

These data are first used to confirm the relation from the existing analysis of a large PMS population, that of the COUP (Feigelson et al., 2005), which shows the relation between the absorbing hydrogen column density (N_{H}) and the median detected photon energy (E_{median}) above a certain threshold. For the brightest PMS

5.1 General Results of the Sub-Populations

stars in the sample, their spectrally derived N_{H} values were plotted against their observed E_{median} , shown in Figure 5.4, and is consistent with Figure 8 of Feigelson et al. (2005) which contains only one stellar population. The plot shown in Figure 5.4 contains data for several stellar populations and thus suggests that this relation holds across all clusters of various age and line of sight absorption.

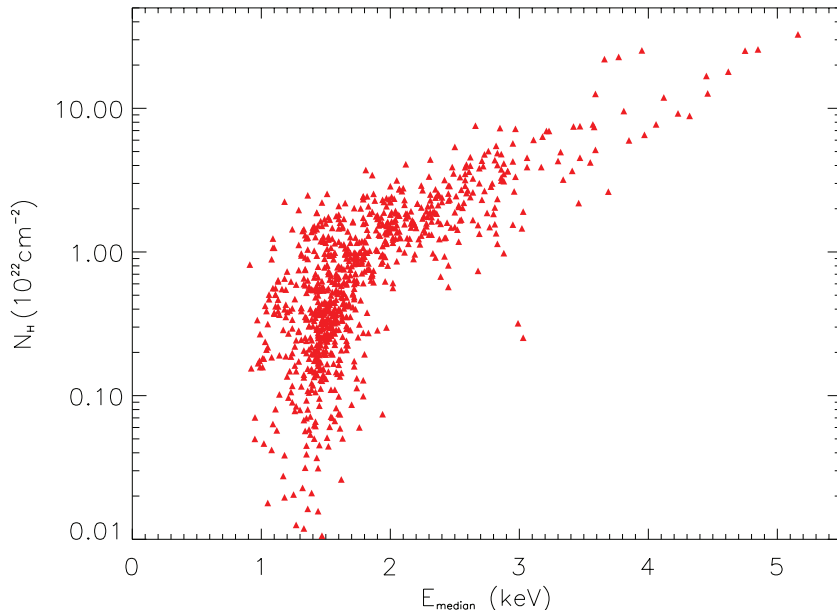


Figure 5.4: Plots of spectrally derived N_{H} against E_{median} for all of the PMS stars in the programme clusters with > 50 counts.

The variation in the properties of the programme cluster PMS populations is now investigated using the median cluster E_{median} and L_{X} values of their PMS populations. These values are calculated for the entire population and the quiescent populations in order to inspect the effects the flaring population has on the derived overall values. These quantities are plotted against the age of each cluster in Figure 5.5.

The first readily noticeable feature of the plots is that in most clusters, the inclusion of the variable sources in the cluster values has only a minor effect on the derived 2-8 keV L_{X} values. By far the most affected is Wd1 where the separation in L_{X} is an order of magnitude. This is due to a low number of detected sources and the fact that almost all of the brighter sources in the cluster showed signs of variability. The overall trend of a reduction of median L_{X} with age of the clusters is observed. This is to be expected given that the X-ray luminosity of PMS stars

5.1 General Results of the Sub-Populations

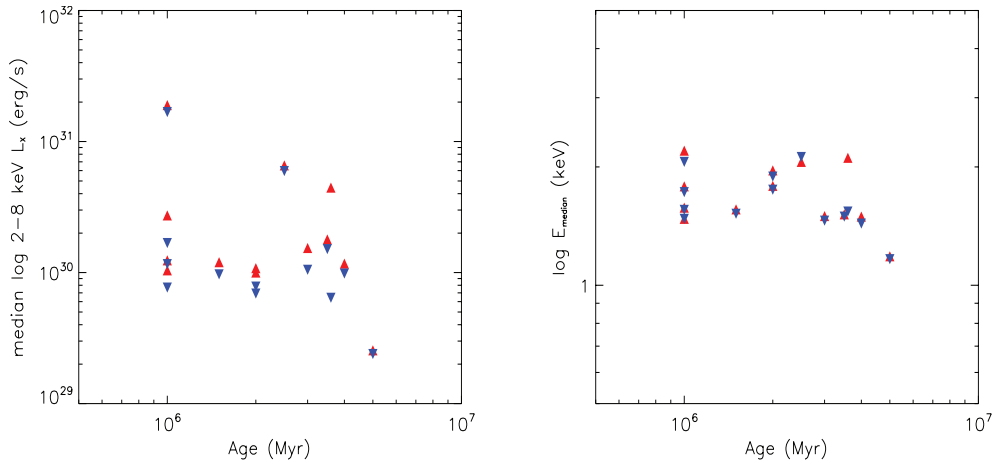


Figure 5.5: Left: Plots of median 2-8 keV L_X for all of the PMS stars (red) and quiescent PMS stars (blue) against the age of the programme clusters. Right: Plots of median E_{median} for all of the PMS stars (red) and quiescent PMS stars (blue) against the age of the programme clusters.

is found to decay following the relation of [Preibisch and Feigelson \(2005\)](#). There is a very slight decrease in observed median E_{median} with cluster age. It must be noted however that the E_{median} value is linked to the N_{H} value in the direction of the sources, though a trend to higher E_{median} with increasing plasma temperature is observed by [Feigelson et al. \(2005\)](#). As such, it is likely that there is some reduction in source kT values as the stars age. This can be explored further by considering only the sources bright enough for a spectral analysis. The plots in Figure 5.5 are recreated, this time with median spectrally derived L_X and kT values against the cluster age, shown in Figure 5.6.

The left panel of Figure 5.6 shows that in general, the brightest PMS sources in the programme clusters are of similar luminosity. The main exception is the low L_X NGC 2362 data point, likely due to the relatively old age and thus the reduced L_X of its PMS stars. In the median kT plot, there is a definite trend toward lower kT with age. This is likely due to a decreasing number of accretion disks in the PMS population as the clusters age. In Section 1.4.5, the evolution of a YSO is described. As these objects age their circumstellar disks are accreted or evaporated, leading to a reduction in the material available for the X-ray emitting mechanism and a reduction of the star-disk magnetic interaction. This may result in lower shocked plasma temperatures than in younger stars, observed as a reduction in derived kT .

5.2 Evolution of X-ray Emission in the Clusters

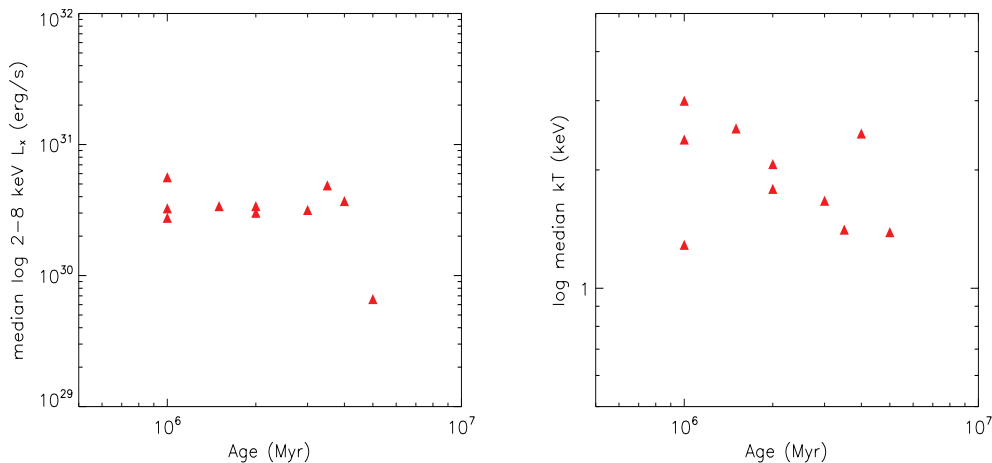


Figure 5.6: Left: Plots of median 2-8 keV L_X of the brightest PMS stars against age of the programme clusters. Right: Plots of median kT values against age of the programme clusters. The NGC 3603, Wd1 and Wd2 data points are omitted here due to several of their sources likely being OB stars.

If indeed this is the case, the trend in Figure 5.6 may be used to infer the cluster age from an X-ray analysis of the bright PMS population of a cluster.

5.2 Evolution of X-ray Emission in the Clusters

Oskinova (2005) used the cluster wind model of Stevens and Hartwell (2003) together with models of the stellar population to simulate the evolution of X-ray emission in a cluster, and compare the results to observations. One of the main conclusions of the analysis was that in massive clusters younger than 2 Myr, the X-ray luminosity of the cluster wind is low and the observed diffuse emission is dominated by an unresolved PMS population. At ages above 2 Myr the massive stars enter the evolved WR phase at which point their fast, dense winds increase the mass and energy input to the cluster wind, driving up its luminosity. The wind begins to dominate the unresolved PMS population at this stage. Following the cluster analyses of Chapter 3 we have, not only observationally derived X-ray luminosities for each of the programme clusters, but also quantitative estimates of the unresolved PMS contribution to this emission and theoretical estimates of the contribution due to a cluster wind. As such, this conclusion of Oskinova (2005) can be compared to observations to determine whether the model holds to clusters across a range of masses and ages.

5.2 Evolution of X-ray Emission in the Clusters

The results of the diffuse emission analyses are, for convenience, presented in Table 5.3. During the analysis of some of the programme clusters it was obvious that a cluster wind was contributing very little to the observed diffuse emission and thus estimates of a cluster wind were not derived. For the purposes of this analysis (and completeness), these small values were nevertheless calculated and are included in Table 5.3.

Table 5.3: Properties of the Diffuse X-ray Emission of the Programme Clusters

Cluster	Age (Myr)	Observed log 2-8 keV L_X (erg s ⁻¹)	log 2-8 keV L_{Xwind} (erg s ⁻¹)	log 2-8 keV L_{Xpms} (erg s ⁻¹)
Bica 1	2	32.2	30.8	32.3
Bica 2	2	32.1	31.5	31.8
IC 1590	4	31.3	27.8	32.0
IC 1805	1	32.0	29.8	32.2
NGC 1893	3	32.0	28.5	32.7
NGC 2362	5	30.6	28.0	30.8
NGC 3603	1	34.2	32.0	34.0
NGC 6611	2	33.1	29.8	32.9
NGC 6618	1	33.2	30.2	33.0
Tr 14	1	33.0	30.9	33.0
Tr 16	4	33.4	33.7	32.9
Wes 1	4	34.2	34.3	33.0
Wes 2	3	33.6	31.1	33.0-34.0

I define here the parameter X_r , the ratio of the X-ray luminosity due to the cluster wind to that of the unresolved PMS population, given as:

$$X_r = \frac{L_{Xwind}}{L_{Xpms}} \quad (5.1)$$

so that low values of X_r indicate that an unresolved PMS population is the dominant contributor to the diffuse emission. This parameter allows us to assess the interplay between the cluster wind and the unresolved PMS sources across the various mass and age ranges of the programme clusters. The X_r values for each of the clusters are plotted against cluster age, shown in Figure 5.7.

The predictions of [Oskinova \(2005\)](#) are largely confirmed for the clusters with rich O star populations. In IC 1805, NGC 3603, NGC 6611, NGC 6618 and Tr 14 which are all younger than 2 Myr, the unresolved PMS population is the dominant

5.2 Evolution of X-ray Emission in the Clusters

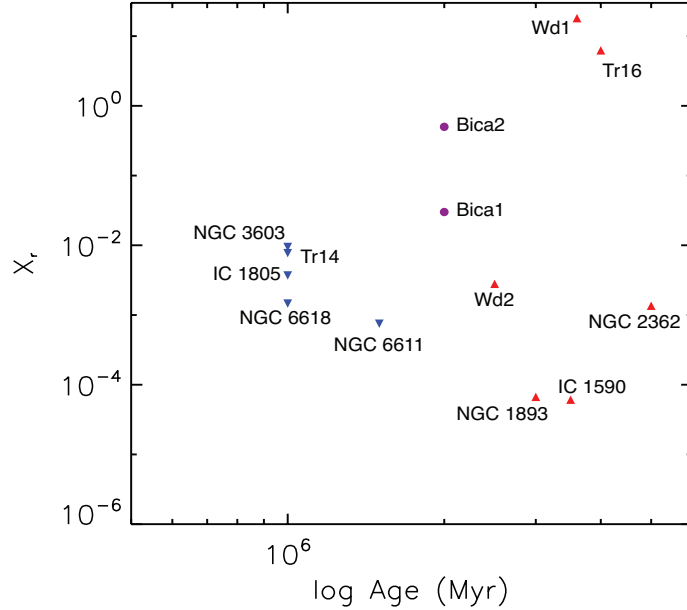


Figure 5.7: Plot of the cluster X_r values against age. Cluster names are marked. The blue inverted triangles indicate ages below the 2 Myr threshold, red triangles > 2 Myr and purple circles = 2 Myr.

contributor to the observed diffuse emission by 2-3 orders of magnitude. Bica 1 and Bica 2, which are on the 2 Myr threshold, have an increased contribution from a cluster wind. As well as main-sequence O stars, both of these clusters harbour early O supergiants which inject more mass into the cluster wind. Though these clusters are not very massive, they are physically small, meaning the contributing stars are confined in a small region, which serves to increase the wind L_X . The diffuse emission is dominated by the cluster wind in Wd1 and Tr 16 (both of which are much older than 2 Myr) due to the large amount of WRs in Wd1 and primarily η Carinae in Tr 16. The location of Wd2 is somewhat strange. One would expect the cluster wind to contribute much more to the diffuse emission in this cluster, particularly as it hosts several evolved O stars including 3 WRs. This is likely due to the uncertain estimate of the unresolved unidentified population contribution (see Section 3.12.1). The Wd2 data point in Figure 5.7 was determined using the midpoint of the 10^{33-34} erg s $^{-1}$ luminosity range determined for this clusters unresolved population. Assuming the lower end of this range results in $X_r \sim 10^{-1.9}$, which moves the Wd2 data point into a region consistent with the trend seen for the other rich clusters. The diffuse emission in the remaining clusters (i.e. IC 1590, NGC 1893 and NGC 2362) is dominated by an unresolved PMS population. These clusters have much

5.2 Evolution of X-ray Emission in the Clusters

less rich O star populations than the other programme clusters, consisting primarily of late O stars which have relatively weak winds and take longer to evolve.

The X_r parameter has proved to be a useful tool in assessing the model predictions of [Oskinova \(2005\)](#) but can it be used to predict properties of the diffuse emission in clusters itself? If we wish to achieve this we must compare X_r to a measure of the contribution of either the cluster wind or the unresolved PMS population. Determining the unresolved PMS contribution is a somewhat long affair as has been demonstrated in this thesis. However, [Stevens and Hartwell \(2003\)](#) define the so called cluster wind scaling parameter (denoted X_{cl}) which is proportional to the X-ray luminosity of the cluster wind. X_{cl} is given as:

$$X_{cl} = \frac{\dot{M}_*^2}{R_c \bar{V}_*} \quad (5.2)$$

where \dot{M}_* is the total stellar mass wind injection rate, R_c is the cluster radius, and \bar{V}_* is the mean weighted terminal velocity for the stellar winds. Following [Stevens and Hartwell \(2003\)](#), X_{cl} is calculated using the natural units with \dot{M}_* in $M_\odot \text{ yr}^{-1}$, R_c in pc and \bar{V}_* in km s^{-1} . Thus, X_{cl} can be calculated using only the physical parameters of the massive stars and the cluster radius. X_{cl} was calculated for each cluster and plotted against X_r , shown in [Figure 5.8](#).

X_r and X_{cl} are quite well correlated with increasing X_{cl} corresponding to an increase in X_r , which is expected. A regression analysis, excluding the uncertain Wd2 data point, yields the following relation:

$$\log X_r \approx 0.8(\log X_{cl}) + 8.6 \quad (5.3)$$

The scatter around the best fit is likely due to a number of effects, such as slight variations in the shape of the cluster XLFs as opposed to that of the COUP. An additional reason for the scatter is the cluster model used to determine the contribution of the cluster wind. As mentioned in [Section 1.4.7.1](#), the model used assumes no mass loading and a thermalization efficiency of 1 (i.e. - no radiative losses in the conversion of the stellar wind energies to the cluster wind). This is simplistic and it is noted here that a change in either parameter would serve to increase the predicted cluster wind L_X and X_r values. Using this empirical relation, we can estimate the ratios of the contributions to diffuse emission in a cluster using the physical parameters of the O or WR stars and the cluster radius. Additionally,

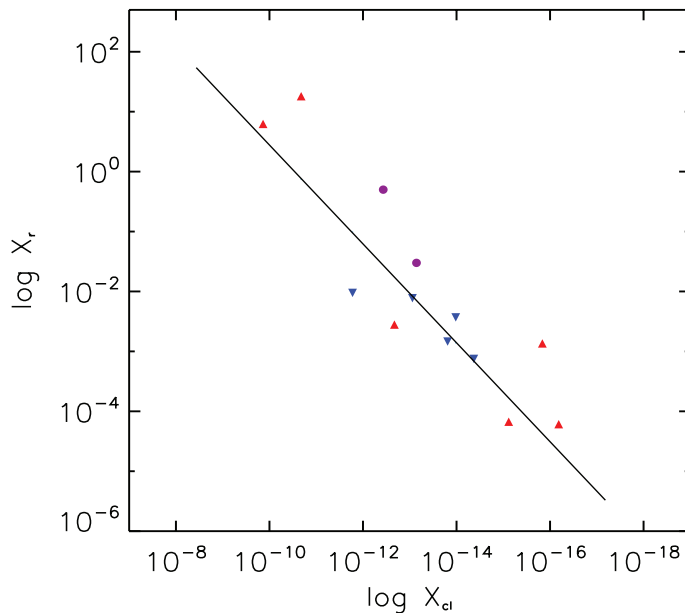


Figure 5.8: Plot of the cluster X_r values against X_{cl} . The blue inverted triangles indicate ages below the 2 Myr threshold, red triangles > 2 Myr and purple circles = 2 Myr. The best fit to the data is indicated by the solid black line.

if an X-ray spectrum is available, estimates of the actual L_X values for the wind and unresolved population can be derived.

5.3 Probing the IMF using the XLF

As described in Section 1.2, the distribution of stellar masses in a stellar system is described by the IMF. The IMF has observationally been determined to be generally invariant from one stellar system to another, be they small open clusters or large samples of Galactic field stars. As such, the distribution of X-ray luminosities in stellar systems, described by the XLF, should also be invariant, once corrected for temporal and incompleteness effects. Using the XLFs constructed during the earlier cluster analyses, this postulate can be qualitatively tested for the programme clusters studied by the comparison of the shape of the XLF for individual cluster stars (i.e. -omitting binaries) to that of the well known ONC, corrected for aging effects of the stellar population using the relation of [Preibisch and Feigelson \(2005\)](#) where appropriate. This is essentially achieved in the 2-8 keV XLF comparison plotted for each of the clusters in Chapter 3 which, for convenience, are gathered in Figure 5.9. Inspection of the XLFs plotted in Figure 5.9 shows that in general, all programme

5.3 Probing the IMF using the XLF

clusters have a high end XLF shape consistent with the ONC. The most unusual cluster XLF is that of Wd 2, which exhibits a slightly steeper slope. As discussed in Section 3.12.1, this is likely due the assumed distance to the cluster which is still a controversial issue. Another unusual XLF is that of Wd1 not because of its shape but the underlying population it infers. This XLF indicates a surprisingly small stellar population, suggesting the cluster IMF is truncated at the lower masses. The generally consistent shape of the high end XLF of the programme clusters with that of the ONC points to a similar underlying IMF, indicating approximately consistent IMF slope.

5.3 Probing the IMF using the XLF

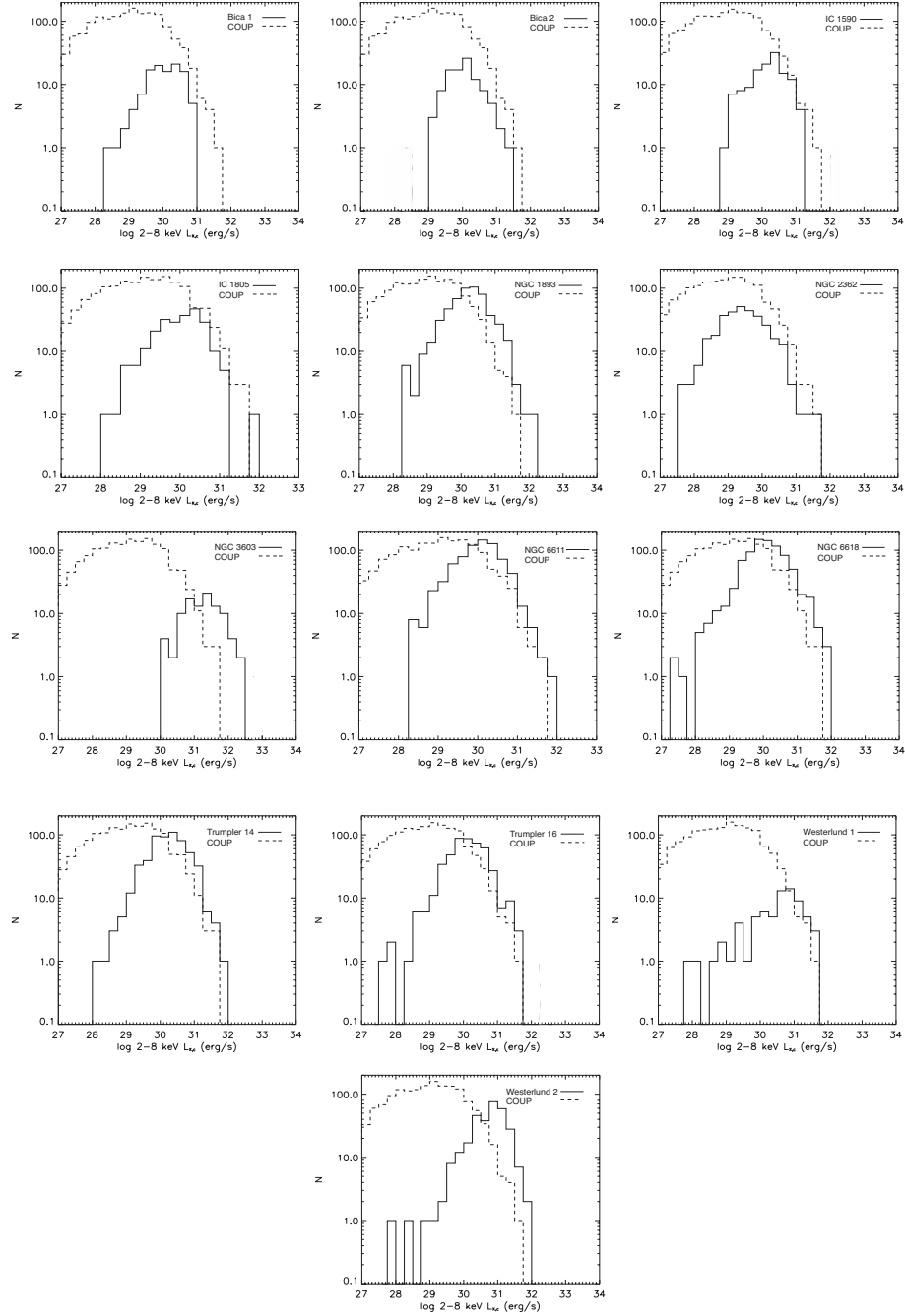


Figure 5.9: The PMS X-ray luminosity function (XLF) for all the programme clusters is shown in comparison with the COUP XLF.

Chapter 6

Conclusions and Future Prospects

The study of young star clusters remains one of the most important fields of astrophysics. These objects, the most massive of which can have devastating impacts on entire Galaxies, present an astrophysical laboratory where stellar evolution theories can be tested as well as the evolution of stellar systems as a whole. Additionally, these clusters are the engines by which material in the Universe is recycled. Their stars form from molecular clouds, with the most massive stars quickly producing heavy elements and redistributing them throughout the region via their winds and supernovae. This is a process best observed at X-rays due to the temperature of the winds, be they stellar or supernova or both. An unfortunate problem with these observations is that, in such clusters, large numbers of unresolved sources can mask the emission from the winds themselves making them hard to trace and their strength hard to quantify.

In this Ph.D. project I have investigated this issue by characterising the X-ray emission from the youngest Galactic star clusters and determining the strength of the relative contributions to the observed diffuse emission. This undertaking led to a wealth of information on the various cluster sub-populations as well as the clusters as a whole. Trends in the properties of the sub-populations with cluster age were investigated verifying previous observational results from the literature as well as demonstrating new trends, such as the frequency of magnetic wind sources in the youngest clusters. Following this the resolved X-ray point source populations were used to determine the contribution of the unresolved sources by invoking the universally observed stellar mass distribution, the Initial Mass Function, which is tightly connected to the underlying X-ray luminosity distribution of a stellar population, the X-ray Luminosity Function. To determine the contribution of a cluster wind

to the diffuse emission, a theoretical model was used which determines the X-ray luminosity of the cluster wind using the physical properties of massive stars in the cluster. Both these derived quantities were then compared to the observations to determine the nature of the diffuse emission in each of the clusters. These results were compared to a theoretical model of the X-ray luminosity in massive stellar clusters, which were largely verified. Additionally elements of the theoretical models used were combined with the observational findings to derive an empirical relation which can infer the ratio of the contributions to the diffuse emission using only the physical properties of the massive stellar population and the cluster radius. Supplementary to these analyses, the universality of the Initial Mass Function was probed in these clusters using the X-ray Luminosity Function. This was achieved by comparing the derived cluster X-ray Luminosity Function to a well known and surveyed stellar population. It was found that the shape of the X-ray Luminosity Function of the clusters were generally consistent with that of the calibration cluster implying a similar underlying Initial Mass Function.

So where does the future lie for this research? The obvious avenue is to extend the cluster database, adding even more clusters and assessing the effect of their inclusion into the above analysis. In this thesis, clusters were selected from an optical catalogue of open clusters based on age criteria. This catalogue does not include all of the well known young Galactic clusters however with two notable exceptions being the very massive Arches and Quintuplet clusters which are known to exhibit strong diffuse emission. These clusters are very heavily obscured due to their position in the Galactic centre and are not optically visible. As such they escape inclusion in the catalogue. Additionally, the cluster age limit could be extended to include clusters with much more evolved stellar populations and potentially have SNRs contributing to the cluster wind. One cluster population not considered at all for this thesis is that of the Magellanic Clouds. These satellite galaxies harbour rich massive clusters such as NGC 346 and R136. The addition of such clusters to the current database would allow inspection of diffuse emission up to Super Star Cluster scales. This would additionally allow the inspection of the Initial Mass Function via the X-ray Luminosity Function in more extreme star forming regions. By far the most massive cluster in the current sample is Wd1, the physical properties of which approach Super Star Cluster ranges. This cluster was found to have a somewhat less than expected underlying stellar population inferred from the X-ray Luminosity Function, suggesting truncation of the Initial Mass Function at lower

masses. A similar effect (though determined via a different method) is also seen in the Arches and Quintuplet with an X-ray derived deficiency of Young Stellar Objects in the clusters (Wang et al., 2006). Is this normal in very massive clusters? Only the addition of such massive clusters to the above analyses will answer this question.

During this analysis, several trends were observed such as the interplay of the cluster wind and unresolved Pre-Main Sequence population, the variation in the X-ray luminosities of OB stars and Colliding Wind Binaries and the variation in the global properties of PMS populations with age. Such data can be used as the foundation of an empirical cluster model. Using population synthesis techniques (using the Starburst 99 code for example Leitherer et al., 1999), observational X-ray luminosities and trends can be assigned to the various X-ray emitting sources in a simulated cluster. This model could then be used to predict the expected X-ray luminosity from a cluster and its temporal evolution based on observationally derived parameters. Before this can be achieved however, limitations of synthesis codes such as Starburst 99 must be overcome, in particular the inclusion of binary systems. Such techniques have already been used to simulate the X-ray emission from clusters (see Norci et al., 2006; Oskinova, 2005, with the former including a binary treatment) however, none of these models incorporate all of the X-ray emitting sources, be they point-like or diffuse. Also, given that we additionally have information on the trends in spectral parameters, synthetic spectra could be generated for the various sources and the cluster as a whole, which could also be directly compared to observations.

Appendix A

Data Reduction and Analysis

Commands

A.1 *Chandra* Data Reduction

When reducing *Chandra* data, the data files contained in the datasets are named according to a convention whereby observational values such as the instrument used and data source are included in the filenames (e.g. - acisf123456789N000_evt1.fits is the filename given to the Level 1 event file (evt1) taken in flight (f) using the ACIS instrument (acis) starting at 123456789, etc.). These filenames are somewhat clumsy so in the following section the names will be shortened to include only the instrument used and data content (e.g. - acisf123456789N000_evt1.fits → acis_evt1.fits).

The goal of the *Chandra* data reduction is to produce a Level 2 event file from the Level 1 data products, hence the ‘Reprocessing Data to Create a New Level=2 Event File’ thread from the CXC website is used (<http://cxc.harvard.edu/ciao/threads/createL2/>). Before producing the Level 2 event file, the pipeline processing software version used to produce the Level 1 data products must be checked to ensure it was sufficiently recent so as to forego some preceding steps in the reduction. The version of the pipeline software used is stored in the ‘ASCDSVER’ keyword in the header of the Level 1 data products and is checked using the command:

A.1 *Chandra* Data Reduction

```
unix% dmkeypar acis_evt1.fits ASCDSVER echo+
```

Providing the value returned by this command was ‘7.6.7’ or later (which it was for all of the retrieved datasets), the data reduction could proceed. The next step was to determine the ‘eventdef’ parameter, to be used later in the reduction, which specifies the format of the input and output event files and is related to the observation mode used in acquiring the data. The observation mode is determined by viewing the ‘READMODE’ and ‘DATAMODE’ keywords in the Level 1 event file. This is achieved using the commands:

```
unix% dmkeypar acis_evt1.fits READMODE echo+
```

```
unix% dmkeypar acis_evt1.fits DATAMODE echo+
```

For each of the reduced datasets in this project, the ‘READMODE’ and ‘DATAMODE’ keywords showed either ‘TIMED’ and ‘FAINT’ respectively or ‘TIMED’ and ‘VFaint’ respectively. The table in the ‘Determine the eventdef’ section of the analysis thread shows that the ‘eventdef’ parameter that corresponds to these modes is ‘stdlev1’.

The next step in the reduction is to use the `acis_process_events` command to create a new Level 1 event file by correcting the Level 1 event file in the retrieved dataset for bad pixels (using the ‘acis_bpix1.fits’ Level 1 file), applying the aspect solution (using the ‘acis_asol1.fits’ Level 1 file) and applying the latest calibrations from the CALDB. The calibrations are applied by default and include charge transfer inefficiency correction, gain correction and PHA and pixel randomization. The ‘eventdef’ parameter above is also supplied. The new Level 1 event file ‘acis_new_evt1.fits’ is produced by issuing the following commands:

```
unix% punlearn acis_process_events
```

```
unix% pset acis_process_events infile=acis_evt1.fits
```

```
unix% pset acis_process_events outfile=acis_new_evt1.fits
```

```
unix% pset acis_process_events badpixfile=acis_bpix1.fits
```

```
unix% pset acis_process_events acaofffile=acis_asol1.fits
```

```
unix% acis_process_events
```

The final steps in the data reduction involve filtering the ‘acis_new_evt1.fits’ event file. The first filtering step removes events with bad grades and/or bad status columns from the event file. Grades are assigned to every event during an observation and can be thought of as the shape an incoming photon makes on the ACIS CCD array. Certain grades indicate a real photon event whereas others may indicate a cosmic ray detection for example. Limited grade filtering is applied on board *Chandra* to limit the telemetry bandwidth whereas the remaining bad grades are removed in this reduction step. This step also filters for a ‘clean’ status column. The status column in the data file consists of 32 bits, each of which indicates a potential issue with each event and thus, those events with a bad status column are removed. This filtering step is run using the following commands:

```
unix% punlearn dmcoppy
```

```
unix% dmcoppy ‘‘acis_new_evt1.fits[EVENTS] [grade=0,2,3,4,6,status=0]’’  
acisflt_evt1.fits
```

where ‘acisflt_evt1.fits’ is the cleaned event list. The next step involves filtering this cleaned event list for Good Time Intervals (GTIs). GTIs are supplied in the Level 1 ‘acisflt1.fits’ produced by the pipeline. This file indicates the periods of the observation when the mission time line parameters (all time series data that affect the quality of the event data) fall within acceptable levels. Essentially this filtering step removes periods of the observation that are deemed not to produce quality event data (such as the first few frames of the observation, gaps in the aspect solution, etc.). The cleaned event file is filtered for GTIs to create a Level 2 event file (‘acis_evt2.fits’) using the command:

```
unix% punlearn dmcoppy
```

```
unix% dmcoppy ‘‘acisflt_evt1.fits[EVENTS] [@acisflt1.fits]
```

```
cols -phas
'' acis_evt2.fits
```

The penultimate step in the data reduction is to filter this Level 2 event file into a desired energy range, i.e.- the 0.5-8 keV energy range at which the ACIS instrument is most sensitive. To achieve this the following commands are run:

```
unix% punlearn dmcopu

unix% dmcopu ''acis_evt2.fits[energy=500:8000]''
acis_0.5-8keV_pre-evt2.fits
```

The final step is to clean this Level 2 event file of flaring periods that may have contaminated the observation. For this we must define a region of the image free from point sources that may exhibit strong flares themselves during the observation. This region was defined on the ACIS image using the *DS9* visualization software and saved as 'flare.reg'. An event file was extracted for this region using `dmcopu` :

```
unix% punlearn dmcopu

unix% dmcopu ''acis_0.5-8keV_pre-evt2.fits[sky=region(flare.reg)]''
acis_flare.fits
```

Following this, a lightcurve is created for this extracted region using the following commands:

```
unix% punlearn dmextract

unix% dmextract ''acis_flare.fits[bin time=:259.28]''
outfile=acis_flare.lc opt=ltc1
```

This lightcurve is now analysed using the `deflare` algorithm which outputs a GTI file identifying periods of the observation unaffected by flares:

```
unix% punlearn deflare
```

```
unix% deflare acis_flare.lc acis_flare.gti method=clean
```

Finally the all FOV Level 2 event file is filtered for the GTI's defined by the `deflare` algorithm:

```
unix% punlearn dmcopu
```

```
unix% dmcopu 'acis_0.5-8keV_pre-evt2.fits[@acis_flare.gti]'
```

```
acis_0.5-8keV_evt2.fits
```

The calibrated and filtered Level 2 event file `acis_0.5-8keV_evt2.fits` is the final output of the data reduction and the subject of the data analysis.

A.1.1 Diffuse Emission

Diffuse emission spectra are extracted from the calibrated and filtered Level 2 event file `acis_0.5-8keV_evt2.fits`. Before this however, appropriate 'blank sky' backgrounds must be defined. To do this the 'ACIS Blank Sky Background' thread is followed¹. The first step is to identify 'blank sky' files within the *CALDB* that match the observation. This is achieved via the `acis_bkgrnd_lookup` *CIAO* task:

```
unix% acis_bkgrnd_lookup acis_0.5-8keV_evt2.fits
```

This command outputs appropriate 'blank sky' files for each individual ccd chip active during the observation which for convenience we will call `acis_i1.bkg`, `acis_i2.bkg`, etc. These files are copied to the working directory and merged to produce a full field 'blank sky' background file using the `dmmerge` task:

```
unix% punlearn dmmerge
```

```
unix% dmmerge 'acis_i1.bkg, acis_i2.bkg, acis_i3.bkg, acis_i4.bkg'
```

```
merged_acis_bkgrnd.fits
```

¹See <http://cxc.harvard.edu/ciao/threads/acisbackground/index.py.html>

A.1 *Chandra* Data Reduction

Unfortunately this process suffers from a bug which is due to the fact that the `dmmerge` task was designed to combine multiple observations. Because of this, `dmmerge` sums the exposure related keywords when combining files. Given that each of the ccd ‘blank sky’ files has an associated exposure time, the `dmmerge` task sums these values and assigns the resulting exposure time to the output merged file. This, of course, is incorrect and thus must be fixed. This is achieved by determining the actual values of the exposure related keywords from one of the ccd ‘blank sky’ files, using the `dmlist` task with `egrep`, and editing these into the corresponding merged file header, using the `dmhedit` task. The commands are as follows:

```
unix% punlearn dmlist
```

```
unix% dmlist acis_i0.bkg header | egrep '(ONTIM | EXPOS | LIV)'
```

This will yield the same value for each of the keywords, e.g. - 1500000.0, to be edited into the merged background file header:

```
unix% punlearn dmhedit
```

```
unix% dmhedit merged_acis_bkgrnd.fits filelist=' ' op=add  
key=EXPOSURE value=1500000.0 unit=s
```

```
unix% punlearn dmhedit
```

```
unix% dmhedit merged_acis_bkgrnd.fits filelist=' ' op=add  
key=ONTIME value=1500000.0 unit=s
```

```
unix% punlearn dmhedit
```

```
unix% dmhedit merged_acis_bkgrnd.fits filelist=' ' op=add  
key=LIVTIME value=1500000.0 unit=s
```

An additional adjustment to the merge background file header is the adding of the pointing header keyword (PNT) which indicates the where the optical axis was during the observation. For the ACIS ‘blank sky’ files, this keyword is set to zero as they are generic files. Thus this value in the merged background file should be

adjusted to that of the observation file to avoid problems later in the analysis. This is achieved using the following commands:

```
unix% punlearn dmmakepar

unix% dmmakepar acis_0.5-8keV_evt2.fits event_header.par

unix% grep _pnt event_header.par > event_pnt.par

unix% chmod +w merged_acis_bkgrnd.fits

unix% punlearn dmreadpar

unix% dmreadpar event_pnt.par ‘‘merged_acis_bkgrnd.fits[events]’’
clobber+
```

A final check of the merged background file is made to ensure the gain file used to produce the ‘blank sky’ backgrounds matches that of the observation, achieved via the `dmkeypar` command:

```
unix% punlearn dmkeypar

unix% dmkeypar acis_0.5-8keV_evt2.fits GAINFILE echo+

unix% punlearn dmkeypar

unix% dmkeypar merged_acis_bkgrnd.fits GAINFILE echo+
```

If the outputs of these commands are the same (which they were for each of the cluster analyses) then the analysis can proceed. If not the background file must be reprocessed with the new gain file using `acis_process_events`¹. The final correction to the merged background file is to reproject the data to match the aspect of the observation. This is done using the *CIAO* task `reproject_events` as follows:

¹See <http://cxc.harvard.edu/ciao/threads/acisbackground/index.py.html> for details.

```
unix% punlearn reproject_events
```

```
unix% reproject_events infile=merged_acis_bkgrnd.fits
outfile=rep_acis_bkgrnd.fits aspect=acis_asol1.fits
match=acis_0.5-8keV_evt2.fits random=0
```

To ensure the reprojected background matched the aspect of the observation, both are plotted in *DS9* and visually inspected. With the creation of this reprojected ‘blank sky’ background file we are ready to extract the diffuse spectra and backgrounds, and generate the response files. All of this is achieved using the *CIAO* task *specextract*. An extraction region is defined and saved in *CIAO* format as ‘diffuse.reg’ using *DS9*, which is used to extract the diffuse spectrum from the observational data and background spectrum from the ‘blank sky’ background data. This is performed using the commands:

```
unix% punlearn specextract
```

```
unix% specextract infile='acis_0.5-8keV_evt2.fits[sky=region
(diffuse.reg)]' outroot=diffuse bkgfile='rep_acis_bkgrnd.fits[sky=
region(diffuse.reg)]' pbkfile=acis_pbk0.fits grouptype=NUM_CTS
binspec=15
```

This task creates all of the files required to spectrally fit the diffuse spectrum in as well as grouping the spectra and linking the response files.

A.2 *ACIS Extract* Setup and Usage

As mentioned in Section 2.1.2, *ACIS Extract* (*AE*) is written in the *IDL* language and incorporates several other analysis softwares. Table A.1 lists the software packages and versions of all those used by *AE* and *AE* itself.

Table A.1: *ACIS Extract* Dependent Softwares and Versions

Software Package	Version
<i>ACIS Extract</i> ¹	08.08.2006
<i>IDL</i> ²	6.4
<i>CIAO</i> ³	4.0
<i>CALDB</i> ⁴	3.4.2
<i>SAOImage DS9</i> ⁵	5.0
<i>MARX</i> ⁶	4.3.0
<i>FTOOLS</i> ⁷	6.5
<i>XSPEC</i> ⁸	12.3.1
<i>IDL Astronomy Users Library</i> ⁹	12.2006
<i>TARA</i> ¹⁰	01.2007

1 - http://www.astro.psu.edu/xray/docs/TARA/ae_users_guide.html

2 - <http://www.ittvis.com/ProductServices/IDL.aspx>

3 - <http://cxc.harvard.edu/ciao/>

4 - <http://cxc.harvard.edu/caldb/>

5 - <http://hea-www.harvard.edu/RD/ds9/>

6 - <http://space.mit.edu/cxc/marx/>

7 - http://heasarc.gsfc.nasa.gov/lheasoft/ftools/ftools_menu.html

8 - <http://heasarc.gsfc.nasa.gov/docs/xanadu/xspec/>

9 - <http://idlastro.gsfc.nasa.gov/>

10 - <http://www.astro.psu.edu/xray/docs/TARA/>

For this project, these softwares were run on the *Ubuntu 8.04 LTS*¹ operating system and were installed according to the instructions given on the *AE* website (http://www.astro.psu.edu/xray/docs/TARA/ae_users_guide/node36.html#sec:install). While using *AE*, it is very convenient to have two terminals open simultaneously, one *tsh* (a member of the shell family required by *AE*) and one with *IDL*. In the following descriptions of the setup and usage of *AE*, commands written to the *tsh* terminal are preceded with `unix%` whereas commands written to the *IDL* terminal will be preceded by `idl>`. The *AE* commands and procedures which follow were obtained from the *AE Users Guide* http://www.astro.psu.edu/xray/docs/TARA/ae_users_guide.html.

¹Available at <http://releases.ubuntu.com/8.04/>

A.2.1 Setup

Prior to running the *AE* tasks on observational data, some preparatory work is required to facilitate *AE*'s automated analysis capabilities. This entails the setting up of a standard directory structure containing some of the Level 2 data files from the Chandra data reduction. However, before this is done, there are two further data files that must be created which are not produced in a standard *Chandra* data reduction, namely the Analysis Reference Data Library parameter file ('ardlib.par') and the exposure map.

The 'ardlib.par' file is used by several *CIAO* tools as an interface to instrument specific calibration data and contains pointers to some of the Level 1 data files from each observational dataset, in particular the bad pixel files. As such, each observational dataset requires its own specific 'ardlib.par' file to be produced. This is achieved via the *CIAO* task `acis_set_ardlib`:

```
unix% punlearn acis_set_ardlib
```

```
unix% acis_set_ardlib acis_bpix1.fits
```

This amends the default 'ardlib.par' file in the users *CIAO* installation directory. This file is then simply copied to the working data directory.

The exposure map is an image of the effective area associated with each sky position averaged over the aspect motion of the telescope during the observation. The exposure map is used to convert a counts image into an image in flux units and is especially important near detector edges and near bad pixels and columns where the effective area may vary quite dramatically over the course of the observations. Since the effective area is energy dependent so is the exposure map. Although an energy dependent exposure map can be created, it was decided to calculate the exposure map at one specific energy (1 keV) for each of the clusters as an energy dependent exposure map is typically calculated adopting the spectrum from a source in the FOV to weight the exposure map and is thus very dependent on the chosen source. Hence, the 'mono-energetic' exposure map is more suited to our needs since we require a generic analysis for the programme clusters. To generate an exposure map, the *AE* accessory tool `ae_make_emap` is used and is run from the directory containing

A.2 ACIS Extract Setup and Usage

the Level 1 and Level 2 data files used in the *Chandra* data reduction.

```
idl> .run acis_extract_tools

idl> ae_make_emap, 'acis_0.5-8keV_evt2.fits' , 'obs.emap', CCD_LIST
='0123', ARDLIB.FILENAME='./ardlib.par', ASPECT_FN='acis_asol1.fits',
PBKFILE='acis_pbk0.fits', MASKFILE='acis_msk1.fits', MONOENERGY=1.0
```

This command produces the 1 keV exposure map 'obs.emap' for the ACIS-I array (set using the CCD IDs 0,1,2 and 3 which are adjusted appropriately for an S array exposure map). In addition, this command produces the 'asphist' directory which contains files required later by *AE*.

Now that all of the required files have been created, the *AE* standard directory structure can be set up. For each cluster directory, at least two subdirectories are required (depending on the number of observations for the cluster). These are the observational data directory(ies) and the point source directory. Each data directory will contain the appropriate Level 2 event file, the aspect solution file and the parameter block file (renamed to 'spectral.evt', 'obs.asol' and 'obs.pbkfile' respectively), and will also contain the 'ardlib.par' file, 'obs.emap' exposure map and 'asphist' files produced above. The point source directory will initially contain the results file of the point source detection (i.e. - the positions, etc. of sources in the FOV) 'wavdetect.fits' and the *AE XSPEC* scripts which are used later in the analysis to fit source spectra. As the analysis proceeds, the point source directory is used to house data files and results for each individual source in the FOV. A schematic of the standard directory structure and required files is shown in Table A.2.

A.2.2 Usage

The *AE* analysis can now proceed. From here on, all *AE* commands are issued from the 'point_sources' directory. The first step in the *AE* analysis is to read the detected point sources from the 'wavdetect.fits' file and create subdirectories in 'point_sources' for each of the sources. Additionally this step sorts the sources into ascending RA and writes the source list to the ascii file 'all.srclist' which is used in

Table A.2: *ACIS Extract* Standard Directory Structure and Initial Files

cluster/		
	obsXXXX/	
		ardlib.par
		asphist/
		ccd0.asphist
		ccd1.asphist
		ccd2.asphist
		ccd3.asphist
		obs.asol
		obs.emap
		obs.pbkfile
		spectral.evt
	obsXXXY/	

	point_sources/	
		xspec_scripts/
		wavdetect.fits

A.2 *ACIS Extract* Setup and Usage

most of the following steps. The commands are as follows:

```
idl> bt = mrdfits('wavdetect.fits',1)

idl> RA = bt.RA

idl> DEC = bt.DEC

idl> .run ae_recipe

idl> ae_source_manager, /ADD, RA=ra, DEC=dec, POSITION_TYPE=
'wavdetect'

idl> ae_source_manager, /SORT_RA

idl> ae_source_manager, /SET_LABEL_AS_SEQUENCE
```

The next step in the analysis is to define source extraction and mask regions. Although *CIAOs* `wavdetect` task (run earlier in the analysis, see Section 2.1.2) gives estimates of source dimensions and properties, it does so without any explicit knowledge of the *Chandra* PSF. As such it is not uncommon for `wavdetect` to determine extraction apertures which differ substantially from the PSF. *AE* circumvents this issue by deriving extraction regions from the local PSF via ray-trace simulations with *MARX* (the *Chandra* ray-trace simulation software). The extraction regions defined by *AE* are sized to enclose 90% of the local PSF but, in crowded regions, this is iteratively reduced to avoid overlapping extraction apertures. (In cases of extreme crowding, even this reduction in aperture may be insufficient to stop contamination by the PSF wings of nearby sources. However, this is addresses later in the analysis). Mask regions are also constructed for use later in the analysis to exclude all point source photons from the FOV. These source masks are circular regions with radii 1.1 times that of the radius that encloses 99% of the PSF. These extraction and mask regions are defined in the 'CONSTRUCT_REGIONS' stage of *AE* using the following command:

```
idl> acis_extract, 'all.srclist', 'XXXX', '../obsXXXX/spectral.evt',
/CONSTRUCT_REGIONS, EMAP_FILENAME='../obsXXXX/obs.emap', ASPECT_FN=
```

A.2 ACIS Extract Setup and Usage

```
'../obsXXXX/obs.asol' (, /S_AIMPOINT)
```

where 'XXXX' refers to the Obs. Id. assigned to the data subdirectory 'obsXXXX' in the *AE* directory structure. The '/S_AIMPOINT' option is provided if the data were taken with the ACIS-S array.

Now that extraction apertures have been defined for each of the sources, source spectra and associated calibration files can be produced. This is achieved using the 'EXTRACT_SPECTRA' stage of *AE*. During this step, source statistics are also computed and written to appropriate files in their respective subdirectories. The command is as follows:

```
idl> acis_extract, 'all.srclist', 'XXXX', '../obsXXXX/spectral.evt',  
/EXTRACT_SPECTRA, ENERGY_RANGE=[0.5,8], EMAP_FILENAME='../obsXXXX/ obs.  
emap', ASPHIT_DIR='../obsXXXX/asphist', ARDLIB_FILENAME='../obsXXXX/  
ardlib.par', PBKFILE='../obsXXXX/ obs.pbkfile', ASPECT_FN='../obsXXXX/  
obs.asol'
```

After the 'EXTRACT_SPECTRA' stage is run, each of the source subdirectories contains (among other things) a source event list, a source spectrum file, a source redistribution matrix file (RMF) and an ancillary response file (ARF) which are required for photometric and spectroscopic analysis. However, before these analyses can be undertaken, background spectra must be produced for each of the sources. To facilitate this, a background event file and background exposure map are required. These files can be constructed using a combination of *CIAO* and *DS9* commands to filter the existing event file and exposure map for point sources using a DS9 region file containing the mask regions produced in the 'CONSTRUCT_REGIONS' stage of *AE*. These mask regions were saved in the 'extract.reg' files of each of the source subdirectories. The *DS9* region file 'mask.reg' is produced with the following UNIX commands, issued from the 'obsXXXX' directory:

```
unix% echo '#Region file format: DS9 version 3.0' > mask.reg  
  
unix% grep -h background ../point_sources/*/XXXX/extract.reg | awk '{print  
"-",$1}' >> mask.reg
```

A.2 ACIS Extract Setup and Usage

The ‘mask.reg’ region file is in DS9 format but, for use in *CIAO*, must be converted to *CIAO* format. This is done by simply loading the regions in *DS9*, changing the region file format and saving. For clarity, this is saved as ‘mask_ciao.reg’. This region file could now be used to filter the exposure map using *CIAO*’s dmcopy command to create the background exposure map ‘background.emap’:

```
unix% punlearn dmcopy
```

```
unix% dmcopy ‘obs.emap[exclude sky=region(mask_ciao.reg)] [opt full,
update=no]’ background.emap
```

This background exposure map was in turn be used to discard events in the event file where the background exposure map is zero to create the background event file ‘background.evt’:

```
unix% punlearn dmimgpick
```

```
unix% dmimgpick ‘spectral.evt[cols time,ccd_id,chip,det,sky,pi,
energy]’ background.emap temp.evt method=closest
```

```
unix% punlearn dmcopy
```

```
unix% dmcopy ‘temp.evt[#8>1]’ background.evt
```

The ‘background.emap’ and ‘background.evt’ files were then loaded with the mask regions in *DS9* and visually inspected to identify any unmasked source events. If any source events were missed, the mask regions were adjusted appropriately and saved and new ‘background.emap’ and ‘background.evt’ files were produced with this new region file.

With these new background files, the ‘EXTRACT_BACKGROUND’ stage of *AE* could be run. During this stage, *AE* identifies a local annular background to each of the sources using criteria such as a minimum number of events. Once the background regions are defined, background event lists and spectra are extracted and scaled according to the integrated exposure map in the region. This stage is

A.2 ACIS Extract Setup and Usage

run by executing the following command:

```
idl> acis_extract, 'all.srclist', 'XXXX', '../obsXXXX/background
.evt', /EXTRACT_BACKGROUNDS, EMAP_FILENAME='../obsXXXX/background.emap',
MIN_NUM_CTS=20
```

At this point, each of the point source subdirectories contains a background spectrum file. However, they are not yet ready for spectral fitting. In observations where there is significant source crowding (which was encountered several times in this project) these background spectra may, in addition to the normal background, be significantly contaminated by the PSF wings of neighbouring sources. *AE* contains a very complex tool to correct for this known as 'ae_better_backgrounds' and is run as follows:

```
idl> ae_better_backgrounds, 'XXXX', EMAP_ENERGY=1, EVTFILE_BASENAME
='spectral.evt'
```

where the 'EMAP_ENERGY' option is set to that energy at which the exposure maps 'obs.emap' (and thus 'background.emap'), was calculated. This command produces the final background spectra and associated files ready for photometric and spectroscopic analysis.

In addition to a photometric and spectroscopic analysis, *AE* also has the ability to perform a temporal analysis, which is done in the 'TIMING' stage. During this stage, *AE* creates lightcurves and quantifies the time variability of each source by comparing a uniform count rate model to the observed count times and computing the 1-sample Kolmogorov-Smirnov statistic. This stage is executed with the following command:

```
idl> acis_extract, 'all.srclist', 'XXXX', '../obsXXXX/spectral.evt',
/TIMING, ENERGY_RANGE=[0.5,8], SNR_RANGE=[2,20], NUM_GROUPS_RANGE=[2,100]
```

The commands to this point were run for each individual observation of a given cluster. The results and files for each individual source from each observation must now be combined. This is handled in the 'MERGE_OBSERVATIONS' stage of *AE*.

A.2 *ACIS Extract* Setup and Usage

During this stage, individual source spectra, background spectra, lightcurves, source statistics, etc. are combined and weighted RMFs and ARFs are computed. In addition, photometry is performed over a set of energy ranges including the 0.5-2 keV (soft), 2-8 keV (hard) and 0.5-8 keV (total) ranges. Even if there is only one observation for a given cluster, 'MERGE_OBSERVATIONS' is run:

```
idl> acis_extract, 'all.srclist', /MERGE_OBSERVATIONS
```

After the 'MERGE_OBSERVATIONS' stage is completed, all the files necessary for a spectral analysis on each source are present in their respective subdirectories. The 'FIT_SPECTRA' stage of *AE* can now be run to perform automated spectral fitting for each of the sources. As a first run, each spectrum is fitted with an absorbed thermal plasma model (the APEC model in *XSPEC*). *AE* provides the *XSPEC* fitting scripts which are in the 'xspec_scripts' directory of the standard directory structure. Any source for which the absorbed thermal plasma mode gives a poor fit can either manually be fit with more complex models or can be fit with a more complex *AE XSPEC* model script. The 'FIT_SPECTRA' stage can be run as follows:

```
idl> acis_extract, 'all.srclist', /FIT_SPECTRA, CHANNEL_RANGE=[35,548],  
MODEL_FILENAME='xspec_scripts/thermal/tbabs_vapec.xcm'
```

Plots of source spectra and fit results from the 'FIT_SPECTRA' stage are saved to appropriate files in the source subdirectories. The final stage of *AE* is the 'COLLATED_FILENAME' stage. This stage collates the temporal, photometric and spectroscopic results, statistics and properties for all of the sources into one file which can be used as a database for further analysis and is executed as follows:

```
idl> acis_extract, 'all.srclist', /COLLATED_FILENAME='all.collated'
```

The file 'all.collated' now contains all of the information for each individual source output by all of the preceding stages of *AE*.

Appendix B

Programme Cluster Figures and Tables

B.1 Bica 1 and Bica 2

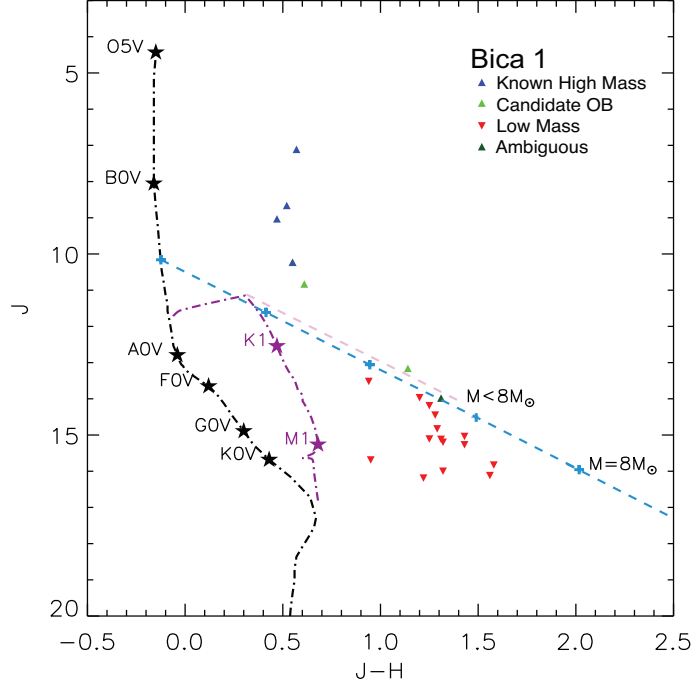


Figure B.1: Bica 1 2MASS J vs J-H colour magnitude diagram. The blue triangles indicate the known high mass stars, the light green triangles indicate the candidate OB stars, the dark green circles indicate the ambiguous sources and the red inverted triangles indicate low mass sources. The black dashed dotted line is the 2 Myr main sequence isochrone with spectral types marked calculated for $A_V = 0$. The purple dashed dotted line is the 2 Myr PMS isochrone with spectral types marked. The light blue dashed line is the $8M_\odot$ reddening vector with the crosses marking every $A_V = 5$. The light purple dashed line marks the reddening vector of the maximum J value of the PMS evolutionary track. Sources between this and the $8M_\odot$ reddening vector may be above or below $8M_\odot$ and are hence labelled as ambiguous sources.

Table B.1: Bica 1 Known High Mass Star X-ray Spectral Parameters

<i>Chandra</i> Source (CXO J)	Name	Sp. Type	<i>Net Cts.</i>	N_{H} (10^{22} cm^2)	kT (keV)	kT_2 (keV)	χ^2/ν	$\log F_{X_{h,c}}$ ($\text{erg cm}^{-2} \text{ s}^{-1}$)	$\log F_{X_{t,c}}$ ($\text{erg cm}^{-2} \text{ s}^{-1}$)	$\log L_{X_{h,c}}$ (erg s^{-1})	$\log L_{X_{t,c}}$ (erg s^{-1})
203308.76+411318.7	Schulte 22	O3I + O6V	1336	$2.09^{+0.25}_{-1.93}$	$0.60^{+0.68}_{-0.56}$	-	1.20/57	-13.36	-11.95	31.23	32.64
203309.58+411300.8	V2188 Cyg	O9V	101	$1.57^{+1.01}_{-1.77}$	$0.77^{+0.46}_{-1.15}$	-	0.86/3	-14.45	-13.09	30.13	31.50
203313.24+411328.8	ALS 15148	O6V	105	$1.24^{+1.83}_{-0.85}$	$0.68^{+0.91}_{-0.45}$	-	0.86/5	-14.62	-13.34	29.97	31.24
203313.66+411305.8	ALS 15128	O8V	103	$1.72^{+2.14}_{-1.18}$	$0.59^{+1.96}_{-0.41}$	-	0.93/5	-14.59	-13.16	30.00	31.43
203317.39+411238.7	2MASS J20331740+4112387	B0V	14	-	-	-	-	-	-	-	-

High mass sources identified using the high mass source lists of [Wright and Drake \(2009\)](#) and the SIMBAD database. Only those sources with > 50 counts were fit in *XSPEC*.

Table B.2: Bica 1 Candidate OB Star X-ray Spectral Parameters

<i>Chandra</i> Source (CXO J)	Name	Sp. Type	<i>Net Cts.</i>	N_{H} (10^{22} cm^2)	kT (keV)	kT_2 (keV)	χ^2/ν	$\log F_{X_{h,c}}$ ($\text{erg cm}^{-2} \text{ s}^{-1}$)	$\log F_{X_{t,c}}$ ($\text{erg cm}^{-2} \text{ s}^{-1}$)	$\log L_{X_{h,c}}$ (erg s^{-1})	$\log L_{X_{t,c}}$ (erg s^{-1})
203307.44+411226.7	2MASS J20330746+4112266	-	175	1.28_{-}	28.1_{-}	-	0.75/7	-13.45	-13.31	31.14	31.28
203309.14+411343.5	2MASS J20330915+4113434	-	46	-	-	-	-	-	-	-	-

Source names determined using the SIMBAD database. Only those sources with > 50 counts were fit in *XSPEC*.

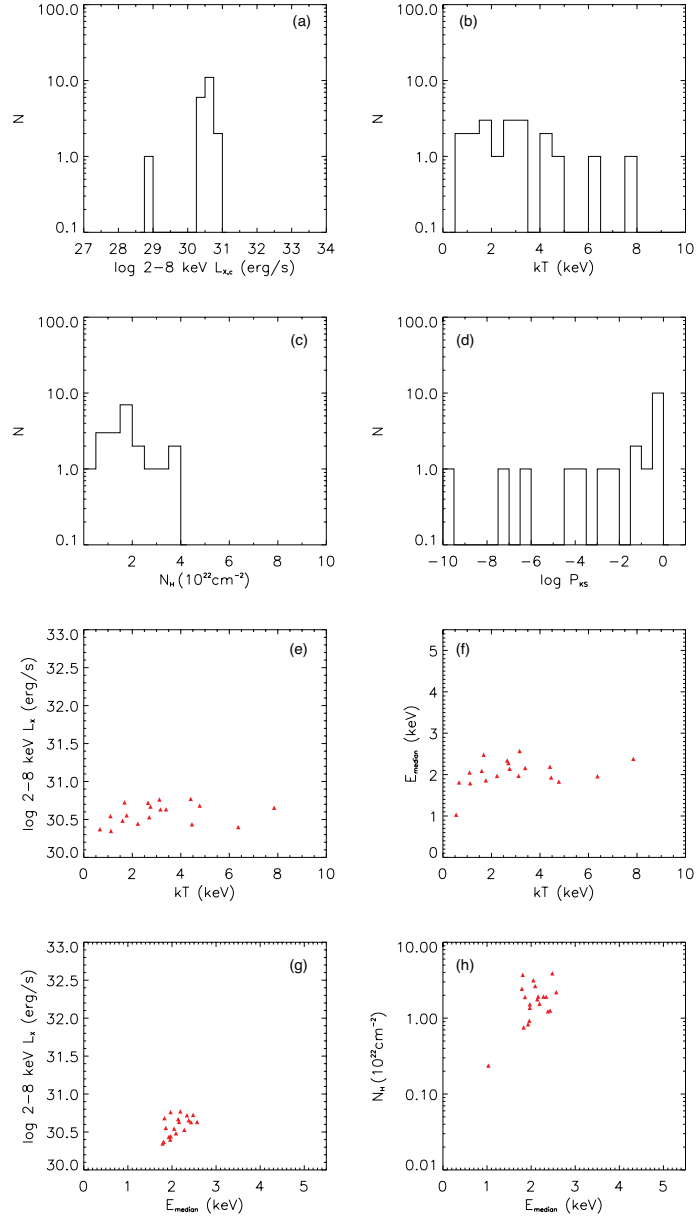


Figure B.2: Plots of derived source parameters for the bright PMS population of Bica 1. (a) Distribution of absorption corrected 2-8 keV L_X . (b) Distribution of best fit thermal plasma temperature (kT). (c) Distribution of best fit absorbing hydrogen column (N_H). (d) Distribution of Kolmogorov-Smirnov variability statistic with $\log P_{KS} < 0.05$ indicating variability. (e) Plot of absorption corrected 2-8 keV L_X against best fit thermal plasma temperature (kT). (f) Plot of median photon energy (E_{median}) against best fit thermal plasma temperature (kT). (g) Plot of absorption corrected 2-8 keV L_X against median photon energy (E_{median}). (h) Plot of best fit absorbing hydrogen column (N_H) against median photon energy (E_{median}).

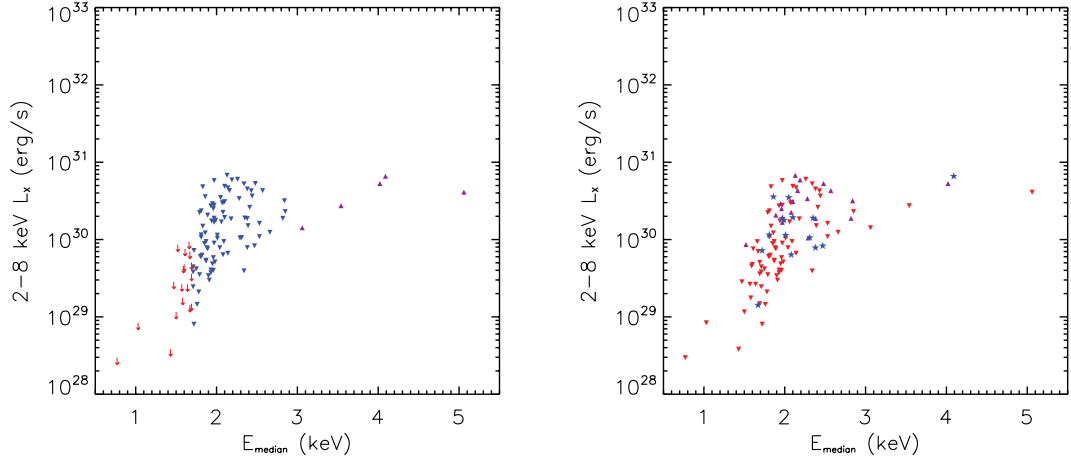


Figure B.3: Plot of the 2-8 keV L_X against the median detected photon energy (E_{median}) for the Bica 1 PMS population divided according to E_{median} (left) and variability (right). Left: the red arrows mark $E_{\text{median}} < 1.7$ keV (indicating an upper limit of $\log N_{\text{H}} \lesssim 22.0 \text{ cm}^{-2}$), blue inverted triangles 1.7-3 keV (indicating the lightly obscured population) and purple triangles > 3 keV (indicating the heavily obscured population). Right: Inverted red triangles refer to non-variable sources, blue stars representing variable sources and the purple triangles representing strongly variable flaring sources.

Table B.3: Bica1 Diffuse Emission X-ray Spectral Parameters

Region	N_{H} (10^{22} cm^2)	kT (keV)	kT_2 (keV)	Z/Z_{\odot}	χ^2/ν	$\log F_{X_{h,c}}$ ($\text{erg cm}^{-2} \text{ s}^{-1}$)	$\log F_{X_{t,c}}$ ($\text{erg cm}^{-2} \text{ s}^{-1}$)	$\log L_{X_{h,c}}$ (erg s^{-1})	$\log L_{X_{t,c}}$ (erg s^{-1})
total	$1.15_{-0.91}^{+1.39}$	$0.59_{-0.39}^{+0.83}$	$5.39_{-3.04}^{+}$	$0.14_{-0.05}^{+0.37}$	0.99/176	-12.47	-11.76	32.20	32.57
core	$1.23_{-1.00}^{+1.41}$	$0.76_{-0.59}^{+0.96}$	10.03_{-}	$0.27_{-0.10}^{+0.99}$	0.90/87	-12.84	-12.13	31.49	32.20

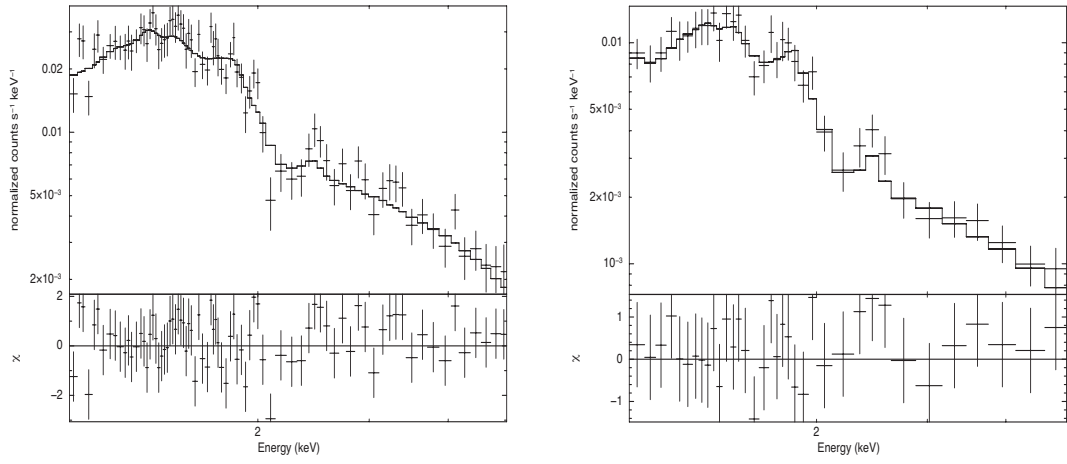


Figure B.4: Bica 1 total cluster diffuse emission spectrum (left) and cluster core diffuse emission spectrum (right). The spectra were rebinned for plotting purposes using XSPEC's *setplot rebin* command. Only the 1-5 keV energy range is shown as the spectra approach background levels outside this range.

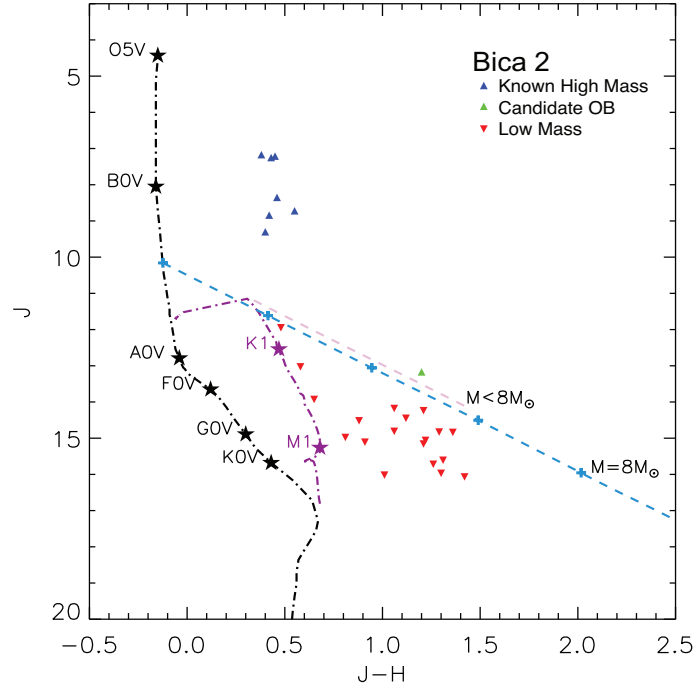


Figure B.5: Bica 2 2MASS J vs J-H colour magnitude diagram. The blue triangles indicate the known high mass stars, the light green triangles indicate the candidate OB stars and the red inverted triangles indicate low mass sources. The black dashed dotted line is the 2 Myr main sequence isochrone with spectral types marked calculated for $A_V = 0$. The purple dashed dotted line is the 2 Myr PMS isochrone with spectral types marked. The light blue dashed line is the $8M_{\odot}$ reddening vector with the crosses marking every $A_V = 5$.

Table B.4: Bica 2 Known High Mass Star X-ray Spectral Parameters

<i>Chandra</i> Source (CXO J)	Name	Sp. Type	<i>Net Cts.</i>	N_{H} (10^{22}cm^2)	kT (keV)	kT_2 (keV)	χ^2/ν	$\log F_{X_{h,c}}$ ($\text{erg cm}^{-2} \text{s}^{-1}$)	$\log F_{X_{t,c}}$ ($\text{erg cm}^{-2} \text{s}^{-1}$)	$\log L_{X_{h,c}}$ (erg s^{-1})	$\log L_{X_{t,c}}$ (erg s^{-1})
203302.89+411743.3	ALS 15131	O8V	96	$1.62^{2.55}_{0.71}$	$0.65^{1.18}_{0.37}$	-	0.22/1	-14.55	-13.23	30.04	31.36
203314.10+412022.0	VI CYG 7	O3If	1786	$1.75^{1.81}_{1.63}$	$0.61^{0.67}_{0.56}$	-	1.53/74	-13.28	-11.87	31.31	32.71
203314.31+411933.5	ALS 15175	B5	52	1.6^-	0.55^-	-	2/4	-14.98	-13.48	29.60	31.11
203314.75+411841.9	VI CYG 8B	O6.5III	280	$0.72^{1.11}_{0.36}$	$0.55^{0.77}_{0.38}$	-	1.65/10	-14.37	-12.90	30.22	31.69
203315.05+411850.6	VI CYG 8A	O6If + O5.5III(f)	38195	$1.18^{1.13}_{1.22}$	$0.72^{0.75}_{0.63}$	$2.07^{2.13}_{2.01}$	1.93/239	-11.16	-10.52	33.43	34.07
203315.69+412017.5	VI CYG 23	O9.5V	44	-	-	-	-	-	-	-	-
203316.33+411902.1	VI CYG 8D	O8.5V	26	-	-	-	-	-	-	-	-
203317.45+411709.4	Schulte 24	O7.5V	125	1.36^-	0.54^-	-	0.87/3	-14.72	-13.13	29.87	31.45
203317.97+411831.3	VI CYG 8C	O5I	397	$1.52^{1.86}_{1.27}$	$0.48^{0.58}_{0.38}$	-	1.55/19	-14.06	-12.34	30.53	32.24
203321.00+411740.2	ALS 15123	O8.5V	43	-	-	-	-	-	-	-	-

High mass sources identified using the high mass source lists of [Wright and Drake \(2009\)](#) and the SIMBAD database. Only those sources with > 50 counts were fit in *XSPEC*.

Table B.5: Bica 2 Candidate OB Star X-ray Spectral Parameters

<i>Chandra</i> Source (CXO J)	Name	Sp. Type	<i>Net Cts.</i>	N_{H} (10^{22}cm^2)	kT (keV)	kT_2 (keV)	χ^2/ν	$\log F_{X_{h,c}}$ ($\text{erg cm}^{-2} \text{s}^{-1}$)	$\log F_{X_{t,c}}$ ($\text{erg cm}^{-2} \text{s}^{-1}$)	$\log L_{X_{h,c}}$ (erg s^{-1})	$\log L_{X_{t,c}}$ (erg s^{-1})
203308.57+411915.3	2MASS J20330859+4119154	-	16	-	-	-	-	-	-	-	-

Source names determined using the SIMBAD database. Only those sources with > 50 counts were fit in *XSPEC*.

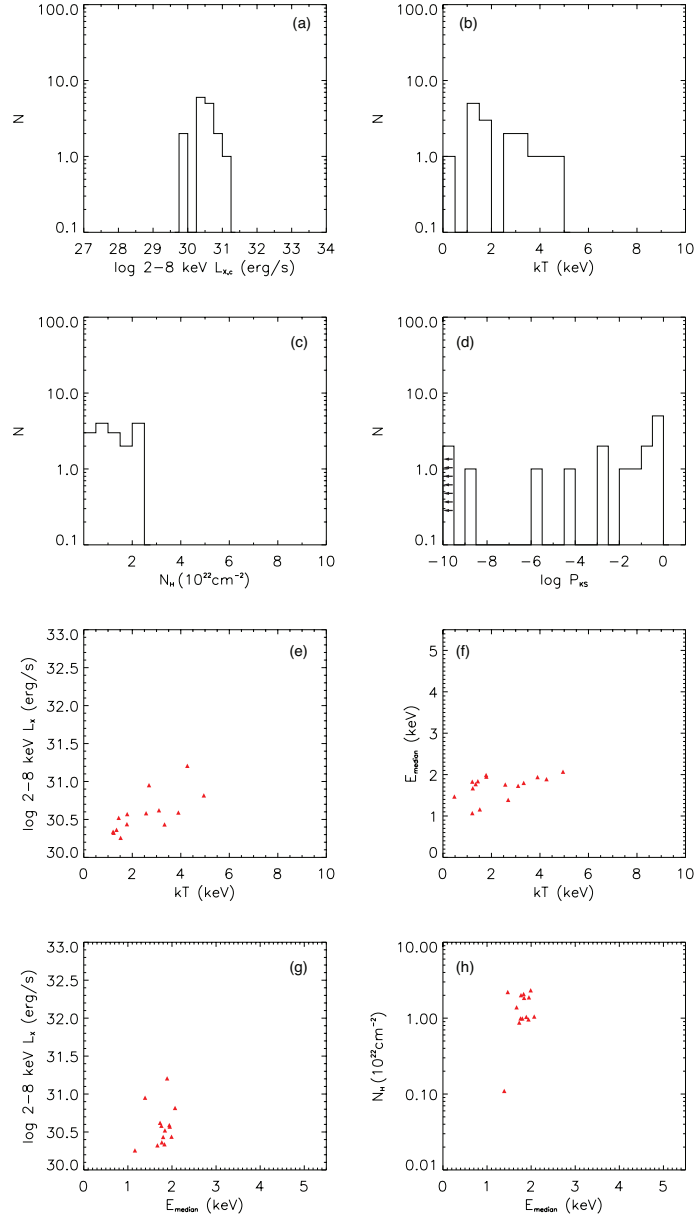


Figure B.6: Plots of derived source parameters for the bright PMS population of Bica 2. (a) Distribution of absorption corrected 2-8 keV L_X . (b) Distribution of best fit thermal plasma temperature (kT). (c) Distribution of best fit absorbing hydrogen column (N_H). (d) Distribution of Kolmogorov-Smirnov variability statistic with $\log P_{KS} < 0.05$ indicating variability. (e) Plot of absorption corrected 2-8 keV L_X against best fit thermal plasma temperature (kT). (f) Plot of median photon energy (E_{median}) against best fit thermal plasma temperature (kT). (g) Plot of absorption corrected 2-8 keV L_X against median photon energy (E_{median}). (h) Plot of best fit absorbing hydrogen column (N_H) against median photon energy (E_{median}).

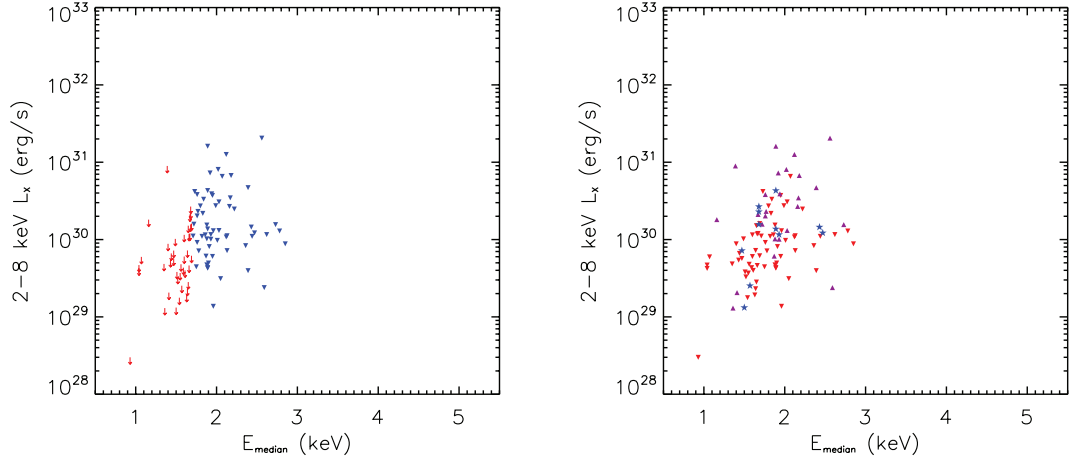


Figure B.7: Plot of the 2-8 keV L_X against the median detected photon energy (E_{median}) for the Bica 2 PMS population divided according to E_{median} (left) and variability (right). Left: the red arrows mark $E_{\text{median}} < 1.7$ keV (indicating an upper limit of $\log N_{\text{H}} \lesssim 22.0 \text{ cm}^{-2}$), blue inverted triangles 1.7-3 keV (indicating the lightly obscured population) and purple triangles > 3 keV (indicating the heavily obscured population). Right: Inverted red triangles refer to non-variable sources, blue stars representing variable sources and the purple triangles representing strongly variable flaring sources.

Table B.6: Bica 2 Diffuse Emission X-ray Spectral Parameters

Region	N_{H} (10^{22} cm^2)	kT (keV)	kT_2 (keV)	Z/Z_{\odot}	χ^2/ν	$\log F_{X_{h,c}}$ ($\text{erg cm}^{-2} \text{ s}^{-1}$)	$\log F_{X_{t,c}}$ ($\text{erg cm}^{-2} \text{ s}^{-1}$)	$\log L_{X_{h,c}}$ (erg s^{-1})	$\log L_{X_{t,c}}$ (erg s^{-1})
total	$0.71^{0.86}_{0.58}$	$0.54^{0.65}_{0.42}$	$2.45^{4.27}_{1.95}$	$0.15^{0.25}_{0.08}$	0.92/230	-12.25	-11.41	32.09	32.93
core	$1.22^{1.38}_{1.01}$	$0.23^{0.34}_{0.18}$	$1.39^{1.58}_{1.19}$	$0.28^{0.63}_{0.12}$	1.10/142	-12.61	-11.90	31.72	32.43

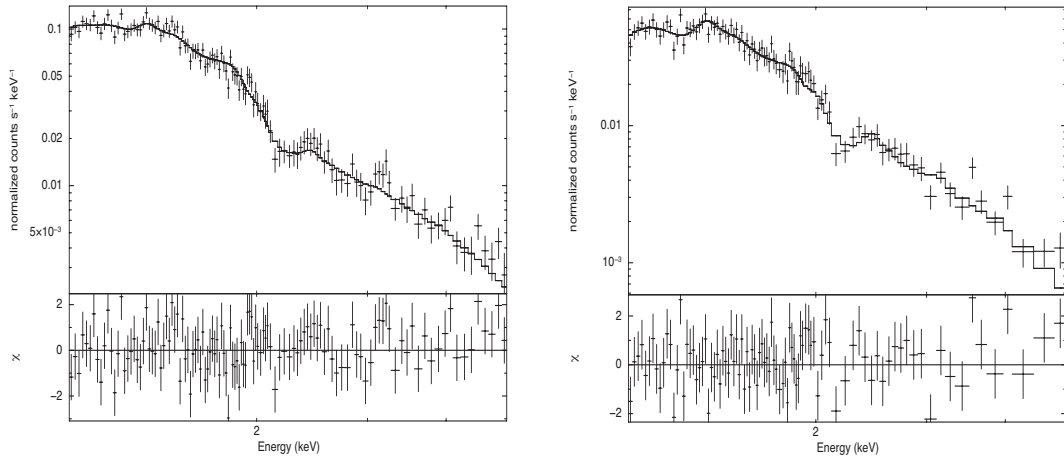


Figure B.8: Bica 2 total cluster diffuse emission spectrum (left) and cluster core diffuse emission spectrum (right). The spectra were rebinned for plotting purposes using XSPEC's *'setplot rebin'* command. Only the 1-5 keV energy range is shown as the spectra approach background levels outside this range.

B.2 IC 1590

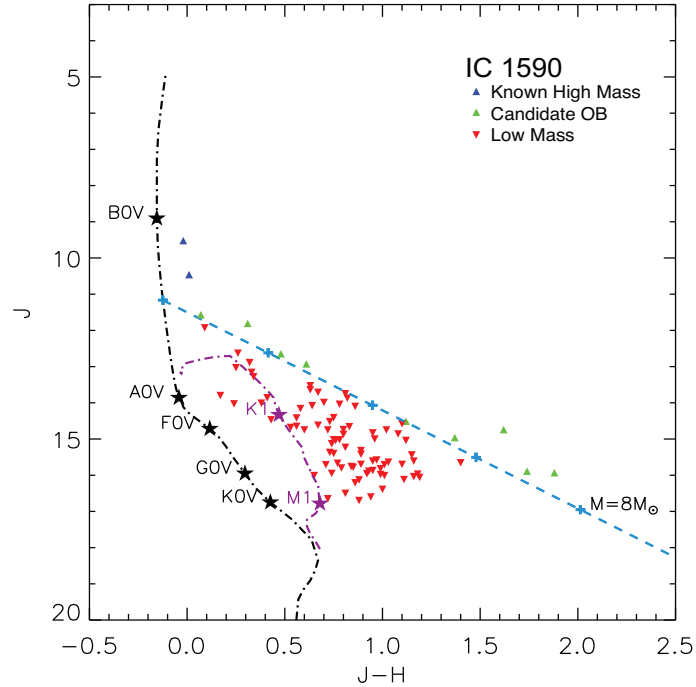


Figure B.9: IC 1590 2MASS J vs J-H colour magnitude diagram. The blue triangles indicate the known high mass stars, the light green triangles indicate the candidate OB stars and the red inverted triangles indicate low mass sources. The black dashed dotted line is the 3.5 Myr main sequence isochrone with spectral types marked calculated for $A_V = 0$. The purple dashed dotted line is the 3.5 Myr PMS isochrone with spectral types marked. The light blue dashed line is the $8M_{\odot}$ reddening vector with the crosses marking every $A_V = 5$.

Table B.7: IC 1590 Known High Mass Star X-ray Spectral Parameters

<i>Chandra</i> Source (CXO J)	Name	Sp. Type	<i>Net Cts.</i>	N_{H} (10^{22}cm^2)	kT (keV)	kT_2 (keV)	χ^2/ν	$\log F_{X_{h,c}}$ ($\text{erg cm}^{-2} \text{s}^{-1}$)	$\log F_{X_{t,c}}$ ($\text{erg cm}^{-2} \text{s}^{-1}$)	$\log L_{X_{h,c}}$ (erg s^{-1})	$\log L_{X_{t,c}}$ (erg s^{-1})
005244.78+563706.4	CDS 103	B	8	-	-	-	-	-	-	-	-
005248.96+563731.0	BD+55 191D	O9.5	92	0.01_{-}	0.70_{-}	-	4.9/5	-14.63	-14.07	30.38	30.95
005249.10+563907.8	GT 65	B1.5V	15	-	-	-	-	-	-	-	-
005249.25+563739.5	BD+55 191B	O8	607	$0.25_{0.11}^{0.40}$	$0.31_{0.39}^{0.25}$	-	1.45/23	-14.68	-13.08	30.33	31.94
005249.57+563736.8	BD+55 191C	O9V	88	$0.21_{0.64}^{-}$	$0.40_{0.60}^{0.15}$	-	0.81/5	-14.92	-13.65	30.09	31.36
005249.82+563936.7	BD+55 191A	O6.5V((f))	19	-	-	-	-	-	-	-	-

High mass sources identified using the SIMBAD database. Only those sources with > 50 counts were fit in *XSPEC*.

Table B.8: IC 1590 Candidate OB Star X-ray Spectral Parameters

<i>Chandra</i> Source (CXO J)	Name	Sp. Type	<i>Net Cts.</i>	N_{H} (10^{22}cm^2)	kT (keV)	kT_2 (keV)	χ^2/ν	$\log F_{X_{h,c}}$ ($\text{erg cm}^{-2} \text{s}^{-1}$)	$\log F_{X_{t,c}}$ ($\text{erg cm}^{-2} \text{s}^{-1}$)	$\log L_{X_{h,c}}$ (erg s^{-1})	$\log L_{X_{t,c}}$ (erg s^{-1})
005218.88+563305.8	-	-	31	-	-	-	-	-	-	-	-
005222.23+563242.8	-	-	4	-	-	-	-	-	-	-	-
005222.43+563426.6	-	-	16	-	-	-	-	-	-	-	-
005223.17+563319.5	-	-	6	-	-	-	-	-	-	-	-
005227.32+563403.1	-	-	6	-	-	-	-	-	-	-	-
005238.83+563737.0	-	-	19	-	-	-	-	-	-	-	-
005240.60+563550.2	-	-	40	-	-	-	-	-	-	-	-
005243.47+563711.6	-	-	7	-	-	-	-	-	-	-	-
005257.64+563838.8	-	-	58	0.01_{-}	1.78_{-}	-	2.01/2	-14.56	-14.09	30.45	30.93

Source names determined using the SIMBAD database. Only those sources with > 50 counts were fit in *XSPEC*.

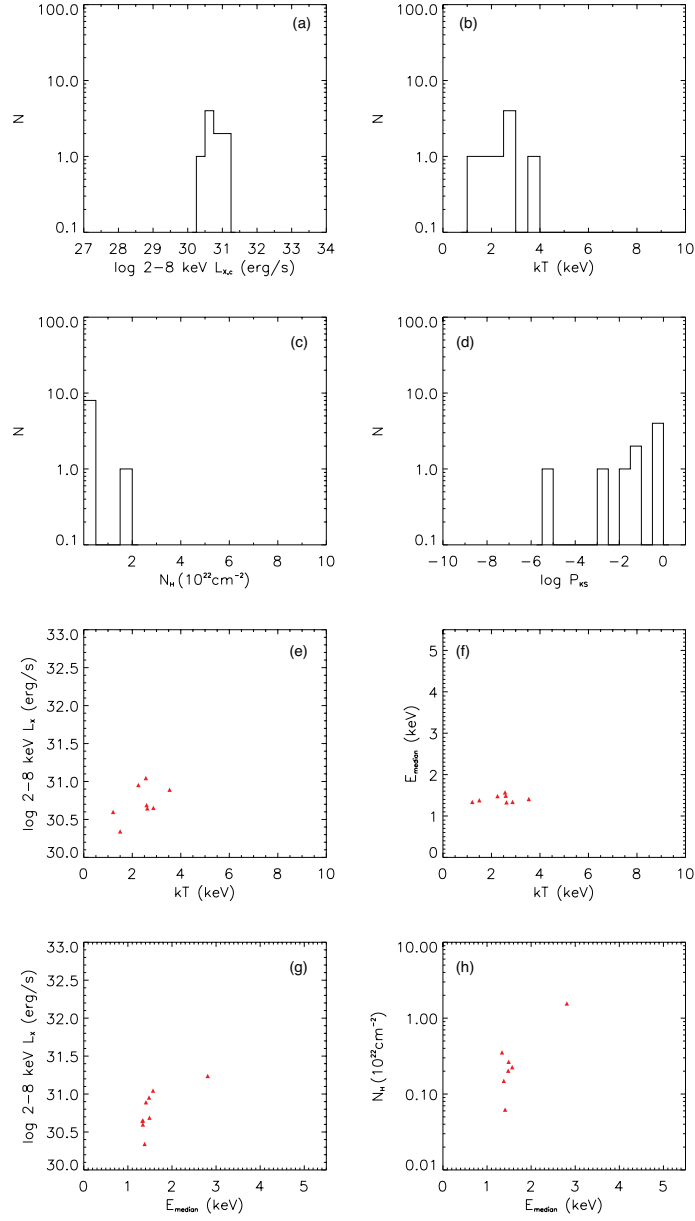


Figure B.10: Plots of derived source parameters for the bright PMS population of IC 1590. (a) Distribution of absorption corrected 2-8 keV L_X . (b) Distribution of best fit thermal plasma temperature (kT). (c) Distribution of best fit absorbing hydrogen column (N_H). (d) Distribution of Kolmogorov-Smirnov variability statistic with $\log P_{KS} < 0.05$ indicating variability. (e) Plot of absorption corrected 2-8 keV L_X against best fit thermal plasma temperature (kT). (f) Plot of median photon energy (E_{median}) against best fit thermal plasma temperature (kT). (g) Plot of absorption corrected 2-8 keV L_X against median photon energy (E_{median}). (h) Plot of best fit absorbing hydrogen column (N_H) against median photon energy (E_{median}).

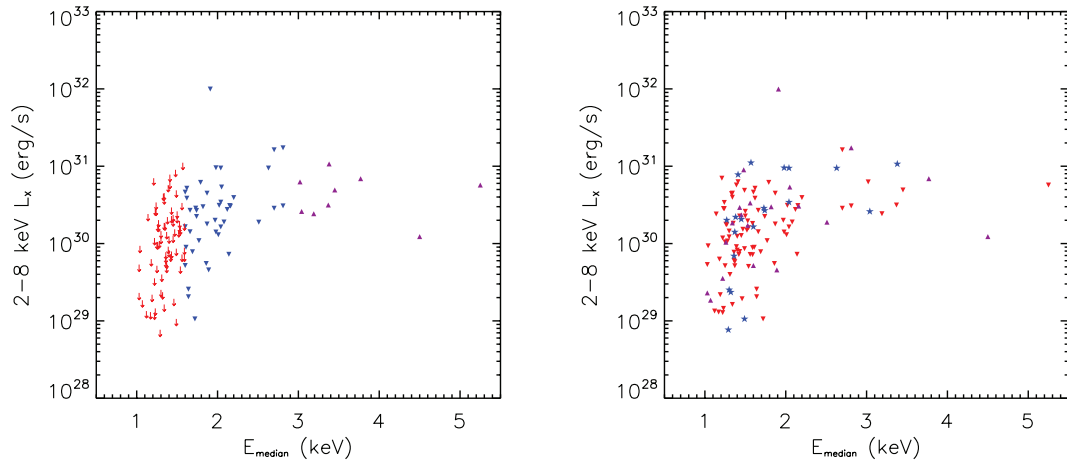


Figure B.11: Plot of the 2-8 keV L_X against the median detected photon energy (E_{median}) for the IC 1590 PMS population divided according to E_{median} (left) and variability (right). Left: the red arrows mark $E_{\text{median}} < 1.6$ keV (indicating an upper limit of $\log N_{\text{H}} \lesssim 22.0 \text{ cm}^{-2}$), blue inverted triangles 1.6-3 keV (indicating the lightly obscured population) and purple triangles > 3 keV (indicating the heavily obscured population). Right: Inverted red triangles refer to non-variable sources, blue stars representing variable sources and the purple triangles representing strongly variable flaring sources.

Table B.9: IC 1590 Diffuse Emission X-ray Spectral Parameters

Region	N_{H} (10^{22} cm^2)	kT (keV)	Z/Z_{\odot}	χ^2/ν	$\log F_{X_{h,c}}$ ($\text{erg cm}^{-2} \text{ s}^{-1}$)	$\log F_{X_{t,c}}$ ($\text{erg cm}^{-2} \text{ s}^{-1}$)	$\log L_{X_{h,c}}$ (erg s^{-1})	$\log L_{X_{t,c}}$ (erg s^{-1})
'total'	$0.65^{+0.93}_{-0.28}$	$0.76^{+1.19}_{-0.28}$	$1.21^{+0.25}_{-0.25}$	0.75/36	-13.57	-12.31	31.35	32.71

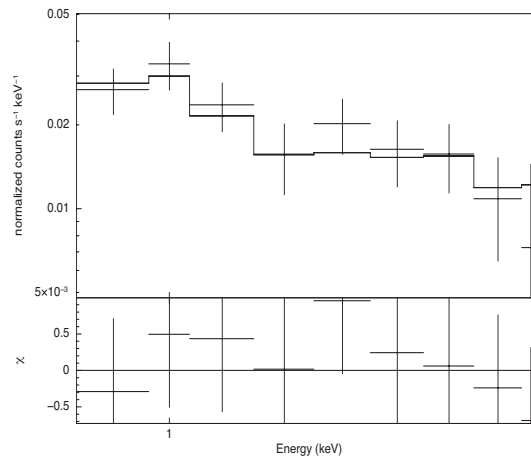


Figure B.12: IC 1590 total cluster diffuse emission spectrum. The spectrum was rebinned for plotting purposes using XSPEC's *'setplot rebin'* command. Only the 0.9-1.5 keV energy range is shown as the spectrum approaches background levels outside this range.

B.3 NGC 1893

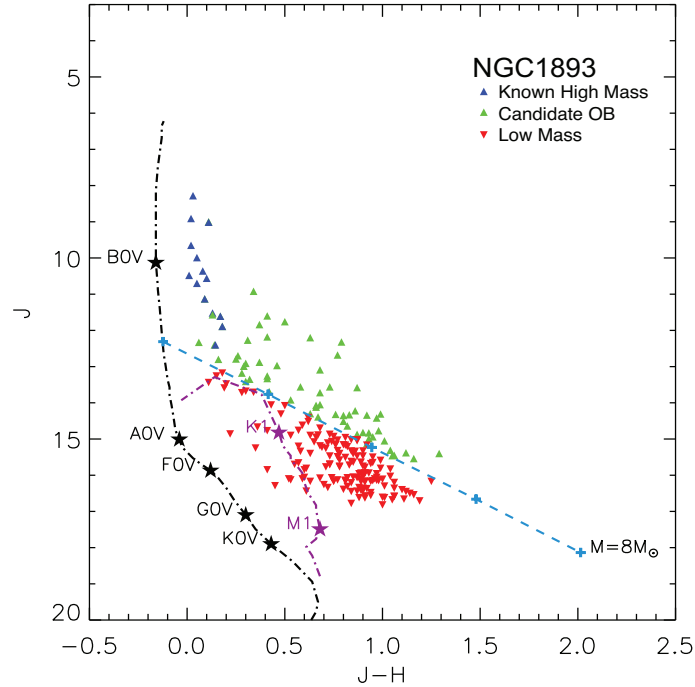


Figure B.13: NGC 1893 2MASS J vs J-H colour magnitude diagram. The blue triangles indicate the known high mass stars, the light green triangles indicate the candidate OB stars and the red inverted triangles indicate low mass sources. The black dashed dotted line is the 3 Myr main sequence isochrone with spectral types marked calculated for $A_V = 0$. The purple dashed dotted line is the 3 Myr PMS isochrone with spectral types marked. The light blue dashed line is the $8M_{\odot}$ reddening vector with the crosses marking every $A_V = 5$.

Table B.10: NGC 1893 Known High Mass Star X-ray Spectral Parameters

<i>Chandra</i> Source (CXO J)	Name	Sp. Type	<i>Net Cts.</i>	N_{H} (10^{22} cm^2)	kT (keV)	kT_2 (keV)	χ^2/ν	$\log F_{X_{h,c}}$ ($\text{erg cm}^{-2} \text{ s}^{-1}$)	$\log F_{X_{t,c}}$ ($\text{erg cm}^{-2} \text{ s}^{-1}$)	$\log L_{X_{h,c}}$ (erg s^{-1})	$\log L_{X_{t,c}}$ (erg s^{-1})
052218.44+332820.8	HOAG 14	B2V	246	$0.18_{-0.04}^{0.37}$	$1.93_{-1.47}^{2.72}$	-	0.61/10	-14.48	-14.04	30.86	31.30
052229.30+333050.2	HD 242908	O4V((f))	4976	$0.21_{-0.16}^{0.25}$	$0.60_{-0.57}^{0.64}$	$6.17_{-13.69}^{3.55}$	1.13/126	-13.36	-12.70	31.98	32.66
052236.74+332312.4	-	B1.5V	30	-	-	-	-	-	-	-	-
052239.01+332626.6	CUF 3113	B5IV	133	$0.29_{-0.08}^{0.54}$	$2.05_{-1.43}^{3.35}$	-	0.22/5	-14.76	-14.34	30.59	31.01
052239.69+332218.1	HOAG 4	O8	816	$0.19_{-0.05}^{0.28}$	$0.64_{-0.58}^{0.74}$	-	1.59/34	-14.87	-13.52	30.48	31.83
052240.01+331909.5	HD 242926	O8V((f))	161	$0.43_{-0.13}^{0.86}$	$0.27_{-0.18}^{0.50}$	-	0.54/4	-14.93	-13.38	29.41	31.97
052243.99+332626.5	Hoag 5	O7V	364	$0.31_{-0.2}^{0.52}$	$0.47_{-0.36}^{0.58}$	-	0.57/17	-15.54	-13.80	29.80	31.54
052244.77+332636.4	-	B0.5V	56	$0.16_{-}^{0.76}$	$2.13_{-0.46}^{5.89}$	-	1.13/6	-15.12	-14.71	30.23	30.64
052245.11+332423.1	Hoag 16	B2.5V	34	-	-	-	-	-	-	-	-
052246.54+332511.2	HD 242935	O7.5V((f))	578	$0.01_{-}^{0.07}$	$0.63_{-0.69}^{0.56}$	-	0.92/23	-15.23	-13.90	31.11	31.44
052257.53+332600.0	HOAG 21	B2V	134	$0.07_{-}^{0.27}$	$2.25_{-1.58}^{3.99}$	-	0.99/5	-14.69	-14.30	30.65	31.04
052258.59+332402.3	HOAG 25	B1.5V	67	0.02_{-}	1.8_{-}	-	2.58/5	-15.27	-14.80	30.08	30.55
052300.81+332947.5	-	B1.5V	20	-	-	-	-	-	-	-	-
052302.25+333137.5	Hoag 11	B0.2V	410	$0.37_{-0.25}^{0.53}$	$3.84_{-2.91}^{5.22}$	-	1.55/21	-14.07	-13.79	31.28	31.55
052307.52+332837.3	-	B2.5V	29	-	-	-	-	-	-	-	-
052314.32+333350.5	Hoag 7	B0.2V	35	-	-	-	-	-	-	-	-
052319.41+332707.9	Hoag 9	B0.2V	18	-	-	-	-	-	-	-	-
052319.72+333211.2	Hoag 12	B0.3V	24	-	-	-	-	-	-	-	-

High mass sources identified using the high mass source lists of [Massey et al. \(1995\)](#) and the SIMBAD database. Only those sources with > 50 counts were fit in *XSPEC*.

Table B.11: NGC 1893 Candidate OB Star X-ray Spectral Parameters

<i>Chandra</i> Source (CXO J)	Name	Sp. Type	<i>Net Cts.</i>	N_{H} (10^{22} cm^2)	kT (keV)	kT_2 (keV)	χ^2/ν	$\log F_{X_{h,c}}$ ($\text{erg cm}^{-2} \text{ s}^{-1}$)	$\log F_{X_{t,c}}$ ($\text{erg cm}^{-2} \text{ s}^{-1}$)	$\log L_{X_{h,c}}$ (erg s^{-1})	$\log L_{X_{t,c}}$ (erg s^{-1})
052214.85+332907.3	2MASS J05221483+3329075	-	110	0.05 $_{-}$	0.7 $_{-}$	-	1.42/6	-15.77	-14.52	29.57	30.82
052216.32+333140.7	2MASS J05221635+3331410	-	137	0.26 $_{-}^{0.88}$	1.27 $_{0.76}^{1.84}$	-	0.53/5	-14.99	-14.32	30.36	31.02
052221.52+332851.0	2MASS J05222153+3328515	-	223	0.56 $_{0.29}^{0.92}$	1.77 $_{0.94}^{2.37}$	-	0.57/9	-14.47	-14.00	30.87	31.35
052225.01+333106.2	2MASS J05222153+3328515	-	21	-	-	-	-	-	-	-	-
052230.64+332454.5	-	-	49	-	-	-	-	-	-	-	-
052232.88+332420.1	-	-	50	-	-	-	-	-	-	-	-
052237.35+332005.3	-	-	419	0.37 $_{0.21}^{0.59}$	2.01 $_{1.49}^{2.6}$	-	1.04/19	-14.16	-13.74	31.18	31.61
052238.20+332152.6	-	-	241	0.48 $_{0.29}^{0.72}$	2.43 $_{1.66}^{3.76}$	-	0.44/10	-14.32	-13.95	31.03	31.40
052238.23+333202.9	2MASS J05223822+3332032	-	19	-	-	-	-	-	-	-	-
052238.34+332141.8	2MASS J05223832+3321420	-	92	0.11 $_{-}^{0.46}$	3.92 $_{1.8}^{23.9}$	-	0.37/5	-14.71	-14.44	30.63	30.90
052238.41+333136.9	2MASS J05223840+3331370	-	138	-	-	-	-	-	-	-	-
052241.51+332050.0	-	-	79	0.09 $_{-}$	5.44 $_{-}$	-	2.08/5	-14.62	-14.39	30.72	30.95
052241.94+332218.7	-	-	39	-	-	-	-	-	-	-	-
052242.48+332313.0	-	-	149	0.27 $_{0.07}^{0.61}$	2.02 $_{1.14}^{3.21}$	-	0.6/6	-14.61	-14.19	30.73	31.16
052243.32+332845.7	2MASS J05224331+3328459	-	21	-	-	-	-	-	-	-	-
052243.77+332525.5	2MASS J05224378+3325257	-	145	1.92 $_{1.42}^{5.8}$	2.48 $_{1.72}^{3.7}$	-	0.61/6	-14.19	-13.82	31.16	31.52
052244.29+332443.2	HOAG 29	-	33	-	-	-	-	-	-	-	-
052244.61+332517.1	[MJD95] J052244.61+332517.9	-	376	0.25 $_{0.15}^{0.4}$	2.33 $_{1.75}^{3.03}$	-	1.32/18	-14.21	-13.82	31.14	31.52
052245.76+332816.2	2MASS J05224578+3328162	-	8	-	-	-	-	-	-	-	-
052246.15+332520.7	[MJD95] J052246.15+332521.2	-	695	0.30 $_{0.21}^{0.42}$	5.44 $_{4.21}^{7.54}$	-	0.94/36	-13.75	-13.52	31.60	31.82
052246.37+332612.3	-	-	52	0.2 $_{-}^{1.2}$	1.93 $_{0.38}^{4.63}$	-	0.09/5	-15.23	-14.79	30.11	30.56
052246.83+332927.9	2MASS J05224683+3329279	-	69	0.26 $_{-}^{0.67}$	1.21 $_{0.92}^{1.81}$	-	0.48/5	-15.32	-14.62	30.02	30.72
052247.14+332228.9	-	-	90	0.19 $_{-}^{0.64}$	1.61 $_{1.02}^{3}$	-	0.33/5	-15.07	-14.55	30.27	30.79
052247.84+332639.3	2MASS J05224784+3326394	-	291	0.24 $_{0.13}^{0.4}$	2.88 $_{2.09}^{4.07}$	-	0.46/14	-14.33	-14.01	31.01	31.34
052249.19+332548.2	2MASS J05224920+3325482	-	282	0.28 $_{0.16}^{0.53}$	1.48 $_{1.13}^{1.71}$	-	1/13	-14.64	-14.07	30.71	31.27
052249.25+332541.8	2MASS J05224924+3325421	-	349	0.24 $_{0.13}^{0.37}$	2.68 $_{2.14}^{3.52}$	-	1.14/17	-14.29	-13.95	31.06	31.40
052249.35+332902.0	-	-	81	0.29 $_{0.06}^{0.78}$	1.45 $_{1.12}^{2.37}$	-	1.14/5	-15.21	-14.63	30.14	30.71
052249.36+332555.4	-	-	183	0.21 $_{0.06}^{0.41}$	2.86 $_{1.93}^{4.5}$	-	1.31/8	-14.56	-14.23	30.78	31.11
052249.59+333001.8	2MASS J05224957+3330015	-	13	-	-	-	-	-	-	-	-
052250.02+332602.2	2MASS J05225003+3326023	-	225	0.19 $_{0.07}^{0.36}$	1.61 $_{1.31}^{1.96}$	-	1.1/10	-14.70	-14.18	30.64	31.17
052252.29+332407.2	2MASS J05225229+3324074	-	314	0.23 $_{0.11}^{0.37}$	3.17 $_{2.4}^{4.25}$	-	0.5/15	-14.24	-13.93	31.11	31.42
052252.74+332207.7	-	-	169	0.07 $_{-}^{0.27}$	2.51 $_{1.69}^{4.37}$	-	0.71/6	-14.64	-14.28	30.70	31.06

Table B.12: NGC 1893 Candidate OB Star X-ray Spectral Parameters (Cont.)

<i>Chandra</i> Source (CXO J)	Name	Sp. Type	<i>Net Cts.</i>	N_{H} (10^{22}cm^2)	kT (keV)	kT_2 (keV)	χ^2/ν	$\log F_{X_{h,c}}$ ($\text{erg cm}^{-2} \text{s}^{-1}$)	$\log F_{X_{t,c}}$ ($\text{erg cm}^{-2} \text{s}^{-1}$)	$\log L_{X_{h,c}}$ (erg s^{-1})	$\log L_{X_{t,c}}$ (erg s^{-1})
052253.14+333116.3	2MASS J05225315+3331164	-	435	$0.13_{0.05}^{0.24}$	$4.22_{3.14}^{6.13}$	-	1.49/22	-14.07	-13.81	31.28	31.54
052253.42+333032.3	2MASS J05225338+3330326	-	164	$0.42_{0.13}^{0.82}$	$8.6_{3.65}^{56.7}$	-	0.87/6	-14.18	-13.99	31.17	31.36
052253.52+333124.9	2MASS J05225352+3331248	-	332	$0.19_{0.08}^{0.34}$	$2.95_{2.21}^{4.15}$	-	1.25/17	-14.25	-13.93	31.09	31.42
052253.96+332927.8	2MASS J05225397+3329277	-	12	-	-	-	-	-	-	-	-
052254.07+332632.8	-	-	188	$0.41_{0.21}^{1.53}$	$1.5_{0.61}^{1.83}$	-	0.54/8	-14.71	-14.15	30.63	31.19
052257.36+332822.4	2MASS J05225734+3328226	-	13	-	-	-	-	-	-	-	-
052300.05+333038.9	-	-	74	$0.14_{-}^{0.47}$	$2.2_{1.33}^{4.71}$	-	0.44/5	-15.03	-14.63	30.32	30.72
052300.85+332817.0	2MASS J05230087+3328169	-	102	0.01_{-}	7.28_{-}	-	1.02/5	-14.66	-14.46	30.68	30.89
052302.51+332709.4	-	-	30	-	-	-	-	-	-	-	-
052302.94+333214.6	2MASS J05230293+3332146	-	20	-	-	-	-	-	-	-	-
052303.16+332704.5	-	-	83	0.28_{-}	3.13_{-}	-	2.1/5	-14.85	-14.54	30.49	30.80
052303.30+332925.0	2MASS J05230331+3329251	-	23	-	-	-	-	-	-	-	-
052303.82+332923.8	2MASS J05230382+3329241	-	65	$0.72_{0.27}^{1.62}$	$1.49_{1.09}^{2.33}$	-	0.1/6	-14.82	-14.26	30.52	31.08
052304.20+332858.2	2MASS J05230422+3328582	-	108	$0.32_{0.05}^{0.67}$	$4.94_{2.56}^{17.8}$	-	0.87/5	-14.60	-14.36	30.74	30.98
052305.37+332313.7	2MASS J05230537+3323138	-	316	$0.29_{0.16}^{0.46}$	$1.25_{1.09}^{1.45}$	-	1/15	-14.60	-13.92	30.75	31.42
052306.72+332432.6	2MASS J05230671+3324327	-	173	0.01_{-}	1.52_{-}	-	3.77/7	-14.89	-14.34	30.46	31.00
052308.37+332837.6	-	-	316	$2.25_{1.98}^{2.77}$	$2.53_{1.96}^{3.34}$	-	0.76/15	-13.86	-13.50	31.48	31.84
052308.92+332831.3	NMI E17	-	540	$0.46_{0.34}^{0.62}$	$2.39_{1.97}^{2.99}$	-	0.64/28	-14.03	-13.66	31.31	31.69
052309.47+332425.0	2MASS J05230948+3324251	-	131	$0.16_{-}^{0.4}$	$2.28_{1.88}^{3.71}$	-	1.05/5	-14.73	-14.34	30.61	31.00
052309.91+332908.2	2MASS J05230995+3329087	-	23	-	-	-	-	-	-	-	-
052311.63+332408.6	2MASS J05231160+3324082	-	83	$0.45_{0.11}^{1.33}$	$1.64_{0.86}^{3.1}$	-	0.23/6	-14.98	-14.47	30.37	30.88
052311.76+332832.2	2MASS J05231175+3328321	-	37	-	-	-	-	-	-	-	-
052311.85+332845.4	2MASS J05231187+3328454	-	114	0.06_{-}	1.07_{-}	-	1.3/5	-15.40	-14.60	29.95	30.75
052312.62+333040.0	-	-	73	$0.5_{0.09}^{1.36}$	$1.88_{1.23}^{4.05}$	-	0.92/6	-14.97	-14.51	30.38	30.83
052315.71+332419.8	2MASS J05231568+3324192	-	33	-	-	-	-	-	-	-	-
052319.36+333231.7	-	-	352	-	-	-	-	-	-	-	-
052321.20+332944.5	2MASS J05232121+3329447	-	827	-	-	-	-	-	-	-	-

Source names determined using the SIMBAD database. Only those sources with > 50 counts were fit in *XSPEC*.

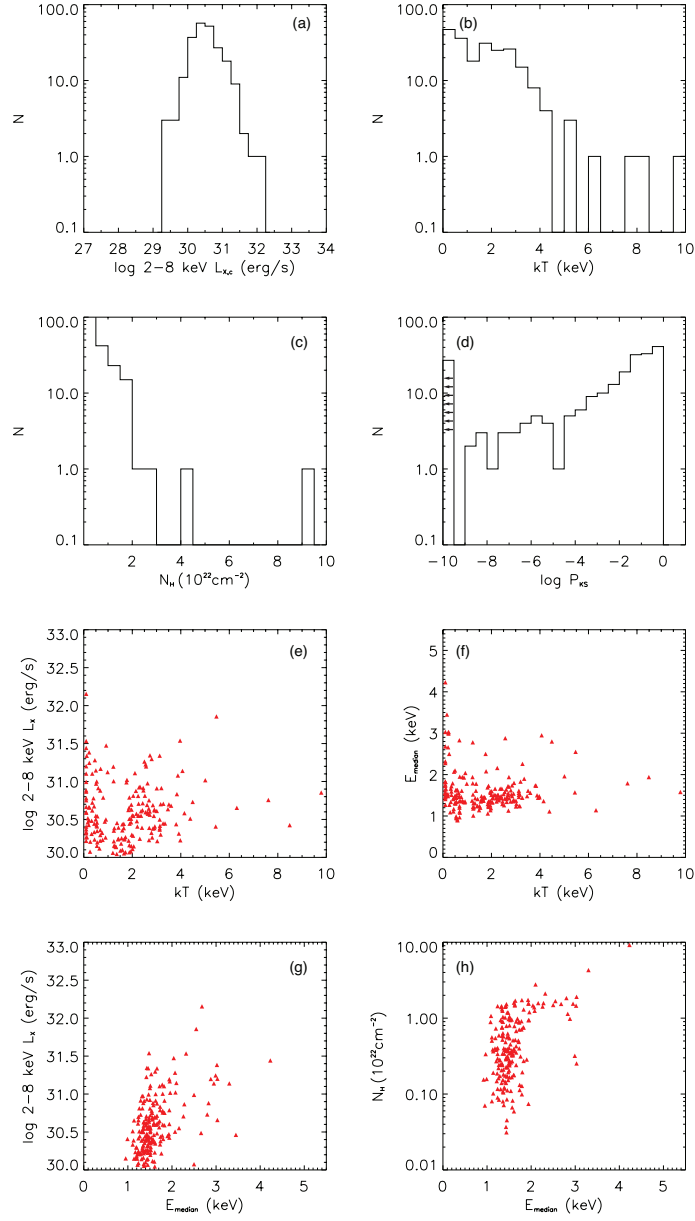


Figure B.14: Plots of derived source parameters for the bright PMS population of NGC 1893. (a) Distribution of absorption corrected 2-8 keV L_X . (b) Distribution of best fit thermal plasma temperature (kT). (c) Distribution of best fit absorbing hydrogen column (N_H). (d) Distribution of Kolmogorov-Smirnov variability statistic with $\log P_{KS} < 0.05$ indicating variability. (e) Plot of absorption corrected 2-8 keV L_X against best fit thermal plasma temperature (kT). (f) Plot of median photon energy (E_{median}) against best fit thermal plasma temperature (kT). (g) Plot of absorption corrected 2-8 keV L_X against median photon energy (E_{median}). (h) Plot of best fit absorbing hydrogen column (N_H) against median photon energy (E_{median}).

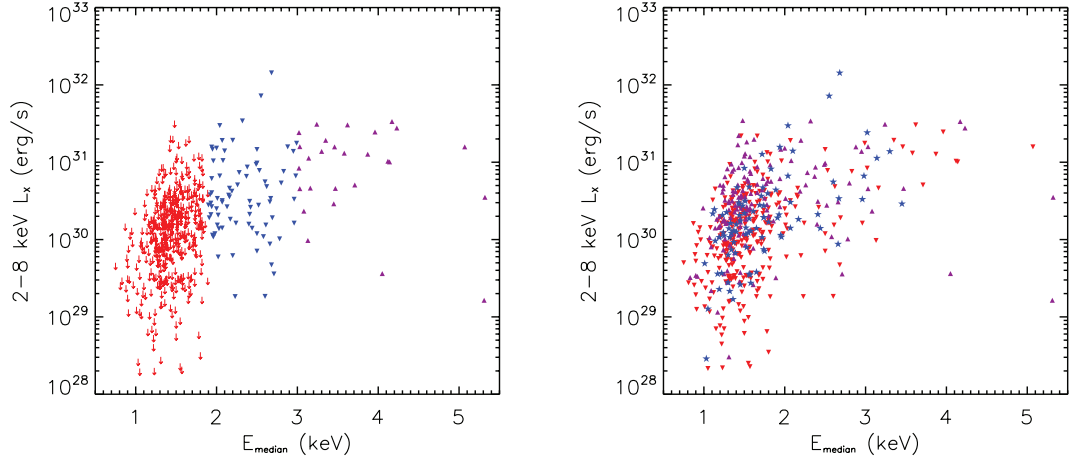


Figure B.15: Plot of the 2-8 keV L_X against the median detected photon energy (E_{median}) for the NGC 1893 PMS population divided according to E_{median} (left) and variability (right). Left: the red arrows mark $E_{\text{median}} < 1.9$ keV (indicating an upper limit of $\log N_{\text{H}} \lesssim 22.3 \text{ cm}^{-2}$), blue inverted triangles 1.9-3 keV (indicating the lightly obscured population) and purple triangles > 3 keV (indicating the heavily obscured population). Right: Inverted red triangles refer to non-variable sources, blue stars representing variable sources and the purple triangles representing strongly variable flaring sources.

Table B.13: NGC 1893 Diffuse Emission X-ray Spectral Parameters

Region	N_{H} (10^{22} cm^2)	kT (keV)	Z/Z_{\odot}	χ^2/ν	$\log F_{X_{h,c}}$ ($\text{erg cm}^{-2} \text{ s}^{-1}$)	$\log F_{X_{t,c}}$ ($\text{erg cm}^{-2} \text{ s}^{-1}$)	$\log L_{X_{h,c}}$ (erg s^{-1})	$\log L_{X_{t,c}}$ (erg s^{-1})
all FOV	$0.18_{-0.36}^{0.60}$	$0.88_{1.06}^{0.72}$	$0.04_{0.09}^{0.02}$	1.05/137	-13.33	-12.41	32.02	32.94
core	$0.20_{0.02}^{0.36}$	$0.90_{0.79}^{1.09}$	$0.05_{0.02}^{0.09}$	0.92/239	-13.54	-12.64	31.80	32.71

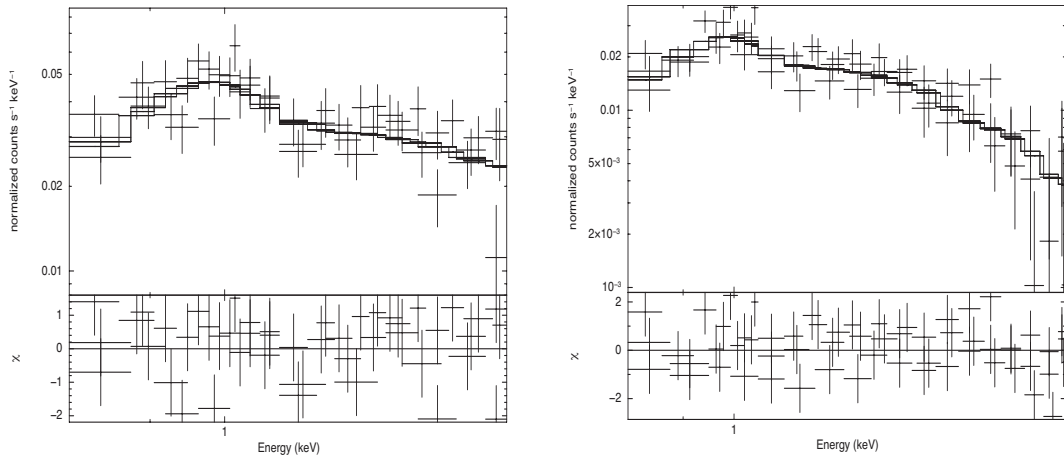


Figure B.16: NGC 1893 total cluster diffuse emission spectrum (left) and cluster core diffuse emission spectrum (right). The spectra were rebinned for plotting purposes using XSPEC's `'setplot rebin'` command. Only the 0.8-1.5 keV and 0.8-2 keV energy ranges are shown for the all FOV and core spectra respectively, as they approach background levels outside these ranges.

B.4 NGC 2362

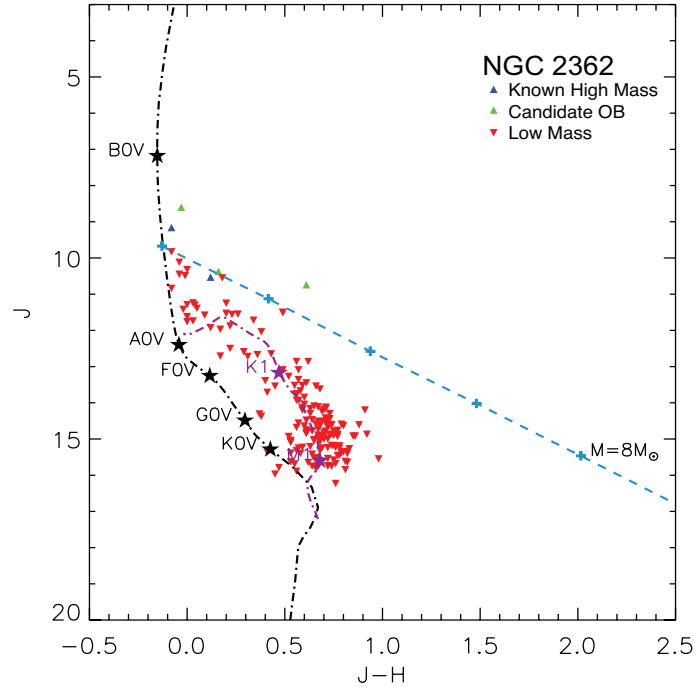


Figure B.17: NGC 2362 2MASS J vs J-H colour magnitude diagram. The blue triangles indicate the known high mass stars, the light green triangles indicate the candidate OB stars and the red inverted triangles indicate low mass sources. The black dashed dotted line is the 5 Myr main sequence isochrone with spectral types marked calculated for $A_V = 0$. The purple dashed dotted line is the 5 Myr PMS isochrone with spectral types marked. The light blue dashed line is the $8M_{\odot}$ reddening vector with the crosses marking every $A_V = 5$.

Table B.14: NGC 2362 Known High Mass Star X-ray Spectral Parameters

<i>Chandra</i> Source (CXO J)	Name	Sp. Type	<i>Net Cts.</i>	N_{H} (10^{22}cm^2)	kT (keV)	kT_2 (keV)	χ^2/ν	$\log F_{X_{h,c}}$ ($\text{erg cm}^{-2} \text{s}^{-1}$)	$\log F_{X_{t,c}}$ ($\text{erg cm}^{-2} \text{s}^{-1}$)	$\log L_{X_{h,c}}$ (erg s^{-1})	$\log L_{X_{t,c}}$ (erg s^{-1})
071838.37-245819.9	2MASS J07183841-2458200	B2	121	$0.50_{-0.18}^{1.30}$	$0.54_{0.18}^{1.92}$	-	0.27/2	-15.82	-13.26	29.61	31.14
071841.04-250011.3	CD-24 5175	B2	18	-	-	-	-	-	-	-	-
071842.45-245715.7	τ CMa	O9Ib	7181	0.02_{-}	0.22_{-}	0.66_{-}	3.79/108	-13.74	-12.21	30.69	32.22
071846.17-245747.3	2MASS J07184619-2457476	B3	5	-	-	-	-	-	-	-	-
071858.39-245741.1	2MASS J07185844-2457410	B3Vw	261	$0.01_{-}^{0.05}$	$0.96_{0.80}^{1.10}$	-	1.54/13	-14.39	-13.68	30.04	30.75
071913.09-245721.2	MX CMa	B2V	71	$0.05_{-}^{0.70}$	$0.64_{0.20}^{0.78}$	-	0.38/4	-15.63	-14.21	28.80	30.22

High mass sources identified using the SIMBAD database. Only those sources with > 50 counts were fit in *XSPEC*.

Table B.15: NGC 2362 Candidate OB Star X-ray Spectral Parameters

<i>Chandra</i> Source (CXO J)	Name	Sp. Type	<i>Net Cts.</i>	N_{H} (10^{22}cm^2)	kT (keV)	kT_2 (keV)	χ^2/ν	$\log F_{X_{h,c}}$ ($\text{erg cm}^{-2} \text{s}^{-1}$)	$\log F_{X_{t,c}}$ ($\text{erg cm}^{-2} \text{s}^{-1}$)	$\log L_{X_{h,c}}$ (erg s^{-1})	$\log L_{X_{t,c}}$ (erg s^{-1})
071829.87-245438.2	2MASS J07182989-2454385	-	75	$0.71_{-0.22}^{1.64}$	$0.72_{0.22}^{3.99}$	-	0.94/2	-14.73	-13.65	29.70	30.77
071848.49-245656.0	2MASS J07184853-2456559	-	8	-	-	-	-	-	-	-	-
071851.58-250537.9	-	-	51	$0.03_{-}^{2.24}$	$0.52_{0.15}^{0.68}$	-	0.60/2	-15.48	-14.33	28.95	30.10

Source names determined using the SIMBAD database. Only those sources with > 50 counts were fit in *XSPEC*.

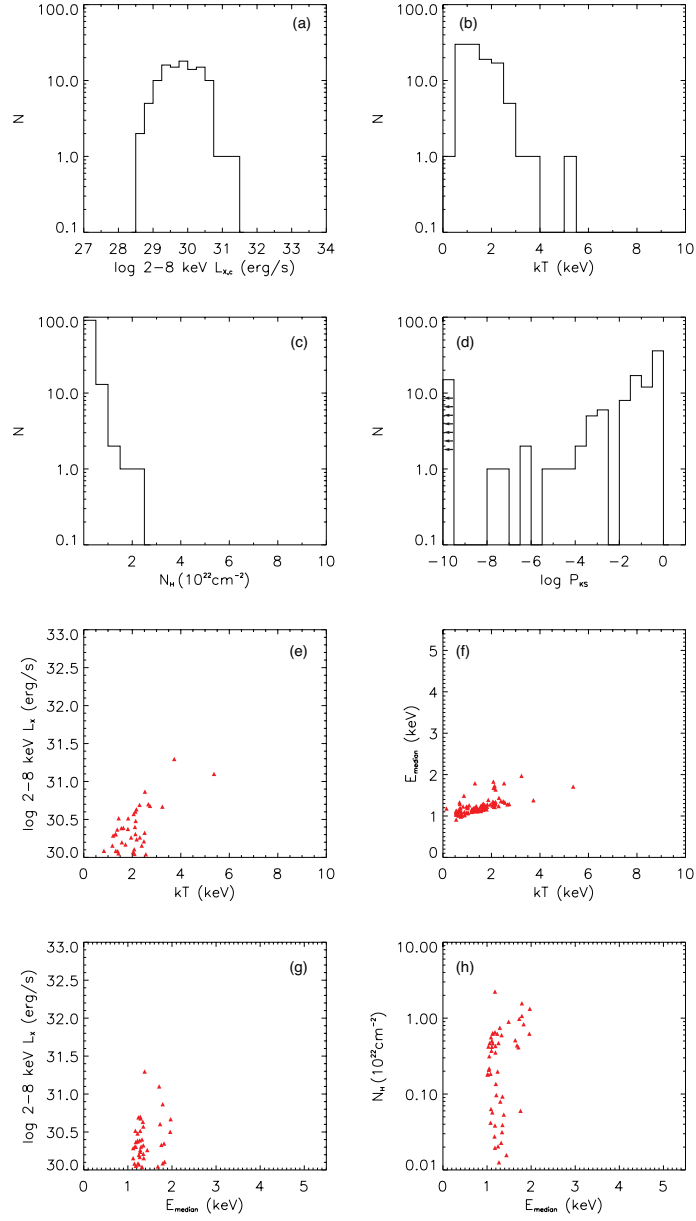


Figure B.18: Plots of derived source parameters for the bright PMS population of NGC 2362. (a) Distribution of absorption corrected 2-8 keV L_X . (b) Distribution of best fit thermal plasma temperature (kT). (c) Distribution of best fit absorbing hydrogen column (N_H). (d) Distribution of Kolmogorov-Smirnov variability statistic with $\log P_{KS} < 0.05$ indicating variability. (e) Plot of absorption corrected 2-8 keV L_X against best fit thermal plasma temperature (kT). (f) Plot of median photon energy (E_{median}) against best fit thermal plasma temperature (kT). (g) Plot of absorption corrected 2-8 keV L_X against median photon energy (E_{median}). (h) Plot of best fit absorbing hydrogen column (N_H) against median photon energy (E_{median}).

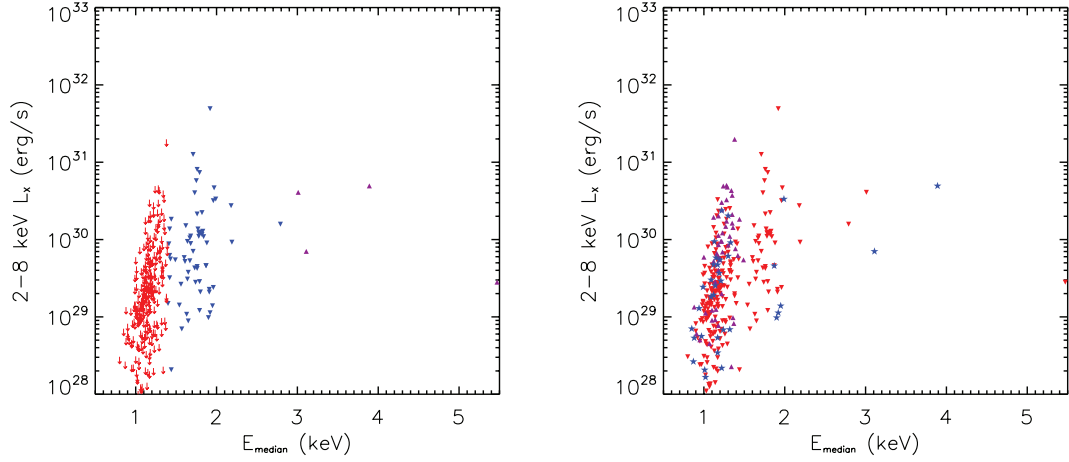


Figure B.19: Plot of the 2-8 keV L_X against the median detected photon energy (E_{median}) for the NGC 2362 PMS population divided according to E_{median} (left) and variability (right). Left: the red arrows mark $E_{\text{median}} < 1.4$ keV (indicating an upper limit of $\log N_{\text{H}} \lesssim 21.9 \text{ cm}^{-2}$), blue inverted triangles 1.4-3 keV (indicating the lightly obscured population) and purple triangles > 3 keV (indicating the heavily obscured population). Right: Inverted red triangles refer to non-variable sources, blue stars representing variable sources and the purple triangles representing strongly variable flaring sources.

Table B.16: NGC 2362 Diffuse Emission X-ray Spectral Parameters

Region	N_{H} (10^{22} cm^2)	kT (keV)	Z/Z_{\odot}	χ^2/ν	$\log F_{X_{h,c}}$ ($\text{erg cm}^{-2} \text{ s}^{-1}$)	$\log F_{X_{t,c}}$ ($\text{erg cm}^{-2} \text{ s}^{-1}$)	$\log L_{X_{h,c}}$ (erg s^{-1})	$\log L_{X_{t,c}}$ (erg s^{-1})
all FOV	$0.37_{-}^{1.04}$	$0.76_{0.61}^{0.84}$	$0.12_{0.06}^{3.78}$	0.75/43	-13.83	-12.33	30.60	32.10
core	$0.44_{0.38}^{0.50}$	$0.58_{0.53}^{0.62}$	$0.49_{0.28}^{1.52}$	0.83/86	-13.99	-12.37	30.44	32.06

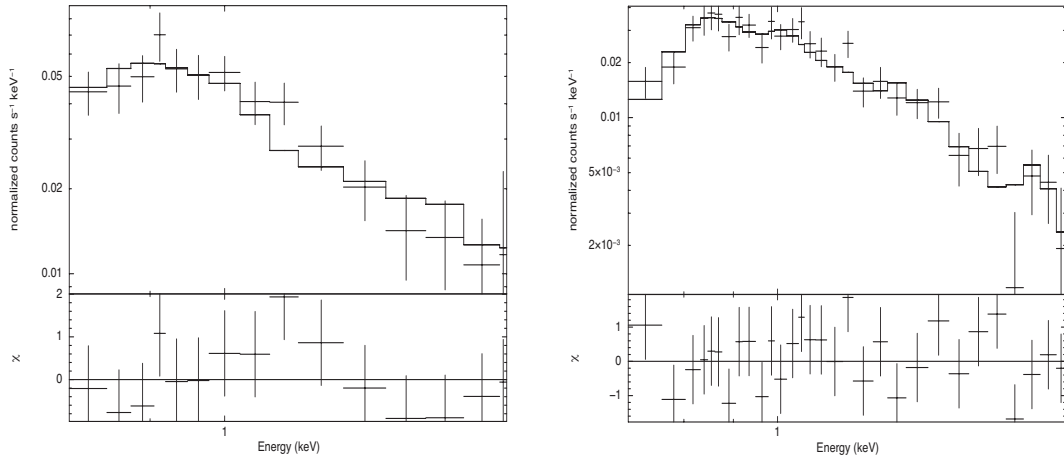


Figure B.20: NGC 2362 total cluster diffuse emission spectrum (left) and cluster core diffuse emission spectrum (right). The spectra were rebinned for plotting purposes using XSPEC's `'setplot rebin'` command. Only the 0.8-1.5 keV and 0.7-2 keV energy ranges are shown for the all FOV and core spectra respectively, as they approach background levels outside these ranges.

B.5 NGC 3603

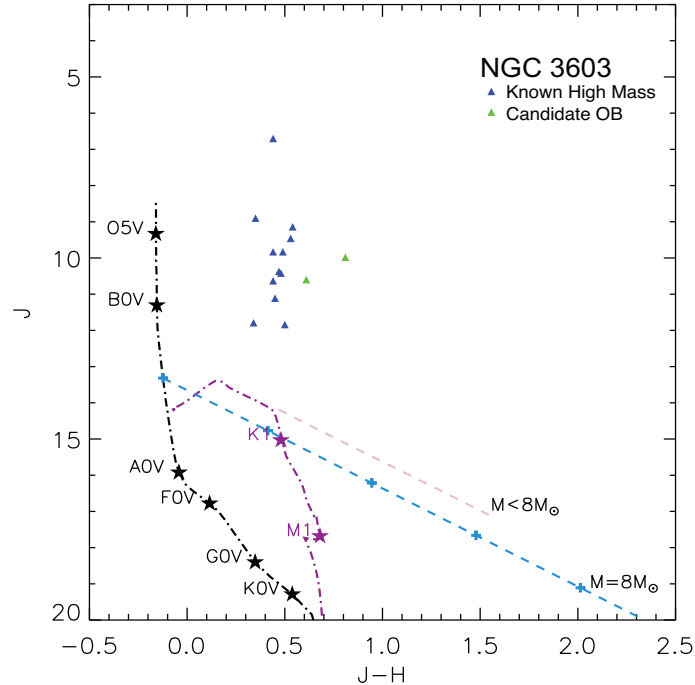


Figure B.21: NGC 3603 2MASS J vs J-H colour magnitude diagram. The blue triangles indicate the known high mass stars and the light green triangles indicate the candidate OB stars. The black dashed dotted line is the 1 Myr main sequence isochrone with spectral types marked calculated for $A_V = 0$. The purple dashed dotted line is the 1 Myr PMS isochrone with spectral types marked. The light blue dashed line is the $8M_{\odot}$ reddening vector with the crosses marking every $A_V = 5$. The light purple dashed line marks the reddening vector of the maximum J value of the PMS evolutionary track. Unlike in most other clusters, only the two candidate OB stars in NGC 3603 had high quality 2MASS photometry. The known high mass sources shown here were plotted using low quality 2MASS photometry to offer a relative indicator to the candidate OB stars.

Table B.17: NGC 3603 Known High Mass Star X-ray Spectral Parameters

<i>Chandra</i> Source (CXO J)	Name	Sp. Type	<i>Net Cts.</i>	N_{H} (10^{22}cm^2)	kT (keV)	kT_2 (keV)	χ^2/ν	$\log F_{X_{h,c}}$ ($\text{erg cm}^{-2} \text{s}^{-1}$)	$\log F_{X_{t,c}}$ ($\text{erg cm}^{-2} \text{s}^{-1}$)	$\log L_{X_{h,c}}$ (erg s^{-1})	$\log L_{X_{t,c}}$ (erg s^{-1})
111506.21-611536.6	103	O3V((f))	68	$1.58_{1.12}^{2.59}$	$0.64_{0.35}^{0.99}$	-	1.36/5	-14.50	-13.16	31.34	32.68
111506.61-611524.0	Sh 50	-	14	-	-	-	-	-	-	-	-
111506.81-611535.6	111	-	238	$0.46_{0.3}^{0.76}$	$2.13_{1.63}^{2.63}$	-	1.61/11	-13.61	-13.20	32.23	32.64
111506.83-611544.6	Sh 63	O3.5III(f)	25	-	-	-	-	-	-	-	-
111507.24-611534.8	104	O3III(f)	70	$0.45_{0.08}^{1.71}$	$0.8_{0.18}^{1.07}$	-	1.42/6	-14.92	-13.84	30.92	32.00
111507.27-611538.3	A1,A2,A3,B	WN6,O3V,O3III(f*),WN6	2854	$1.48_{1.29}^{1.55}$	$0.60_{0.54}^{0.69}$	$2.89_{2.00}^{3.85}$	1.59/154	-12.33	-111.24	33.51	34.60
111507.49-611546.0	Sh 56	O3III(f)+O?	46	-	-	-	-	-	-	-	-
111507.56-611537.9	C	WN6+abs	7320	$1.34_{1.24}^{1.43}$	$0.66_{0.57}^{0.80}$	$1.85_{1.72}^{2.09}$	1.02/238	-11.18	-10.43	34.66	35.41
111507.59-611530.2	117	O6V	23	-	-	-	-	-	-	-	-
111507.78-611527.8	Sh 64	O3V((f))	25	-	-	-	-	-	-	-	-
111508.16-611547.1	Sh 57	O3III(f)	115	$1.54_{0.47}^{2.4}$	$0.62_{0.35}^{1.31}$	-	0.06/1	-14.30	-12.91	31.54	32.93
111508.46-611537.1	108	O5.5V	69	-	-	-	-	-	-	-	-
111508.68-611559.9	Sh 18	O3.5If	80	$1.85_{0.66}^{2.55}$	$0.98_{0.61}^{1.76}$	-	0.29/5	-13.79	-12.91	32.05	32.93
111509.09-611533.2	Sh 49	O7.5V	52	$1.08_{0.47}^{2.22}$	$1.59_{0.86}^{3.07}$	-	0.76/5	-14.24	-13.72	31.60	32.12
111509.33-611601.9	Sh 47	O4V	426	$0.99_{0.78}^{1.39}$	$1.38_{1.08}^{1.64}$	-	0.54/22	-13.04	-12.43	32.80	33.41
111509.82-611530.0	Sh 23	OC9.7Ia	8	-	-	-	-	-	-	-	-
111510.05-611538.0	Sh 22	O3III(f)	238	$0.45_{0.29}^{0.69}$	$1.89_{1.49}^{2.42}$	-	0.98/11	-13.70	-13.25	32.14	32.59
111511.28-611555.6	Sh 19	O3V((f))	14	-	-	-	-	-	-	-	-

High mass sources identified using the high mass source lists of [Melena et al. \(2008\)](#) and the SIMBAD database. Only those sources with > 50 counts were fit in *XSPEC*.

Table B.18: NGC 3603 Candidate OB Star X-ray Spectral Parameters

<i>Chandra</i> Source (CXO J)	Name	Sp. Type	<i>Net Cts.</i>	N_{H} (10^{22}cm^2)	kT (keV)	kT_2 (keV)	χ^2/ν	$\log F_{X_{h,c}}$ ($\text{erg cm}^{-2} \text{s}^{-1}$)	$\log F_{X_{t,c}}$ ($\text{erg cm}^{-2} \text{s}^{-1}$)	$\log L_{X_{h,c}}$ (erg s^{-1})	$\log L_{X_{t,c}}$ (erg s^{-1})
111521.30-611504.2	-	-	892	$1.23_{1.04}^{1.43}$	$2.09_{1.78}^{2.57}$	-	1.02/46	-12.68	-11.88	31.75	32.55
111459.47-611433.7	-	-	3880	$1.96_{1.81}^{2.10}$	$0.54_{0.56}^{0.84}$	$4.97_{3.99}^{7.24}$	1.21/169	-11.93	-11.31	33.92	34.53

Source names determined using the SIMBAD database. Only those sources with > 50 counts were fit in *XSPEC*.

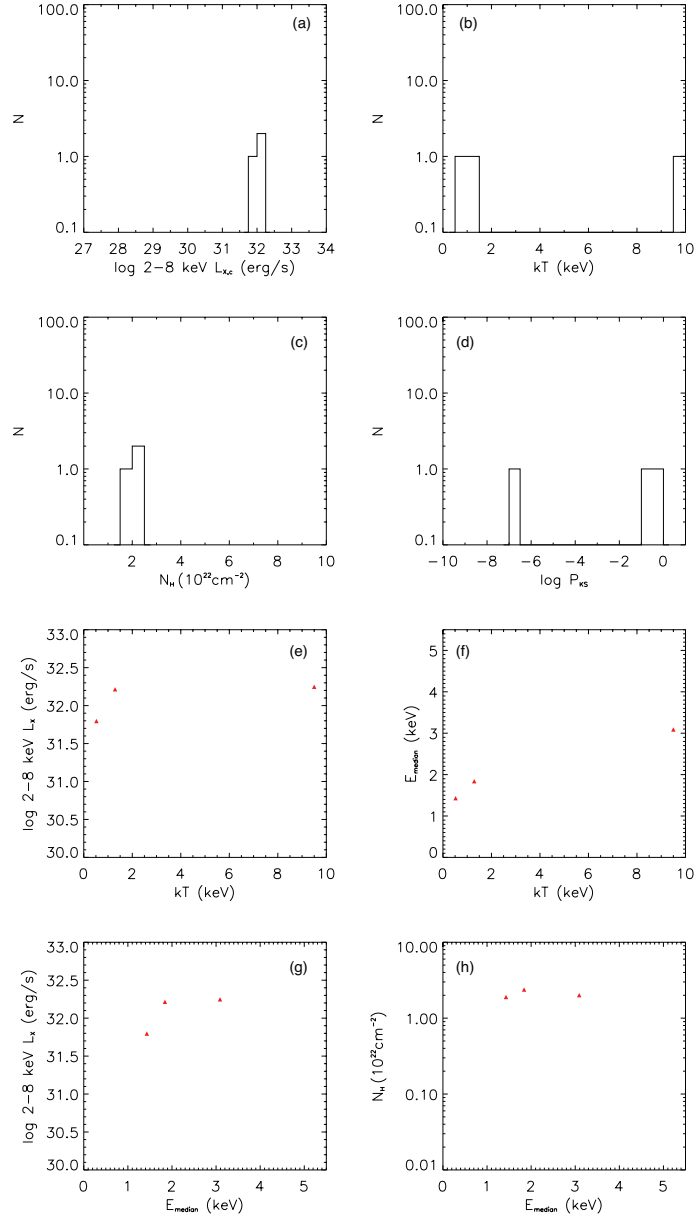


Figure B.22: Plots of derived source parameters for the bright ‘unidentified’ source population of NGC 3603. (a) Distribution of absorption corrected 2-8 keV L_X . (b) Distribution of best fit thermal plasma temperature (kT). (c) Distribution of best fit absorbing hydrogen column (N_H). (d) Distribution of Kolmogorov-Smirnov variability statistic with $\log P_{KS} < 0.05$ indicating variability. (e) Plot of absorption corrected 2-8 keV L_X against best fit thermal plasma temperature (kT). (f) Plot of median photon energy (E_{median}) against best fit thermal plasma temperature (kT). (g) Plot of absorption corrected 2-8 keV L_X against median photon energy (E_{median}). (h) Plot of best fit absorbing hydrogen column (N_H) against median photon energy (E_{median}).

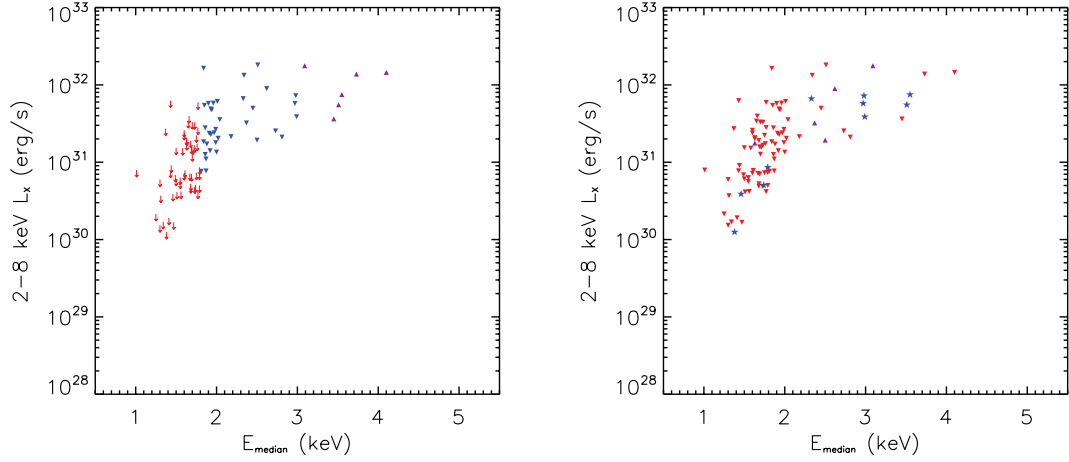


Figure B.23: Plot of the 2-8 keV L_X against the median detected photon energy (E_{median}) for the NGC 3603 ‘unidentified’ source population divided according to E_{median} (left) and variability (right). Left: the red arrows mark $E_{\text{median}} < 1.8$ keV (indicating an upper limit of $\log N_{\text{H}} \lesssim 22.2$ cm $^{-2}$), blue inverted triangles 1.8-3 keV (indicating the lightly obscured population) and purple triangles > 3 keV (indicating the heavily obscured population). Right: Inverted red triangles refer to non-variable sources, blue stars representing variable sources and the purple triangles representing strongly variable flaring sources.

Table B.19: NGC 3603 Diffuse Emission X-ray Spectral Parameters

Region	N_{H} (10^{22} cm^2)	kT (keV)	kT_2 (keV)	Z/Z_{\odot}	χ^2/ν	$\log F_{X_{h,c}}$ ($\text{erg cm}^{-2} \text{ s}^{-1}$)	$\log F_{X_{t,c}}$ ($\text{erg cm}^{-2} \text{ s}^{-1}$)	$\log L_{X_{h,c}}$ (erg s^{-1})	$\log L_{X_{t,c}}$ (erg s^{-1})
total	$1.11^{1.19}_{1.01}$	$0.63^{0.69}_{0.58}$	$4.28^{4.89}_{3.92}$	$0.57^{0.72}_{0.44}$	1.13/288	-11.60	-11.05	34.24	34.78
core	$0.95^{1.15}_{0.67}$	$0.72^{0.85}_{0.59}$	$3.30^{4.10}_{2.98}$	$0.40^{0.63}_{0.20}$	1.02/180	-12.05	-11.55	33.79	34.29

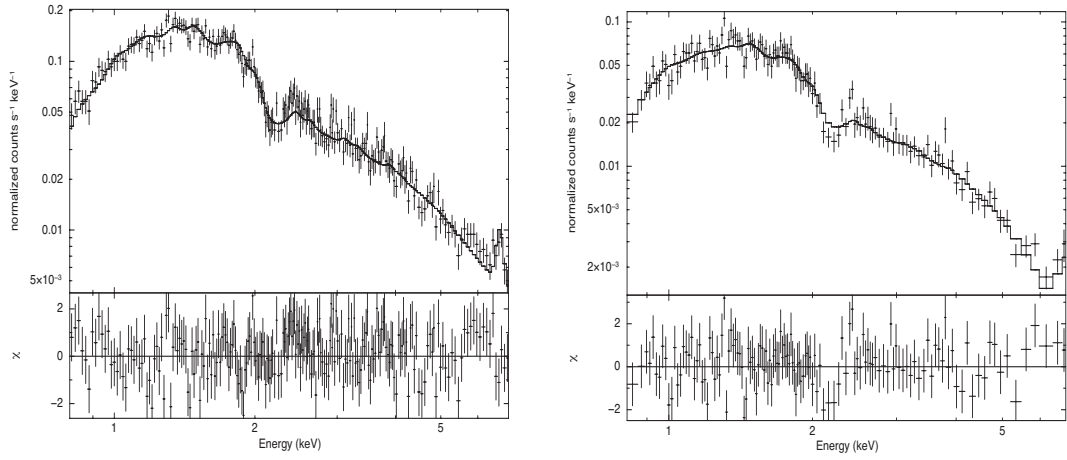


Figure B.24: NGC 3603 total cluster diffuse emission spectrum (left) and cluster core diffuse emission spectrum (right). The spectra were rebinned for plotting purposes using XSPEC's *'setplot rebin'* command. Only the 0.8-7 keV energy range is shown as the spectra approach background levels outside this range.

B.6 NGC 6611

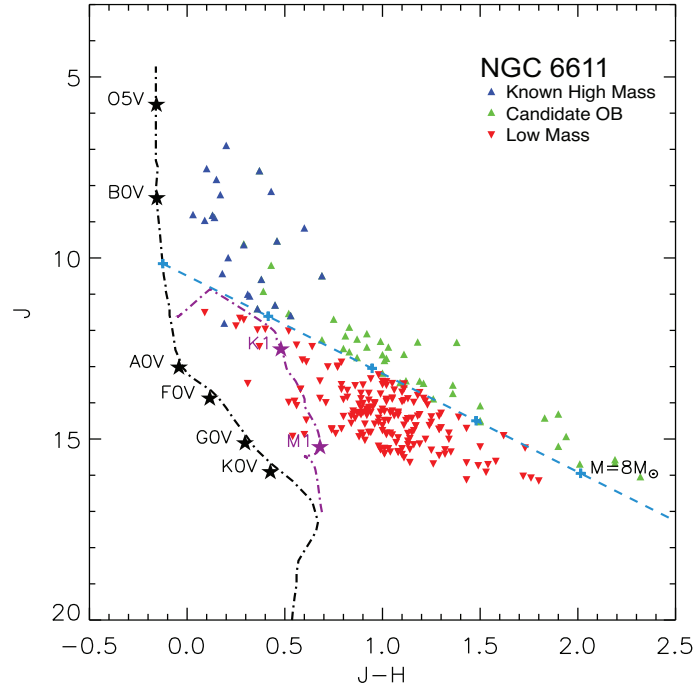


Figure B.25: NGC 6611 2MASS J vs J-H colour magnitude diagram. The blue triangles indicate the known high mass stars, the light green triangles indicate the candidate OB stars and the red inverted triangles indicate low mass sources. The black dashed dotted line is the 1.5 Myr main sequence isochrone with spectral types marked calculated for $A_V = 0$. The purple dashed dotted line is the 1.5 Myr PMS isochrone with spectral types marked. The light blue dashed line is the $8M_{\odot}$ reddening vector with the crosses marking every $A_V = 5$.

Table B.20: NGC 6611 Known High Mass Star X-ray Spectral Parameters

<i>Chandra</i> Source (CXO J)	Name	Sp. Type	<i>Net Cts.</i>	N_{H} (10^{22} cm^{-2})	kT (keV)	kT_2 (keV)	χ^2/ν	$\log F_{X_{h,c}}$ ($\text{erg cm}^{-2} \text{ s}^{-1}$)	$\log F_{X_{t,c}}$ ($\text{erg cm}^{-2} \text{ s}^{-1}$)	$\log L_{X_{h,c}}$ (erg s^{-1})	$\log L_{X_{t,c}}$ (erg s^{-1})
181809.30-134654.7	GMD 1194	B0.5V	65	0.66_{-}^{-}	1.77_{-}^{-}	-	0.5/4	-14.25	-13.77	30.18	30.66
181826.19-135005.4	BD 13 4920	B1V	31	-	-	-	-	-	-	-	-
181830.95-134307.9	029	O8.5V	206	0.26_{-}^{-}	0.82_{-}^{-}	-	2.40/8	-14.34	-13.42	30.33	31.26
181832.24-134847.9	017	O9V	146	$0.81_{0.28}^{1.16}$	$0.28_{0.15}^{0.67}$	-	1.25/4	-15.40	-12.65	29.27	32.03
181832.74-134511.8	BD 13 4923	O5.5V	1213	$0.64_{0.49}^{0.79}$	$0.56_{0.48}^{0.62}$	-	0.96/48	-13.82	-12.31	30.86	31.37
181833.71-134058.9	GMD 592	B0V	39	-	-	-	-	-	-	-	-
181836.05-134736.3	003	O6-7((f))	981	0.26_{-}^{-}	0.62_{-}^{-}	-	2.08/40	-14.20	-12.82	30.47	31.86
181836.43-134802.3	002	O4III((f+))	744	$0.66_{0.46}^{0.74}$	$0.64_{0.59}^{0.69}$	-	0.81/33	-13.76	-12.25	30.92	32.43
181837.05-134529.3	GMD 678	B	1207	$0.45_{0.36}^{0.53}$	$9.67_{6.57}^{20.87}$	-	1.01/61	-12.87	-12.51	31.99	32.16
181837.48-134339.4	080	O7V((f))	172	$1.52_{1.14}^{1.93}$	$0.42_{0.30}^{0.58}$	-	1.02/7	-14.65	-12.71	30.03	31.97
181837.66-134512.9	GMD 666	B8Ve	63	$0.42_{1.39}^{1.09}$	$2.27_{1.39}^{5.54}$	-	1.04/5	-14.37	-13.98	30.06	30.45
181838.15-134425.4	GMD 664	B2V	196	$0.84_{0.04}^{1.33}$	$3.59_{1.65}^{-}$	-	1.11/6	-13.50	-13.23	31.18	31.44
181838.40-134708.9	066	B2V	136	$0.96_{0.56}^{1.39}$	$0.85_{0.44}^{8.89}$	-	1.80/4	-14.43	-13.20	30.25	31.47
181838.46-134556.0	GMD 712	B1V	157	$0.6_{0.33}^{0.9}$	$2.54_{1.74}^{4.04}$	-	1.44/7	-13.90	-13.54	30.53	30.89
181840.10-134518.6	008	O7II(f)	260	$0.37_{0.22}^{1.10}$	$0.47_{0.22}^{1.26}$	-	1.20/9	-14.62	-13.05	30.06	31.63
181840.37-134618.1	GMD 1152	B2Ve	47	-	-	-	-	-	-	-	-
181840.93-134529.5	PPM 73	B0V	18	-	-	-	-	-	-	-	-
181841.62-134247.7	GMD 1250	B1.5V	16	-	-	-	-	-	-	-	-
181842.78-134650.7	015	O9.5V	62	$0.59_{0.14}^{0.96}$	$0.55_{0.41}^{0.80}$	-	1.34/5	-14.85	-13.32	29.83	31.36
181844.67-134756.1	042	B1.5V	40	-	-	-	-	-	-	-	-
181845.86-134630.6	011	O9V	95	$0.30_{0.36}^{0.50}$	$0.55_{0.36}^{0.94}$	-	0.27/5	-15.38	-13.83	29.30	30.85
181849.20-134804.1	085	B5III	8	-	-	-	-	-	-	-	-
181850.68-134812.8	027	B1V	15	-	-	-	-	-	-	-	-
181852.68-134942.4	006	O9.7IIIp	117	$0.25_{0.28}^{0.52}$	$0.43_{0.28}^{0.59}$	-	1.05/3	-15.72	-13.64	28.96	31.04
181855.83-134654.0	GMD 227	B9III	79	$0.92_{0.55}^{1.32}$	$0.76_{0.49}^{1.09}$	-	0.4/5	-14.70	-13.56	29.73	30.87
181856.20-134830.9	004	O8.5V	403	$0.53_{0.27}^{0.77}$	$0.27_{0.18}^{0.41}$	-	0.57/15	-15.35	-12.50	29.33	32.18
181904.93-134818.4	020	B0.5Vn	12	-	-	-	-	-	-	-	-

High mass sources identified using the high mass source lists of Dufton2006 and the SIMBAD database.

Only those sources with > 50 counts were fit in *XSPEC*.

Table B.21: NGC 6611 Candidate OB Star X-ray Spectral Parameters

<i>Chandra</i> Source (CXO J)	Name	Sp. Type	<i>Net Cts.</i>	N_{H} (10^{22} cm^2)	kT (keV)	kT_2 (keV)	χ^2/ν	$\log F_{X_{h,c}}$ ($\text{erg cm}^{-2} \text{ s}^{-1}$)	$\log F_{X_{t,c}}$ ($\text{erg cm}^{-2} \text{ s}^{-1}$)	$\log L_{X_{h,c}}$ (erg s^{-1})	$\log L_{X_{t,c}}$ (erg s^{-1})
181829.12-134532.5	GMD 610	-	132	1.04 $_{-}$	3.06 $_{-}$	-	2.26/5	-13.68	-13.36	30.75	31.07
181830.89-133958.6	GMD 599	-	37	-	-	-	-	-	-	-	-
181833.30-134928.2	GMD 259	-	27	-	-	-	-	-	-	-	-
181834.69-134548.8	GMD 709	-	82	0.83 $^{1.44}_{0.36}$	2.71 $^{6.56}_{1.67}$	-	0.32/5	-14.06	-13.71	30.37	30.72
181834.99-134218.4	GMD 583	-	29	-	-	-	-	-	-	-	-
181835.37-134548.0	GMD 138	-	70	0.25 $^{0.67}_{-}$	3 $^{13.22}_{1.52}$	-	1.37/6	-14.34	-14.02	30.09	30.41
181835.43-134512.8	GMD 634	-	92	1.42 $^{1.93}_{0.43}$	0.93 $^{1.41}_{0.63}$	-	0.86/5	-14.34	-13.41	30.09	31.02
181837.29-134156.2	GMD 587	-	122	1.89 $_{-}$	1.20 $_{-}$	-	2.14/3	-13.81	-13.46	30.62	30.97
181837.43-134607.9	GMD 281	-	49	-	-	-	-	-	-	-	-
181838.89-134612.4	GMD 1132	-	530	0.73 $^{0.91}_{0.59}$	2.42 $^{3.09}_{1.95}$	-	0.77/27	-13.34	-12.97	31.09	31.46
181839.79-134735.1	GMD 958	-	381	0.57 $^{0.67}_{0.42}$	1.53 $^{1.78}_{1.29}$	-	0.88/19	-13.64	-13.09	30.79	31.34
181839.83-134744.0	GMD 1139	-	184	0.55 $^{0.84}_{0.32}$	3.26 $^{5.42}_{2.16}$	-	1.15/8	-13.71	-13.41	30.72	31.02
181840.12-134631.1	GMD 301	-	32	-	-	-	-	-	-	-	-
181840.28-134558.8	GMD 703	-	35	-	-	-	-	-	-	-	-
181841.81-134615.1	GMD 1023	-	343	0.35 $^{0.66}_{0.11}$	2.96 $^{8.10}_{1.68}$	-	1.31/16	-13.45	-13.10	30.98	31.33
181842.96-135215.5	GMD 1049	-	12	-	-	-	-	-	-	-	-
181842.97-134310.4	GMD 572	-	23	-	-	-	-	-	-	-	-
181843.03-134402.1	GMD 560	-	12	-	-	-	-	-	-	-	-
181846.90-134916.2	GMD 306	-	49	-	-	-	-	-	-	-	-
181847.22-134114.7	GMD 390	-	64	2.8 $_{-}$	58.24 $_{-}$	-	1.88/3	-13.47	-13.33	30.96	31.10
181847.81-134815.2	GMD 267	-	728	0.4 $_{-}$	3.4 $_{-}$	-	2.53/15	-13.20	-12.91	31.23	31.52
181847.98-134836.1	GMD 274	-	32	-	-	-	-	-	-	-	-
181848.23-134908.0	GMD 293	-	80	0.19 $^{0.47}_{-}$	2.57 $^{5.63}_{1.6}$	-	0.29/6	-14.29	-13.94	30.14	30.49
181848.48-134346.5	GMD 565	-	173	1.31 $^{0.56}_{2.57}$	59.36 $_{-}$	-	1.11/5	-13.30	-13.10	31.13	31.33
181849.16-134230.0	GMD 688	-	39	-	-	-	-	-	-	-	-
181849.48-134845.3	GMD 869	-	86	1.17 $_{-}$	32.51 $_{-}$	-	2.71/3	-13.58	-13.08	30.85	31.35
181849.67-134418.7	GMD 1235	-	71	2.24 $^{3.4}_{1.68}$	3.16 $^{8.56}_{2.04}$	-	0.36/6	-13.84	-13.54	30.59	30.89
181849.91-134659.5	GMD 204	-	106	0.68 $^{1.36}_{0.37}$	2.88 $^{4.74}_{1.53}$	-	0.45/5	-13.99	-13.66	30.44	30.77
181851.68-134759.5	GMD 763	-	33	-	-	-	-	-	-	-	-
181852.40-134407.7	GMD 52	-	88	1.47 $_{-}$	52.57 $_{-}$	-	3.39/3	-13.68	-13.55	30.75	30.88
181852.47-134415.6	GMD 535	-	13	-	-	-	-	-	-	-	-
181852.89-135705.9	GMD 1203	-	70	6.75 $_{-}$	59.36 $_{-}$	-	3.19/3	-13.13	-12.99	31.30	31.44

Table B.22: NGC 6611 Candidate OB Star X-ray Spectral Parameters (Cont.)

<i>Chandra</i> Source (CXO J)	Name	Sp. Type	Net Cts.	N_{H} (10^{22} cm^2)	kT (keV)	kT_2 (keV)	χ^2/ν	$\log F_{X_{h,c}}$ ($\text{erg cm}^{-2} \text{ s}^{-1}$)	$\log F_{X_{t,c}}$ ($\text{erg cm}^{-2} \text{ s}^{-1}$)	$\log L_{X_{h,c}}$ (erg s^{-1})	$\log L_{X_{t,c}}$ (erg s^{-1})
181858.57-134534.3	GMD 34	-	32	-	-	-	-	-	-	-	-
181900.22-134539.8	GMD 476	-	56	$0.36_{-0.8}^{0.8}$	$2.34_{1.15}^{5.51}$	-	0.79/6	-14.45	-14.07	29.98	30.36
181901.61-134515.9	GMD 386	-	319	$0.31_{0.18}^{0.46}$	$2_{1.6}^{2.48}$	-	1.14/16	-13.72	-13.29	30.71	31.14
181903.16-134510.8	GMD 486	-	261	$0.49_{0.33}^{0.78}$	$2.16_{1.68}^{2.67}$	-	0.88/13	-13.69	-13.29	30.74	31.14
181904.57-134358.1	GMD 438	-	73	$0.45_{0.08}^{1.03}$	$3.47_{1.74}^{10.62}$	-	1.07/5	-14.08	-13.79	30.35	30.64
181906.62-134536.3	GMD 33	-	93	1.56_{-}	2.42_{-}	-	0.72/3	-13.86	-13.49	30.57	30.94

Source names determined from the SIMBAD database. Only those sources with > 50 counts were fit in *XSPEC*.

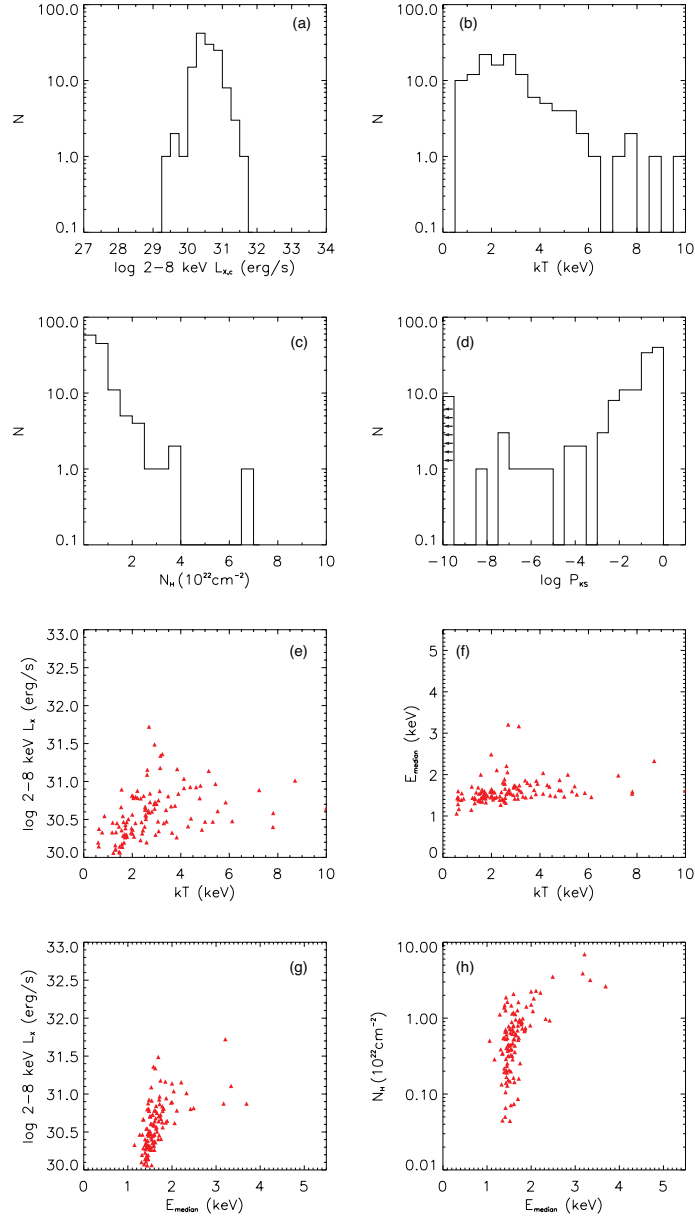


Figure B.26: Plots of derived source parameters for the bright PMS population of NGC 6611. (a) Distribution of absorption corrected 2-8 keV L_X . (b) Distribution of best fit thermal plasma temperature (kT). (c) Distribution of best fit absorbing hydrogen column (N_H). (d) Distribution of Kolmogorov-Smirnov variability statistic with $\log P_{KS} < 0.05$ indicating variability. (e) Plot of absorption corrected 2-8 keV L_X against best fit thermal plasma temperature (kT). (f) Plot of median photon energy (E_{median}) against best fit thermal plasma temperature (kT). (g) Plot of absorption corrected 2-8 keV L_X against median photon energy (E_{median}). (h) Plot of best fit absorbing hydrogen column (N_H) against median photon energy (E_{median}).

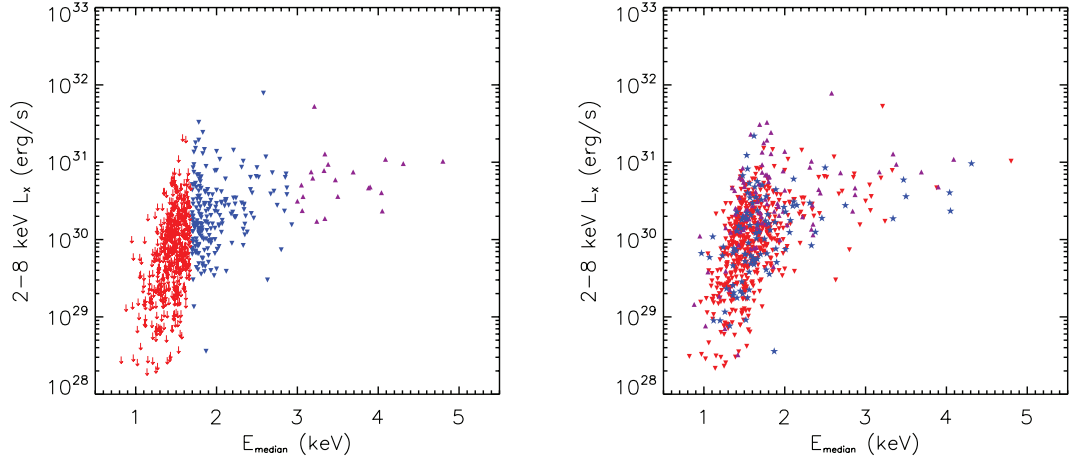


Figure B.27: Plot of the 2-8 keV L_X against the median detected photon energy (E_{median}) for the NGC 6611 PMS population divided according to E_{median} (left) and variability (right). Left: the red arrows mark $E_{\text{median}} < 1.7$ keV (indicating an upper limit of $\log N_{\text{H}} \lesssim 22.0 \text{ cm}^{-2}$), blue inverted triangles 1.7-3 keV (indicating the lightly obscured population) and purple triangles > 3 keV (indicating the heavily obscured population). Right: Inverted red triangles refer to non-variable sources, blue stars representing variable sources and the purple triangles representing strongly variable flaring sources.

Table B.23: NGC 6611 Diffuse Emission X-ray Spectral Parameters

Region	N_{H} (10^{22}cm^2)	kT (keV)	kT_2 (keV)	Z/Z_{\odot}	χ^2/ν	$\log F_{X_{h,c}}$ ($\text{erg cm}^{-2} \text{s}^{-1}$)	$\log F_{X_{t,c}}$ ($\text{erg cm}^{-2} \text{s}^{-1}$)	$\log L_{X_{h,c}}$ (erg s^{-1})	$\log L_{X_{t,c}}$ (erg s^{-1})
all FOV	$0.42_{-0.34}^{+0.49}$	$0.71_{-0.69}^{+0.73}$	$10.85_{-9.58}^{+12.27}$	$1.03_{-0.72}^{+2.28}$	1.53/288	-11.33	-11.08	33.10	33.35
core	$0.37_{-0.14}^{+0.63}$	$0.80_{-0.74}^{+0.98}$	$4.52_{-3.96}^{+5.54}$	$0.35_{-0.14}^{+0.63}$	1.09/280	-11.95	-11.60	32.48	32.83

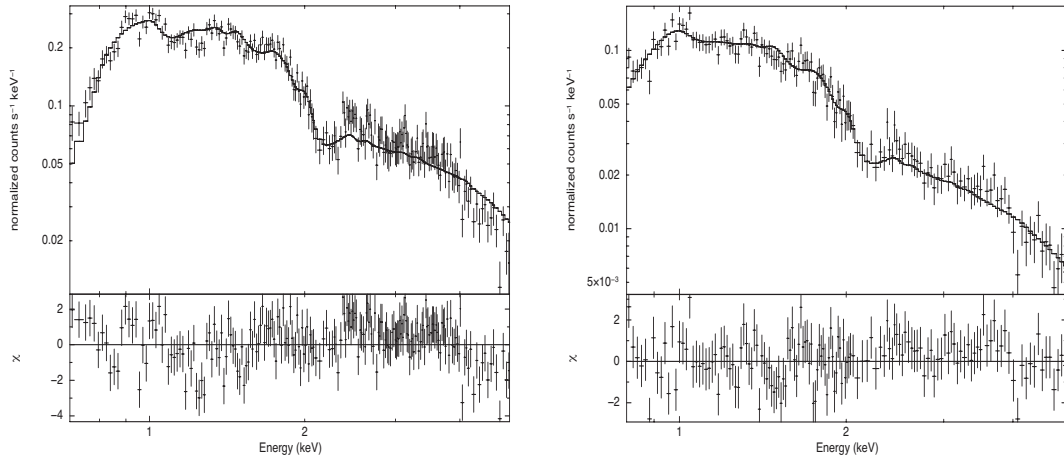


Figure B.28: NGC 6611 all FOV diffuse emission spectrum (left) and cluster core diffuse emission spectrum (right). The spectra were rebinned for plotting purposes using XSPEC's `'setplot rebin'` command. Only the 0.7-5 keV energy range is shown as the spectra approach background levels outside this range.

B.7 NGC 6618

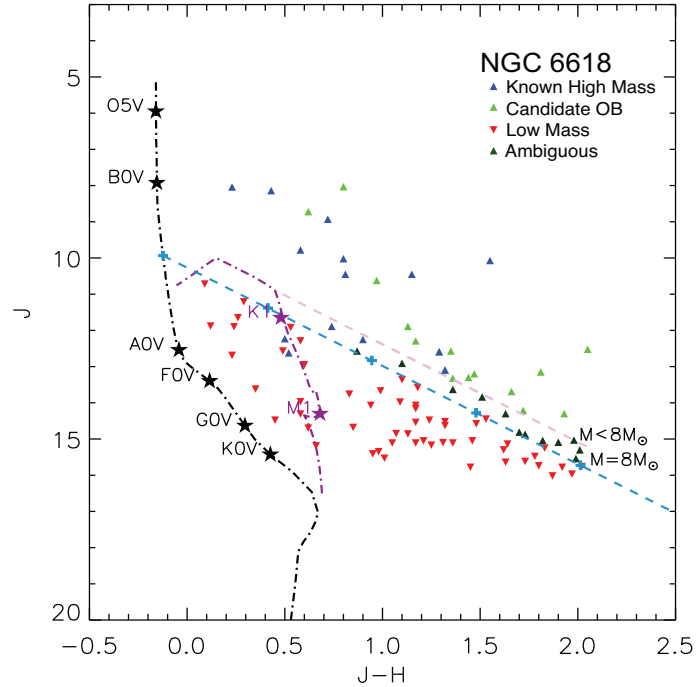


Figure B.29: NGC 6618 2MASS J vs J-H colour magnitude diagram. The blue triangles indicate the known high mass stars, the light green triangles indicate the candidate OB stars, the dark green circles indicate the ambiguous sources and the red inverted triangles indicate low mass sources. The black dashed dotted line is the 1 Myr main sequence isochrone with spectral types marked calculated for $A_V = 0$. The purple dashed dotted line is the 1 Myr PMS isochrone with spectral types marked. The light blue dashed line is the $8M_\odot$ reddening vector with the crosses marking every $A_V = 5$. The light purple dashed line marks the reddening vector of the maximum J value of the PMS evolutionary track. Sources between this and the $8M_\odot$ reddening vector may be above or below $8M_\odot$ and are hence labelled as ambiguous sources.

Table B.24: NGC 6618 Known High Mass Star X-ray Spectral Parameters

<i>Chandra</i> Source (CXO J)	Name	Sp. Type	<i>Net Cts.</i>	N_{H} (10^{22} cm^{-2})	kT (keV)	kT_2 (keV)	χ^2/ν	$\log F_{X_{h,c}}$ ($\text{erg cm}^{-2} \text{ s}^{-1}$)	$\log F_{X_{t,c}}$ ($\text{erg cm}^{-2} \text{ s}^{-1}$)	$\log L_{X_{h,c}}$ (erg s^{-1})	$\log L_{X_{t,c}}$ (erg s^{-1})
182021.43-160939.0	CEN 35	O9.5V	146	$1.73_{0.98}^{2.32}$	$2.73_{2.10}^{7.58}$	-	1.47/5	-13.78	-13.46	30.70	31.02
182022.10-161021.1	CEN 13	B3V	39	-	-	-	-	-	-	-	-
182022.70-160833.9	CEN 16	O9V	179	$0.35_{0.16}^{0.62}$	$2.39_{1.51}^{3.61}$	-	1.04/8	-14.21	-13.84	30.27	30.65
182022.85-160814.3	CEN 75	B2V	12	-	-	-	-	-	-	-	-
182024.38-160843.2	CEN 31	O9.5V	38	-	-	-	-	-	-	-	-
182024.59-161139.1	IRS 5	O6V	76	$3.16_{1.79}^{4.92}$	$2.94_{1.43}^{23.86}$	-	1.65/4	-13.88	-13.58	30.59	30.69
182024.83-161135.9	UC1 pos1	B0V	15	-	-	-	-	-	-	-	-
182025.07-161133.8	UC1 pos2	B0V	31	-	-	-	-	-	-	-	-
182025.31-160939.5	CEN 36	O9.5V	47	-	-	-	-	-	-	-	-
182025.34-161021.8	CEN 49	B2V	134	$0.77_{0.55}^{1.27}$	$7.54_{3.58}^{39.69}$	-	1.11/5	-13.92	-13.73	30.56	30.76
182025.87-160832.3	CEN 18	O6V	188	$1.75_{1.38}^{2.06}$	$0.80_{0.61}^{1.01}$	-	1.12/7	-14.12	-12.84	30.41	31.61
182026.03-161104.4	CEN 26	B3V	86	$0.89_{0.36}^{1.74}$	$2.59_{1.75}^{3.6}$	-	0.14/4	-13.43	-13.21	31.06	31.16
182026.65-160708.7	H 6500	B2V	61	$2.59_{1.75}^{3.6}$	$0.43_{0.24}^{0.66}$	-	0.73/5	-14.84	-12.93	29.65	31.56
182026.79-160749.3	B 240	B0V	18	-	-	-	-	-	-	-	-
182027.30-161025.2	CEN 23	B3V	12	-	-	-	-	-	-	-	-
182027.42-161330.8	OI 345	O6V	900	$1.15_{0.98}^{1.27}$	$0.62_{0.56}^{0.71}$	-	1.92/38	-14.04	-12.67	30.44	31.82
182028.65-161211.3	IRS 15	B0.5V	125	$1.95_{1.39}^{2.75}$	$2.98_{1.97}^{5.73}$	-	0.47/5	-13.94	-13.61	30.55	30.87
182028.68-160925.9	CEN 30	O9V	94	$2.25_{1.42}^{3.85}$	$2.39_{1.37}^{4.27}$	-	0.73/5	-14.03	-13.66	30.45	30.83
182029.13-161054.1	CEN 55	B0Ve	175	$1.80_{1.34}^{2.48}$	$1.61_{1.16}^{2.28}$	-	0.72/6	-13.84	-13.33	30.64	31.16
182029.20-161110.6	CEN 42	B2V	16	-	-	-	-	-	-	-	-
182029.81-161045.3	CEN 1b	O4V	11781	$2.30_{2.21}^{2.39}$	$0.93_{0.80}^{1.05}$	$3.05_{2.65}^{3.39}$	0.86/236	-11.79	-11.20	32.70	33.29
182029.90-161044.3	CEN 1a	O4V	12323	$1.94_{1.85}^{2.02}$	$0.90_{0.79}^{0.99}$	$5.20_{3.83}^{6.58}$	0.83/233	-11.83	-11.29	32.65	33.20
182029.96-161137.0	CEN 27	O9V	15	-	-	-	-	-	-	-	-
182030.22-161034.7	CEN 61	O9V	104	$1.96_{1.08}^{2.74}$	$1.15_{0.8}^{1.59}$	-	0.41/5	-14.31	-13.57	30.17	30.91
182030.43-161052.8	CEN 37	O6V	250	$0.76_{-}^{1.91}$	$1.80_{0.93}^{5.51}$	-	1.38/7	-13.97	-13.77	30.51	31.72
182030.48-161034.5	CEN 61 pos2	O9V	98	$2.06_{0.82}^{4.06}$	$2.94_{1.32}^{34.92}$	-	1.85/4	-13.92	-13.60	30.57	30.88
182030.84-161007.4	CEN 25	O7V	77	$2.48_{1.37}^{3.24}$	$0.28_{0.17}^{0.58}$	-	0.32/5	-15.30	-12.52	29.19	31.96
182031.11-160929.7	B 159	B1	1000	$1.30_{1.10}^{1.56}$	$5.44_{3.79}^{9.17}$	-	0.98/52	-12.96	-12.74	31.52	31.75
182031.69-160945.7	B 152	B2	98	$1.01_{0.59}^{1.62}$	$1.66_{1.01}^{3.55}$	-	1.03/4	-13.83	-13.33	30.65	31.15
182031.84-161138.1	CEN 28	B2V	31	-	-	-	-	-	-	-	-
182032.87-161239.4	B140	B3V	36	-	-	-	-	-	-	-	-
182033.06-161121.3	CEN 43	O5V	98	$1.01_{0.59}^{1.62}$	$1.66_{1.00}^{3.55}$	-	1.03/4	-13.83	-13.33	30.64	31.15
182034.49-161011.7	CEN 2	O5V	1866	$0.95_{0.79}^{1.06}$	$0.61_{0.55}^{0.67}$	$3.78_{2.20}^{9.52}$	0.87/76	-13.41	-12.23	31.08	32.26
182035.24-160842.4	H 12556	B3V	130	$0.99_{0.59}^{1.70}$	$4.44_{2.27}^{14.93}$	-	1.31/4	-13.95	-13.67	30.55	30.81
182035.38-161048.4	CEN 3	O9V	383	$0.81_{0.64}^{0.97}$	$0.56_{0.49}^{0.67}$	-	0.93/18	-14.67	-13.16	29.81	31.33
182035.61-161055.2	CEN 45	B2V	108	$0.46_{0.18}^{0.84}$	$3.37_{1.86}^{7.29}$	-	0.55/5	-14.26	-13.96	30.23	30.53

High mass sources identified using the high mass source lists of [Hoffmeister et al. \(2008\)](#) and the SIMBAD database. Only those sources with > 50 counts were fit in *XSPEC*.

Table B.25: NGC 6618 Candidate OB Star X-ray Spectral Parameters

<i>Chandra</i> Source (CXO J)	Name	Sp. Type	<i>Net Cts.</i>	N_{H} (10^{22}cm^2)	kT (keV)	kT_2 (keV)	χ^2/ν	$\log F_{X_{h,c}}$ ($\text{erg cm}^{-2} \text{s}^{-1}$)	$\log F_{X_{t,c}}$ ($\text{erg cm}^{-2} \text{s}^{-1}$)	$\log L_{X_{h,c}}$ (erg s^{-1})	$\log L_{X_{t,c}}$ (erg s^{-1})
181957.54-161204.8	2MASS J18195753-1612049	-	233	$0.28_{0.1}^{0.5}$	$1.95_{1.47}^{2.73}$	-	1.35/10	-14.15	-13.71	30.34	30.78
182001.69-160529.0	2MASS J18200174-1605288	-	186	0.03_{-}	1.96_{-}	-	0.44/7	-14.34	-13.91	30.14	30.58
182002.98-160206.5	2MASS J18200299-1602068	-	338	$1.72_{1.45}^{2.16}$	$0.54_{0.41}^{0.64}$	-	1.44/14	-14.25	-12.68	30.24	31.81
182016.30-160225.2	-	-	159	$1.02_{0.54}^{1.59}$	$6.49_{-}^{2.96}$	-	1.66/3	-13.69	-13.49	30.79	31.00
182026.94-160347.2	2MASS J18202695-1603473	-	482	$1.40_{1.12}^{1.88}$	$5.10_{8.55}^{2.97}$	-	0.85/24	-13.18	-12.94	31.31	31.55
182027.20-160419.9	2MASS J18202721-1604202	-	92	$1.60_{0.76}^{2.45}$	$3.24_{1.87}^{27.18}$	-	0.64/4	-13.95	-13.68	30.53	30.80
182028.15-161049.1	-	-	369	$2.24_{1.86}^{2.73}$	$2.24_{1.92}^{2.81}$	-	1.01/18	-13.35	-12.95	31.14	31.53
182030.45-161009.8	B 171	-	157	$1.63_{1.18}^{2.28}$	$3.26_{2.16}^{5.35}$	-	0.53/6	-13.87	-13.57	30.62	30.92
182031.96-160925.0	B 147	-	109	$0.86_{0.49}^{1.59}$	$5.83_{4.42}^{52.15}$	-	0.88/4	-14.00	-13.74	30.49	30.74
182033.21-161058.4	B 133	-	113	$3.24_{2.42}^{4.51}$	$1.76_{1.24}^{2.52}$	-	0.13/5	-13.74	-13.24	30.74	31.24
182033.76-161304.8	B 125	-	54	$2.48_{1.48}^{4.23}$	$1.78_{1.05}^{3.41}$	-	0.11/5	-14.29	-13.82	30.20	30.67
182035.86-161542.9	2MASS J18203586-1615431	-	4200	$0.97_{0.9}^{1.05}$	$2.89_{2.61}^{3.18}$	-	1.49/153	-12.58	-12.26	31.90	32.23
182039.71-161312.6	B 42	-	299	$1.13_{0.88}^{1.47}$	$4.02_{2.70}^{6.66}$	-	0.83/13	-13.55	-13.29	30.93	31.20
182043.41-161245.9	B 7	-	495	$0.96_{0.67}^{1.22}$	$1.59_{1.31}^{2.17}$	-	0.90/24	-13.57	-13.05	30.92	31.44

Source names determined using the SIMBAD database. Only those sources with > 50 counts were fit in *XSPEC*.

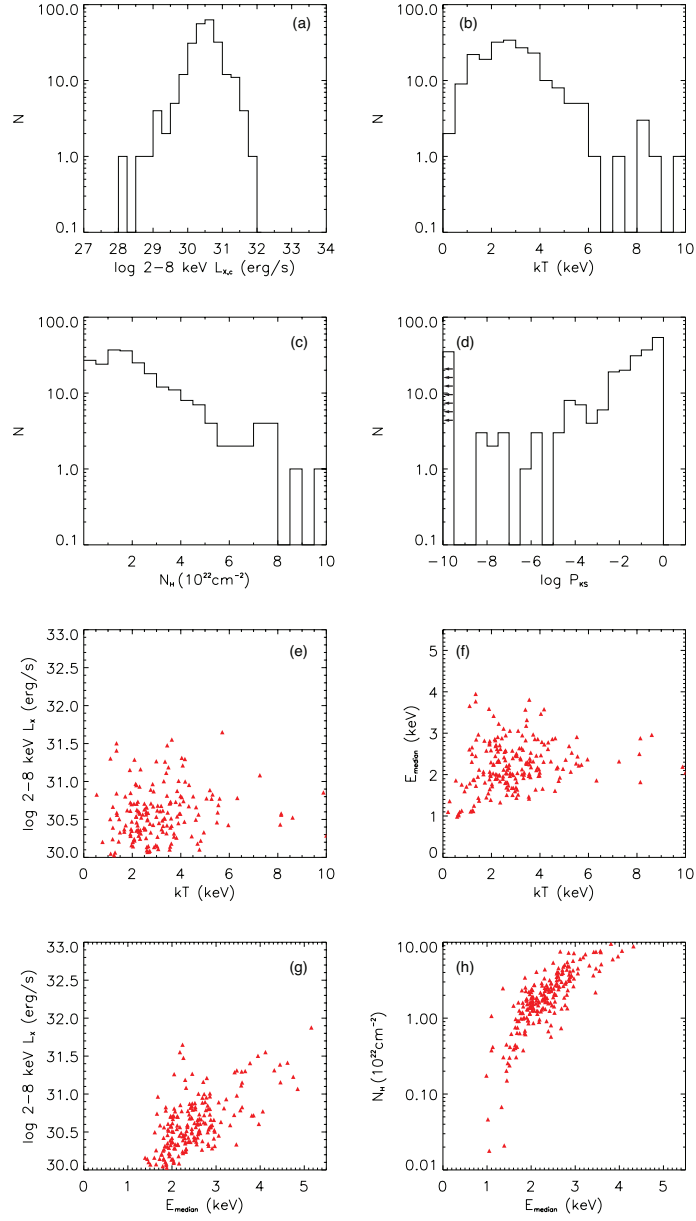


Figure B.30: Plots of derived source parameters for the bright PMS population of NGC 6618. (a) Distribution of absorption corrected 2-8 keV L_X . (b) Distribution of best fit thermal plasma temperature (kT). (c) Distribution of best fit absorbing hydrogen column (N_H). (d) Distribution of Kolmogorov-Smirnov variability statistic with $\log P_{KS} < 0.05$ indicating variability. (e) Plot of absorption corrected 2-8 keV L_X against best fit thermal plasma temperature (kT). (f) Plot of median photon energy (E_{median}) against best fit thermal plasma temperature (kT). (g) Plot of absorption corrected 2-8 keV L_X against median photon energy (E_{median}). (h) Plot of best fit absorbing hydrogen column (N_H) against median photon energy (E_{median}).

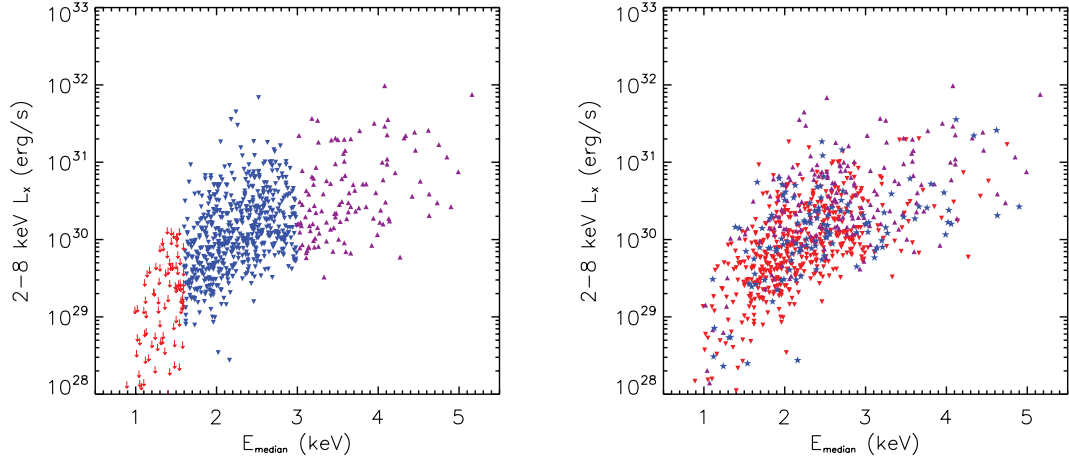


Figure B.31: Plot of the 2-8 keV L_X against the median detected photon energy (E_{median}) for the NGC 6618 PMS population divided according to E_{median} (left) and variability (right). Left: the red arrows mark $E_{\text{median}} < 1.6$ keV (indicating an upper limit of $\log N_{\text{H}} \lesssim 22.0 \text{ cm}^{-2}$), blue inverted triangles 1.6-3 keV (indicating the lightly obscured population) and purple triangles > 3 keV (indicating the heavily obscured population). Right: Inverted red triangles refer to non-variable sources, blue stars representing variable sources and the purple triangles representing strongly variable flaring sources.

Table B.26: NGC 6618 Diffuse Emission X-ray Spectral Parameters

Region	N_{H} (10^{22} cm^2)	kT (keV)	kT_2 (keV)	kT_3 (keV)	Z/Z_{\odot}	χ^2/ν	$\log F_{X_{h,c}}$ ($\text{erg cm}^{-2} \text{ s}^{-1}$)	$\log F_{X_{t,c}}$ ($\text{erg cm}^{-2} \text{ s}^{-1}$)	$\log L_{X_{h,c}}$ (erg s^{-1})	$\log L_{X_{t,c}}$ (erg s^{-1})
all FOV	$0.67^{0.71}_{0.63}$	$0.15^{0.17}_{0.14}$	$0.58^{0.60}_{0.55}$	$10.85^{10.06}_{12.70}$	$2.21^{4.25}_{1.04}$	1.61/210	-11.26	-10.06	33.22	34.43
core	$0.91^{0.99}_{0.81}$	$0.64^{0.70}_{0.59}$	$3.72^{4.24}_{3.33}$	-	$0.16^{0.23}_{0.11}$	0.98/399	-11.94	-11.39	32.55	33.10

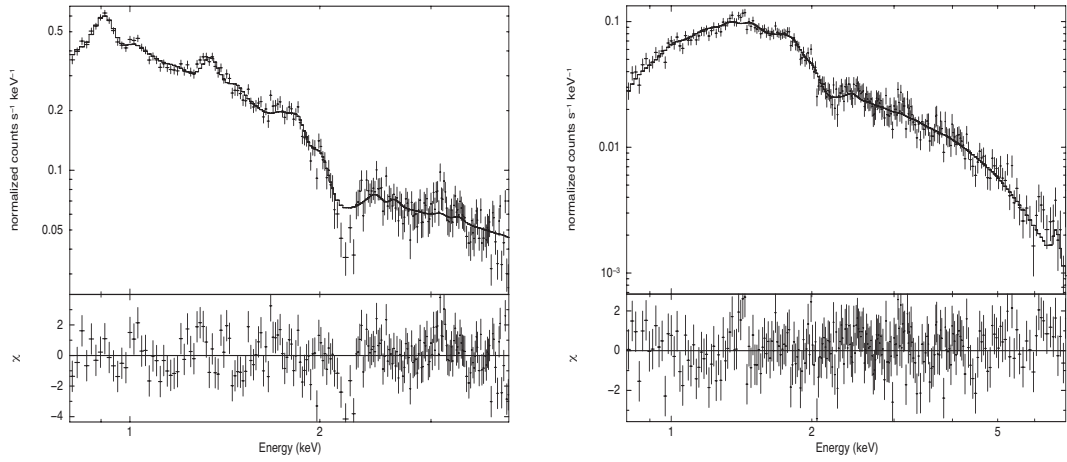


Figure B.32: NGC 6618 all FOV diffuse emission spectrum (left) and cluster core diffuse emission spectrum (right). The spectra were rebinned for plotting purposes using XSPEC's *'setplot rebin'* command. Only the 0.8-4 keV and 0.8-2 keV energy ranges are shown for the all FOV and core spectra respectively, as they approach background levels outside these ranges.

B.8 Trumpler 14

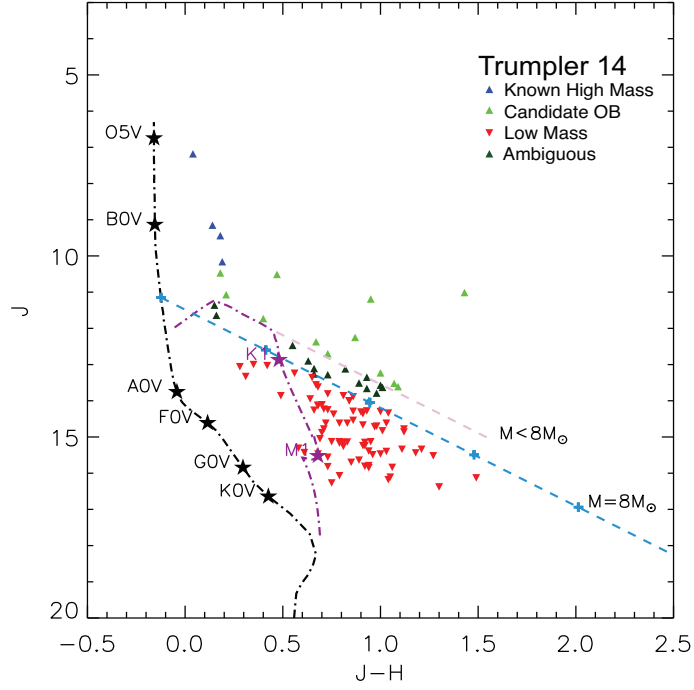


Figure B.33: Trumpler 14 2MASS J vs J-H colour magnitude diagram. The blue triangles indicate the known high mass stars, the light green triangles indicate the candidate OB stars, the dark green circles indicate the ambiguous sources and the red inverted triangles indicate low mass sources. The black dashed dotted line is the 1 Myr main sequence isochrone with spectral types marked calculated for $A_V = 0$. The purple dashed dotted line is the 1 Myr PMS isochrone with spectral types marked. The light blue dashed line is the $8M_{\odot}$ reddening vector with the crosses marking every $A_V = 5$. The light purple dashed line marks the reddening vector of the maximum J value of the PMS evolutionary track. Sources between this and the $8M_{\odot}$ reddening vector may be above or below $8M_{\odot}$ and are hence labelled as ambiguous sources.

Table B.27: Trumpler 14 Known High Mass Star X-ray Spectral Parameters

<i>Chandra</i> Source (CXO J)	Name	Sp. Type	<i>Net Cts.</i>	N_{H} (10^{22} cm^2)	kT (keV)	kT_2 (keV)	χ^2/ν	$\log F_{X_{h,c}}$ ($\text{erg cm}^{-2} \text{ s}^{-1}$)	$\log F_{X_{t,c}}$ ($\text{erg cm}^{-2} \text{ s}^{-1}$)	$\log L_{X_{h,c}}$ (erg s^{-1})	$\log L_{X_{t,c}}$ (erg s^{-1})
104330.88-592924.0	MJ 61	-	49	-	-	-	-	-	-	-	-
104333.48-593511.3	MJ 71	B0III-IV	7	-	-	-	-	-	-	-	-
104341.32-593548.6	MJ 92	-	45	-	-	-	-	-	-	-	-
104344.16-593348.4	MJ 102	O9V	11	-	-	-	-	-	-	-	-
104346.69-593254.8	MJ 115	O6V((f))	162	$0.5^{1.12}_{0.27}$	$0.37^{0.49}_{0.2}$	-	0.71/7	-15.23	-13.09	29.57	31.71
104348.70-593324.3	MJ 127	O9V	79	$0.06^{0.69}_{0.37}$	$0.8^{1.05}_{0.37}$	-	0.18/5	-15.04	-13.96	29.76	30.85
104353.11-593259.6	MJ 149	B0.5IV-V	42	-	-	-	-	-	-	-	-
104354.40-593257.5	HD 93128	O3V((f))	506	$0.34^{0.52}_{0.18}$	$0.48^{0.59}_{0.4}$	-	1.36/22	-14.40	-12.69	30.40	32.12
104355.19-593314.7	MJ 163	B0V	22	-	-	-	-	-	-	-	-
104355.35-593248.9	MJ 165	O8V	84	0.01_{-}	0.59_{-}	-	0.55/5	-15.32	-13.88	29.49	30.92
104356.74-593240.6	MJ 173	-	69	-	-	-	-	-	-	-	-
104357.46-593251.4	HD 93129 A	O2If*	4421	$0.81^{0.87}_{0.74}$	$0.58^{0.61}_{0.55}$	$2.46^{2.78}_{2.18}$	1.57/129	-12.52	-11.56	32.24	33.24
104357.65-593253.8	HD 93129 B	O3.5Vf+	623	$0.22^{0.58}_{0.07}$	$0.52^{0.63}_{0.28}$	-	0.84/24	-14.60	-12.80	30.20	31.96
104357.55-593338.7	MJ 178	B1V	15	-	-	-	-	-	-	-	-
104359.87-593524.3	MJ 195	O9V	34	-	-	-	-	-	-	-	-
104359.91-593225.5	MJ 192	O6.5V((f))	95	0.01_{-}	0.52_{-}	-	2.86/5	-15.45	-13.84	29.35	30.96
104400.95-593545.8	MJ 200	O9V	33	-	-	-	-	-	-	-	-
104402.43-592936.7	MJ 203	O9III	19	-	-	-	-	-	-	-	-
104405.83-593511.7	MJ 224	B1V	117	0.15_{-}	2.03_{-}	-	2.98/5	-14.16	-13.73	30.64	31.07
104407.26-593430.7	HD 93160	O6III(f)	627	$0.33^{0.47}_{0.19}$	$0.64^{0.72}_{0.56}$	-	1.69/27	-14.22	-12.88	30.58	31.92
104408.90-593434.6	HD 93161A	O8V + O9V	490	$0.07^{0.23}_{-}$	$0.71^{0.78}_{0.58}$	-	1.18/20	-14.38	-13.16	30.42	31.64
104409.07-593435.5	HD 93161	O6V	332	$0.29^{0.49}_{0.15}$	$0.54^{0.64}_{0.38}$	-	0.71/13	-14.56	-12.99	30.25	31.81

High mass sources identified using the high mass source lists of [Massey and Johnson \(1993\)](#) and the SIMBAD database. Only those sources with > 50 counts were fit in *XSPEC*.

Table B.28: Trumpler 14 Candidate OB Star X-ray Spectral Parameters

<i>Chandra</i> Source (CXO J)	Name	Sp. Type	<i>Net Cts.</i>	N_{H} (10^{22}cm^2)	kT (keV)	kT_2 (keV)	χ^2/ν	$\log F_{X_{h,c}}$ ($\text{erg cm}^{-2} \text{s}^{-1}$)	$\log F_{X_{t,c}}$ ($\text{erg cm}^{-2} \text{s}^{-1}$)	$\log L_{X_{h,c}}$ (erg s^{-1})	$\log L_{X_{t,c}}$ (erg s^{-1})
104341.57-593206.5	DETC Tr 14 J104341.6-593206	-	109	$0.25_{-}^{1.64}$	$0.71_{0.23}^{1.74}$	-	0.79/3	-14.68	-13.57	30.12	31.23
104346.01-593329.0	DETC Tr 14 J104346.0-593329	-	23	-	-	-	-	-	-	-	-
104346.36-593113.9	2MASS J10434636-5931138	-	451	$0.36_{0.24}^{0.49}$	$8.28_{5.21}^{40.14}$	-	0.93/23	-12.95	-12.73	31.85	31.99
104346.78-593356.3	DETC Tr 14 J104346.8-593356	-	27	-	-	-	-	-	-	-	-
104349.96-593656.0	-	-	14	-	-	-	-	-	-	-	-
104352.25-593659.0	Y 491	-	17	-	-	-	-	-	-	-	-
104353.89-592823.3	2MASS J10435391-5928232	-	36	-	-	-	-	-	-	-	-
104355.04-593624.0	DETC Tr 14 J104355.0-593624	-	9	-	-	-	-	-	-	-	-
104355.77-593106.6	DETC Tr 14 J104355.0-593624	-	52	$1.2_{0.17}^{2.26}$	$0.78_{0.37}^{1.67}$	-	0.72/5	-14.62	-13.51	30.18	31.29
104358.71-592809.4	-	-	17	-	-	-	-	-	-	-	-
104406.84-593611.6	2MASS J10440683-5936116	-	135	$0.09_{-}^{0.28}$	$2.73_{1.82}^{4.97}$	-	0.54/5	-13.94	-13.60	30.86	31.20
104416.48-593510.1	2MASS J10441648-5935100	-	77	$0.03_{-}^{0.27}$	$1.81_{1.27}^{2.95}$	-	0.65/5	-14.42	-13.95	30.39	30.85

Source names determined using the SIMBAD database. Only those sources with > 50 counts were fit in *XSPEC*.

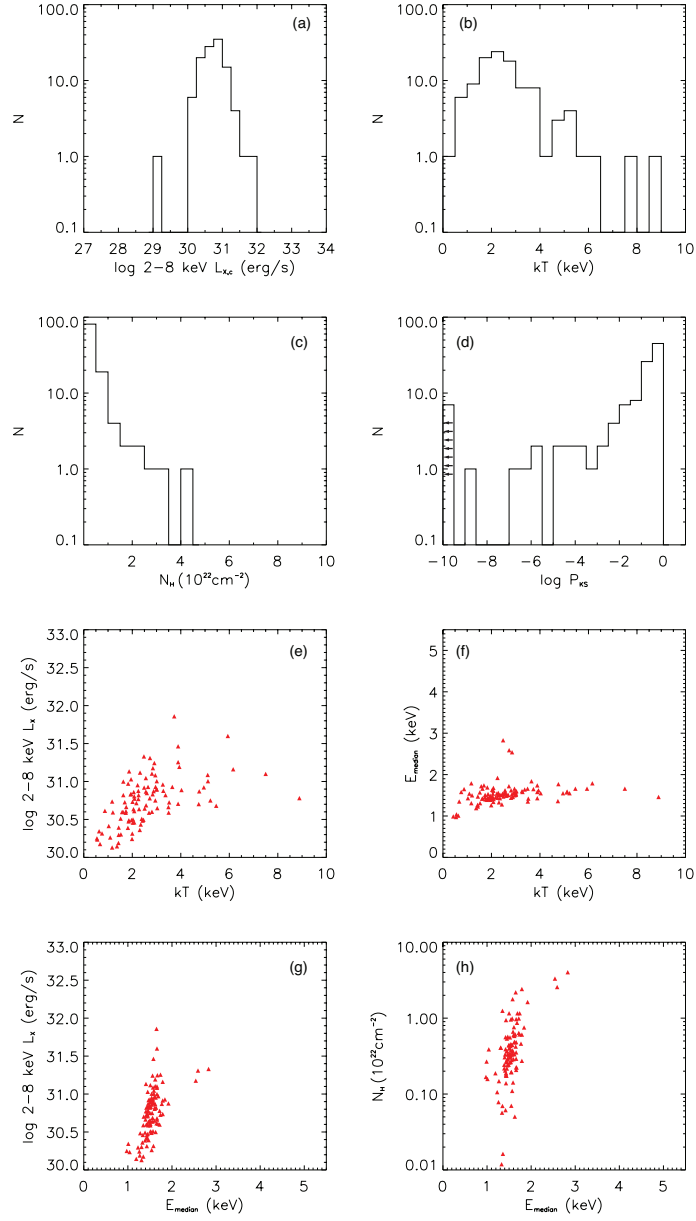


Figure B.34: Plots of derived source parameters for the bright PMS population of Trumpler 14. (a) Distribution of absorption corrected 2-8 keV L_X . (b) Distribution of best fit thermal plasma temperature (kT). (c) Distribution of best fit absorbing hydrogen column (N_H). (d) Distribution of Kolmogorov-Smirnov variability statistic with $\log P_{KS} < 0.05$ indicating variability. (e) Plot of absorption corrected 2-8 keV L_X against best fit thermal plasma temperature (kT). (f) Plot of median photon energy (E_{median}) against best fit thermal plasma temperature (kT). (g) Plot of absorption corrected 2-8 keV L_X against median photon energy (E_{median}). (h) Plot of best fit absorbing hydrogen column (N_H) against median photon energy (E_{median}).

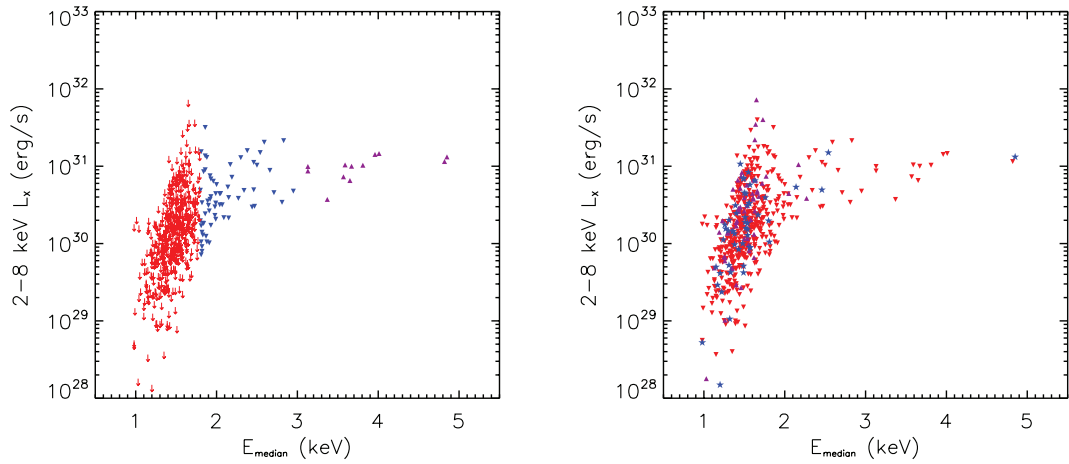


Figure B.35: Plot of the 2-8 keV L_X against the median detected photon energy (E_{median}) for the Trumpler 14 PMS population divided according to E_{median} (left) and variability (right). Left: the red arrows mark $E_{\text{median}} < 1.8$ keV (indicating an upper limit of $\log N_{\text{H}} \lesssim 22.2 \text{ cm}^{-2}$), blue inverted triangles 1.8-3 keV (indicating the lightly obscured population) and purple triangles > 3 keV (indicating the heavily obscured population). Right: Inverted red triangles refer to non-variable sources, blue stars representing variable sources and the purple triangles representing strongly variable flaring sources.

Table B.29: Trumpler 14 Diffuse Emission X-ray Spectral Parameters

Region	N_{H} (10^{22} cm^2)	kT (keV)	kT_2 (keV)	kT_3 (keV)	Z/Z_{\odot}	χ^2/ν	$\log F_{X_{h,c}}$ ($\text{erg cm}^{-2} \text{ s}^{-1}$)	$\log F_{X_{t,c}}$ ($\text{erg cm}^{-2} \text{ s}^{-1}$)	$\log L_{X_{h,c}}$ (erg s^{-1})	$\log L_{X_{t,c}}$ (erg s^{-1})
total	$0.10_{0.07}^{0.14}$	$0.18_{0.22}^{0.15}$	$0.74_{0.71}^{0.77}$	$3.83_{3.32}^{4.15}$	$0.54_{0.35}^{0.78}$	1.11/355	-11.80	-11.09	33.00	33.71
core	$0.05_{-}^{0.11}$	$0.78_{0.73}^{0.84}$	$3.47_{3.01}^{5.62}$	-	$0.14_{0.07}^{0.26}$	1.05/243	-12.22	-11.79	32.58	33.01

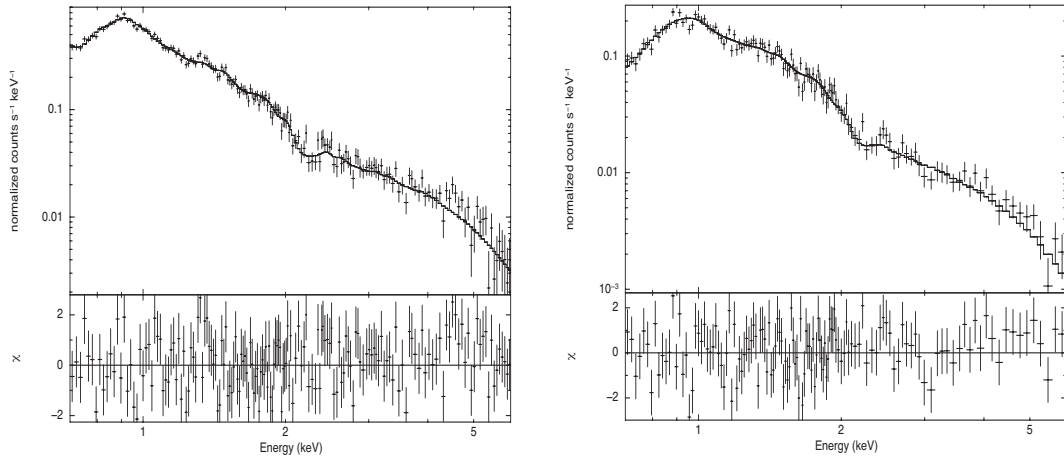


Figure B.36: Trumpler 14 total cluster diffuse emission spectrum (left) and cluster core diffuse emission spectrum (right). The spectra were rebinned for plotting purposes using XSPEC's `'setplot rebin'` command. Only the 0.7-6 keV energy range is shown for the spectra as they approach background levels outside this range.

B.9 Trumpler 16

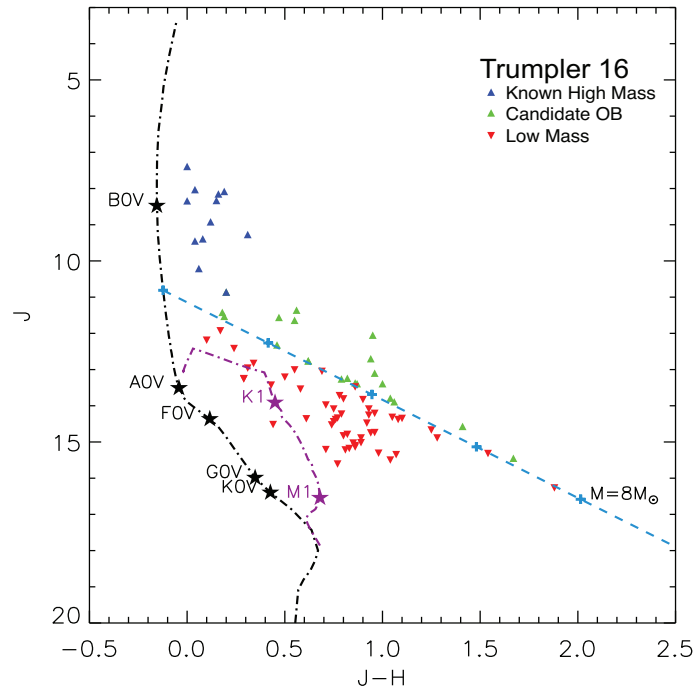


Figure B.37: Trumpler 16 2MASS J vs J-H colour magnitude diagram. The blue triangles indicate the known high mass stars, the light green triangles indicate the candidate OB stars and the red inverted triangles indicate low mass sources. The black dashed dotted line is the 4 Myr main sequence isochrone with spectral types marked calculated for $A_V = 0$. The purple dashed dotted line is the 4 Myr PMS isochrone with spectral types marked. The light blue dashed line is the $8M_{\odot}$ reddening vector with the crosses marking every $A_V = 5$.

Table B.30: Trumpler 16 Known High Mass Star X-ray Spectral Parameters

<i>Chandra</i> Source (CXO J)	Name	Sp. Type	<i>Net Cts.</i>	N_{H} (10^{22}cm^2)	kT (keV)	kT_2 (keV)	χ^2/ν	$\log F_{X_{h,c}}$ ($\text{erg cm}^{-2}\text{s}^{-1}$)	$\log F_{X_{t,c}}$ ($\text{erg cm}^{-2}\text{s}^{-1}$)	$\log L_{X_{h,c}}$ (erg s^{-1})	$\log L_{X_{t,c}}$ (erg s^{-1})
104432.36-594431.0	HD 93204	O5V((f))	505	$0.17_{-0.03}^{0.37}$	$0.51_{-0.39}^{0.62}$	-	1.05/21	-14.80	-13.16	30.08	31.71
104433.77-594415.4	HD 93205	O3V	2843	$0.22_{-0.16}^{0.28}$	$0.62_{-0.58}^{0.66}$	-	1.93/77	-13.87	-12.49	31.01	32.39
104437.71-593959.2	MJ 357	B0.5V	25	-	-	-	-	-	-	-	-
104447.34-594353.2	MJ 408	O7V((f))	188	$0.12_{-}^{0.37}$	$0.66_{-0.48}^{0.8}$	-	0.52/8	-14.75	-13.45	30.12	31.43
104454.09-594129.5	MJ 427	B1V	152	0.30_{-}	2.61_{-}	-	2.01/4	-13.95	-13.22	30.92	31.66
104459.92-594314.9	2MASS J10445990-5943149	B1	8	-	-	-	-	-	-	-	-
104503.59-594104.3	η Car	LBV	29603	-	-	-	-	> -11.00	> -10.00	> 34.00	> 35.00
104505.82-594519.7	MJ 484	O7V	204	$0.51_{-0.29}^{1.17}$	$0.52_{-0.28}^{0.63}$	-	1.16/9	-14.96	-13.36	29.92	31.52
104505.88-594307.8	MJ 481	O9.5V	76	$0.51_{-}^{1.80}$	$0.34_{-0.09}^{1.30}$	-	0.20/2	-15.35	-12.07	29.52	31.80
104505.93-594005.9	HDE 303308	O3V((f))	1617	$0.17_{-0.1}^{0.24}$	$0.57_{-0.53}^{0.62}$	-	1.46/59	-14.22	-12.73	30.66	32.14
104506.72-594156.4	MJ 488	O8.5V	89	0.01_{-}	0.53_{-}	-	2.18/3	-15.10	-14.11	29.77	30.76
104508.25-594049.4	MJ 493	B0	68	$0.32_{-}^{0.70}$	$0.64_{-0.22}^{0.78}$	-	1.45/3	-14.56	-14.00	29.31	30.88
104508.26-594606.9	MJ 496	O8.5V	1816	$0.91_{-0.68}^{1.07}$	$0.74_{-0.62}^{0.85}$	$2.04_{-1.78}^{2.38}$	0.94/81	-12.93	-12.21	31.94	32.66
104512.26-594500.5	HD 93343	O7V(n)	478	$0.38_{-}^{0.71}$	$0.71_{-0.58}^{1.06}$	-	1.19/20	-14.31	-13.08	30.56	31.80
104512.75-594446.2	MJ 516	O8.5V	382	$0.29_{-0.15}^{0.46}$	$0.63_{-0.52}^{0.74}$	-	0.45/18	-14.63	-13.27	30.24	31.60
104512.91-594419.3	MJ 517	O8V	561	$0.44_{-0.32}^{0.6}$	$0.66_{-0.57}^{0.73}$	-	0.79/26	-14.33	-13.02	30.55	31.85
104516.55-594337.1	MJ 535	O6V((f))	626	$0.55_{-0.49}^{0.61}$	$0.56_{-0.46}^{0.61}$	-	1.05/28	-14.30	-12.71	30.57	32.16
104520.59-594251.1	MJ 554	O8.5V	73	0.01_{-}	0.68_{-}	-	1.76/4	-15.46	-14.06	29.51	30.79

High mass sources identified using the high mass source lists of ???? and the SIMBAD database. Only those sources with > 50 counts were fit in *XSPEC*.

Table B.31: Trumpler 16 Candidate OB Star X-ray Spectral Parameters

<i>Chandra</i> Source (CXO J)	Name	Sp. Type	<i>Net Cts.</i>	N_{H} (10^{22}cm^2)	kT (keV)	kT_2 (keV)	χ^2/ν	$\log F_{X_{h,c}}$ ($\text{erg cm}^{-2} \text{s}^{-1}$)	$\log F_{X_{t,c}}$ ($\text{erg cm}^{-2} \text{s}^{-1}$)	$\log L_{X_{h,c}}$ (erg s^{-1})	$\log L_{X_{t,c}}$ (erg s^{-1})
104455.46-594453.3	DETW Tr 16 J104455.5-594453	-	101	$0.6_{0.28}^{1.65}$	$1.64_{0.83}^{2.42}$	-	0.27/5	-14.28	-13.77	30.59	31.10
104457.05-593827.1	2MASS J10445706-5938268	-	140	$0.29_{0.04}^{0.54}$	$0.58_{0.32}^{0.77}$	-	1.51/3	-14.88	-13.42	29.99	31.45
104500.13-594701.8	-	-	18	-	-	-	-	-	-	-	-
104506.83-594446.1	DETW Tr 16 J104506.8-594446	-	67	$0.41_{0.2}^{0.92}$	$3.61_{1.8}^{22.9}$	-	0.24/6	-14.24	-13.96	30.63	30.92
104510.56-594512.2	DETW Tr 16 J104510.6-594512	-	22	-	-	-	-	-	-	-	-
104511.12-594533.4	-	-	66	$0.72_{0.19}^{1.67}$	$1.24_{0.68}^{1.71}$	-	0.86/5	-14.61	-13.93	30.27	30.95
104517.19-594701.1	-	-	42	-	-	-	-	-	-	-	-
104518.89-594217.8	DETW Tr 16 J104519.0-594218	-	39	-	-	-	-	-	-	-	-
104520.86-594013.3	DETW Tr 16 J104520.9-594013	-	31	-	-	-	-	-	-	-	-
104521.01-594548.6	2MASS J10452096-5945488	-	49	-	-	-	-	-	-	-	-
104522.08-594145.7	2MASS J10452206-5941458	-	68	0.06_{-}	7.18_{-}	-	2.05/4	-14.27	-14.06	30.61	30.82
104528.26-594556.1	-	-	21	-	-	-	-	-	-	-	-
104528.90-594347.7	[ARV2008] 210	-	176	0.40_{-}	3.07_{-}	-	2.18/5	-13.86	-13.55	31.01	31.32
104531.29-594113.5	DETW Tr 16 J104531.4-594113	-	41	-	-	-	-	-	-	-	-
104535.47-594544.9	-	-	48	-	-	-	-	-	-	-	-
104536.93-594619.8	-	-	34	-	-	-	-	-	-	-	-
104538.37-594207.6	DETW Tr 16 J104538.4-594207	-	53	$1.1_{0.19}^{2.82}$	$3.58_{1.17}^{-}$	-	0.45/6	-14.10	-13.81	30.78	31.06
104538.55-594513.4	DETW Tr 16 J104538.7-594513	-	38	-	-	-	-	-	-	-	-
104543.74-594148.4	2MASS J10454366-5941481	-	83	$0.62_{0.26}^{1.45}$	$2.92_{1.43}^{56.8}$	-	0.07/1	-14.10	-13.77	30.77	31.10

Source names determined using the SIMBAD database. Only those sources with > 50 counts were fit in *XSPEC*.

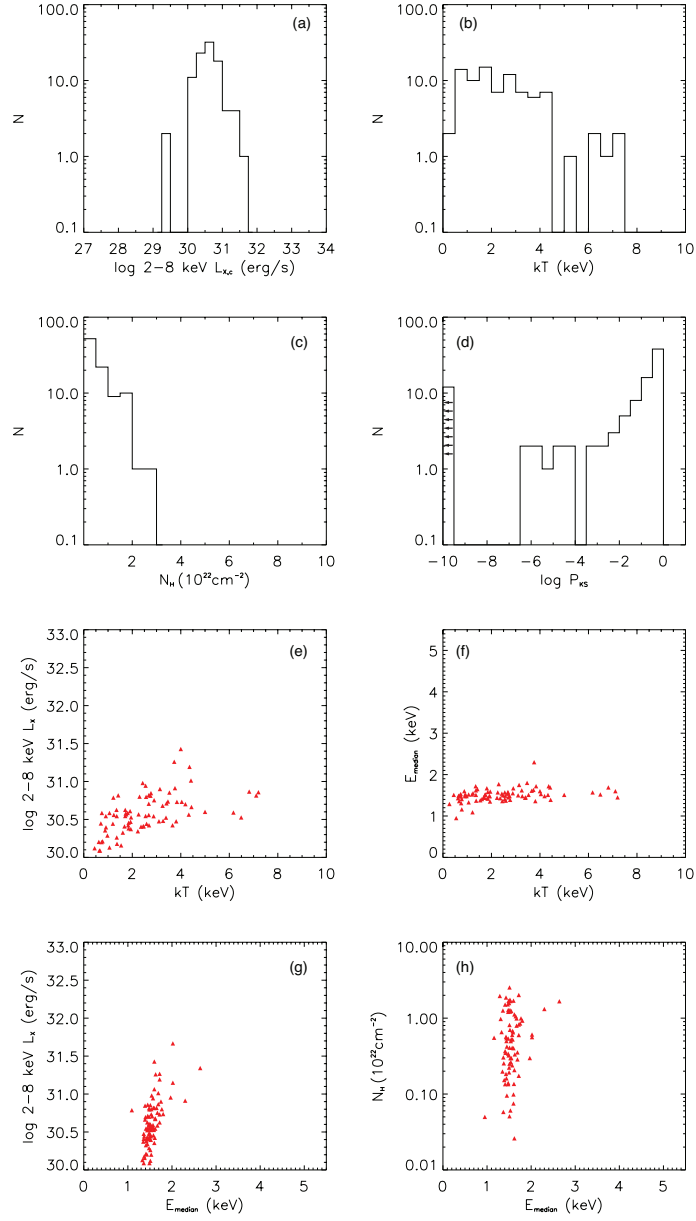


Figure B.38: Plots of derived source parameters for the bright PMS population of Trumpler 16. (a) Distribution of absorption corrected 2-8 keV L_X . (b) Distribution of best fit thermal plasma temperature (kT). (c) Distribution of best fit absorbing hydrogen column (N_H). (d) Distribution of Kolmogorov-Smirnov variability statistic with $\log P_{KS} < 0.05$ indicating variability. (e) Plot of absorption corrected 2-8 keV L_X against best fit thermal plasma temperature (kT). (f) Plot of median photon energy (E_{median}) against best fit thermal plasma temperature (kT). (g) Plot of absorption corrected 2-8 keV L_X against median photon energy (E_{median}). (h) Plot of best fit absorbing hydrogen column (N_H) against median photon energy (E_{median}).

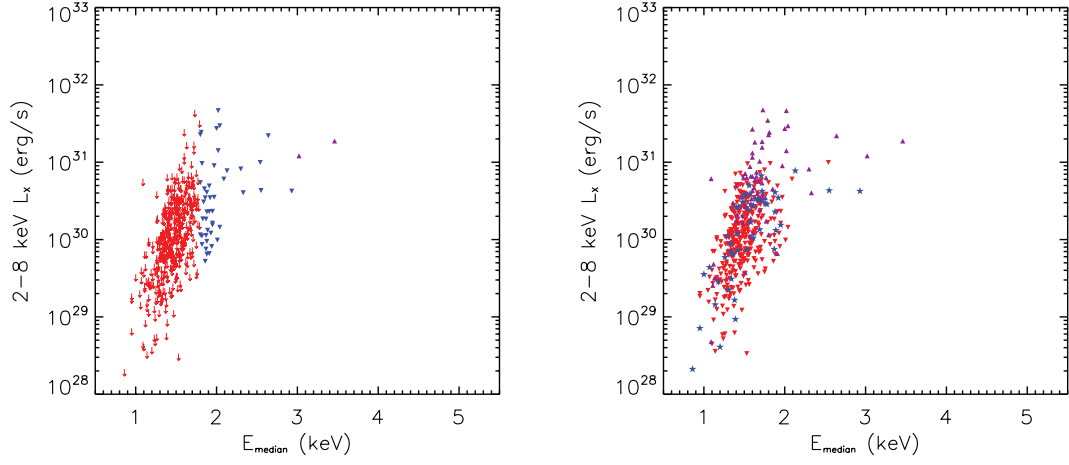


Figure B.39: Plot of the 2-8 keV L_X against the median detected photon energy (E_{median}) for the Trumpler 16 PMS population divided according to E_{median} (left) and variability (right). Left: the red arrows mark $E_{\text{median}} < 1.8$ keV (indicating an upper limit of $\log N_{\text{H}} \lesssim 22.2 \text{ cm}^{-2}$), blue inverted triangles 1.8-3 keV (indicating the lightly obscured population) and purple triangles > 3 keV (indicating the heavily obscured population). Right: Inverted red triangles refer to non-variable sources, blue stars representing variable sources and the purple triangles representing strongly variable flaring sources.

Table B.32: Trumpler 16 Diffuse Emission X-ray Spectral Parameters

Region	N_{H} (10^{22}cm^2)	kT (keV)	kT_2 (keV)	kT_3 (keV)	Z/Z_{\odot}	χ^2/ν	$\log F_{X_{h,c}}$ ($\text{erg cm}^{-2} \text{s}^{-1}$)	$\log F_{X_{t,c}}$ ($\text{erg cm}^{-2} \text{s}^{-1}$)	$\log L_{X_{h,c}}$ (erg s^{-1})	$\log L_{X_{t,c}}$ (erg s^{-1})
total	$0.11^{0.14}_{0.07}$	$0.31^{0.33}_{0.29}$	$0.64^{0.67}_{0.60}$	64_{-}	1 (frozen)	1.33/417	-11.52	-10.89	33.35	33.98
core	$0.11^{0.16}_{0.05}$	$0.30^{0.31}_{0.29}$	$0.68^{0.72}_{0.64}$	64_{-}	1 (frozen)	1.56/424	-11.68	-10.89	33.20	33.98

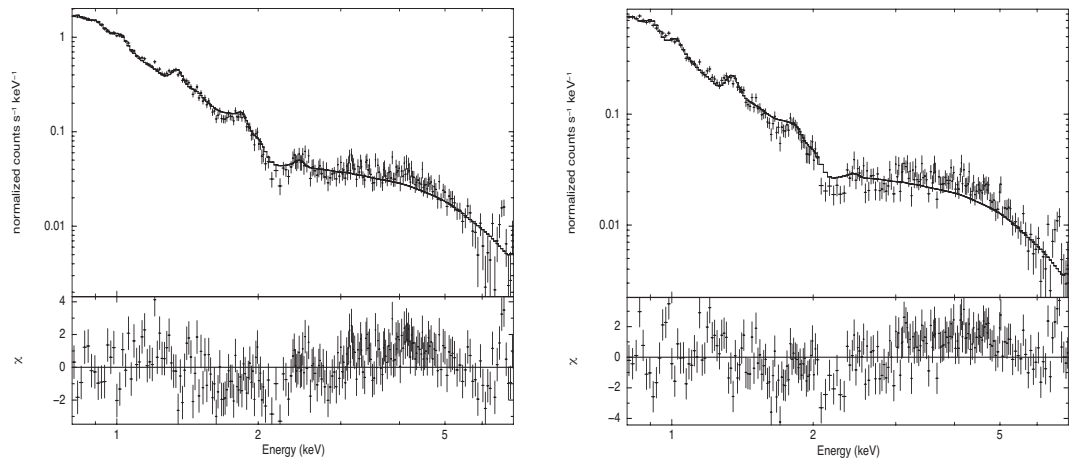


Figure B.40: Trumpler 16 total cluster diffuse emission spectrum (left) and cluster core diffuse emission spectrum (right). The spectra were rebinned for plotting purposes using XSPEC's *'setplot rebin'* command. Only the 0.8-7 keV energy range is shown for the spectra as they approach background levels outside this range.

B.10 Westerlund 1

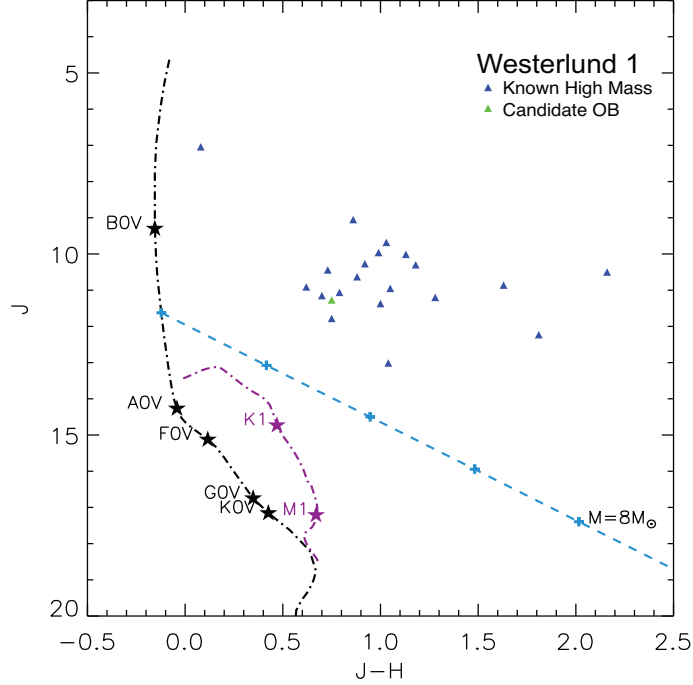


Figure B.41: Westerlund 1 2MASS J vs J-H colour magnitude diagram. The blue triangles indicate the known high mass stars and the light green triangles indicate the candidate OB stars. The black dashed dotted line is the 3.6 Myr main sequence isochrone with spectral types marked calculated for $A_V = 0$. The purple dashed dotted line is the 3.6 Myr PMS isochrone with spectral types marked. The light blue dashed line is the $8M_{\odot}$ reddening vector with the crosses marking every $A_V = 5$. Unlike in most other clusters, only the candidate OB star in NGC 3603 had high quality 2MASS photometry. The known high mass sources shown here were plotted using low quality 2MASS photometry to offer a relative indicator to the candidate OB star.

Table B.33: Westerland 1 Known High Mass Star X-ray Spectral Parameters

<i>Chandra</i> Source (CXO J)	Name	Sp. Type	<i>Net Cts.</i>	N_{H} (10^{22} cm^2)	kT (keV)	kT_2 (keV)	χ^2/ν	$\log F_{X_{h,c}}$ ($\text{erg cm}^{-2} \text{ s}^{-1}$)	$\log F_{X_{t,c}}$ ($\text{erg cm}^{-2} \text{ s}^{-1}$)	$\log L_{X_{h,c}}$ (erg s^{-1})	$\log L_{X_{t,c}}$ (erg s^{-1})
164654.30-455154.8	C07-X7	B0Iab	9	-	-	-	-	-	-	-	-
164658.81-455302.1	W228b	O9Ib	12	-	-	-	-	-	-	-	-
164658.86-455146.2	W56b	O9.5Ib	15	-	-	-	-	-	-	-	-
164659.05-455028.4	W84	O9.5Ib	12	-	-	-	-	-	-	-	-
164659.39-455047.1	W1	-	10	-	-	-	-	-	-	-	-
164700.39-455132.0	W53	-	56	$3.74_{2.37}^{5.67}$	$0.46_{0.28}^{0.85}$	-	0.89/5	-14.36	-12.59	30.82	32.59
164401.26-455130.7	W52	B1.5Ia	13	-	-	-	-	-	-	-	-
164701.40-455150.8	W59	-	10	-	-	-	-	-	-	-	-
164701.44-455234.8	W232	B1Iab	10	-	-	-	-	-	-	-	-
164702.14-455113.1	W24	O9Iab	13	-	-	-	-	-	-	-	-
164702.49-455137.9	W62a	B0.5Ib	15	-	-	-	-	-	-	-	-
164702.60-455118.1	W47	-	15	-	-	-	-	-	-	-	-
164702.68-455050.6	W40a	OB SG	30	-	-	-	-	-	-	-	-
164702.71-455057.7	W41	O9Iab	11	-	-	-	-	-	-	-	-
164702.79-455213.1	C07-X4	O9-9.5Ia	10	-	-	-	-	-	-	-	-
164702.88-455046.4	W38	O9Iab	10	-	-	-	-	-	-	-	-
164703.04-455023.6	W6	B0.5Iab + O9.5III	10	-	-	-	-	-	-	-	-
164703.22-455157.9	W63a	B0Iab	21	-	-	-	-	-	-	-	-
164703.64-455051.6	W42a	B9Ia ⁽⁺⁾	11	-	-	-	-	-	-	-	-
164703.74-455058.4	W43c	O9Ib	24	-	-	-	-	-	-	-	-
164704.02-455125.1	WR G	WN7o	84	$2.24_{1.47}^{3.31}$	$4.17_{2.23}^{23.08}$	-	0.58/5	-13.60	-13.35	31.58	31.82
164704.11-455039.2	W30a	O9-B0.5Ia	477	$2.51_{2.12}^{3.18}$	$1.42_{1.05}^{1.73}$	-	1.11/24	-13.16	-12.58	32.02	32.60
164704.14-455031.4	W9	sgB[e]	394	$4.28_{3.72}^{5.50}$	$0.71_{0.45}^{0.89}$	64_{-}	0.72/18	-12.83	-11.59	32.35	33.59
164704.20-455107.1	WR L	WN9h	80	$2.47_{1.45}^{3.74}$	$3.28_{1.53}^{34.98}$	-	0.72/4	-13.57	-13.28	31.61	31.90
164704.59-455008.2	C07-X3	O9-9.5Ia	13	-	-	-	-	-	-	-	-
164705.08-455055.1	W36	-	42	-	-	-	-	-	-	-	-
164705.16-455041.4	W27	O9I + OI	35	-	-	-	-	-	-	-	-
164705.20-455225.1	WR F	WC9d	99	4.19_{-}	3.26_{-}	-	1.37/5	-13.34	-13.05	31.84	32.13
164705.37-455104.9	WR B	WN7o	228	$4.65_{2.98}^{8.53}$	$0.50_{0.13}^{1.54}$	$2.87_{0.17}^{-}$	0.26/6	-13.03	-12.02	32.15	33.15
164705.78-455033.4	W25	O9Iab	10	-	-	-	-	-	-	-	-
164705.99-455208.1	WR E	WC9	8	-	-	-	-	-	-	-	-
164706.10-455022.5	WR R	WN5o	15	-	-	-	-	-	-	-	-

Table B.34: Westerlund 1 Known High Mass Star X-ray Spectral Parameters (Cont.)

<i>Chandra</i> Source (CXO J)	Name	Sp. Type	<i>Net Cts.</i>	N_{H} (10^{22}cm^2)	kT (keV)	kT_2 (keV)	χ^2/ν	$\log F_{X_{h,c}}$ ($\text{erg cm}^{-2} \text{s}^{-1}$)	$\log F_{X_{t,c}}$ ($\text{erg cm}^{-2} \text{s}^{-1}$)	$\log L_{X_{h,c}}$ (erg s^{-1})	$\log L_{X_{t,c}}$ (erg s^{-1})
164706.25-455126.7	WR D	WN7o	13	-	-	-	-	-	-	-	-
164706.45-455026.2	W13	B0.5Ia + OB	21	-	-	-	-	-	-	-	-
164706.55-455039.2	WR U	WN6o	144	$2.17_{-}^{\bar{}}$	$0.26_{-}^{\bar{}}$	$2.17_{-}^{\bar{}}$	0.90/3	-13.55	-12.43	31.62	32.74
164706.64-455029.7	W15	O9Ib	9	-	-	-	-	-	-	-	-
164707.09-455013.3	W74	O9.5Iab	10	-	-	-	-	-	-	-	-
164707.51-455228.9	W243	LBV	7	-	-	-	-	-	-	-	-
164707.64-454922.3	WR W	WN6h	22	-	-	-	-	-	-	-	-
164707.66-455236.2	WR O	WN6o	54	$1.3_{-}^{\bar{}}$	$1.53_{-}^{\bar{}}$	-	1.29/5	-14.07	-13.67	31.10	31.51
164708.35-455045.5	WR A	WN7b	642	$3.53_{2.81}^{4.38}$	$0.28_{0.23}^{0.34}$	$3.68_{2.77}^{5.69}$	1.32/31	-12.72	-11.50	32.45	33.68
164709.21-455048.6	W71	B2.5Ia	9	-	-	-	-	-	-	-	-
164710.06-455050.1	W70	B3Ia	21	-	-	-	-	-	-	-	-

High mass sources identified using the high mass source lists of [Clark et al. \(2005\)](#); [Negueruela et al. \(2010\)](#) and the SIMBAD database. Only those sources with > 50 counts were fit in *XSPEC*.

Table B.35: Westerlund 1 Candidate OB Star X-ray Spectral Parameters

<i>Chandra</i> Source (CXO J)	Name	Sp. Type	<i>Net Cts.</i>	N_{H} (10^{22}cm^2)	kT (keV)	kT_2 (keV)	χ^2/ν	$\log F_{X_{h,c}}$ ($\text{erg cm}^{-2} \text{s}^{-1}$)	$\log F_{X_{t,c}}$ ($\text{erg cm}^{-2} \text{s}^{-1}$)	$\log L_{X_{h,c}}$ (erg s^{-1})	$\log L_{X_{t,c}}$ (erg s^{-1})
164714.46-454755.0	2MASS J16471442-4547549	-	10	-	-	-	-	-	-	-	-

Source names determined using the SIMBAD database. Only those sources with > 50 counts were fit in *XSPEC*.

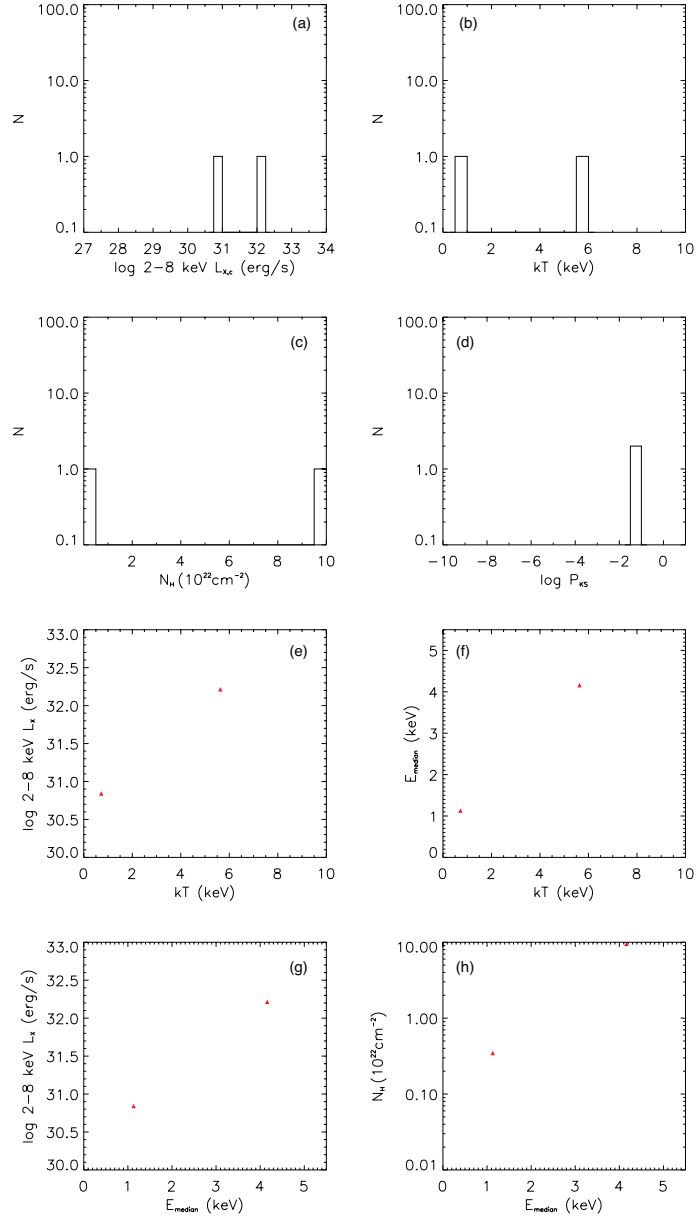


Figure B.42: Plots of derived source parameters for the bright ‘unidentified’ source population of Westerlund 1. (a) Distribution of absorption corrected 2-8 keV L_X . (b) Distribution of best fit thermal plasma temperature (kT). (c) Distribution of best fit absorbing hydrogen column (N_H). (d) Distribution of Kolmogorov-Smirnov variability statistic with $\log P_{KS} < 0.05$ indicating variability. (e) Plot of absorption corrected 2-8 keV L_X against best fit thermal plasma temperature (kT). (f) Plot of median photon energy (E_{median}) against best fit thermal plasma temperature (kT). (g) Plot of absorption corrected 2-8 keV L_X against median photon energy (E_{median}). (h) Plot of best fit absorbing hydrogen column (N_H) against median photon energy (E_{median}).

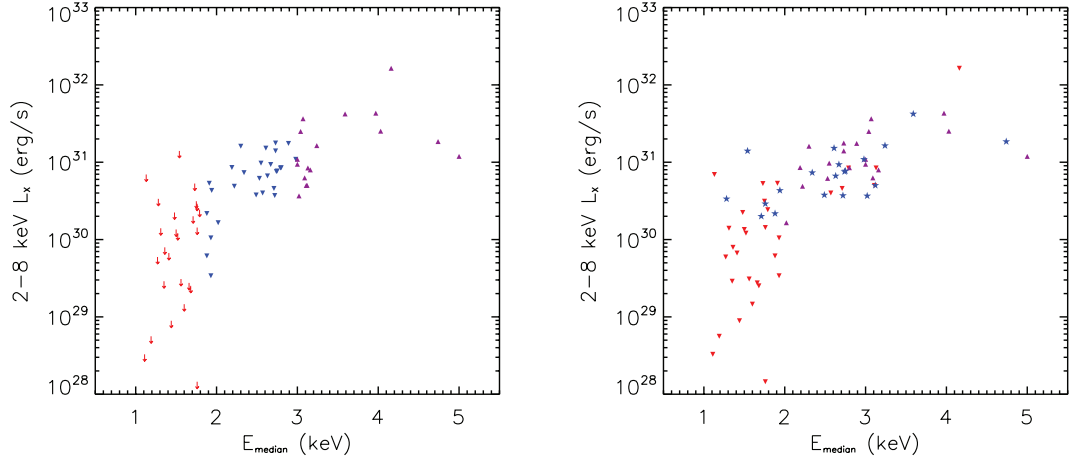


Figure B.43: Plot of the 2-8 keV L_X against the median detected photon energy (E_{median}) for the Westerlund 1 ‘unidentified’ source population divided according to E_{median} (left) and variability (right). Left: the red arrows mark $E_{\text{median}} < 1.8$ keV (indicating an upper limit of $\log N_{\text{H}} \lesssim 22.2$ cm^{-2}), blue inverted triangles 1.8-3 keV (indicating the lightly obscured population) and purple triangles > 3 keV (indicating the heavily obscured population). Right: Inverted red triangles refer to non-variable sources, blue stars representing variable sources and the purple triangles representing strongly variable flaring sources.

Table B.36: Westerlund 1 Diffuse Emission X-ray Spectral Parameters

Region	N_{H} (10^{22}cm^2)	kT (keV)	kT_2 (keV)	Z/Z_{\odot}	χ^2/ν	$\log F_{X_{h,c}}$ ($\text{erg cm}^{-2} \text{s}^{-1}$)	$\log F_{X_{t,c}}$ ($\text{erg cm}^{-2} \text{s}^{-1}$)	$\log L_{X_{h,c}}$ (erg s^{-1})	$\log L_{X_{t,c}}$ (erg s^{-1})
total	$1.59^{1.66}_{1.51}$	$0.60^{0.65}_{0.56}$	9.55_{-}	$2.17^{3.97}_{1.38}$	1.56/525	-11.02	-10.62	34.16	34.56
core	$1.85^{1.94}_{1.75}$	$0.63^{0.73}_{0.58}$	$9.55^{12.45}_{7.03}$	$1.02^{1.68}_{0.66}$	1.16/408	-11.46	-10.86	33.72	34.32

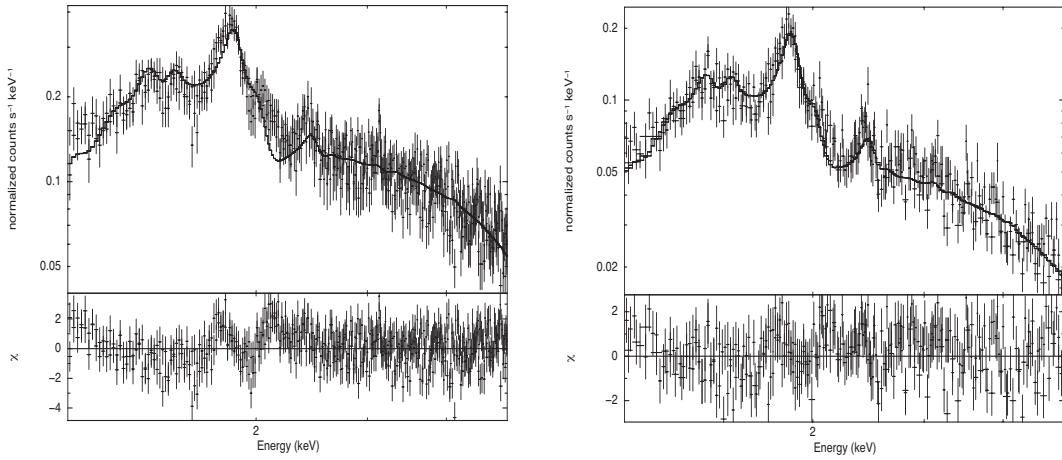


Figure B.44: Westerlund 1 total cluster diffuse emission spectrum (left) and cluster core diffuse emission spectrum (right). The spectra were rebinned for plotting purposes using XSPEC's *'setplot rebin'* command. Only the 1-5 keV energy range is shown as the spectra approach background levels outside this range.

B.11 Westerlund 2

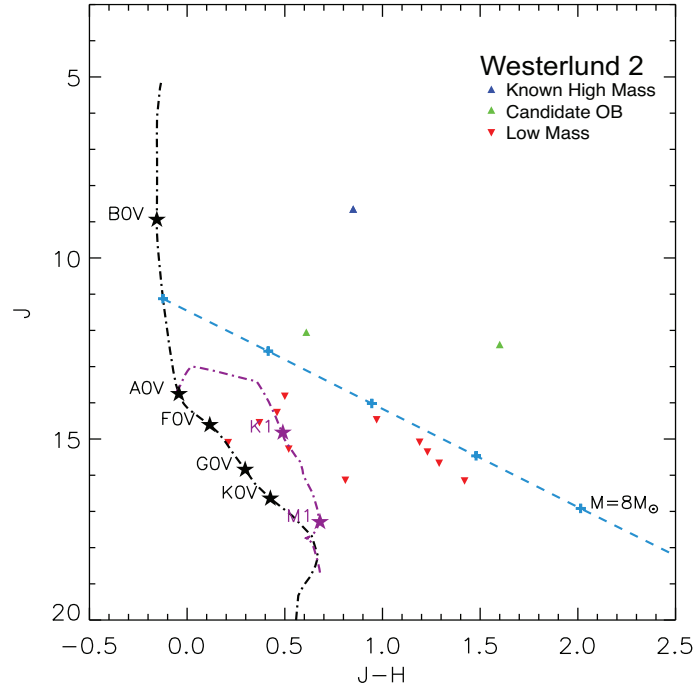


Figure B.45: Westerlund 2 2MASS J vs J-H colour magnitude diagram. The blue triangles indicate the known high mass stars, the light green triangles indicate the candidate OB stars and the red inverted triangles indicate low mass sources. The black dashed dotted line is the 2.5 Myr main sequence isochrone with spectral types marked calculated for $A_V = 0$. The purple dashed dotted line is the 2.5 Myr PMS isochrone with spectral types marked. The light blue dashed line is the $8M_{\odot}$ reddening vector with the crosses marking every $A_V = 5$.

Table B.37: Westerlund 2 Known High Mass Star X-ray Spectral Parameters

<i>Chandra</i> Source (CXO J)	Name	Sp. Type	<i>Net Cts.</i>	N_{H} (10^{22} cm^2)	kT (keV)	kT_2 (keV)	χ^2/ν	$\log F_{X_{h,c}}$ ($\text{erg cm}^{-2} \text{ s}^{-1}$)	$\log F_{X_{t,c}}$ ($\text{erg cm}^{-2} \text{ s}^{-1}$)	$\log L_{X_{h,c}}$ (erg s^{-1})	$\log L_{X_{t,c}}$ (erg s^{-1})
102355.18-574526.9	MSP 165	O7	112	$2.52^{3.58}_{1.43}$	$0.36^{0.59}_{0.23}$	-	1.01/4	-14.27	-12.04	31.05	33.29
102356.22-574530.2	MSP 182	O4V-III	43	-	-	-	-	-	-	-	-
102358.01-574548.9	WR20a	WN6ha+WN6ha	4123	$2.33^{2.56}_{2.16}$	$0.42^{0.49}_{0.33}$	$2.76^{2.16}_{3.12}$	1.22/174	-12.27	-11.43	33.05	33.90
102358.45-574513.0	MSP 120	O9.5V	15	-	-	-	-	-	-	-	-
102359.17-574540.6	MSP 233	O8.5V	31	-	-	-	-	-	-	-	-
102400.46-574445.0	MSP 44	O9.5V	48	-	-	-	-	-	-	-	-
102400.48-574523.9	MSP 151	O7III	41	-	-	-	-	-	-	-	-
102400.79-574525.8	MSP 157	O5.5V	105	$1.47^{1.83}_{0.21}$	$0.86^{3.54}_{0.58}$	-	1.62/5	-14.49	-13.25	30.83	32.07
102401.20-574531.0	MSP 188	O4V-III	1413	$1.23^{1.43}_{0.95}$	$0.65^{0.85}_{0.50}$	$2.80^{7.96}_{2.02}$	1.01/64	-13.15	-12.31	32.17	33.02
102401.39-574529.8	MSP 175	O5.5V-III	138	$1.75^{2.14}_{0.90}$	$0.30^{0.44}_{0.18}$	-	1.03/3	-14.91	-12.30	30.42	33.03
102401.52-574557.0	MSP 263	O6.5V	76	$2.77^{3.53}_{1.85}$	$0.39^{0.56}_{0.26}$	-	0.96/7	-14.83	-12.82	30.49	32.51
102402.06-574527.9	MSP 167	O6III	777	$1.92^{2.14}_{1.69}$	$0.54^{0.61}_{0.44}$	$2.80^{5.14}_{2.23}$	1.37/37	-13.18	-12.07	32.15	33.26
102402.32-574535.3	MSP 203	O6V-III	218	$1.17^{1.50}_{0.60}$	$0.88^{1.14}_{0.68}$	-	0.73/9	-14.23	-13.15	31.09	32.18
102402.37-574530.5	MSP 18	O5.5V-III	266	$1.75^{2.27}_{1.44}$	$0.62^{0.76}_{0.46}$	-	0.92/12	-14.22	-12.84	31.11	32.49
102402.43-574436.1	MSP 183	O4V	2110	$1.48^{1.80}_{1.21}$	$0.38^{0.59}_{0.24}$	$3.06^{3.62}_{2.64}$	0.86/104	-12.60	-11.81	32.73	33.51
102402.67-574534.4	MSP 199	O3V	45	-	-	-	-	-	-	-	-
102404.88-574528.0	MSP 171	O5V	39	-	-	-	-	-	-	-	-
102406.63-574715.9	Src3	O9.5V	16	-	-	-	-	-	-	-	-
102416.24-574343.8	Src2	O8.5III	174	$2.03^{2.57}_{1.73}$	$0.56^{0.80}_{0.36}$	-	1.58/7	-14.25	-12.51	31.08	32.82
102418.40-574829.8	WR 20b	WN6ha	1504	$4.02^{4.90}_{3.37}$	$0.38^{0.50}_{0.28}$	$5.34^{7.94}_{3.77}$	0.93/76	-12.50	-11.58	32.83	33.74

High mass sources identified using the high mass source lists of [Rauw et al. \(2007\)](#) and the SIMBAD database. Only those sources with > 50 counts were fit in *XSPEC*.

Table B.38: Westerlund 2 Candidate OB Star X-ray Spectral Parameters

<i>Chandra</i> Source (CXO J)	Name	Sp. Type	<i>Net Cts.</i>	N_{H} (10^{22} cm^2)	kT (keV)	kT_2 (keV)	χ^2/ν	$\log F_{X_{h,c}}$ ($\text{erg cm}^{-2} \text{ s}^{-1}$)	$\log F_{X_{t,c}}$ ($\text{erg cm}^{-2} \text{ s}^{-1}$)	$\log L_{X_{h,c}}$ (erg s^{-1})	$\log L_{X_{t,c}}$ (erg s^{-1})
102334.02-574703.8	2MASS J10233400-5747038	-	148	$3.59^{4.75}_{2.73}$	$0.78^{1.02}_{0.58}$	-	0.56/6	-13.90	-12.78	31.43	32.54
102345.62-574802.7	2MASS J10234564-5748027	-	68	$1.67^{2.97}_{0.67}$	$1.31^{2.13}_{0.68}$	-	1.06/5	-14.38	-13.63	30.95	31.70

Source names determined using the SIMBAD database. Only those sources with > 50 counts were fit in *XSPEC*.

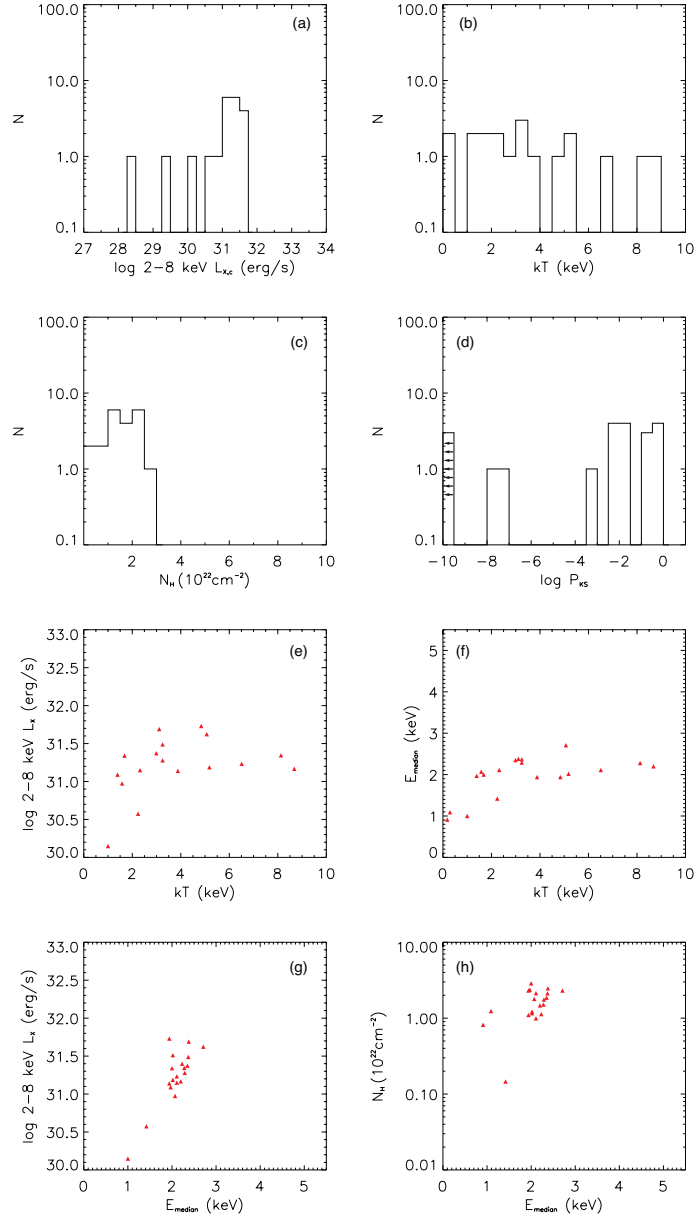


Figure B.46: Plots of derived source parameters for the bright ‘unidentified’ source population of Westerlund 2. (a) Distribution of absorption corrected 2-8 keV L_X . (b) Distribution of best fit thermal plasma temperature (kT). (c) Distribution of best fit absorbing hydrogen column (N_H). (d) Distribution of Kolmogorov-Smirnov variability statistic with $\log P_{KS} < 0.05$ indicating variability. (e) Plot of absorption corrected 2-8 keV L_X against best fit thermal plasma temperature (kT). (f) Plot of median photon energy (E_{median}) against best fit thermal plasma temperature (kT). (g) Plot of absorption corrected 2-8 keV L_X against median photon energy (E_{median}). (h) Plot of best fit absorbing hydrogen column (N_H) against median photon energy (E_{median}).

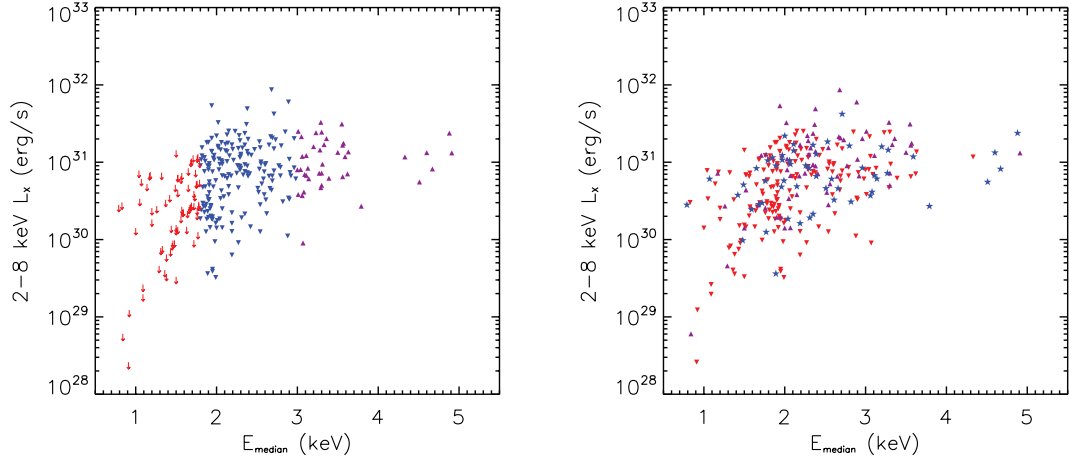


Figure B.47: Plot of the 2-8 keV L_X against the median detected photon energy (E_{median}) for the Westerlund 2 ‘unidentified’ source population divided according to E_{median} (left) and variability (right). Left: the red arrows mark $E_{\text{median}} < 1.8$ keV (indicating an upper limit of $\log N_{\text{H}} \lesssim 22.2$ cm^{-2}), blue inverted triangles 1.8-3 keV (indicating the lightly obscured population) and purple triangles > 3 keV (indicating the heavily obscured population). Right: Inverted red triangles refer to non-variable sources, blue stars representing variable sources and the purple triangles representing strongly variable flaring sources.

Table B.39: Westerlund 2 Diffuse Emission X-ray Spectral Parameters

Region	N_{H} (10^{22} cm^2)	kT (keV)	kT_2 (keV)	Z/Z_{\odot}	χ^2/ν	$\log F_{X_{h,c}}$ ($\text{erg cm}^{-2} \text{ s}^{-1}$)	$\log F_{X_{t,c}}$ ($\text{erg cm}^{-2} \text{ s}^{-1}$)	$\log L_{X_{h,c}}$ (erg s^{-1})	$\log L_{X_{t,c}}$ (erg s^{-1})
total	$1.01^{1.10}_{0.90}$	$0.67^{0.85}_{0.60}$	$4.10^{4.68}_{3.69}$	$0.36^{0.55}_{0.22}$	0.94/772	-11.71	-11.26	33.61	34.06
core	$1.14^{1.26}_{0.98}$	$0.68^{0.78}_{0.61}$	$3.38^{3.88}_{3.10}$	$0.27^{0.39}_{0.14}$	1.18/652	-11.9 9	-11.50	33.33	33.82

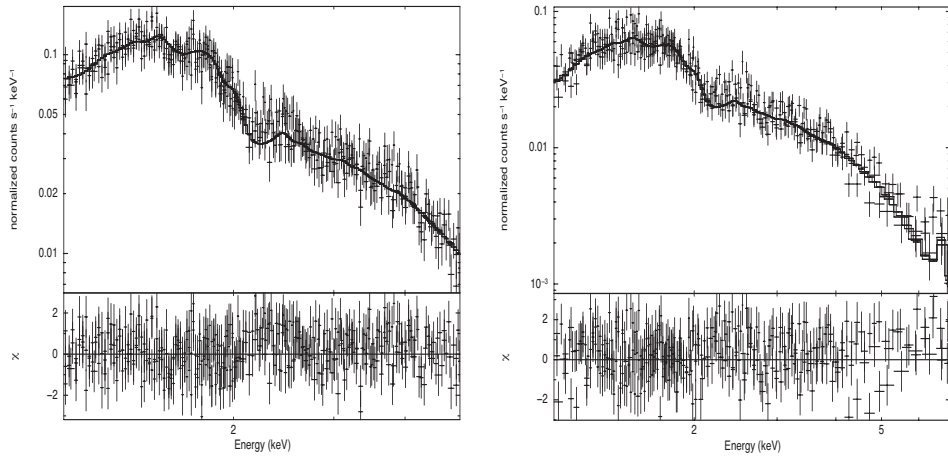


Figure B.48: Westerlund 2 total cluster diffuse emission spectrum (left) and cluster core diffuse emission spectrum (right). The spectra were rebinned for plotting purposes using XSPEC's *'setplot rebin'* command. Only the 1-5 keV and 1-7 keV energy ranges are shown for the total cluster and core spectra respectively, as they approach background levels outside these ranges.

??table.caption.82120 table.caption.82, 121table.caption.82121table.caption.82121

References

- Aharonian, F., Akhperjanian, A. G., Bazer-Bachi, A. R., Beilicke, M., Benbow, W., Berge, D., Bernlöhr, K., et al.: 2007, *A&A* **467**, 1075 [111](#), [112](#)
- Albacete-Colombo, J. F., Damiani, F., Micela, G., Sciortino, S., and Harnden, Jr., F. R.: 2008, *A&A* **490**, 1055 [99](#), [100](#), [133](#)
- Albacete Colombo, J. F., Flaccomio, E., Micela, G., Sciortino, S., and Damiani, F.: 2007, *A&A* **464**, 211 [58](#)
- Albacete Colombo, J. F., Méndez, M., and Morrell, N. I.: 2003, *MNRAS* **346**, 704 [95](#), [100](#)
- Ascenso, J., Alves, J., Beletsky, Y., and Lago, M. T. V. T.: 2007a, *A&A* **466**, 137 [111](#)
- Ascenso, J., Alves, J., Vicente, S., and Lago, M. T. V. T.: 2007b, *A&A* **476**, 199 [94](#)
- Aschenbach, B.: 1985, *Reports on Progress in Physics* **48**, 579 [19](#)
- Babel, J. and Montmerle, T.: 1997a, *ApJ* **485**, L29 [8](#)
- Babel, J. and Montmerle, T.: 1997b, *A&A* **323**, 121 [7](#), [8](#)
- Belikov, A. N., Kharchenko, N. V., Piskunov, A. E., and Schilbach, E.: 1999, *A&AS* **134**, 525 [84](#)
- Benaglia, P. and Koribalski, B.: 2004, *A&A* **416**, 171 [97](#)
- Berghoefer, T. W., Schmitt, J. H. M. M., Danner, R., and Cassinelli, J. P.: 1997, *A&A* **322**, 167 [7](#)
- Bica, E., Bonatto, C., and Dutra, C. M.: 2003, *A&A* **405**, 991 [22](#), [57](#), [59](#)

REFERENCES

- Bonatto, C., Kerber, L. O., Bica, E., and Santiago, B. X.: 2006a, *A&A* **446**, 121 [26](#)
- Bonatto, C., Santos, Jr., J. F. C., and Bica, E.: 2006b, *A&A* **445**, 567 [84](#)
- Brandner, W., Clark, J. S., Stolte, A., Waters, R., Negueruela, I., and Goodwin, S. P.: 2008, *A&A* **478**, 137 [105](#), [110](#), [131](#), [132](#), [134](#)
- Broos, P. S., Feigelson, E. D., Townsley, L. K., Getman, K. V., Wang, J., Garmire, G. P., Jiang, Z., and Tsuboi, Y.: 2007, *ApJS* **169**, 353 [4](#), [16](#), [89](#)
- Broos, P. S., Townsley, L. K., Feigelson, E. D., Getman, K. V., Bauer, F. E., and Garmire, G. P.: 2010, *ApJ* **714**, 1582 [50](#), [54](#)
- Calzavara, A. J. and Matzner, C. D.: 2004, *MNRAS* **351**, 694 [12](#)
- Cantó, J., Raga, A. C., and Rodríguez, L. F.: 2000, *ApJ* **536**, 896 [14](#), [15](#), [61](#), [64](#), [83](#), [88](#), [93](#), [98](#), [103](#), [109](#), [115](#), [129](#), [130](#)
- Caramazza, M., Micela, G., Prisinzano, L., Rebull, L., Sciortino, S., and Stauffer, J. R.: 2008, *A&A* **488**, 211 [69](#)
- Carraro, G. and Munari, U.: 2004, *MNRAS* **347**, 625 [111](#)
- Cherepashchuk, A. M.: 1976, *Soviet Astronomy Letters* **2**, 138 [9](#)
- Chini, R., Hoffmeister, V. H., Kämpgen, K., Kimeswenger, S., Nielbock, M., and Siebenmorgen, R.: 2004, *A&A* **427**, 849 [90](#)
- Churchwell, E., Whitney, B. A., Babler, B. L., Indebetouw, R., Meade, M. R., Watson, C., Wolff, M. J., Wolfire, et al.: 2004, *ApJS* **154**, 322 [111](#)
- Clark, J. S., Munro, M. P., Negueruela, I., Dougherty, S. M., Crowther, P. A., Goodwin, S. P., and de Grijs, R.: 2008, *A&A* **477**, 147 [105](#), [110](#), [117](#), [118](#), [120??](#), [131](#), [132](#)
- Clark, J. S. and Negueruela, I.: 2002, *A&A* **396**, L25 [104](#)
- Clark, J. S. and Negueruela, I.: 2004, *A&A* **413**, L15 [104](#)
- Clark, J. S., Negueruela, I., Crowther, P. A., and Goodwin, S. P.: 2005, *A&A* **434**, 949 [104](#), [107](#), [129](#), [234](#)

REFERENCES

- Comerón, F., Pasquali, A., Rodighiero, G., Stanishev, V., De Filippis, E., López Martí, B., Gálvez Ortiz, M. C., Stankov, A., and Gredel, R.: 2002, *A&A* **389**, 874 [57](#)
- Corcoran, M. F., Hamaguchi, K., Pittard, J. M., Russell, C. M. P., Owocki, S. P., Parkin, E. R., and Okazaki, A.: 2010, *ApJ* **725**, 1528 [100](#)
- Crowther, P. A.: 2007, *ARA&A* **45**, 177 [15](#), [129](#), [136](#)
- Crowther, P. A., Hadfield, L. J., Clark, J. S., Negueruela, I., and Vacca, W. D.: 2006, *MNRAS* **372**, 1407 [129](#)
- Cuffey, J.: 1973, *AJ* **78**, 408 [68](#)
- Dahm, S. E.: 2005, *AJ* **130**, 1805 [74](#)
- Damiani, F., Micela, G., Sciortino, S., Huélamó, N., Moitinho, A., Harnden, Jr., F. R., and Murray, S. S.: 2006, *A&A* **460**, 133 [74](#)
- De Becker, M., Rauw, G., Manfroid, J., and Eenens, P.: 2006a, *A&A* **456**, 1121 [41](#), [46](#)
- De Becker, M., Rauw, G., Sana, H., Pollock, A. M. T., Pittard, J. M., Blomme, R., Stevens, I. R., and van Loo, S.: 2006b, *MNRAS* **371**, 1280 [62](#)
- DeGioia-Eastwood, K., Throop, H., Walker, G., and Cudworth, K. M.: 2001, *ApJ* **549**, 578 [94](#), [99](#)
- Delgado, A. J., González-Martín, O., Alfaro, E. J., and Yun, J.: 2006, *ApJ* **646**, 269 [74](#)
- Dias, W. S., Alessi, B. S., Moitinho, A., and Lépine, J. R. D.: 2002, *A&A* **389**, 871 [20](#)
- Dickey, J. M. and Lockman, F. J.: 1990, *ARA&A* **28**, 215 [34](#)
- Dufton, P. L., Smartt, S. J., Lee, J. K., Ryans, R. S. I., Hunter, I., Evans, C. J., Herrero, A., Trundle, C., et al.: 2006, *A&A* **457**, 265 [84](#), [86](#)
- Dutra, C. M., Bica, E., Soares, J., and Barbuy, B.: 2003, *A&A* **400**, 533 [22](#)
- Ebeling, H., White, D. A., and Rangarajan, F. V. N.: 2006, *MNRAS* **368**, 65 [42](#)

REFERENCES

- Elmegreen, B. G., Lada, C. J., and Dickinson, D. F.: 1979, *ApJ* **230**, 415 [89](#)
- Evans, N. R., Schlegel, E. M., Waldron, W. L., Seward, F. D., Krauss, M. I., Nichols, J., and Wolk, S. J.: 2004, *ApJ* **612**, 1065 [100](#)
- Evans, N. R., Seward, F. D., Krauss, M. I., Isobe, T., Nichols, J., Schlegel, E. M., and Wolk, S. J.: 2003, *ApJ* **589**, 509 [100](#)
- Favata, F. and Micela, G.: 2003, *Space Sci. Rev.* **108**, 577 [10](#)
- Feigelson, E. D., Getman, K., Townsley, L., Garmire, G., Preibisch, T., Grosso, N., Montmerle, T., Muench, A., and McCaughrean, M.: 2005, *ApJS* **160**, 379 [48](#), [60](#), [63](#), [67](#), [72](#), [77](#), [82](#), [87](#), [92](#), [97](#), [103](#), [109](#), [115](#), [144](#), [145](#), [146](#)
- Feigelson, E. D. and Lawson, W. A.: 2004, *ApJ* **614**, 267 [31](#)
- Feigelson, E. D. and Montmerle, T.: 1999, *ARA&A* **37**, 363 [10](#), [11](#), [51](#)
- Flaccomio, E., Damiani, F., Micela, G., Sciortino, S., Harnden, Jr., F. R., Murray, S. S., and Wolk, S. J.: 2003, *ApJ* **582**, 398 [133](#)
- Freeman, P. E., Kashyap, V., Rosner, R., and Lamb, D. Q.: 2002, *ApJS* **138**, 185 [29](#)
- Froebrich, D., Scholz, A., and Raftery, C. L.: 2007, *MNRAS* **374**, 399 [22](#)
- Gagne, M., Caillault, J., Stauffer, J. R., and Linsky, J. L.: 1997, *ApJ* **478**, L87 [7](#)
- Getman, K. V., Feigelson, E. D., Broos, P. S., Townsley, L. K., and Garmire, G. P.: 2010, *ApJ* **708**, 1760 [54](#)
- Getman, K. V., Feigelson, E. D., Townsley, L., Broos, P., Garmire, G., and Tsujimoto, M.: 2006, *ApJS* **163**, 306 [4](#), [16](#), [31](#), [32](#), [34](#), [48](#)
- Getman, K. V., Flaccomio, E., Broos, P. S., Grosso, N., Tsujimoto, M., Townsley, L., Garmire, G. P., Kastner, J., et al.: 2005, *ApJS* **160**, 319 [32](#), [34](#), [132](#)
- Guarcello, M. G., Micela, G., Peres, G., Prisinzano, L., and Sciortino, S.: 2010, *A&A* **521**, A61 [85](#)
- Guarcello, M. G., Prisinzano, L., Micela, G., Damiani, F., Peres, G., and Sciortino, S.: 2007, *A&A* **462**, 245 [84](#)

REFERENCES

- Gudel, M., Guinan, E. F., and Skinner, S. L.: 1998, in R. A. Donahue & J. A. Bookbinder (ed.), *Cool Stars, Stellar Systems, and the Sun*, Vol. 154 of *Astronomical Society of the Pacific Conference Series*, pp 1041 [33](#)
- Guetter, H. H. and Turner, D. G.: 1997, *AJ* **113**, 2116 [65](#)
- Hamaguchi, K., Corcoran, M. F., Gull, T., Ishibashi, K., Pittard, J. M., Hillier, D. J., Damineli, A., Davidson, K., Nielsen, K. E., and Kober, G. V.: 2007, *ApJ* **663**, 522 [100](#)
- Hanson, M. M., Howarth, I. D., and Conti, P. S.: 1997, *ApJ* **489**, 698 [89](#)
- Henley, D. B., Corcoran, M. F., Pittard, J. M., Stevens, I. R., Hamaguchi, K., and Gull, T. R.: 2008, *ApJ* **680**, 705 [100](#)
- Hillenbrand, L. A.: 1997, *AJ* **113**, 1733 [4](#)
- Hillenbrand, L. A., Massey, P., Strom, S. E., and Merrill, K. M.: 1993, *AJ* **106**, 1906 [84](#), [85](#)
- Hillier, D. J., Davidson, K., Ishibashi, K., and Gull, T.: 2001, *ApJ* **553**, 837 [104](#)
- Hoffmeister, V. H., Chini, R., Scheyda, C. M., Schulze, D., Watermann, R., Nürnberger, D., and Vogt, N.: 2008, *ApJ* **686**, 310 [89](#), [91](#), [215](#)
- Howarth, I. D. and Prinja, R. K.: 1989, *ApJS* **69**, 527 [15](#)
- Huensch, M., Schmitt, J. H. M. M., Schroeder, K., and Reimers, D.: 1996, *A&A* **310**, 801 [32](#)
- Immler, S. and Lewin, W. H. G.: 2003, in K. Weiler (ed.), *Supernovae and Gamma-Ray Bursters*, Vol. 598 of *Lecture Notes in Physics*, Berlin Springer Verlag, pp 91–111 [12](#)
- Ishibashi, W. and Courvoisier, T.: 2010, *A&A* **512**, A58 [34](#)
- Jiang, Z., Yao, Y., Yang, J., Ando, M., Kato, D., Kawai, T., Kurita, M., Nagata, et al.: 2002, *ApJ* **577**, 245 [89](#)
- Johnson, H. L.: 1950, *ApJ* **112**, 240 [74](#)
- Kaler, J. B.: 1997, *Stars and their Spectra* [136](#)

REFERENCES

- Kaspi, V. M., Roberts, M. S. E., and Harding, A. K.: 2004, *ArXiv Astrophysics e-prints* [13](#)
- Kharchenko, N. V., Piskunov, A. E., Röser, S., Schilbach, E., and Scholz, R.: 2005, *A&A* **438**, 1163 [65](#), [69](#), [74](#), [99](#), [111](#)
- Knödlseeder, J.: 2000, *A&A* **360**, 539 [57](#)
- Kroupa, P.: 2001, *MNRAS* **322**, 231 [104](#)
- Kroupa, P., Gilmore, G., and Tout, C. A.: 1992, *AJ* **103**, 1602 [74](#)
- Kroupa, P., Tout, C. A., and Gilmore, G.: 1993, *MNRAS* **262**, 545 [3](#)
- Kudritzki, R. and Puls, J.: 2000, *ARA&A* **38**, 613 [15](#)
- Kuntz, K. D. and Snowden, S. L.: 2008, *A&A* **478**, 575 [127](#)
- Lada, C. J., Depoy, D. L., Merrill, K. M., and Gatley, I.: 1991, *ApJ* **374**, 533 [89](#)
- Lada, C. J. and Lada, E. A.: 2003, *ARA&A* **41**, 57 [2](#)
- Leass, E. A., Biller, B., Dame, T. M., and Megeath, S. T.: 2001, in *Bulletin of the American Astronomical Society*, Vol. 33 of *Bulletin of the American Astronomical Society*, pp 1439 [65](#)
- Leitherer, C., Schaerer, D., Goldader, J. D., Delgado, R. M. G., Robert, C., Kune, D. F., de Mello, D. F., Devost, D., and Heckman, T. M.: 1999, *ApJS* **123**, 3 [156](#)
- Leutenegger, M. A., Kahn, S. M., and Ramsay, G.: 2003, *ApJ* **585**, 1015 [10](#), [102](#)
- Leyder, J., Walter, R., and Rauw, G.: 2008, *A&A* **477**, L29 [100](#)
- Linsky, J. L., Gagné, M., Mytyk, A., McCaughrean, M., and Andersen, M.: 2007, *ApJ* **654**, 347 [85](#)
- Liu, Q. Z., van Paradijs, J., and van den Heuvel, E. P. J.: 2006, *A&A* **455**, 1165 [13](#)
- Lucy, L. B.: 1982, *ApJ* **255**, 286 [6](#)
- Lucy, L. B. and White, R. L.: 1980, *ApJ* **241**, 300 [6](#)
- Marco, A., Bernabeu, G., and Negueruela, I.: 2001, *AJ* **121**, 2075 [69](#)
- Marco, A. and Negueruela, I.: 2002, *A&A* **393**, 195 [69](#)

REFERENCES

- Martayan, C., Floquet, M., Hubert, A. M., Neiner, C., Frémat, Y., Baade, D., and Fabregat, J.: 2008, *A&A* **489**, 459 [84](#)
- Martins, F., Schaerer, D., and Hillier, D. J.: 2005, *A&A* **436**, 1049 [136](#)
- Massey, P. and Johnson, J.: 1993, *AJ* **105**, 980 [94](#), [96](#), [99](#), [101](#), [221](#)
- Massey, P., Johnson, K. E., and Degioia-Eastwood, K.: 1995, *ApJ* **454**, 151 [40](#), [44](#), [45](#), [51](#), [56](#), [68](#), [69](#), [71](#), [191](#)
- Melena, N. W., Massey, P., Morrell, N. I., and Zangari, A. M.: 2008, *AJ* **135**, 878 [78](#), [79](#), [80](#), [82](#), [83](#), [203](#)
- Mermilliod, J. and García, B.: 2001, in H. Zinnecker & R. Mathieu (ed.), *The Formation of Binary Stars*, Vol. 200 of *IAU Symposium*, pp 191 [9](#)
- Meyer, M. R., Adams, F. C., Hillenbrand, L. A., Carpenter, J. M., and Larson, R. B.: 2000, *Protostars and Planets IV* pp 121 [3](#)
- Mirabel, I. F., Rodrigues, I., and Liu, Q. Z.: 2004, *A&A* **422**, L29 [40](#)
- Mirtle, J., Altstadt, S., Ling, A., and McDonald, J.: 2008, *JRASC* **102**, 110 [64](#)
- Moffat, A. F. J. and Corcoran, M. F.: 2009, *ApJ* **707**, 693 [102](#)
- Moffat, A. F. J., Corcoran, M. F., Stevens, I. R., Skalkowski, G., Marchenko, S. V., Mücke, A., Ptak, A., Koribalski, et al.: 2002, *ApJ* **573**, 191 [79](#)
- Moffat, A. F. J., Drissen, L., and Shara, M. M.: 1994, *ApJ* **436**, 183 [78](#)
- Moffat, A. F. J., Shara, M. M., and Potter, M.: 1991, *AJ* **102**, 642 [111](#)
- Moitinho, A., Alves, J., Huélamo, N., and Lada, C. J.: 2001, *ApJ* **563**, L73 [74](#)
- Montmerle, T., Grosso, N., Tsuboi, Y., and Koyama, K.: 2000, *ApJ* **532**, 1097 [11](#)
- Moore, S. L.: 2008, *Journal of the British Astronomical Association* **118**, 108 [64](#)
- Moretti, A., Campana, S., Lazzati, D., and Tagliaferri, G.: 2003, *ApJ* **588**, 696 [34](#)
- Muno, M. P., Clark, J. S., Crowther, P. A., Dougherty, S. M., de Grijs, R., Law, C., McMillan, S. L. W., Morris, M. R., et al.: 2006a, *ApJ* **636**, L41 [105](#), [110](#), [117](#), [118](#)

REFERENCES

- Muno, M. P., Gaensler, B. M., Clark, J. S., de Grijs, R., Pooley, D., Stevens, I. R., and Portegies Zwart, S. F.: 2007, *MNRAS* **378**, L44 [105](#), [110](#), [117](#), [118](#)
- Muno, M. P., Law, C., Clark, J. S., Dougherty, S. M., de Grijs, R., Portegies Zwart, S., and Yusef-Zadeh, F.: 2006b, *ApJ* **650**, 203 [15](#), [105](#), [117](#), [135](#)
- Nazé, Y.: 2009, *A&A* **506**, 1055 [138](#), [142](#), [143](#)
- Nazé, Y., Rauw, G., and Manfroid, J.: 2008, *A&A* **483**, 171 [112](#)
- Negueruela, I. and Clark, J. S.: 2005, *A&A* **436**, 541 [104](#)
- Negueruela, I., Clark, J. S., and Ritchie, B. W.: 2010, *A&A* **516**, A78 [105](#), [107](#), [234](#)
- Negueruela, I., Marco, A., Israel, G. L., and Bernabeu, G.: 2007, *A&A* **471**, 485 [69](#)
- Nielbock, M., Chini, R., Jütte, M., and Manthey, E.: 2001, *A&A* **377**, 273 [89](#)
- Norci, L., Hartwell, J., and Meurs, E. J. A.: 2006, in E. J. A. Meurs & G. Fabiano (ed.), *Populations of High Energy Sources in Galaxies*, Vol. 230 of *IAU Symposium*, pp 408–409 [156](#)
- Nürnberg, D. E. A.: 2003, *A&A* **404**, 255 [78](#)
- Oskinova, L. M.: 2005, *MNRAS* **361**, 679 [2](#), [5](#), [6](#), [123](#), [134](#), [136](#), [147](#), [148](#), [150](#), [156](#)
- Oskinova, L. M., Hamann, W., Feldmeier, A., Ignace, R., and Chu, Y.: 2009, *ApJ* **693**, L44 [9](#)
- Oskinova, L. M., Ignace, R., Hamann, W.-R., Pollock, A. M. T., and Brown, J. C.: 2003, *A&A* **402**, 755 [9](#)
- Piatti, A. E., Bica, E., and Claria, J. J.: 1998, *A&AS* **127**, 423 [104](#), [111](#)
- Piskunov, A. E., Kharchenko, N. V., Röser, S., Schilbach, E., and Scholz, R.: 2006, *A&A* **445**, 545 [26](#)
- Pollock, A. M. T.: 1987, *ApJ* **320**, 283 [9](#)
- Povich, M. S., Stone, J. M., Churchwell, E., Zweibel, E. G., Wolfire, M. G., Babler, B. L., Indebetouw, R., Meade, M. R., and Whitney, B. A.: 2007, *ApJ* **660**, 346 [89](#)

REFERENCES

- Preibisch, T. and Feigelson, E. D.: 2005, *ApJS* **160**, 390 [61](#), [64](#), [68](#), [73](#), [77](#), [88](#), [104](#), [110](#), [116](#), [146](#), [151](#)
- Prilutskii, O. F. and Usov, V. V.: 1976, *Soviet Ast.* **20**, 2 [9](#)
- Rauw, G. and De Becker, M.: 2004, *A&A* **421**, 693 [40](#)
- Rauw, G., Manfroid, J., Gosset, E., Nazé, Y., Sana, H., De Becker, M., Foellmi, C., and Moffat, A. F. J.: 2007, *A&A* **463**, 981 [111](#), [113](#), [240](#)
- Robin, A. C., Reylé, C., Derrière, S., and Picaud, S.: 2003, *A&A* **409**, 523 [32](#)
- Russeil, D.: 2003, *A&A* **397**, 133 [89](#)
- Salpeter, E. E.: 1955, *ApJ* **121**, 161 [3](#)
- Sana, H., Rauw, G., Nazé, Y., Gosset, E., and Vreux, J.: 2006, *MNRAS* **372**, 661 [143](#)
- Sanchawala, K., Chen, W., Lee, H., Chu, Y., Nakajima, Y., Tamura, M., Baba, D., and Sato, S.: 2007a, *ApJ* **656**, 462 [99](#), [100](#)
- Sanchawala, K., Chen, W., Ojha, D., Ghosh, S. K., Nakajima, Y., Tamura, M., Baba, D., Sato, S., and Tsujimoto, M.: 2007b, *ApJ* **667**, 963 [94](#), [99](#)
- Schmitt, J. H. M. M.: 1997, *A&A* **318**, 215 [32](#)
- Schmitt, J. H. M. M., Fleming, T. A., and Giampapa, M. S.: 1995, *ApJ* **450**, 392 [32](#)
- Schulz, N. S., Canizares, C., Huenemoerder, D., and Tibbets, K.: 2003, *ApJ* **595**, 365 [8](#), [142](#)
- Seward, F. D., Butt, Y. M., Karovska, M., Prestwich, A., Schlegel, E. M., and Corcoran, M.: 2001, *ApJ* **553**, 832 [10](#), [102](#)
- Seward, F. D. and Chlebowski, T.: 1982, *ApJ* **256**, 530 [6](#)
- Sharma, S., Pandey, A. K., Ojha, D. K., Chen, W. P., Ghosh, S. K., Bhatt, B. C., Maheswar, G., and Sagar, R.: 2007, *MNRAS* **380**, 1141 [69](#)
- Shi, H. M. and Hu, J. Y.: 1999, *A&AS* **136**, 313 [40](#), [56](#)
- Siess, L., Dufour, E., and Forestini, M.: 2000, *A&A* **358**, 593 [46](#)

REFERENCES

- Skinner, S. L., Zhekov, S. A., Güdel, M., Schmutz, W., and Sokal, K. R.: 2010, *AJ* **139**, 825 [9](#), [38](#), [108](#)
- Smith, R. K., Brickhouse, N. S., Liedahl, D. A., and Raymond, J. C.: 2001, *ApJ* **556**, L91 [37](#), [130](#)
- Stevens, I. R. and Hartwell, J. M.: 2003, *MNRAS* **339**, 280 [14](#), [15](#), [130](#), [147](#), [150](#)
- Stolte, A., Brandner, W., Brandl, B., Zinnecker, H., and Grebel, E. K.: 2004, *AJ* **128**, 765 [78](#)
- Sung, H. and Bessell, M. S.: 2004, *AJ* **127**, 1014 [78](#), [79](#), [82](#)
- Tapia, M., Costero, R., Echevarria, J., and Roth, M.: 1991, *MNRAS* **253**, 649 [68](#), [69](#)
- Tapia, M., Roth, M., Vázquez, R. A., and Feinstein, A.: 2003, *MNRAS* **339**, 44 [39](#), [94](#), [99](#)
- Townsley, L. K.: 2006, *ArXiv Astrophysics e-prints* [94](#), [98](#), [112](#)
- Townsley, L. K., Feigelson, E. D., Montmerle, T., Broos, P. S., Chu, Y., and Garmire, G. P.: 2003, *ApJ* **593**, 874 [89](#)
- Tsujimoto, M., Feigelson, E. D., Townsley, L. K., Broos, P. S., Getman, K. V., Wang, J., Garmire, G. P., Baba, D., Nagayama, T., Tamura, M., and Churchwell, E. B.: 2007, *ApJ* **665**, 719 [111](#), [112](#)
- Vazquez, R. A., Baume, G., Feinstein, A., and Prado, P.: 1996, *A&AS* **116**, 75 [94](#)
- Velázquez, P. F., Koenigsberger, G., and Raga, A. C.: 2003, *ApJ* **584**, 284 [12](#), [131](#)
- Verner, E., Bruhweiler, F., and Gull, T.: 2005, *ApJ* **624**, 973 [102](#)
- Vuong, M. H., Montmerle, T., Grosso, N., Feigelson, E. D., Verstraete, L., and Ozawa, H.: 2003, *A&A* **408**, 581 [33](#)
- Walborn, N. R., Howarth, I. D., Lennon, D. J., Massey, P., Oey, M. S., Moffat, A. F. J., Skalkowski, G., Morrell, N. I., Drissen, L., and Parker, J. W.: 2002, *AJ* **123**, 2754 [94](#)
- Wang, J., Townsley, L. K., Feigelson, E. D., Getman, K. V., Broos, P. S., Garmire, G. P., and Tsujimoto, M.: 2007, *ApJS* **168**, 100 [4](#), [16](#), [48](#)

REFERENCES

- Wang, Q. D., Dong, H., and Lang, C.: 2006, *MNRAS* **371**, 38 [156](#)
- Westerlund, B.: 1961, *PASP* **73**, 51 [104](#), [110](#)
- Whitmore, B. C.: 2000, *ArXiv Astrophysics e-prints* [1](#)
- Wilms, J., Allen, A., and McCray, R.: 2000, *ApJ* **542**, 914 [37](#)
- Wright, N. J. and Drake, J. J.: 2009, *ApJS* **184**, 84 [58](#), [59](#), [62](#), [176](#), [181](#)